Sergio M. Savaresi
Mara Tanelli

Advances in Industrial Control

Active Braking Control Systems Design for Vehicles

Springer

Advances in Industrial Control

Other titles published in this series:

Digital Controller Implementation and Fragility
Robert S.H. Istepanian and James F. Whidborne (Eds.)

Optimisation of Industrial Processes at Supervisory Level
Doris Sáez, Aldo Cipriano and Andrzej W. Ordys

Robust Control of Diesel Ship Propulsion
Nikolaos Xiros

Hydraulic Servo-systems
Mohieddine Jelali and Andreas Kroll

Model-based Fault Diagnosis in Dynamic Systems Using Identification Techniques
Silvio Simani, Cesare Fantuzzi and Ron J. Patton

Strategies for Feedback Linearisation
Freddy Garces, Victor M. Becerra, Chandrasekhar Kambhampati and Kevin Warwick

Robust Autonomous Guidance
Alberto Isidori, Lorenzo Marconi and Andrea Serrani

Dynamic Modelling of Gas Turbines
Gennady G. Kulikov and Haydn A. Thompson (Eds.)

Control of Fuel Cell Power Systems
Jay T. Pukrushpan, Anna G. Stefanopoulou and Huei Peng

Fuzzy Logic, Identification and Predictive Control
Jairo Espinosa, Joos Vandewalle and Vincent Wertz

Optimal Real-time Control of Sewer Networks
Magdalene Marinaki and Markos Papageorgiou

Process Modelling for Control
Benoît Codrons

Computational Intelligence in Time Series Forecasting
Ajoy K. Palit and Dobrivoje Popovic

Modelling and Control of Mini-Flying Machines
Pedro Castillo, Rogelio Lozano and Alejandro Dzul

Ship Motion Control
Tristan Perez

Hard Disk Drive Servo Systems (2nd Ed.)
Ben M. Chen, Tong H. Lee, Kemao Peng and Venkatakrishnan Venkataramanan

Measurement, Control, and Communication Using IEEE 1588
John C. Eidson

Piezoelectric Transducers for Vibration Control and Damping
S.O. Reza Moheimani and Andrew J. Fleming

Manufacturing Systems Control Design
Stjepan Bogdan, Frank L. Lewis, Zdenko Kovačić and José Mireles Jr.

Windup in Control
Peter Hippe

Nonlinear H_2/H_∞ Constrained Feedback Control
Murad Abu-Khalaf, Jie Huang and Frank L. Lewis

Practical Grey-box Process Identification
Torsten Bohlin

Control of Traffic Systems in Buildings
Sandor Markon, Hajime Kita, Hiroshi Kise and Thomas Bartz-Beielstein

Wind Turbine Control Systems
Fernando D. Bianchi, Hernán De Battista and Ricardo J. Mantz

Advanced Fuzzy Logic Technologies in Industrial Applications
Ying Bai, Hanqi Zhuang and Dali Wang (Eds.)

Practical PID Control
Antonio Visioli

(continued after Index)

Sergio M. Savaresi · Mara Tanelli

Active Braking Control Systems Design for Vehicles

Springer

Prof. Sergio M. Savaresi
Dr. Mara Tanelli

Politecnico di Milano
Dipartimento di Elettronica e Informazione (DEI)
Via Ponzio 34/5
20133 Milano
Italy

savaresi@elet.polimi.it
tanelli@elet.polimi.it

ISSN 1430-9491
ISBN 978-1-84996-349-7 e-ISBN 978-1-84996-350-3
DOI 10.1007/978-1-84996-350-3
Springer London Dordrecht Heidelberg New York

British Library Cataloguing in Publication Data
A catalogue record for this book is available from the British Library

Library of Congress Control Number: 2010934758

Cover design: eStudioCalamar, Girona/Berlin

Printed on acid-free paper

Springer is part of Springer Science+Business Media (www.springer.com)

Advances in Industrial Control

Professor (Emeritus) O.P. Malik
Department of Electrical and Computer Engineering
University of Calgary
2500, University Drive, NW
Calgary, Alberta
T2N 1N4
Canada

Professor K.-F. Man
Electronic Engineering Department
City University of Hong Kong
Tat Chee Avenue
Kowloon
Hong Kong

Professor G. Olsson
Department of Industrial Electrical Engineering and Automation
Lund Institute of Technology
Box 118
S-221 00 Lund
Sweden

Professor A. Ray
Department of Mechanical Engineering
Pennsylvania State University
0329 Reber Building
University Park
PA 16802
USA

Professor D.E. Seborg
Chemical Engineering
3335 Engineering II
University of California Santa Barbara
Santa Barbara
CA 93106
USA

Doctor K.K. Tan
Department of Electrical and Computer Engineering
National University of Singapore
4 Engineering Drive 3
Singapore 117576

Professor I. Yamamoto
Department of Mechanical Systems and Environmental Engineering
The University of Kitakyushu
Faculty of Environmental Engineering
1-1, Hibikino,Wakamatsu-ku, Kitakyushu, Fukuoka, 808-0135
Japan

To Cristina, Claudio and Stefano (S.M.S.)
To Marco (M.T.)

Series Editors' Foreword

The series *Advances in Industrial Control* aims to report and encourage technology transfer in control engineering. The rapid development of control technology has an impact on all areas of the control discipline. New theory, new controllers, actuators, sensors, new industrial processes, computer methods, new applications, new philosophies…, new challenges. Much of this development work resides in industrial reports, feasibility study papers and the reports of advanced collaborative projects. The series offers an opportunity for researchers to present an extended exposition of such new work in all aspects of industrial control for wider and rapid dissemination.

Over the last few decades, automobile technology has evolved considerably. One direction for this evolution has been the introduction of engines that use a wide range of fuels, including petrol, diesel, and ethanol, and that can operate in dual fuel mode. The electric car has also begun to gain a market share, especially the small *runabout-the-town* vehicle; however, perhaps an equally important development is the introduction of electronic components to manage car operations and in some cases replace or significantly modify mechanical components. A relevant example is the adoption of *brake-by-wire*. The use of electronic components in automobiles has a number of benefits for car manufacturers:

- Electronic components allow units to be mass-produced and modularised and these are more easily fitted giving a reduction in assembly time and manufacturing costs.
- If components are electronic, manual tuning can be avoided and plug-in computer-based tuning used instead; this gives better reliability in the tuning process, and also reduces assembly time and costs.
- Using electronic components and eliminating mechanical linkages releases space, and reduces car weight; thus manufacturers are able to introduce new design features that improve and diversify the automobile product thereby gaining a market advantage.

There are also benefits for the car purchaser, the driver and the passenger:

- The design freedom that electronic components create brings more diversity of choice for the purchaser in engine type and management, with better fuel economy, a better ride and more interior space.
- Cars are more reliable and safer, even if the driver understands less of what goes on under the bonnet. In addition, routine maintenance becomes a computer-based operation that is speedier and more consistent than manual procedures.
- The driver interface is much more sophisticated giving more "drive" information to the driver; from this should flow safer driving as the driver is more aware of the potential hazards they may have to cope with.

The opportunities flowing from the use of electronic components include the use of better and more advanced control strategies that reduce fuel consumption, limit emissions, improve ride control and make braking a better and safer operation. It is this last topic that concerns this *Advances in Industrial Control* monograph by Sergio M. Savaresi and Mara Tanelli which comes in three parts. Part I, comprising two chapters, supplies the context for the use of control system design in braking systems. There is an instructive introduction including a historical perspective section (Chapter 1) and a thorough presentation of the models used in the study of braking systems and their control (Chapter 2). Part II, comprising three chapters, reports the basic braking system control design solutions (Chapters 3 and 4) and the methods for the identification of the longitudinal wheel slip parameter (Chapter 5). Part III, comprising three chapters, reports more advanced design solutions, and more identification of driving parameters, this time, road–tyre friction parameters. Two very useful appendices on some aspects of nonlinear control that are used by the authors and on the practical issues relating to wheel encoder signal processing close the monograph.

Sergio M. Savaresi and Mara Tanelli have produced a comprehensive monograph that succeeds in showing how advanced control can contribute to the design of new braking system technologies. Industrial and academic readers will find the volume quite accessible; academic control lecturers may find the case studies can be used to demonstrate industrial control theory in practice. Overall, the monograph is highly topical and industrially relevant and will find many interested readers from the control community and the automobile industry. The series Editors are pleased to have this monograph in the series since it nicely complements the recent series monograph by Pietro J. Dolcini, Carlos Canudas-de-Wit and Hubert Béchart titled *Dry Clutch Control for Automotive Applications* (ISBN: 978-1-84996-067-0, 2010) and ensures that the series continues to report on the growing field of advanced control applications in the automobile industry.

Industrial Control Centre
Glasgow
Scotland, UK
2010

M.J. Grimble
M.A. Johnson

Preface

The control of wheel slip dynamics is one of the most critical and intriguing areas of chassis control, since it is the basis for most of the main chassis control subsystems like braking control, traction control and stability control. Moreover, it is an unusual combination of seemingly simple dynamics (whose dominant features can be easily captured by a second-order dynamical model) and challenging features (nonlinear behaviour, stability properties which change according to the considered working condition, time-varying parameters, large parameter variations, unknown environment-dependent parameters, *etc.*).

This book is mainly devoted to the analysis and development of wheel slip control strategies. However, to keep the book focused and to perform the analysis in depth, most of the work presented here refers to the specific problem of controlling the longitudinal dynamics of a vehicle during braking.

There are three main reasons for focusing on *braking control*, while keeping traction control and stability control in the background:

- Braking control is the first chassis control subsystem to be made available to the mass market. Anti-lock braking systems (ABS) have become a standard for all modern cars, whereas traction control and stability control subsystems are still confined to be niche applications.
- Braking control must face the challenge of the coordination of the braking force on all the wheels, whereas traction control is typically limited to half of the vehicle wheels, *i.e.*, the driving ones.
- Braking control is also self consistent and meaningful when the analysis is restricted to longitudinal dynamics, whereas stability control inherently requires the coupling of longitudinal, lateral and yaw dynamics.

Needless to say, all the material developed for the specific problem of controlling the wheel slip during braking can be straightforwardly re-used also within traction and stability control problems.

From the technological point of view, the design of automatic braking control systems is clearly highly dependent on the braking system characteristics and actuator performance.

As a matter of fact, ABS systems for wheeled vehicles equipped with traditional hydraulic actuated brakes – that is, those commonly available in all passenger cars – pose specific design constraints as they have to cope with an *on/off* modulation of the brake pressure. On the other hand, recent technological advances in actuators which have led to both electro-hydraulic and electro-mechanical braking systems have radically changed the starting point of braking control systems design. In fact, these brake systems enable a continuous modulation of the braking torque, thereby allowing the use of classical control theory tools for controller design.

A great boost to the research in this field comes directly from the industrial world, which poses challenging problems by asking for reliable control systems with the simplest possible architecture, reduced sensors layout and the capability of coping with transmission delays and significant measurement errors and parametric uncertainties.

This book develops within this challenging and evolving context, with the aim of providing a thorough analysis of active braking control systems and proposing both basic and innovative solutions, which are both effective and applicable from an industrial viewpoint and theoretically sound from a methodological perspective.

In particular, the book is devoted to the analysis and design of active braking control systems together with the main estimation and identification problems that arise in the braking control context.

The considered control design problems are linked to two different brake technologies. Namely, braking control systems based on classical hydraulic actuated brakes (HAB) with *on-off* dynamics and braking control systems tailored to brake-by-wire (BBW) control, in particular based on electromechanical brakes (EMB).

The BBW control approaches can be further split into two main families, because of the fact that the control algorithms are based either on linearised or nonlinear models of the braking dynamics.

The book shows how these different control approaches are complementary, in that each of them has specific peculiarities either in terms of performance or in terms of structural properties of the closed-loop system.

Finally, the book presents some original approaches to three different estimation and identification problems closely related to braking control systems design, namely

- estimation of the longitudinal wheel slip;
- estimation of the tyre–road friction coefficient; and
- direct estimation of tyre–road contact forces *via* in-tyre sensors,

with the aim of providing the reader with a comprehensive treatment of active vehicle braking control from a wider perspective. A significant part of

the work presented in the book was developed within joint projects between the Politecnico di Milano and leading automotive industries, thereby being firmly linked to industrial reality.

Contributions and Organisation of the Book

The book includes survey sections, where the problem and the methodologies are introduced in a historical and tutorial framework, to suit a wide readership. Therefore, this book can be effectively accessed at three reading levels: a tutorial level for students, an application-oriented level for engineers and practitioners and a methodology-oriented level for researchers.

To enforce these different reading levels and to present the material in an incremental manner from the basic to the most advanced control approaches, the book has been conceptually divided into three parts.

The *first part* of the book is composed of *Chapters 1* and *2*: the former provides the introductory material on the history of ABS systems and their development and future perspectives together with the description of the different braking systems considered in this book and their mathematical description, whereas the latter introduces the control-oriented dynamical models of the braking dynamics.

The *second part* of the book is composed of Chapters 3, 4 and 5, which deal with the main aspects of both control and estimation issues. Specifically, Chapters 3 and 4 are devoted to presenting the basic solutions to braking control systems design, according to the two different types of actuators; *Chapter 3* discusses the design of braking controllers based on actuators with continuous dynamics, whereas *Chapter 4* treats in detail the case of braking systems with on/off dynamics. Furthermore, *Chapter 5* studies a fundamental estimation problem that is inextricably linked with active braking controller design: the wheel slip estimation.

The *third part* of the book presents more advanced and research-oriented solutions both to active braking control systems design and to tyre–road friction estimation. Specifically, *Chapter 6* discusses the mixed slip-deceleration control, which is an advanced control solution based on linearised models of the braking dynamics, while *Chapter 7* presents a nonlinear control approach to wheel slip regulation, grounded on Lyapunov-based synthesis methods, which yields a particular closed-loop behaviour having practical advantages. Finally, *Chapter 8* addresses the problem of estimating the tyre–road friction conditions and outlines a method to directly estimate the contact forces from sensors inserted in the tyre.

In writing the book, we assumed that the reader is familiar with basic notions of dynamical systems and linear control systems design. Accordingly, we complemented the book with *Appendix A*, which provides the basic defini-

tions and the notions of the nonlinear systems analysis and synthesis methods employed in the book. This Appendix is intended to provide only a quick tutorial reference to these topics, a thorough study of which should be pursued using specialist books, some of which are referenced in the Appendix itself.

Finally, *Appendix B* provides a dedicated treatment to the problem of estimating the wheel speed from encoders, which are the fundamental sensors that one has to deal with when developing active braking and traction control systems. The Appendix presents the two main speed estimation algorithms and highlights their merits and drawbacks, presenting also some insights on signal filtering issues arising from the analysis of experimental data.

Overall, the first two parts of the book present the topic at a level of depth that can be considered appropriate for practitioners and for a course on vehicle control at the MSc level, while the third part can constitute additional material of interest for graduate studies and for researchers in automotive control.

Milano, *Sergio Matteo Savaresi*
July 19, 2010 *Mara Tanelli*

Acknowledgements

This book is the result of several years of collaborations both with academic and industrial partners. Some of the results of these collaborations have been reported in the papers [21, 73, 90, 92, 93, 105–111, 113, 115–120].

We are grateful to all our co-authors: Alessandro Astolfi, Ivo Boniolo, Sebastiano Campo, Carlo Cantoni, Fabio Codecà, Matteo Corno, Mario di Bernardo, Luigi del Re, Luca Fabbri, Andrea Fortina, Alessandra Gragnani, Peter Langthaler, Alessandro Mergenthaler, Alessandro Moia, Gustavo Osorio, Giulio Panzani, Luigi Piroddi, Maria Prandini, Roberto Sartori and Annalisa Zappavigna for all the stimulating discussions and for their constant help and friendship.

In the industrial world, we are particularly indebted to Carlo Cantoni of Brembo S.p.A., Luca Fabbri of Piaggio Group S.p.A., and to Sebastiano Campo of FIAT Automobiles S.p.A. for their constant support and interest in investigating advanced solutions and for providing us with an industrial perspective on several research topics.

The material presented in this book was also developed thanks to the activity of the motor vehicle control team (http://move.dei.polimi.it/) of the Politecnico di Milano: we would like to thank all its present and past members for their collaboration in all these years, with a special mention for Matteo Corno. We are grateful to Matteo for his help, his insight and his endless passion for research.

Further, we want to thank all our present and former students, who helped us to organise and refine the presentation of the different topics since the beginning of the course on Vehicle Control at the Politecnico di Milano.

We are especially indebted to Alessandro Astolfi, Mario di Bernardo and Luigi del Re for all the joint work and for their hospitality when visiting their institutions. We also would like to thank Guido Guardabassi for his help and patience in reviewing the draft of this book.

Finally, we want to thank Professor Robin Sharp and Professor Björn Wittenmark for the time they devoted to reading and evaluating the Ph.D. thesis which constituted the starting point for this book and for the constructive

comments which helped to improve the thesis contents and guide its evolution toward this book.

Contents

List of Abbreviations xxi

Part I Braking Control Systems Design: Introduction and Modelling

1 Introduction to Active Braking Control Systems 3
1.1 Introduction 3
1.2 ABS Systems: a Historical Perspective 4
1.3 The Actuators: Main Technologies and Functional Description 5
1.4 The X-by-wire Approach 11
1.5 State-of-the-art in Active Braking Control Design 12
1.6 Recent Evolutions: Brake-based Global Chassis Control 14
1.7 Summary 16

2 Control-oriented Models of Braking Dynamics 17
2.1 Introduction 17
2.2 Tyre–road Contact Forces 17
2.2.1 Friction Models 20
2.2.2 Relaxation Dynamics 24
2.3 The Single-corner Model 24
2.4 The Double-corner Model 27
2.5 Linearised Models and Dynamic Analysis 30
2.5.1 Single-corner Model Analysis 31
2.5.2 Double-corner Model Analysis 42
2.6 Summary 52

Part II Braking Control Systems Design: Basic Solutions

3 Braking Control Systems Design: Actuators with Continuous Dynamics 55
3.1 Introduction 55

3.2 Wheel Slip Control 55
3.3 Wheel Deceleration Control 58
3.4 Linear Wheel Slip Controller Design 61
3.5 Effects of Actuator Dynamics 65
3.6 Performance Analysis: a Numerical Example 67
3.7 Activation and Deactivation Logic 69
3.7.1 Activation Conditions 71
3.7.2 De-activation Conditions 72
3.8 Slip Controller Analysis Based on the Double-corner Model . . 74
3.8.1 Closed-loop Stability Analysis 75
3.8.2 Controlling the Rear Wheel: Slip *versus* Relative Slip Control 78
3.8.3 Wheel Slip Control on Curves 82
3.9 Summary 84

4 Braking Control Systems Design: Actuators with Discrete Dynamics 85
4.1 Introduction 85
4.2 Problem Setting 86
4.3 Existence and Stability of Limit Cycles 90
4.4 Limit Cycle Stability Analysis 99
4.5 Effects of the Actuator Rate-limit Variation 100
4.6 Summary of the Actuators' Performance 103
4.7 Summary 105

5 Longitudinal Wheel Slip Estimation 107
5.1 Introduction 107
5.2 Interaction Between Braking Control and Speed Estimation . . 108
5.3 A Solution for Vehicle Speed Estimation 112
5.4 Performance Evaluation of the Estimation Algorithm 116
5.5 Summary 119

Part III Braking Control Systems Design: Advanced Solutions

6 Mixed Slip and Deceleration Control 123
6.1 Introduction 123
6.2 Mixed Slip-deceleration Control 123
6.2.1 Analysis of the Open-loop Dynamics 126
6.2.2 Closed-loop Stability for MSD Control 127
6.3 Disturbance Analysis of Slip Control and MSD Control 130
6.4 Steady-state Slip Values in MSD Control 136
6.5 Numerical Analysis 138
6.6 Summary 141

7 Nonlinear Wheel Slip Control Design 143
7.1 Introduction 143
7.2 Lyapunov-based Wheel Slip Control 144
7.2.1 Assumptions 145
7.2.2 Controller Design 145
7.3 Numerical Analysis 155
7.4 Summary 157

8 Identification of Tyre–road Friction Conditions 159
8.1 Introduction 159
8.2 Detection of the Friction-curve Peak by Wheel-deceleration Measurements 160
8.2.1 Online Detection of the Sign of the Friction Curve Slope 161
8.2.2 ABS Supervisory Control Logic 163
8.2.3 Experimental Results 164
8.3 Real-time Identification of Tyre–road Friction Conditions 166
8.3.1 Identification Strategies 169
8.3.2 Numerical Analysis 171
8.3.3 Experimental Results 177
8.4 Direct Estimation of Contact Forces *via* In-tyre Sensors 182
8.4.1 Introduction 183
8.4.2 Experimental Set Up 185
8.4.3 Main Concept 185
8.4.4 Signal Processing 188
8.4.5 Experimental Results 195
8.5 Summary 198

A Analysis and Synthesis Tools for Dynamical Systems 201
A.1 Introduction 201
A.2 Dynamical Systems Analysis 202
A.2.1 Stability of Equilibrium Points: Lyapunov's Theory . . . 206
A.2.2 A Special Case: Second-order Dynamical Systems 214
A.3 Nonlinear Design Tools 223
A.4 Summary 227

B Signal Processing of Wheel Encoders 229
B.1 Introduction 229
B.2 Wheel Encoders' Signals 229
B.2.1 Velocity Estimation Algorithms 231
B.2.2 Wheel Radius Calibration 237
B.3 Analysis and Filtering of the Wheel Encoders' Signal 240
B.4 Summary 243

References 245

Index 253

List of Abbreviations

The following abbreviations are used throughout the book.

ABS	Anti-lock braking system
BBW	Brake-by-wire
BVP	Boundary value problem
CAN	Controller area network
ECU	Electronic control unit
EHB	Electro-hydraulic brake
EMB	Electro-mechanical brake
ESC	Electronic stability control
ESP	Electronic stability program
FIR	Finite impulse response
FSM	Finite state machine
GAS	Globally asymptotically stable
GES	Globally exponentially stable
GCC	Global chassis control
GPS	Global positioning system
HMI	Human machine interface
IBCU	Intelligent braking control unit
LAS	Locally asymptotically stable
LS	Least squares
MIMO	Multiple input multiple output
ML	Maximum likelihood
MSD	Mixed slip deceleration
OEM	Original equipment manufacturer
RLS	Recursive least squares
RML	Recursive maximum likelihood
SISO	Single input single output
TSC	Traction control system
VDC	Vehicle dynamics control
XBW	X-by-wire

Part I
Braking Control Systems Design: Introduction and Modelling

This part of the book starts presenting the history of active braking control systems, followed by a discussion on their industrial and academic development and the future research perspectives. Furthermore, the functional description of the braking systems considered in this book is provided, together with their mathematical description. Finally, the control-oriented dynamical models of the braking dynamics used for controller design are discussed. Overall, these topics constitute the introductory material based on which all the considered control approaches tackled in the subsequent parts of the book are developed.

Chapter 1
Introduction to Active Braking Control Systems

1.1 Introduction

It can be certainly acknowledged that skidding has been a problem for as long as wheeled vehicles have existed. A 1952 paper by A.C. Gunsaulus of Goodyear Aircraft Corporation [28] defines skidding as simply the "unwanted sideways movement [of an automotive vehicle] not planned by the driver... Its prime cause is a combination of a lessened grip of the tyre on the road coupled with a sideways force that is greater than the tyre's grip. Its effect is usually a partial or, it may be, a total loss of control of the vehicle by the driver."

In road vehicles, the unwanted skidding phenomenon can be prevented by means of active braking control systems.

As a matter of fact, most modern road vehicles are equipped with electronic ABS. ABS can greatly improve the safety of a vehicle in extreme circumstances, since it can maximise the longitudinal tyre–road friction while keeping large lateral (directional) forces that ensure vehicle driveability. The use of automatic braking control systems has also been extended to electronic stability control (ESC) systems (see, *e.g.*, [27, 39, 45, 88]).

The design of automatic braking control systems is clearly highly dependent on the braking system characteristics and actuator performance. As is well known, standard ABS systems for wheeled vehicles equipped with traditional hydraulic actuators mainly use rule-based control logics (see, *e.g.*, [124]).

On the other hand, recent technological advances in actuators have led to both electro-hydraulic and electro-mechanical braking systems, which enable a continuous modulation of the braking torque, thereby allowing us to formulate active braking control as a classical regulation problem (see, *e.g.*, [15, 23, 41, 90]). In the field of automatic braking control, a large number of methods and approaches have been proposed in the last decade, rang-

ing from classical regulation loops, to sliding-mode, fuzzy-neural, or hybrid architectures (see, *e.g.*, [15, 38, 39, 53, 54, 59, 60, 95, 101, 122]).

This chapter will provide an overview of ABS systems, both in terms of their historical development and of the results in this field available in the scientific literature. Further, the main features of the brake systems considered in this book are discussed and their mathematical description is provided. Finally, the chapter offers a brief discussion on recent evolutions in active chassis control systems which involve the braking controllers as subsystems to achieve the so-called global chassis control (GCC).

1.2 ABS Systems: a Historical Perspective

The current hydraulic ABS systems were conceived from systems developed for trains in the early 1900s. In particular, the first patents in the field (*An Improved Safety Device for Preventing the Jamming of the Running Wheels of Automobiles when Braking*) dates back to 1932, while a similar result was reported in a U.S. patent (*Apparatus for Preventing Wheel Sliding*) issued in 1936.

Nevertheless, none of these early devices could react quickly enough to the wheels locking to lessen the stopping distance or to provide greater vehicle control in a panic situation. The problem of skidding wheels gained new prominence during the Second World War with the success of air warfare. After the war, several aircraft producers and their subcontractors began to work on designing an anti-skid device for aircraft brakes. In 1947, the first use of anti-lock brakes on airplanes was on B-47 bombers to avoid tyre blowout on dry concrete and spin-outs on icy runways. Mechanical skid prevention devices appeared on both military and commercial planes in the early 1950s.

The first automotive use of ABS was in 1954 on a limited number of Lincoln cars which were equipped with an ABS from a French aircraft. In 1965, Jensen FF offered a mechanical ABS system developed by Dunlop. In the late 1960s, Ford, Chrysler and Cadillac offered ABS on their top-end models. These very first systems used analogue computers and vacuum-actuated modulators. Since the vacuum actuated modulators cycled very slowly, the actual vehicle stopping distance significantly increased, even though the level of safety improved and the lateral stability of the vehicle increased.

In Japan, Nissan and Toyota announced the development of an electronic ABS system, while in Germany a joint-venture between Telefunken and Bendix was trying to put an ABS system called Tekline on the market. However, the electronic design tools were not reliable yet and the analogue circuits still suffered large interferences coming from the car, which were due to large working temperature variations, humidity and most of all vibrations. These problems caused many industrial projects to fail, and legal concerns

then literally put the development on hold in the U.S., while the European companies took the lead in the next 10–20 years.

In fact, in 1978 Bosch announced its *anti-blockier system* (from which the ABS acronym was coined) and this started the spread of the ABS technology in the automotive field; the modern age of ABS had begun.

By 1985, Mercedes, BMW and Audi had introduced Bosch ABS systems and Ford introduced its first Teves system. By the late 1980s, ABS systems were offered on many high-priced luxury and sports cars. Today, braking systems on most passenger cars and many light-duty vehicles have become complex, computer-controlled systems. Since the mid 1980s, vehicle manufacturers have introduced dozens of different anti-lock braking systems. These systems differ in their hardware configurations as well as in their control strategy.

Today, 50 years after their first appearance on a commercial car, these active braking control systems have become standard on all passenger cars.

Notwithstanding this historical development full of significant evolutions, the research and development of new technologies and new control strategies is far from complete. Every step forward either in braking force actuation technology and/or in the available sensors asks for a significant re-design of the main control algorithms. In particular, the forthcoming advent of EMBs and of wheel-hub electric motors with high boosting capabilities will probably be the next revolution in active braking control.

1.3 The Actuators: Main Technologies and Functional Description

The ABS available on most passenger cars are equipped with hydraulic actuators (HAB: hydraulic actuated brakes) with discrete dynamics. Such systems are depicted in Figure 1.1.

In these systems the pressure exerted by the driver on the pedal is transmitted to the hydraulic system *via* a build valve (see also Figure 1.1), which communicates with the brake cylinder. Moreover, the hydraulic system has a second valve, the dump valve (again see Figure 1.1), which can discharge the pressure and which is connected to a low pressure accumulator. A pump completes the overall system. The braking force acts on the wheel cylinder, which transmits it to the pads and, finally, to the brake discs.

According to its physical characteristics, the HAB actuator is only capable of providing three different control actions. *Increase* the brake pressure: in this case the build valve is open and the dump one closed. *Hold* the brake pressure: in this case both valves are closed, and *decrease* the brake pressure: in this case the build valve is closed and the dump one open.

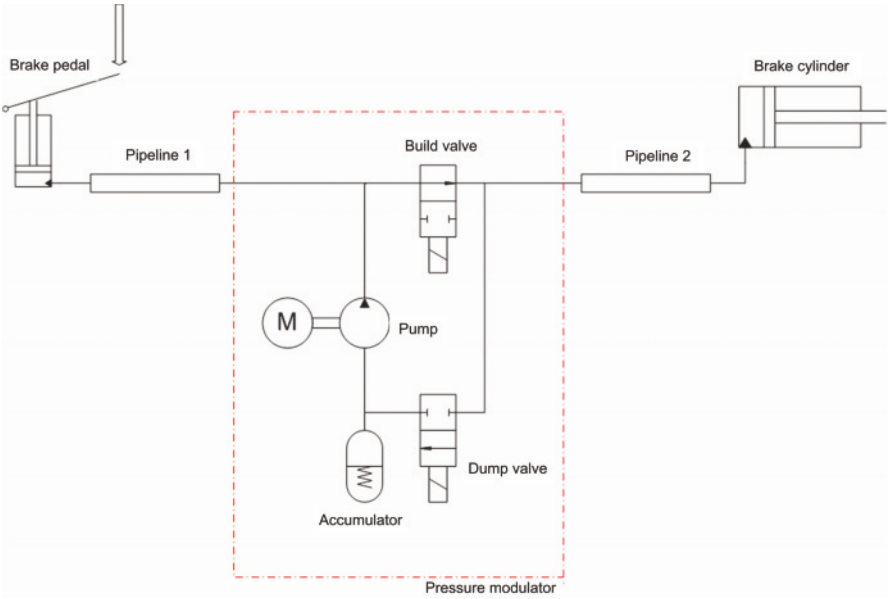

Figure 1.1 Hydraulic braking system

In dealing with this type of actuator for braking control design a static brake pad friction model is assumed, *i.e.*, the braking torque T_b is computed from the measured brake pressure p_b as

$$T_b = r_d \, \nu \, A \, p_b, \tag{1.1}$$

where r_d is the brake disc radius, ν is the (constant) brake pad friction coefficient and A is the brake piston area. Note that the brake pads friction coefficient is in general not perfectly constant over the brake life, as it varies mainly due to brake usage. However, the variation of the braking dynamic behaviour is, in general, compensated for by the servo-control loop, which regulates the brake pressure. Therefore, we assume that the braking pressure p_b considered for the conversion is the one provided as output by the servo-control of the braking system, which copes with the system uncertainties so that a constant coefficient ν can be used.

Note further that the increase and decrease pressure actions are physically limited by the actuator rate limit k, which defines the actuator performance. According to this description, the braking torque dynamics for the HAB actuator will be described as

$$\frac{\mathrm{dT_b}}{\mathrm{dt}} = u, \tag{1.2}$$

with $u = \{-k, 0, k\}$. According to the value of the control variable u, we model the three possible actuator actions, *i.e.*, $u = -k$ corresponds to the *decrease* control action, $u = 0$ corresponds to the *hold* control action and $u = k$ corresponds to the *increase* control action. The rate limit $k \in \mathbb{R}^+$ is a known parameter. Its nominal value in this book will be set to 5 kN/s.

Note that, in some industrial braking systems, the rate at which the brake pressure increases or decreases is not perfectly constant, mainly due to the (unknown) pressure difference between each wheel brake cylinder and the main brake cylinder [124]. Nonetheless, the assumption of either a *fixed* or a *user-selectable* (within physical limits) actuator rate limit has been used in several works on rule-based ABS, as for example in [26, 49, 74]. In the control design approach discussed in this book a constant actuator rate limit is employed, which is considered to be equal for the increase and the decrease control action, in order to simplify the notation.

The HAB are characterised by a long life-cycle and high reliability, and this is the main motivation which has up to now prevented the new generation of braking systems (electro-hydraulic and electro-mechanical) to enter the mass production.

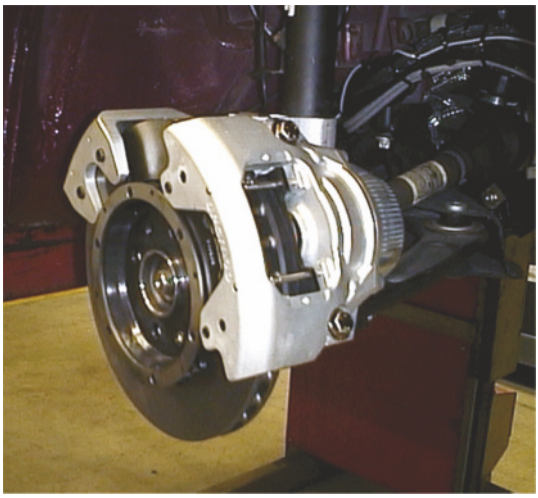

Figure 1.2 Electro-mechanical brake (courtesy of Brembo S.p.A.)

On the other hand, the disadvantage of HAB is related to ergonomic issues: with these brakes, in fact, the driver feels pressure vibrations on the brake pedal when the ABS is activated, due to the large pressure gradient in the hydraulic circuit. In fact, the HAB are wired to the brake pedal, hence their action cannot bypass that of the driver, but it is superimposed onto it.

The new generation of braking control systems will be based on either electro-hydraulic or electro-mechanical brakes; the latter will be the technology employed in upcoming *brake-by-wire* (BBW) systems.

In EHBs, a force feedback is provided at the brake pedal (so as to have the drivers feel the pressure they are exerting) and an electric signal measured *via* a position sensor is transmitted to a hydraulic unit endowed with an electronic control unit (ECU), physically connected to the *caliper* (*i.e.,* the system made of the external brake body). The EMBs are characterised by a completely *dry* electrical component system that replaces conventional actuators with electric motor-driven units (see also Figure 1.2).

Table 1.1 Comparison of braking systems actuators

	HAB	**EHB**	**EMB**
Technology	Hydraulic	Electro-hydraulic	Electro-mechanical
Force Modulation	Discrete (on/off)	Continuous	Continuous
Ergonomics	Pedal vibrations	No vibrations	No vibrations
Environmental Issues	Toxic oils	Toxic oils	No oil

With respect to the traditional brakes based on solenoid valves, the main potential benefits of EMBs are the following:

- they allow an *accurate continuous adjustment of the braking force*;
- no disturbances (pressure vibrations) are present on the brake pedal, even if the ABS system is active;
- the integration with the other active control systems is easier thanks to the electronic interface;
- there is a pollution reduction, as the toxic hydraulic oils are completely removed.

A final concise comparison between the different actuators is given in Table 1.1. It is now worth describing the main characteristics for the EMB and introducing its servo-controller basic features.

A typical EMB is shown in Figure 1.3. As can be seen, the main components of such a braking system are the following:

- an electric brushless motor;
- a planetary gear;
- a reversible ball screw;
- a piston, integral with the ball screw;
- two brake pads;
- a brake disc;
- the brake external body, called *caliper*, to which the motor and the external pad are fixed; and
- a force and/or a position sensor.

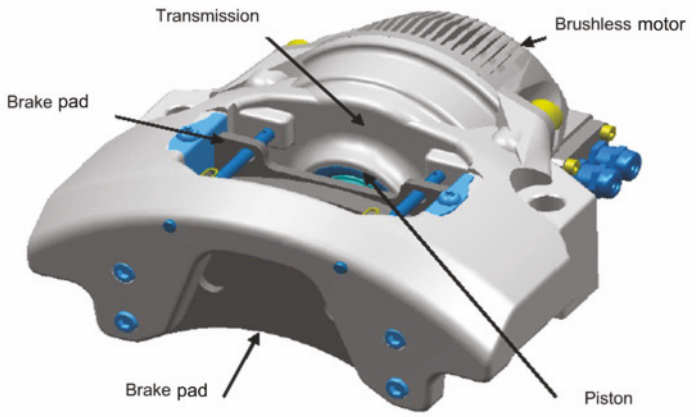

Figure 1.3 Components of a typical EMB

When a braking force is requested by the driver, an electric signal is transmitted to the motor control unit, which feeds the motor with an electric current. The motor generates a traction torque which, *via* the planetary gear and the ball screw, is scaled and converted into a linear force that moves the piston and the pad until contact with the brake disc is established.

When the pads are in contact with the disc, the piston is shifted again and this induces a deformation of the brake external body, which allows the external pad to keep contact with the disc and actuate the brake force.

When no more force is requested, the brake system must go back to the initial position; this is mainly achieved by exploiting the ball screw reversibility.

Clearly, the EMB is a highly uncertain system, mainly due to the asymmetrical friction characteristics in the pads and piston motion, the high variability of the disc-pad friction coefficient, the temperature drifts and the ageing of the brake pads.

Hence, to obtain acceptable braking performance, the EMB must be equipped with a servo-control, which counteracts all the above–mentioned sources of uncertainty and ensures repeatability of the braking manoeuvre.

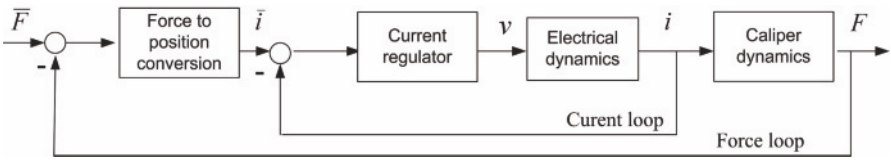

Figure 1.4 Block diagram of the EMB servo-control

This book will not directly deal with the EMB servo-control design. Hence, we only present the servo control structure, depicted in Figure 1.4, which will be needed in the next chapters.

As shown in Figure 1.4, the caliper control is usually composed of two different control loops, namely:

- a current loop, which regulates the electrical dynamics of the motor; and
- a force loop, which regulates the brake action when pads and disc are in contact.

Note that some EMBs are equipped with a position sensor (an incremental encoder placed on the electric motor shaft) instead of a force sensor (a load cell placed between the piston and the internal pad), and in this case the external loop is a position control loop. In the most sophisticated EMBs, however, there are both the position and the force sensor. These brakes are thus endowed with three nested control loops, where the position one is mostly devoted to controlling the so-called *in air* braking phase, *i.e.*, the pads and piston motion until contact with the brake disc is established. With this architecture, often the position control loop is kept active only until the force sensor measures a non-null braking force. From then on, the force loop takes care of regulating the braking force and it manages the overall manoeuvre.

In this book, a proportionality relation between braking force and braking torque is assumed, namely

$$T_b = \kappa_b \, F_b, \tag{1.3}$$

where F_b is the braking force and $\kappa_b \in \mathbb{R}^+$ is the proportionality constant.

For our purposes, unless otherwise stated, the servo-controlled EMB will be considered, and its closed-loop dynamics will be described as a first-order system with delay with transfer function

$$G_{\text{caliper}}(s) = \frac{\omega_{\text{act}}}{s + \omega_{\text{act}}} e^{-s\tau}, \tag{1.4}$$

with $\omega_{\text{act}} = 70$ rad/s and $\tau = 10$ ms.

Note that the delay accounts for both that possibly due to the actuator dynamics and for that due to the signal transmission introduced by the networked vehicle architecture, which manages the data transmission. Of course, the real value of the pure delay must be carefully established in any practical situation. Finally, note that the EMB, as any actuator, has physical limits which determine a saturation of the admissible braking torque values. Such a saturation must be taken into account when implementing the braking control algorithms. The lower bound on the braking torque is of course equal to 0, whereas the upper bound is braking-system dependent and must be carefully evaluated.

1.4 The X-by-wire Approach

In a vehicle, there are three main human-machine-interfaces (HMIs), which ensure the interaction between the driver and the vehicle: the steering wheel, the accelerator pedal and the braking pedal. These are usually linked to the respective physical actuators *via* mechanical or hydraulic connections.

In the *x-by-wire* (XBW) approach the links between each HMI and the vehicle are replaced by an electronic digital link. The x usually stands for the actuator of interest, thus either steer, brake, or throttle. Sometimes, in the case of the traction subsystem, the locution *drive-by-wire* is used.

There are different motivations leading automotive original equipment manufacturers (OEMs) toward XBW. A frank discussion on XBW technology cannot be but twofold: on the one hand it undeniably offers significant improvements and potentials for performance advancements; on the other, especially when tailored to safety critical vehicle systems (such as the braking system), it still has to prove its ability of providing the same safety standards of hydraulic braking circuits. As for the potential benefits of a full XBW system (those specific to the EMB have been already introduced above), we can mention the following [55]:

- Improved ride and handling. By-wire computer control of chassis dynamics allows steering, braking, and suspension to work together.
- Enhanced stability control. Sensors and controllers work together to detect and correct abnormal yaw moments that could result in spin-outs or rollovers.
- Easier integration of additional safety systems. By-wire technology provides the communication link necessary to enable automated safety systems like lane keeping and collision avoidance.
- Increased modularity. Fully functional by-wire modules reduce OEM assembly time and cost.
- Improved driver interface. The elimination of mechanical connections to the steering column gives OEMs more flexibility in designing the driver interface with regard to location, type, feel, and performance.
- Enhanced passive safety. An x-by-wire cockpit can simplify and improve occupant restraint management.
- Added flexibility. Vehicle designers will have more flexibility in the placement of hardware under the hood and in the interior to support alternative powertrains, enhance styling and improve interior functionality.
- Deployment time reduction. OEMs will be able to use a laptop computer to perform soft tuning capabilities instead of manually adjusting mechanical components.

Nonetheless, these systems must fulfill several requirements. Specifically, for brake-by-wire systems, these are the following [32]:

- Safety: after an arbitrary fault, the system must be available in a satisfying manner, *e.g.*, the brakes have to work with an adequate braking force.

- Reliability: the reliability of a by-wire system must be at least as high as that of a comparable mechanical system.
- Availability: it must be at least as high as that of the braking systems currently in use.
- Maintainability: the time interval over which the system is maintainable must be at least as long as that of the braking systems currently in use.
- Lifetime: it must be at least as long as that of the braking systems currently in use.
- Cost: it must be no more (or only slightly more) expensive than conventional braking systems.
- Compartment: it must be small enough for easy integration of the components.
- Legal aspects: they must be fulfilled, *i.e.*, to be considered safe, a brake system must provide performance within specific tolerance levels.

Finally, it is worth noting that an important principle behind by-wire systems in general is the *physical redundancy* of the system. In fact, to comply with the safety standards, it is necessary to provide at least a double redundancy of the main hardware components, so as to be able to recover from a failure.

1.5 State-of-the-art in Active Braking Control Design

The control systems evolution in the automotive field is well described by Figure 1.5 (see [55]). One may notice that since electronics has been integrated into vehicles, the advances in the development of active vehicle control systems has been inextricably linked to advances in sensors and actuators technology.

Hence, also the results available in the scientific literature are unavoidably dependent on the brake system under consideration. As a matter of fact, standard ABS systems for wheeled vehicles equipped with traditional hydraulic actuators use rule-based control logics (see, *e.g.*, [124]), as they have to deal with the on/off dynamics of the HAB system (see also Figure 1.1). On the other hand, as discussed in Section 1.3, EHB and EMB enable a continuous modulation of the braking torque, thereby allowing active braking control to be formulated as a classical regulation problem (see, *e.g.*, [15, 23, 41, 90]). In braking control systems, two output variables are usually considered for regulation purposes: wheel deceleration and wheel longitudinal slip. These output variables have characteristics which are somehow complementary.

Wheel deceleration is the controlled output traditionally used in ABS, since it can be easily measured with a simple wheel encoder (see also Appendix B); however, the dynamics of a classical regulation loop on the wheel deceleration critically depend on the road conditions. Henceforth, deceleration-based control strategies inherently require the online estimation

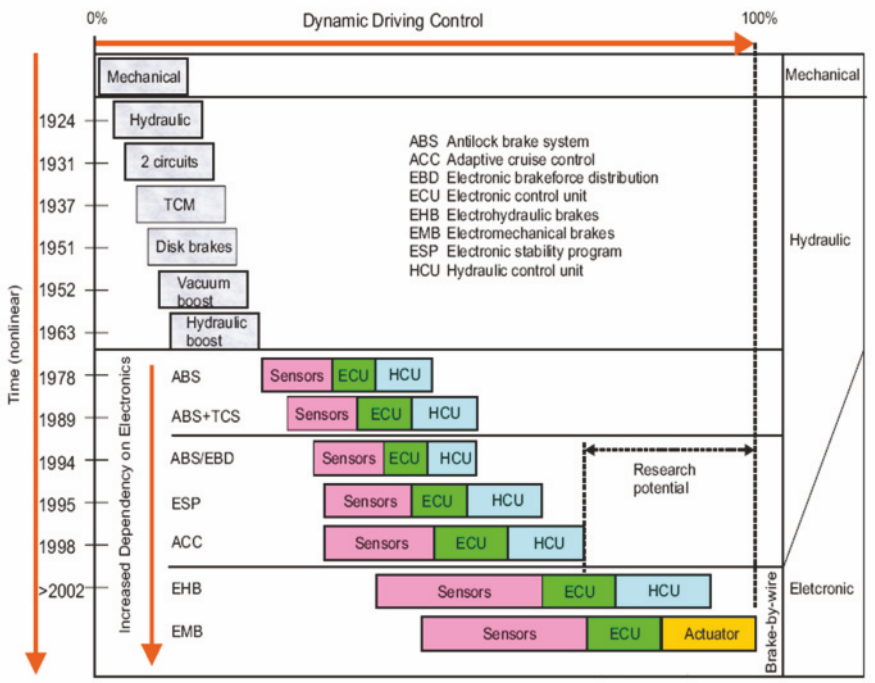

Figure 1.5 Evolution of braking systems [55, 77]

of the road characteristics; moreover, deceleration control usually is not implemented as a classical regulation loop, but heuristic threshold-based rules are used (see, *e.g.*, [88, 124]).

On the other hand, a regulation loop on the wheel longitudinal slip is simpler and dynamically robust. However, the wheel slip measurement is particularly critical since it requires the estimation of the longitudinal speed of the vehicle body, which cannot be directly measured (see Chapter 5 for a detailed treatment of this issue).

As a matter of fact, the current trend in braking control is to move from threshold-based control rules mainly based on the wheel deceleration to genuine slip control (see, *e.g.*, [15, 40, 41, 100, 131]). Slip control is particularly attractive since it can be straightforwardly and seamlessly extended from ABS to TCS and ESC applications. The challenge is to alleviate the high sensitivity of slip control to poor slip measurements, which is particularly critical at low speed and around low-slip set-points.

Moreover, to regulate the wheel slip the knowledge of vehicle speed is necessary, so that a lot of research efforts have been devoted to devise reliable and low-cost filtering and estimation algorithms. As a matter of fact, the vehicle speed can be directly measured (by means of laser beams) only for testing and for prototyping purposes. In commercial cars it must be estimated

by indirect measurements, *e.g.*, by using longitudinal accelerometers or some filtering and identification tools — see, *e.g.*, [37,48,85,119] and the references cited therein. In Chapter 5 a speed estimation algorithm will be described, together with a detailed analysis of the state of the art in this specific field.

Another active research field inherently linked to active braking control systems design is that focused on the estimation of the tyre–road friction characteristics, (see, *e.g.*, [12, 24, 29, 65, 69, 92, 118, 127, 129]).

This topic will be thoroughly discussed in Chapter 8, where, together with a specific approach to the problem, we also provide some insights on the results available in the scientific literature.

1.6 Recent Evolutions: Brake-based Global Chassis Control

Traditionally, all the active control systems on board of the vehicle, such as suspension, steering and braking control systems, are designed and implemented independently from each other, and each of them is studied so as to solve *local* problems. This is due to the fact that approaching the control design for a MIMO system, of which a vehicle is a quite complex example, by local decoupled SISO loops makes the problem easier and guarantees acceptable yet suboptimal performance in the case where the couplings are weak enough. The significant work carried out with this approach has allowed the development of reliable and effective solutions for the control of the single subsystems, both comfort and safety-oriented (see, for example, the developments in active and semi-active suspensions, steering, braking and traction control systems).

Relying on these advancements, the research focus is moving toward solutions that envisage communication and coordination between the different local control systems, which comprise sensors, controllers and actuators, so as to pursue global safety and performance objectives which involve all the chassis dynamics and can aim at achieving some optimality features.

Of course, such an approach may lead to conflicting or inappropriate control objectives. As such, research efforts are being devoted to devising sound control methodologies in order to orchestrate the collaboration among these subsystems. These new control approaches are being developed within what is called global chassis control (GCC), see, *e.g.*, [3, 52, 81, 132]. Note that, however, the price to pay when working toward GCC in comparison to the traditional subsystem approach is a centralised controller of significant complexity.

While different approaches are being developed, the underlying idea is to control the global vehicle dynamical behaviour and to consider the vehicle as an object (characterised by a certain position and orientation in the space)

that moves in a constrained space and can react to the different working situations *via* constrained and heterogeneous actuators.

Several solutions to active chassis stability control have been proposed in the scientific literature, whose common aim is to actively modify the vehicle dynamics by generating suitable yaw moments to restore vehicle stability when dangerous manoeuvres occur, see, *e.g.*, [1, 17, 18].

In the field of active vehicle dynamics control systems tailored to enhance both stability and handling, most of the available solutions are brake-based, see, *e.g.*, [94]; these approaches try to enhance both vehicle performance and stability during curves by imposing — *via* differential braking — an under-steering or over-steering behaviour on the vehicle.

Examples of brake-based approaches can be found in [20, 25]. In [20], the overall control problem is formulated as a tracking problem, where the trajectory is specified as a desired yaw rate and longitudinal acceleration profile, which must be tracked while stabilising the roll and pitch motion. The coordination policy for the two actuators is achieved by solving a constrained optimisation problem. A similar problem within the context of autonomous vehicles is tackled in [25], where the model predictive control approach is used to design control laws acting on active front steering, active braking and active differentials aimed at ensuring that the vehicle follows a given path by controlling the front steering angle, brakes and traction at the four wheels independently, while fulfilling both physical and design constraints. Further examples are presented in [30, 121], where the problem of actuator coordination, in these cases active steering and braking, is setup as based on a dynamic control allocation approach. Specifically, [121] proposes a yaw stabilisation scheme composed of a high level module which deals with the vehicle motion control objective, *i.e.*, the computation of the yaw rate reference and the related tracking problem, and a low level module which handles the braking control for each wheel. The link between the two is ensured by an allocation module which generates the longitudinal wheel slip reference for the braking controller commands and front wheel steering angle corrections. The optimal use of the available control variables is obtained as the solution of a real-time optmisation problem.

An alternative to brake-based solutions is provided by the use of a new generation of torque biasing devices in the vehicle driveline, which can be controlled to actively distribute the driving torque between front and rear axle to improve stability and performance. On-demand torque redirection from front to rear axle can be achieved either *via* electronically-controlled differentials or *via* electronically-controlled central transfer cases, [73, 80]. These torque-biasing devices allow tuning the torque distribution so as to actively change the vehicle configuration and to make it closer to a full front-wheel-drive to pursue safety objectives, or to a four-wheel-drive to optimise performance *via* a more balanced torque distribution to the four wheels.

It is worth pointing out that the GCC has also opened the way to achieving the capability of altering, *via* an electronic control system, the car behaviour, which is in principle dictated from its mechanical layout.

From a broader viewpoint, we believe that the GCC research area will provide a first enabling key for the design a new generation of vehicles, where the driver's preferences and inclinations will be sensed by appropriate control systems and mapped onto specific control systems settings which will enable the vehicle dynamic behaviour which is closest to the driver preferences. Of course, such online vehicle personalisation must be performed while always guaranteeing and enforcing active safety.

In this challenging scenario, braking systems appear to be a strategic subsystem to employ for different control objectives and this motivates us to describe in this book different solutions to the braking control problem which offer specific advantages and may be selected also according to higher level control goals.

1.7 Summary

In this chapter the active braking control problem was introduced and discussed, starting from an historical perspective. Further, the available brake technologies were presented, with specific emphasis on the hydraulic and electro-mechanical brakes, which will be those considered in the design of the control approaches presented in this book. Moreover, the context of XBW has been outlined, highlighting its differences with respect to the current technology and its potential benefits.

Finally, a perspective on the future evolution of braking systems within the context of GCC systems has been provided, to motivate the fact that a thorough understanding of braking control offers the way to tackle and solve new and complex control problems.

Further, a new interesting stream of research both in braking control systems and brake-based GCC systems will be initiated by the new challenges posed by (fully or partially) electric vehicles and actuators. In this context, in fact, energy management and optimisation issues must be considered explicitly also in the control design phase, and the link between the two is one of the new research issues, which will deserve lot of attention in the near future.

Chapter 2
Control-oriented Models of Braking Dynamics

2.1 Introduction

This chapter is devoted to introducing the models of the braking dynamics employed for the design of the different active braking control systems developed in the next chapters, *i.e.*, the single-corner and double-corner models.

As both single-corner and double-corner vehicle models clearly employ a tyre–road friction description, based on which the contact forces can be defined, before introducing the vehicle braking dynamics the force and friction model adopted in this book will be presented.

Note that the treatment of these topics is not intended to provide a comprehensive overview on vehicle modeling nor to present all the available contact forces and tyre–road friction models available in the literature. The aim is to provide the reader with the description of the dynamical models which are of interest for the design of braking control strategies. For a more detailed discussion on these topics, the reader may refer to, *e.g.*, [45, 71, 84].

The chapter is structured as follows. Section 2.2 introduces tyre–road contact forces and presents the adopted friction model. Further, Section 2.3 describes the single-corner model of the braking dynamics, whereas Section 2.4 the double-corner one. In Section 2.5 the considered dynamical models of the braking dynamics are analysed and their linearised version is computed. A numerical analysis of the linearised dynamics is also proposed, to point out the sensitivity of the model dynamics to specific vehicle parameters.

2.2 Tyre–road Contact Forces

The tyres are probably the single component that mostly affects the dynamic behaviour and performance of a road vehicle. In fact, the tyre allows contact between the rigid part of the wheel – the hub – and the road surface to take

place on all surfaces and in every road condition. Moreover, the tyre is the means for ensuring adherence to the road and it is responsible for transferring to the ground the vertical load F_z, which is decomposed – at the contact point on the road plane – into longitudinal F_x (*i.e.*, traction and braking) and lateral F_y friction forces, which guarantee the vehicle steerability (see Figure 2.1).

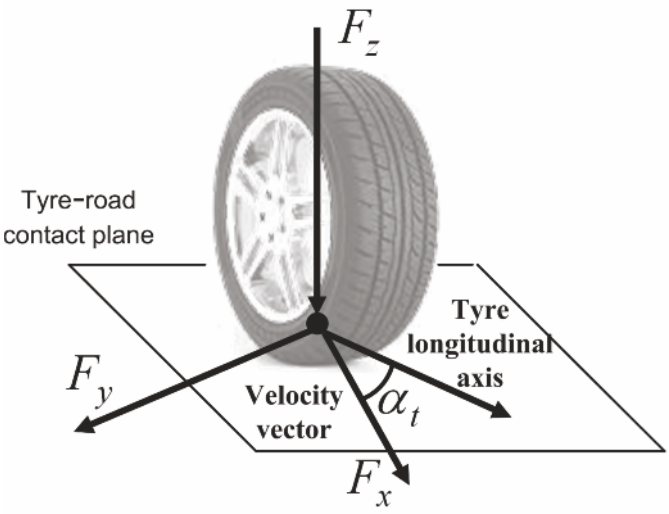

Figure 2.1 Tyre–road contact forces

Both F_x and F_y depend on a large number of features of the road, tyre, and suspensions. Most often, they can be described as

$$F_x = F_x(F_z, \alpha_t, \gamma, \lambda), \tag{2.1}$$
$$F_y = F_y(F_z, \alpha_t, \gamma, \lambda), \tag{2.2}$$

where

- F_z is the vertical force at the tyre-road contact point. In quasi-static conditions it can be simply described as $F_z = mg$, where the mass m can be different for each wheel according to the load distribution of the vehicle and g represents the gravitational acceleration; in a braking manoeuvre F_z can significantly change due to dynamic load transfer.
- α_t is the tyre sideslip angle (see Figure 2.1), *i.e.*, the angle between the tyre longitudinal axis and the speed vector of the contact point.
- γ is the camber angle, *i.e.,* the tyre inclination with respect to the vertical direction.
- λ is the longitudinal wheel slip, *i.e.,* the normalised relative velocity between the road and the tyre, which, in case of zero tyre sideslip angle is

defined as

$$\lambda := \frac{v - \omega r}{\max\{v, \omega r\}}, \tag{2.3}$$

where v is the wheel ground contact point velocity and ωr is the linear speed of the tyre (with radius r and angular speed ω) at the contact point. The presence of a non-zero slip is due, in general, to traction and braking forces exerted on the tyre. Note that (see also Figure 2.1) a non-zero sideslip angle α_t modifies the wheel slip expression in (2.3), which takes the form

$$\lambda = \frac{v - \omega r \cos(\alpha_t)}{\max\{v, \omega r \cos(\alpha_t)\}}. \tag{2.4}$$

In the following, we will mostly concentrate on braking manoeuvres (hence $v \geq \omega r$) and consider the assumption of small tyre sideslip angle, *i.e.*, with $\cos(\alpha_t) \cong 1$. In this case, (2.3) simply becomes

$$\lambda = \frac{v - \omega r}{v}, \tag{2.5}$$

with $\lambda \in [0, 1]$. In particular, $\lambda = 0$ corresponds to a pure rolling wheel and $\lambda = 1$ to a locked wheel.

Finally, note that a normalised expression of the vertical forces (2.1) and (2.2) is typically used, which has the form

$$F_x = F_z \mu_x(\alpha_t, \gamma, \lambda), \tag{2.6}$$

$$F_y = F_z \mu_y(\alpha_t, \gamma, \lambda), \tag{2.7}$$

where the proportionality constants μ_x and μ_y, defined as

$$\mu_x(\alpha_t, \gamma, \lambda) := \frac{F_x}{F_z}, \tag{2.8}$$

$$\mu_y(\alpha_t, \gamma, \lambda) := \frac{F_y}{F_z}, \tag{2.9}$$

are called *longitudinal and lateral friction coefficients*, respectively. It is worth pointing out that the normalised expressions (2.6) and (2.7) rely on the assumption that the relationship between F_x and F_y and the vertical load F_z is linear for all values of F_z. In fact, this assumption does not rigorously hold for very large values of the vertical load, where the relationship between the forces and the vertical load shows a saturation. However, for control design purposes the simplifying assumption of a linear relationship between F_z and both F_x and F_z can in general be used.

The typical behaviour of the longitudinal and lateral friction coefficients for different values of the tyre sideslip angle α_t is depicted in Figures 2.2(a) and 2.2(b). These coefficients describe the tyre capability of transferring the vertical load to the ground in longitudinal and lateral direction.

By inspecting Figure 2.2(a) one may notice that all the curves are characterised by a single maximum, and hence exhibit a peak value. Further, note that for $\lambda = 0$ no longitudinal force can be transmitted to the ground, while for $\lambda = 1$ (*i.e.*, with locked wheels), there is a loss of longitudinal force up to 20-30% with respect to the peak value. As the tyre sideslip angle α_t varies, the peak shifts forward in λ as α_t increases, while the peak value decreases.

On the other hand, from Figure 2.2(b) one may notice that all the curves are monotonically decreasing as functions of λ and they take on their maximum value for $\lambda = 0$. Further, note that for $\lambda = 1$ (*i.e.*, with locked wheels) no lateral force can be transmitted to the ground (independently of the value of α_t); hence, with locked wheels there is no residual vehicle steerability. This is one of the main issues that motivate the design of ABS systems. Finally, the lateral friction coefficient increases as the tyre sideslip angle α_t increases.

Hence, the behaviour of μ_y is somehow dual and complementary with respect to that of μ_x, both as a function of λ and of α_t.

2.2.1 Friction Models

Going back to tyre–road contact forces, one of the most well-known tyre friction models of the form (2.1) and (2.2) is the Pacejka model (see, *e.g.*, [71, 72]), also known as the *magic formula*. The name *magic formula* comes from the fact that the structure of the model equations does not rely on a physical basis and it appears rather complex and with many parameters to be determined. Further, the *magic* comes from the fact that by effectively tuning the parameters such a model does indeed fit a wide variety of tyres in a large range of operating conditions. This model has been shown to suitably match experimental data, obtained under particular steady-state conditions, which assume a constant value of both linear and angular velocities of the tyre. The expression of the longitudinal force in the Pacejka model, under the assumption of symmetric tyres, has the form

$$F_x(F_z, \alpha_t, \gamma, \lambda) = \cos(C_{x\alpha_t} \arctan(B_{x\alpha_t}\alpha_t))F_{x0}, \tag{2.10}$$

where the expression of the different terms appearing in (2.10) depend on F_z, α_t, λ, γ and several constant parameters, which are related to the specific tyre properties and can be identified from experimental data (see, *e.g.*, [71]) according to the following expressions:

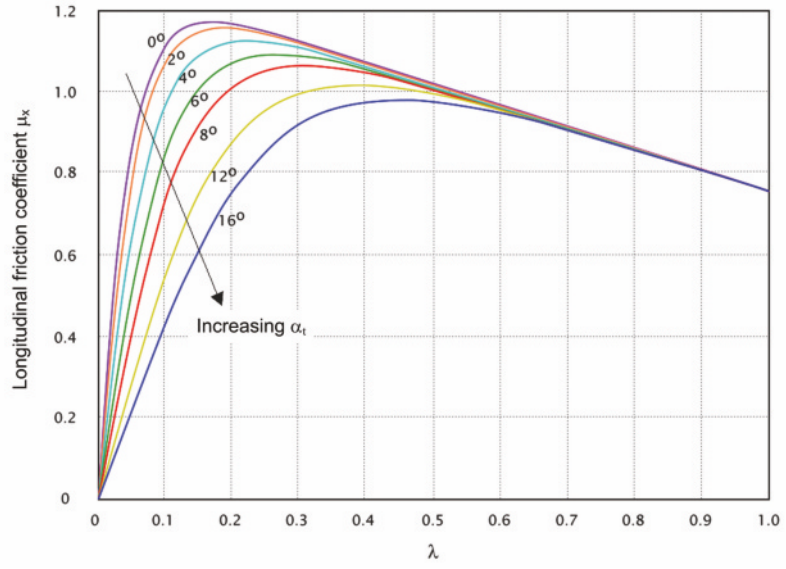

(a)

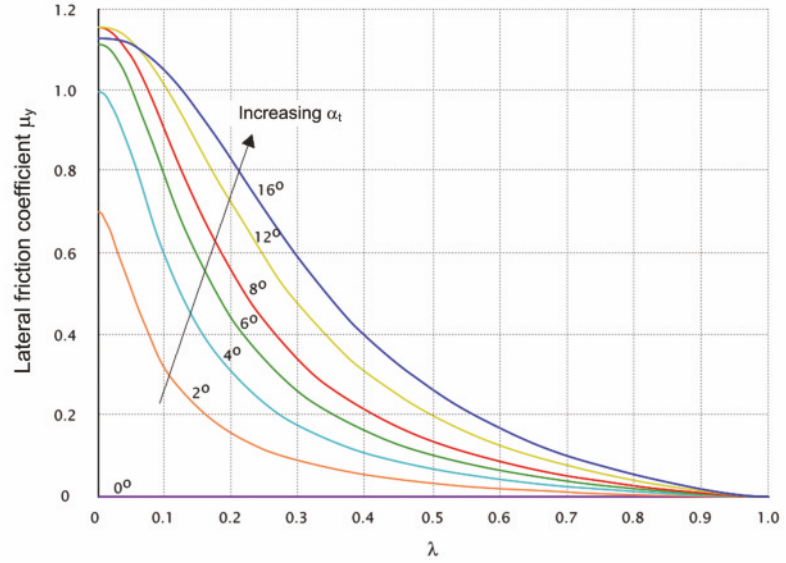

(b)

Figure 2.2 Plot of the longitudinal (a) and lateral (b) friction coefficient as function of the longitudinal wheel slip λ for different values of the tyre sideslip angle α_t

$$\begin{cases} F_{x0} = D_x \sin[C_x \arctan(B_x\kappa - E_x(B_x\kappa - \arctan(B_x\kappa)))], \\ \kappa = \lambda + H_x, \\ H_x = p_{h1} + p_{h2}\, df_z, \\ df_z = (F_z - F_{z0})/F_{z0}, \\ D_x = (p_{dx1} + p_{dx2}\, df_z)F_z, \\ E_x = (p_{ex1} + p_{ex2} df_z + p_{ex3}\, df_z^2)(1 - p_{ex4}\,\mathrm{sign}(\kappa)), \\ K_x = F_z(p_{kx1} + p_{kx2} df_z)e^{p_{kx3} df_z}, \\ B_x = K_x/(C_x D_x), \\ B_{x\alpha_t} = (p_{bx1} + p_{dx3}\gamma^2)\cos(\arctan(p_{dx2}\lambda)). \end{cases}$$

The expression of the lateral force F_y, again under the tyre symmetry assumption, has the form

$$F_y(F_z, \alpha_y, \gamma, \lambda) = \cos(C_{y\lambda} \arctan(B_{y\lambda})F_{x0}, \tag{2.11}$$

where the expression of the different terms appearing in (2.11) depend on F_z, α_t, λ, γ and several constant parameters, which are related to the specific tyre properties and can be identified from experimental data according to the following expressions:

$$\begin{cases} F_{y0} = D_y \sin[C_y \arctan(B_y\alpha_y - E_y(B_y\alpha_y - \arctan(B_y\alpha_y)))] \\ \qquad + C_\gamma \arctan(B_\gamma\gamma - E_\gamma(B_\gamma\gamma - \arctan(B_\gamma\gamma))), \\ \alpha_y = \alpha_t + H_y, \\ H_y = p_{hy1} + p_{hy2}\, df_z + (p_{hy3} + p_{hy4}\, df_z)\gamma, \\ df_z = (F_z - F_{z0})/F_{z0}, \\ D_y = F_z p_{dy1} e^{p_{dy2} df_z}(1 - p_{dy3}\gamma^2), \\ E_y = (p_{ey1} + p_{ey2} df_z)(1 - (p_{ey3} + p_{ey4}\gamma)\,\mathrm{sign}(\alpha_y)), \\ K_{y\alpha} = p_{ky1} F_{z0} \sin(p_{ky2} \arctan(F_z/((p_{ky3} + p_{ky4}\gamma^2)F_{z0})))/(1 + p_{ky5}\gamma^2), \\ B_y = K_{y\alpha}/(C_y D_y), \\ K_{y\gamma} = (p_{ky6} + p_{ky7} df_z)F_z, \\ B_\gamma = K_{y\gamma}/(K_{y\gamma} D_y). \end{cases}$$

The Pacejka friction model is very detailed, and it is the tyre–road friction description most commonly used in commercial vehicle simulators such as, for example, CarSim®, Adams/Tire®, and Bikesim® .

In the rest of the book, for controller design purposes, we will work under the assumptions of small sideslip and camber angles, *i.e.*, $\alpha_t \cong 0$ and $\gamma \cong 0$, and thus consider the longitudinal force only. So, for simplicity, we indicate the friction coefficient μ_x with μ. Further, we assume a proportionality relationship between normal force and longitudinal force, thus obtaining the longitudinal tyre–road force description

$$F_x = F_z \mu(\lambda). \tag{2.12}$$

This simplification will not affect the design of any of the forthcoming control algorithms. In fact, changes in α_t and γ cause a shift in the abscissa of the

peak of the the friction coefficient curve $\mu(\lambda)$ and act as a scaling factor on the curve itself, in this resembling a variation in the vertical load F_z. Accordingly, as none of the proposed controllers will be designed assuming knowledge of the current value of the vertical load, in the same way they can handle non-zero values of α_t and γ.

As for the friction model, in this book the Burckhardt model (see, *e.g.*, [16,45]) will be employed, as it is particularly suitable for analytical purposes while retaining a good degree of accuracy in the description of the friction coefficient $\mu(\lambda)$. Based on this model, the longitudinal coefficient has the following form:

$$\mu(\lambda;\vartheta_r) = \vartheta_{r1}(1 - e^{-\lambda\vartheta_{r2}}) - \lambda\vartheta_{r3}. \tag{2.13}$$

Notice that the vector ϑ_r has three elements only. By changing the values of these three parameters, many different tyre–road friction conditions can be modelled. In Figure 2.3 the shapes of $\mu(\lambda;\vartheta_r)$ in four different road conditions are displayed. The corresponding parameters values ϑ_r are given in Table 2.1.

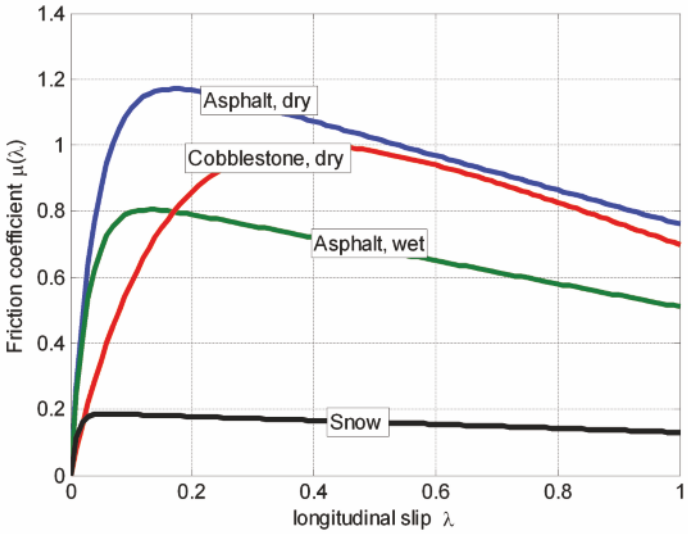

Figure 2.3 Plot of the function $\mu(\lambda;\vartheta_r)$ in different road conditions

In the rest of the book these four curves will be used; moreover, the simplified notation $\mu(\lambda)$ will be adopted, and it will be implicitly assumed that the expression of $\mu(\lambda)$ may change, according to different road conditions.

Finally, it is worth noting that both the Pacejka and Burckhardt models describe the friction forces *via* static maps, which depend on different parameters. For completeness, we must mention that in the scientific literature dynamic friction models have also been proposed (see, *e.g.*, [127] and the references therein for a complete discussion on this type of friction models).

Table 2.1 Values of the parameters vector ϑ_r for different road conditions

Road condition	ϑ_{r1}	ϑ_{r2}	ϑ_{r3}
Dry asphalt	1.28	23.99	0.52
Wet asphalt	0.86	33.82	0.35
Cobblestone	1.37	6.46	0.67
Snow	0.19	94.13	0.06

2.2.2 Relaxation Dynamics

When a rolling pneumatic tyre experiences a step variation in one of the system parameters (*i.e.*, the sideslip angle, the camber angle or the longitudinal wheel slip) both the longitudinal and lateral friction forces undergo a transient leading to a steady-state condition. This mechanism is not an instantaneous phenomenon, mainly due to the time required for the deflection of the tyre. The lag is closely related to the rotation of the tyre, typically taking a fraction of a full revolution of the tyre to effectively reach the steady-state force condition. This distance is often referred to as the *relaxation length* s_{0l}. Hence, the actual longitudinal and lateral forces $F_{x\mathrm{Act}}$ and $F_{y\mathrm{Act}}$ are computed as

$$\begin{aligned} \dot{F}_{x\mathrm{Act}} &= \frac{1}{\tau}\left(F_x - F_{x\mathrm{Act}}\right), \\ \dot{F}_{y\mathrm{Act}} &= \frac{1}{\tau}\left(F_y - F_{y\mathrm{Act}}\right), \end{aligned} \tag{2.14}$$

where F_x and F_y can be computed as in (2.10) and (2.11). The filter time-varying time constant is given by

$$\tau = \frac{s_{0l}}{\omega r},$$

where s_{0l} is the tyre-relaxation length – usually set equal to half of the tyre circumference – and ωr is linear wheel speed at the tyre–road contact point.

From here onward, however, we simply assume that $F_{x\mathrm{Act}} \cong F_x$ and $F_{y\mathrm{Act}} \cong F_y$, and we refer to the longitudinal and lateral forces with F_x and F_y, respectively.

2.3 The Single-corner Model

For the preliminary design and testing of braking control algorithms, a simple but effective model known as the *single-corner model* is typically used.

The model is given by the following set of equations (see also Figure 2.4):

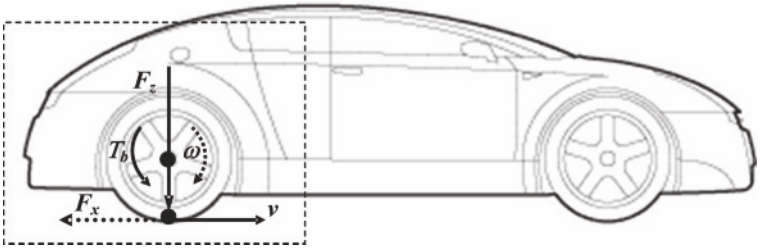

Figure 2.4 Single-corner model

$$\begin{cases} J\dot{\omega} = rF_x - T_b, \\ m\dot{v} = -F_x, \end{cases} \tag{2.15}$$

where

- ω [rad/s] is the angular speed of the wheel;
- v [m/s] is the longitudinal speed of the vehicle centre of mass;
- T_b [Nm] is the braking torque;
- F_x [N] is the longitudinal tyre–road contact force; and
- J [kg m^2], m [kg] and r [m] are the moment of inertia of the wheel, the single-corner mass and the wheel radius, respectively.

With reference to Figure 2.4 and system (2.15), the physical meaning of the geometric and vehicle parameters are given in Table 2.2 together with a set of numerical values used in this book for the numerical examples and simulations carried out with the single-corner model.

Table 2.2 Parameters of the single-corner model

Parameter	Physical meaning	Numerical value
r	Wheel radius	0.3 m
J	Wheel inertia	1 kg m^2
m	Single-corner mass	225 kg

Throughout the book, the normalised linear wheel deceleration

$$\eta := -\frac{\dot{\omega} r}{g} \tag{2.16}$$

will often be employed. Observe that η is the linear deceleration of the contact point of the tyre, normalised with respect to the gravitational acceleration g. It is particularly useful since it can be easily compared with the longitudinal deceleration of the vehicle chassis.

Substituting into the first equation of system (2.15) the expression of F_x given in (2.12) and the definition of the wheel slip in (2.5) yields

$$\begin{cases} J\dot{\omega} = rF_z\mu(\frac{v-\omega r}{v}) - T_b, \\ m\dot{v} = -F_z\mu(\frac{v-\omega r}{v}). \end{cases} \tag{2.17}$$

In system (2.17), the state variables are v and ω. As λ, v and ω are linked by the algebraic relationship (2.5), it is possible to replace the state variable ω with the state variable λ.

Specifically, substituting

$$\dot{\lambda} = -\frac{r}{v}\dot{\omega} + \frac{r\omega}{v^2}\dot{v}$$

and

$$\omega = \frac{v}{r}(1-\lambda)$$

into the first equation of (2.17), one obtains

$$\begin{cases} \dot{\lambda} = -\frac{1}{v}\left(\frac{(1-\lambda)}{m} + \frac{r^2}{J}\right) F_z\mu(\lambda) + \frac{r}{Jv}T_b, \\ m\dot{v} = -F_z\mu(\lambda). \end{cases} \tag{2.18}$$

In the following it is assumed (see, *e.g.*, [41]) that the longitudinal dynamics of the vehicle (expressed by the state variable v) are much slower than the rotational dynamics of the wheel (expressed by the state variable λ or ω) due to large differences in inertia. Henceforth, v can be considered as a slowly-varying parameter. Under this assumption, the second equation (vehicle dynamics) of system (2.15) can be neglected, so that the model reduces to a first-order model of the wheel slip dynamics.

It is worth noticing that the single-corner model relies on the following simplifications:

- The four wheels are treated as *dynamically decoupled*, which means that the dynamic load transfer phenomena induced by pitch motion are neglected. The consequences of this simplification will be subject to a detailed analysis when discussing the double-corner model (see Section 2.4).
- The suspension dynamics are neglected.
- The dependence of the friction forces from the vertical load is modelled as a proportionality relation. This assumption strictly holds only in static conditions. When dynamic load transfer occurs, the dependency is slightly nonlinear with larger directional forces transmitted at lower loads and a saturation effect at very large load values.
- The wheel radius is assumed to be constant. As a matter of fact – during braking – a consequence of the pitch motion is a dynamic change in the wheel radius, which is a function of the instantaneous vertical load.
- Straight-line braking is considered, *i.e.*, the friction forces' dependence on the camber angle γ and on the tyre sideslip angle α_t is neglected.
- The tyre relaxation dynamics, see Equation 2.14, is not explicitly considered.

Despite these simplifications, the single-corner is the dynamical model most widely employed as a starting point for active braking control systems design (see, *e.g.*, [23,39–41,54,59,91,100,131]) as it provides a simple yet sufficiently rich description of the braking dynamics. Clearly, after having derived a wheel slip control system based on this mathematical model, exhaustive tests should be carried out on a complete vehicle dynamics simulator, so as to verify its performance in a more realistic setting before moving to experimental tests.

As a matter of fact, it is interesting to remark that, despite its simple structure, the design of a feedback controller for (2.18) is far from trivial. In fact, the current road condition and the current value of the vertical load are unknown and can suffer substantial and abrupt changes. Moreover, both the equilibria stability properties and the settling time of the system modes are strongly affected by changes in tyre–road friction characteristics and the normal force exerted on the tyre during braking can experience significant changes due to dynamic load transfer phenomena.

Most of the control approaches presented in this book will be derived from the single-corner model. However, in order to study some important aspects of the braking control systems, such as the interactions between braking control and speed estimation treated in Chapter 5, a more complex model of the vehicle dynamics is needed, capable of describing the link between front and rear axles. Thus, in the next section the double-corner model – which includes load transfer dynamics – is presented.

2.4 The Double-corner Model

The *double-corner* model can be regarded as a side view of the vehicle, where one front and one rear wheel are modelled; for our purposes, the main feature of this model is that it allows to describe the load transfer phenomena. It is similar in principle to the *half car* model, which is commonly used to describe the heave dynamics for suspensions control. Consider the double-corner

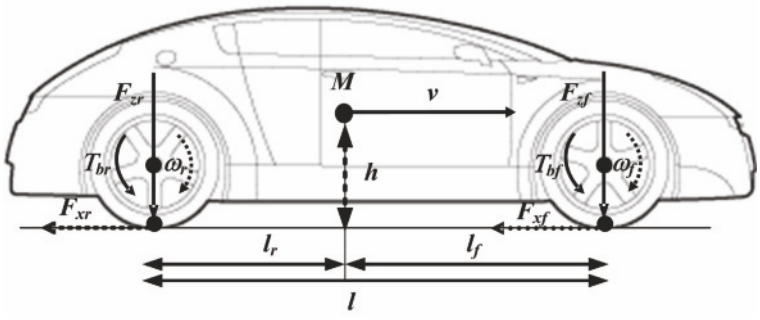

Figure 2.5 Double-corner model

model shown in Figure 2.5, where the dynamic load transfer is assumed to be proportional to the vehicle deceleration only. Namely, the vehicle dynamics are described by the following set of equations:

$$\begin{cases} J\dot{\omega}_f = r_f F_{x_f} - T_{b_f}, \\ J\dot{\omega}_r = r_r F_{x_r} - T_{b_r}, \\ M\dot{v} = -F_{x_f} - F_{x_r}, \end{cases} \tag{2.19}$$

where

- ω_f and ω_r [rad/s] are the angular speed of the front and rear wheels, respectively.
- v [m/s] is the longitudinal speed of the vehicle centre of mass.
- T_{b_f} and T_{b_r} [Nm] are the front and rear braking torques, respectively.
- F_{x_f} and F_{x_r} [N] are the front and rear longitudinal tyre–road contact forces, respectively.
- J [kg m^2], M [kg] and $r_f = r_r = r$ [m] are the moment of inertia of the wheel, the single-corner mass and the wheel radius, respectively (see also Table 2.3). Note that, for simplicity, we assume that the front and rear wheel radii are equal and we denote them both by r.

For the longitudinal forces F_{x_i}, $i = \{f, r\}$ we use the model in (2.12) and express the tyre–road friction forces *via* the coefficient $\mu(\lambda)$ given in (2.13). Thus, to complete the model we only have to specify the expression for the vertical load. To describe the load transfer phenomena between front and rear axles, consider the case where the vehicle is subject to a constant acceleration $\dot{v}$. In this case, considering the force and torque balance at the projection of the centre of mass to the ground with rotations taken to be positive in clockwise direction, gives

$$\begin{aligned} Mg &= F_{z_f} + F_{z_r}, \\ M\dot{v}h &= -F_{z_f} l_f + F_{z_r} l_r, \end{aligned} \tag{2.20}$$

where (see also Figure 2.5 and Table 2.3) l_f and l_r are the distances between the projection of the centre of mass to the ground and the front and rear wheel contact points and h is the height of the centre of mass from the ground. Solving these equations for F_{z_f} and F_{z_r} yields

$$\begin{aligned} F_{z_f} &= W_f - \Delta_{F_z}\dot{v}, \\ F_{z_r} &= W_r + \Delta_{F_z}\dot{v}, \end{aligned} \tag{2.21}$$

where

$$\begin{aligned} W_f &= \frac{Mgl_r}{l}, \\ W_r &= \frac{Mgl_f}{l} \end{aligned} \tag{2.22}$$

are the static vertical loads at the front and rear wheels, and

$$\Delta_{F_z} = \frac{Mh}{l} \tag{2.23}$$

is the coefficient of the load transfer component in (2.21) due to the vehicle acceleration, which is equal and opposite at the front and rear wheels. In (2.22) and (2.23), $l = l_f + l_r$ is the wheelbase, h is the height of the centre of mass and g is the gravitational acceleration.

Note, finally, that $\dot{v}$ is the vehicle *acceleration*, hence is negative during braking. Thus, Equation 2.21 correctly accounts for the fact that the front wheel experiences a positive load variation in the face of a braking manoeuvre, while the opposite is true for the rear wheel

In system (2.19) the state variables are v and ω_i, $i = \{f, r\}$. As λ_i, v and ω_i are linked by the algebraic relation (2.5), it is possible to replace ω_i with λ_i as state variables in the same way as it was done for the single-corner model. As for the centre of mass longitudinal dynamics in (2.19), based on the description of the longitudinal force in (2.12) and in view of (2.21), it can be re-written as

$$\dot{v} = -\frac{W_f \mu(\lambda_f) + W_r \mu(\lambda_r)}{M - \Delta_{F_z}(\mu(\lambda_f) - \mu(\lambda_r))}. \tag{2.24}$$

To compute the expression of the evolution in time of the front and rear wheel slip λ_i, $i = \{f, r\}$, we consider the longitudinal force description given in (2.12) and the vertical force description (2.21). Further, we compute

$$\dot{\lambda}_i = -\frac{r}{v}\dot{\omega}_i + \frac{r\omega_i}{v^2}\dot{v}$$

and use the relationship

$$\omega_i = \frac{v}{r}(1 - \lambda_i)$$

together with the wheel dynamics in (2.19). This leads to the set of equations

$$\begin{aligned} \dot{\lambda_f} &= -\frac{r}{Jv}\left(\Psi_f(\lambda_f, \lambda_r) - T_{b_f}\right), \\ \dot{\lambda_r} &= -\frac{r}{Jv}\left(\Psi_r(\lambda_f, \lambda_r) - T_{b_r}\right), \\ \dot{v} &= -\frac{W_f \mu(\lambda_f) + W_r \mu(\lambda_r)}{M - \Delta_{F_z}(\mu(\lambda_f) - \mu(\lambda_r))}, \end{aligned} \tag{2.25}$$

where

$$\Psi_f(\lambda_f, \lambda_r) = \left[r(W_f - \Delta_{F_z}\dot{v})\mu(\lambda_f) - \frac{J}{r}(1 - \lambda_f)\dot{v}\right], \tag{2.26}$$

$$\Psi_r(\lambda_f, \lambda_r) = \left[r(W_r + \Delta_{F_z}\dot{v})\mu(\lambda_r) - \frac{J}{r}(1 - \lambda_r)\dot{v}\right]. \tag{2.27}$$

Also in this case, we assume that the longitudinal dynamics of the vehicle are much slower than the rotational dynamics of the wheels due to the differences in inertia. Thus, we regard v as a slowly-varying parameter and neglect the third equation of model (2.25).

Note that the double-corner model does not include the suspensions dynamics, as the vertical load is modelled *via* the vehicle deceleration only. In the general case, if the dynamics of the suspensions are taken into account and modelled as a linear spring-damper system, the effect on the wheel slip dynamics is the presence of a resonance and an anti-resonance due to the heave and pitch dynamics, usually located at the chassis frequency, which is lower than the frequency range at which wheel dynamics act. As such, the proposed double-corner model is appropriate for braking control systems design in most cases. The analysis of the effects of the neglected dynamics must again be carried out *via* simulations on full vehicle models and finally based on the tests results obtained on the target vehicle. Of course, particular specifications or specific vehicle geometries might require the suspensions dynamics to be considered explicitly in the control-oriented model of the braking dynamics. Such an issue must be evaluated by the control engineer for each specific case.

Table 2.3 Parameters of the double-corner model

Parameter	**Physical meaning**	**Numerical value**
r	Front and rear wheel radius	0.3 m
h	Height of the centre of mass from ground	0.5 m
J	Wheels inertia	$1\text{kg}\,\text{m}^2$
M	Double-corner mass	450 kg
$l = l_f + l_r$	Wheelbase	2.8 m
l_f, l_r	Front and rear axles length	$l_f = 1.2$ m, $l_r = 1.5$ m

2.5 Linearised Models and Dynamic Analysis

The first step in the analysis of the braking dynamics is the computation and discussion of the equilibrium points for the considered models, followed by their linearisation around the equilibrium points themselves. Based on the linearised models it will be also possible to carry out a dynamic analysis by means of the study of the system frequency response in order to investigate the model sensitivity to some vehicle parameters of interest.

2.5.1 Single-corner Model Analysis

We start by analysing the single-corner model (2.15), computing its equilibrium points and discussing two possible approaches to its linearisation. Further, the transfer function from braking torque to wheel slip will be determined and analysed to illustrate the dynamic dependency of the model on vehicle speed and vertical load.

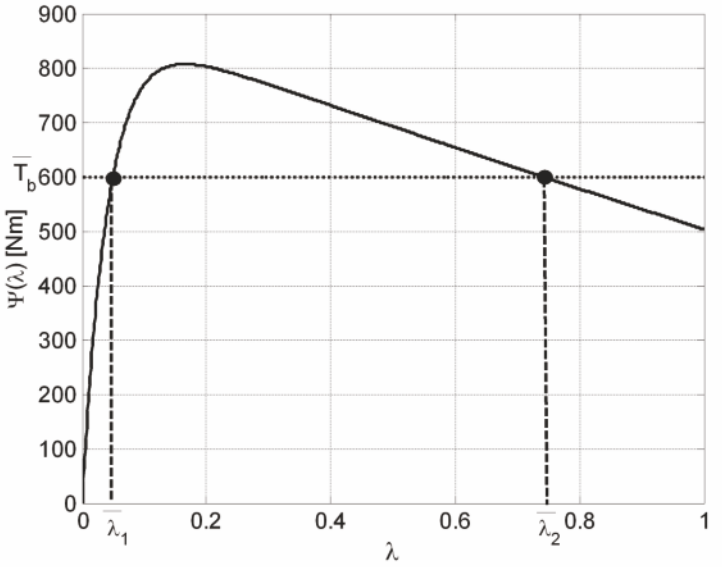

Figure 2.6 Equilibrium points for the single-corner model (2.29) in the (λ, T_b) plane (example with $F_z = mg$ and dry asphalt)

2.5.1.1 Equilibrium Points

To compute the equilibrium points note that by setting $\dot{v} = 0$ and $\dot{\omega} = 0$ in system (2.15), the corresponding equilibrium is given by $\lambda = 0$ and $T_b = 0$. This corresponds to a constant-speed condition without braking; this equilibrium condition is trivial and meaningless for the design of a braking controller. The equilibrium points we are interested in – during braking – are characterised by $\dot{\lambda} = 0$, *i.e.*, constant longitudinal slip $\lambda = \overline{\lambda}$ and thus constant normalised linear wheel deceleration $\eta = \overline{\eta}$ (see Equation 2.16). Moreover, note that for any control input $T_b \geq 0$, the wheel slip is non-negative, *i.e.*, $\lambda \geq 0$. In fact, for non-negative braking torques, the vehicle is either at con-

stant speed or it is braking, and – by the wheel slip definition in (2.5) – $\lambda \in [0, 1]$ during braking.

According to the assumption of regarding the vehicle speed v as a slowly-varying parameter, system (2.18) can be formulated as a first-order model of the wheel slip dynamics only in the form

$$\dot{\lambda} = -\frac{1}{v}\left(\frac{(1-\lambda)}{m} + \frac{r^2}{J}\right) F_z \mu(\lambda) + \frac{r}{Jv} T_b, \tag{2.28}$$

which, expressing v as $v = \frac{\omega r}{1-\lambda}$ and assuming that $\lambda \in [0, 1)$, can be re-written as

$$\dot{\lambda} = -\frac{1-\lambda}{J\omega}\left(\Psi(\lambda) - T_b\right), \tag{2.29}$$

with $\omega > 0$ and

$$\Psi(\lambda) = \left(r + \frac{J}{rm}(1-\lambda)\right) F_z \mu(\lambda). \tag{2.30}$$

When inspecting Equation 2.29, it is obvious that the equilibrium points are characterised by

$$\overline{T}_b = \Psi(\overline{\lambda}). \tag{2.31}$$

Specifically, when $\mu(\lambda)$ is expressed by means of (2.13) and the control input is constant, *i.e.*, $T_b = \overline{T}_b$, the system exhibits the equilibrium points represented, in Figure 2.6, by the intersections between the curve $\Psi(\lambda)$ and the constant value of the braking torque $\overline{T}_b$. To summarise the system behaviour, one may note the following.

1. If $\overline{T}_b > \max_{\lambda} \Psi(\lambda)$, the system has no equilibrium points (recall that the model has been derived under the assumption that $\lambda \in [0, 1)$.
2. If $\overline{T}_b \leq \max_{\lambda} \Psi(\lambda)$, the system has at most two equilibria, namely $\bar{\lambda}_1$ and $\bar{\lambda}_2$ in Figure 2.6, where $\bar{\lambda}_1 \leq \bar{\lambda}_2$ are the two possibly coincident[1] solutions of

$$\overline{T}_b = \Psi(\lambda). \tag{2.32}$$

As the considered nonlinear system (2.29) is a first-order one, the stability properties of the equilibrium points can be easily investigated by analysing the behaviour of the open-loop vector field in the case $\overline{T}_b \leq \max_{\lambda} \Psi(\lambda)$.

To this end, refer to Figure 2.7, where the graph of $\dot{\lambda}$ as a function of λ is displayed for $T_b = \overline{T}_b = 600$ Nm, *i.e.*, the same condition depicted in Figure 2.6. As can be seen from the figure (and also by inspecting (2.29)) $\bar{\lambda}_1$ is a locally asymptotically stable equilibrium, while and $\bar{\lambda}_2$ is unstable (see also Appendix A).

Note further that analysing the expression of $\Psi(\lambda)$ in (2.30), as $rm >> J$, one has $\Psi(\lambda) \simeq rF_z\mu(\lambda)$. As such, the wheel slip value corresponding to the

[1] Note that the two solutions of (2.32) coincide only if $\overline{T}_b = \max_{\lambda} \Psi(\lambda)$.

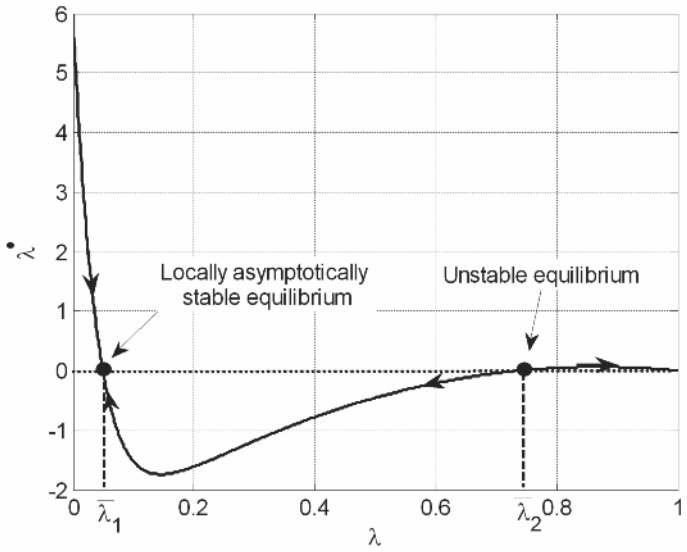

Figure 2.7 Graph of $\dot{\lambda}$ as a function of λ

abscissa of the maximum of $\Psi(\lambda)$ is – for all practical purposes – that of the peak of the friction curve.

As such, the nonlinear analysis performed confirms the common knowledge that, for constant values of the braking torque, the equilibria associated with slip values *beyond* the peak of the tyre–road friction curve (see also Figure 2.3) are unstable. It is well known that the optimal trade-off between longitudinal friction force and lateral directional force is achieved if a set-point value for the wheel slip is chosen close to the peak value of the curve $\mu(\lambda)$.

A final remark about model (2.29) is due. If we remove the assumption that $\lambda \in [0, 1)$, and consider also the value $\lambda = 1$, that is completely locked wheels, as an admissible one, then Equation 2.29 clearly shows that $\lambda = 1$ implies $\dot{\lambda} = 0$ for all values of the braking torque T_b, which means that the condition of locked wheels is an equilibrium point for the system. However, as can be seen from Figure 2.7 the point $\lambda = 1$ is located on the boundary of the domain where the state variable λ is defined and thus its stability properties cannot be directly investigated with the standard analysis tools used in Lyapunov stability theory (see also Appendix A), as the concept of neighbourhood of the equilibrium point cannot be properly defined. Moreover, for model (2.29) to hold one needs $\omega > 0$, which in turn implies that λ cannot in fact be equal to 1, but can only approach 1 from the left.

For the design of a braking controller, it is also interesting to express the equilibrium points of the single-corner model in the (λ, η) plane. To do this, recall first that the wheel slip definition (2.5) gives

$$\lambda = 1 - \frac{\omega r}{v}, \tag{2.33}$$

which, differentiating with respect to time and letting $\dot{\lambda} = 0$, yields

$$\frac{(\omega \dot{v} - v\dot{\omega})}{v^2} = 0,$$

namely

$$\dot{\omega} = \omega \frac{\dot{v}}{v}.$$

By substituting $\omega = v(1-\lambda)/r$ and recalling the second equation of system (2.18), one has

$$\dot{\omega} = -\frac{F_z}{mr}(1-\lambda)\mu(\lambda),$$

which, recalling the definition of η in (2.16), becomes

$$\eta(\lambda) = \Xi(\lambda) := \frac{F_z}{mg}(1-\lambda)\mu(\lambda), \tag{2.34}$$

which is the desired closed-form expression of the steady-state relationship between η and λ.

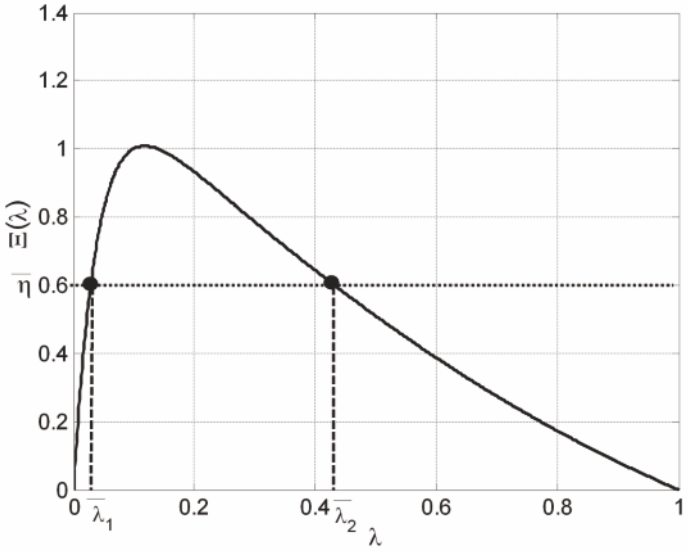

Figure 2.8 Equilibrium points for the single-corner model (2.29) in the (λ, η) plane (example with $F_z = mg$ and dry asphalt)

In Figure 2.8 the equilibrium manifold $\Xi(\lambda)$, see (2.34), is displayed in the (λ, η)-domain for case of $F_z = mg$ and dry asphalt. It is interesting to

observe $\Xi(\lambda)$ (and thus the normalised wheel deceleration η goes to zero as $\overline{\lambda}$ approaches 1, *i.e.*, as the wheel locks). Also notice that since $\Xi(\lambda)$ is a non-monotone function, for each value $\overline{\eta} \leq \max_\lambda \Xi(\lambda)$ there are two admissible slip equilibrium points $\overline{\lambda}_1$ and $\overline{\lambda}_2$, whereas if $\overline{\eta} > \max_\lambda \Xi(\lambda)$ no equilibrium points exist, which is exactly the same condition as that obtained for the case of the braking torque T_b analysed before for $\lambda \in [0, 1)$.

To investigate the stability properties of the equilibrium points, we can carry out the same graphical analysis of the vector field used for the braking torque input, by suitably rearranging the wheel slip dynamic equation and expressing it as a function of the normalised wheel deceleration.

To this end, first note that, substituting the definition of η in the wheel speed dynamics given in the first equation of system (2.17), one obtains that the normalised linear wheel deceleration dynamics are given by

$$\eta = \frac{r}{Jg}(T_b - rF_z\mu(\lambda)). \tag{2.35}$$

Substituting this expression together with the equation for the equilibrium manifold $\Xi(\lambda)$ in (2.34) into the wheel slip dynamics (2.29) and rearranging the equation, one obtains

$$\dot{\lambda} = -g\frac{1-\lambda}{J\omega}\left(\Xi(\lambda) - \eta\right), \tag{2.36}$$

with $\omega > 0$.

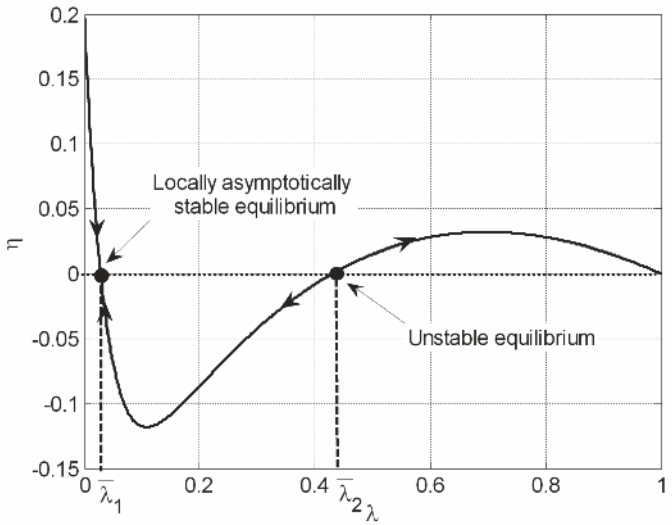

Figure 2.9 Graph of η as a function of λ

The graph of η as a function of λ is shown in Figure 2.9. As can be seen also by inspecting (2.36), $\bar{\lambda}_1$ is a locally stable equilibrium, while $\bar{\lambda}_2$ is unstable (see also Appendix A). Note finally that the discussion on the case $\lambda = 1$ is identical to that carried out previously with reference to the graph of $\dot{\lambda}$ as a function of λ.

2.5.1.2 Model Linearisation

Consider now the following variables, defined around an equilibrium point (characterised by $\overline{T}_b$, $\overline{\lambda}$, $\overline{\eta}$):

$$\delta T_b = T_b - \overline{T}_b; \qquad \delta\lambda = \lambda - \overline{\lambda}; \qquad \delta\eta = \eta - \overline{\eta}.$$

To carry out the linearisation of the system, a crucial issue is how to consider and manage the dynamic dependency on the variable v. Often (see, *e.g.*, [41]), a simple quasi-static assumption is made: v is assumed to be a slowly-varying parameter since it is assumed that the longitudinal dynamics of the vehicle are much slower than the rotational dynamics of the wheel. As such, to linearise the model, the simplest approach is to neglect the second equation (vehicle dynamics) of system (2.15) and work with the first-order model of the wheel dynamics.

To do this, let us define

$$\mu_1(\overline{\lambda}) := \left.\frac{\partial\mu}{\partial\lambda}\right|_{\lambda=\overline{\lambda}}, \tag{2.37}$$

which represents the slope of the $\mu(\lambda)$ curve around an equilibrium point.

By means of this definition, the friction curve $\mu(\lambda)$ is replaced by its first-order Taylor series around the equilibrium point $\overline{\lambda}$, namely

$$\mu(\lambda) \approx \mu(\overline{\lambda}) + \mu_1(\overline{\lambda})\delta\lambda. \tag{2.38}$$

Linearising the wheel dynamics model (2.28) assuming a constant speed value, *i.e.*, $v = \overline{v}$, one obtains

$$\delta\dot{\lambda} = \frac{F_z}{\overline{v}}\left[\frac{\mu(\overline{\lambda})}{m} - \mu_1(\overline{\lambda})\left(\frac{(1-\overline{\lambda})}{m} + \frac{r^2}{J}\right)\right]\delta\lambda + \frac{r}{J\overline{v}}\delta T_b.$$

Thus, the transfer function $G_\lambda(s)$ from δT_b to $\delta\lambda$ takes the form

$$G_\lambda(s) = \frac{\frac{r}{J\overline{v}}}{s + \frac{F_z}{m\overline{v}}\left[\mu_1(\overline{\lambda})\left((1-\overline{\lambda}) + \frac{mr^2}{J}\right) - \mu(\overline{\lambda})\right]}. \tag{2.39}$$

Now, linearising the relationship linking η and $\dot{\omega}$ given in (2.35) one obtains

$$\delta\eta = \frac{r}{Jg}\delta T_b - \frac{r^2}{Jg}\mu_1(\bar{\lambda})F_z\delta\lambda. \tag{2.40}$$

Thus, the transfer function from δT_b to $\delta\eta$ takes the form

$$G_\eta(s) = \frac{\frac{r}{Jg}\left[s + \frac{F_z}{m\bar{v}}\left(\mu_1(\bar{\lambda})(1-\bar{\lambda}) - \mu(\bar{\lambda})\right)\right]}{s + \frac{F_z}{m\bar{v}}\left[\mu_1(\bar{\lambda})\left((1-\bar{\lambda}) + \frac{mr^2}{J}\right) - \mu(\bar{\lambda})\right]}. \tag{2.41}$$

To enlarge the range of validity of the linearised model taking into more direct account the variability of the vehicle speed v, one may use an intermediate approach: the linearisation is done by explicitly considering the variations of v, locally around the non-equilibrium value $\overline{v}$ (namely, $\delta v = v - \overline{v}$); $\overline{v}$ is then considered a slowly-varying parameter in the linearised model.

Thus, no assumptions on the frequency decoupling between chassis and wheel dynamics are while carrying out the linearisation, and the first-order Taylor expansion of the friction curve $\mu(\lambda)$ becomes

$$\begin{aligned}\mu(\lambda(v,\omega)) &\approx \mu(\bar{\lambda}) + \left[\frac{\partial\mu}{\partial\lambda}\frac{\partial\lambda}{\partial v}\right]\Bigg|_{\lambda=\bar{\lambda}}\delta v + \left[\frac{\partial\mu}{\partial\lambda}\frac{\partial\lambda}{\partial\omega}\right]\Bigg|_{\lambda=\bar{\lambda}}\delta\omega = \\ &= \mu(\bar{\lambda}) + \mu_1(\bar{\lambda})\frac{\bar{\omega}r}{\bar{v}^2}\delta v - \mu_1(\bar{\lambda})\frac{r}{\bar{v}}\delta\omega.\end{aligned} \tag{2.42}$$

Linearising system (2.18) with the above expression for the friction curve one obtains the following second-order linear state space representation

$$\begin{aligned}\dot{x}(t) &= Ax(t) + Bu(t),\\ y(t) &= Cx(t),\end{aligned} \tag{2.43}$$

where $x = [\delta\omega \quad \delta v]^T$, $u = \delta T_b$ and

$$A = \begin{bmatrix} -\frac{\mu_1(\bar{\lambda})F_z r^2}{J\bar{v}} & \frac{\mu_1(\bar{\lambda})F_z r^2\bar{\omega}}{J\bar{v}^2} \\ \frac{\mu_1(\bar{\lambda})F_z r}{m\bar{v}} & -\frac{\mu_1(\bar{\lambda})F_z r\bar{\omega}}{m\bar{v}^2}\end{bmatrix}, \qquad B = \begin{bmatrix} -\frac{1}{J} \\ 0\end{bmatrix}.$$

Considering as output the wheel speed $\delta\omega$, namely setting $C = [1 \quad 0]$, the transfer function from δT_b to $\delta\omega$ is obtained as

$$G_\omega(s) = C(sI - A)^{-1}B = -\frac{1}{Js}\frac{s + \frac{\mu_1(\bar{\lambda})F_z}{mv}(1-\bar{\lambda})}{s + \frac{\mu_1(\bar{\lambda})F_z}{mv}\left((1-\bar{\lambda}) + \frac{mr^2}{J}\right)}. \tag{2.44}$$

Note that the pole at the origin of $G_\omega(s)$ corresponds to the physical situation where, in correspondence to a constant braking torque, the angular wheel speed decreases with constant deceleration.

Recalling now the definition of the normalised wheel deceleration η in (2.16), one obtains

$$G_\eta(s) = -\frac{r}{g} G_{\dot{\omega}}(s) = \frac{r}{Jg} \frac{s + \frac{\mu_1(\bar{\lambda}) F_z}{m\bar{v}}(1-\bar{\lambda})}{s + \frac{\mu_1(\bar{\lambda}) F_z}{m\bar{v}} \left((1-\bar{\lambda}) + \frac{mr^2}{J}\right)}. \tag{2.45}$$

Finally, *via* Equation 2.40 and Equation 2.45, the transfer function $G_\lambda(s)$ is obtained as

$$G_\lambda(s) = \frac{r}{J\bar{v}} \frac{1}{s + \frac{\mu_1(\bar{\lambda}) F_z}{m\bar{v}} \left((1-\bar{\lambda}) + \frac{mr^2}{J}\right)}. \tag{2.46}$$

It is now interesting to compare the transfer functions $G_\lambda(s)$ and $G_\eta(s)$ obtained with the two linearisation approaches. The comparison can be carried out considering first the case where $\mu_1(\overline{\lambda}) \cong 0$, *i.e.*, when the linearisation point is close to the peak of the friction curve. In this case, the linearised wheel slip dynamics yielded by the first linearisation method, see Equation 2.39, become

$$G_\lambda(s) = \frac{r/J\bar{v}}{s - \frac{F_z}{m\bar{v}} \mu(\overline{\lambda})}, \tag{2.47}$$

while those obtained with the second linearisation method, see Equation 2.46, give

$$G_\lambda(s) = \frac{r/J\bar{v}}{s}. \tag{2.48}$$

As for $G_\eta(s)$, the two approaches give the same result due to a zero/pole cancellation[2], which holds in both cases and yields

$$G_\eta(s) = \frac{r}{Jg}. \tag{2.49}$$

Thus, the first linearisation method yields an unstable linearised system at the peak of the friction curve, while the second one has the peak of the friction curve as stability boundary for the linearised model, which separates the open-loop (locally) asymptotically stable equilibrium points from the unstable ones.

On the other hand, when $\mu_1(\overline{\lambda})$ is dominant with respect to $\mu(\overline{\lambda})$ (note that due to the friction curves shape – see Figure 2.3 – this is true for most values of λ on all surfaces except snow), the two linearisation approaches provide comparable results.

In the following, when dealing with the single-corner model we work on the transfer functions obtained with the second linearisation procedure, as it yields models that have the friction curve peak as stability boundary and this better reflects the results obtained with the analysis of the nonlinear model.

Thus, we work with $G_\lambda(s)$ and $G_\eta(s)$ having their single pole located at

[2] Note that with the first linearisation approach the pole/zero pair which cancels out has positive real part, as the zero and pole have same the expression as the pole of $G_\lambda(s)$ in (2.47), whereas with the second linearisation approach the cancellation is of a pole/zero pair at the origin (see Equation 2.45).

$$s_p = -\frac{\mu_1(\bar{\lambda})F_z}{m\bar{v}}\left[(1-\bar{\lambda}) + \frac{mr^2}{J}\right], \tag{2.50}$$

and with the zero of $G_\eta(s)$ given by

$$s_z = -\frac{\mu_1(\bar{\lambda})F_z}{m\bar{v}}(1-\bar{\lambda}). \tag{2.51}$$

2.5.1.3 Stability Analysis

Based on the transfer function models (2.46) and (2.45), stability and minimum-phase properties of the linearised system can be analysed easily.

Stability Condition Based on $G_\lambda(s)$ and $G_\eta(s)$

The linearised single-corner model with transfer functions $G_\lambda(s)$ and $G_\eta(s)$ is asymptotically stable if and only if

$$\frac{\mu_1(\overline{\lambda})F_z}{m\overline{v}}\left[(1-\overline{\lambda}) + \frac{mr^2}{J}\right] > 0,$$

which, the term in the brackets being positive, reduces to $\mu_1(\overline{\lambda}) > 0$.

This means that $G_\lambda(s)$ and $G_\eta(s)$ are open-loop unstable if the equilibrium $\overline{\lambda}$ occurs beyond the peak of the curve $\mu(\lambda)$.

Further, it is worth noting that the transfer function $G_\eta(s)$ is minimum phase[3] if and only if its pole and zero are in the left half plane and its static gain is positive. The condition on the pole is $\mu_1(\overline{\lambda}) > 0$, while the others are given by

$$G_\eta(0) = \frac{g\overline{v}}{\mu_1(\overline{\lambda})F_z} > 0,$$

and

$$\frac{\mu_1(\overline{\lambda})F_z}{m\overline{v}}\left(1-\overline{\lambda}\right) > 0,$$

which can be again reduced to $\mu_1(\overline{\lambda}) > 0$.

This means that $G_\eta(s)$ is non-minimum phase if the equilibrium $\overline{\lambda}$ occurs beyond the peak of the curve $\mu(\lambda)$.

This analysis has shown that the choice of the equilibrium point strongly affects the stability and minimum-phase properties of the linearised single-corner model. Specifically, by applying Lyapunov linearisation method (see Section A.2.1.2), one has that for constant values of the braking torque, the

[3] A linear and time-invariant system with transfer function $G(s)$ is said to be minimum phase if $G(s)$ has positive gain, all its zeros and poles are in the left half plane and it does not contain any pure delay.

equilibria of system (2.18) associated with slip values beyond the peak of the tyre–road friction curve are unstable, which is consistent with the analysis carried out on the nonlinear system equations.

This instability can hardly be handled by non-professional drivers and it represents another important motivation for the design of ABS systems.

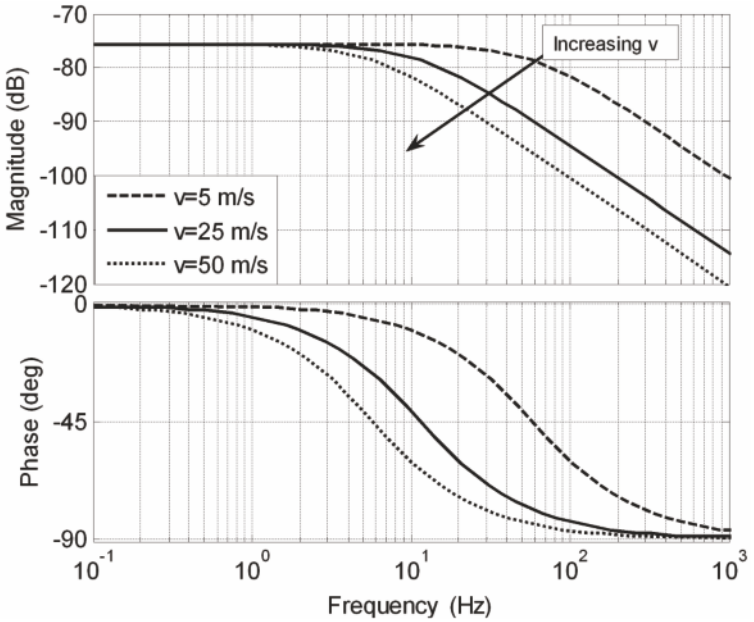

Figure 2.10 Magnitude and phase Bode plots of the frequency response associated with $G_\lambda(s)$ for different longitudinal speed values (the nominal linearisation conditions are as in Table 2.4)

2.5.1.4 Numerical Sensitivity Analysis

It is now worth analysing the effects that some specific system parameters have on the linearised single-corner dynamics. To this end, we first point out that the nominal linearisation conditions are given in Table 2.4. Based on these, we will now analyse the effect of varying the vehicle speed and the vertical load, the latter being represented by the variable F_z.

The analysis carried out in the previous section has shown that the longitudinal vehicle speed v, which is being considered as a slowly-varying parameter, does not affect the stability and minimum-phase properties of the linearised braking dynamics.

However, it has the very awkward effect of acting as a time scale on the wheel dynamics. As a matter of fact, notice that both the pole and the zero

are characterised by the multiplying factor $1/\overline{v}$. In Figure 2.10 the magnitude and phase Bode plots of the frequency response associated with $G_\lambda(s)$ (in the nominal linearisation conditions listed in Table 2.4) are displayed for three different values of $\overline{v}$. Note that the angular frequency of the pole of the linearised wheel dynamics for $v = 3$ m/s is a decade larger than that for $v = 30$ m/s. Clearly, this scaling effect must somehow be taken into account in the design of a braking controller. This issue was extensively considered in [41], where a simple but effective adaptive control strategy was proposed, using a $\overline{v}$-dependent gain-scheduling rationale.

Table 2.4 Nominal linearisation conditions for the single-corner model

Variable	Steady-state value
$\overline{\lambda}$	0.05
$\overline{T}_b$	600 Nm
$\overline{v}$	25 m/s
F_z	mg
Road conditions	Dry asphalt (see Table 2.1)

For braking control design, it is useful to also investigate the effects of the vertical load F_z on $G_\lambda(s)$. To highlight the effect of vertical load variations, it is useful to rewrite $G_\lambda(s)$ as

$$G_\lambda(s) = \frac{\frac{r}{J\overline{v}}}{s + \left[\mu_1(\overline{\lambda})\frac{Ng}{\overline{v}}\left((1-\overline{\lambda}) + \frac{mr^2}{J}\right)\right]}, \tag{2.52}$$

where

$$N = \frac{F_z}{mg} \tag{2.53}$$

represents the ratio between the actual vertical load F_z and its static value mg and allows us to highlight the effects of the load transfer that occurs during braking.

As can be seen in Figure 2.11, and recalling Figure 2.10, the vertical load mainly affects the low frequency behaviour of $G_\lambda(s)$, while the longitudinal speed v is the dominating effect at high frequency, acting as a scaling on the wheel dynamics. In fact, the static gain of $G_\lambda(s)$ is given by

$$G_\lambda(0) = \frac{\frac{r}{JN\overline{v}}}{\frac{\mu_1(\overline{\lambda})F_z}{m\overline{v}}\left[(1-\overline{\lambda}) + \frac{mr^2}{J}\right]}, \tag{2.54}$$

while the high frequency gain has the form

$$\lim_{s\to\infty} s\,G_\lambda(s) = \frac{r}{J\overline{v}}, \tag{2.55}$$

and these expressions explain the behaviour in Figures 2.10 and 2.11.

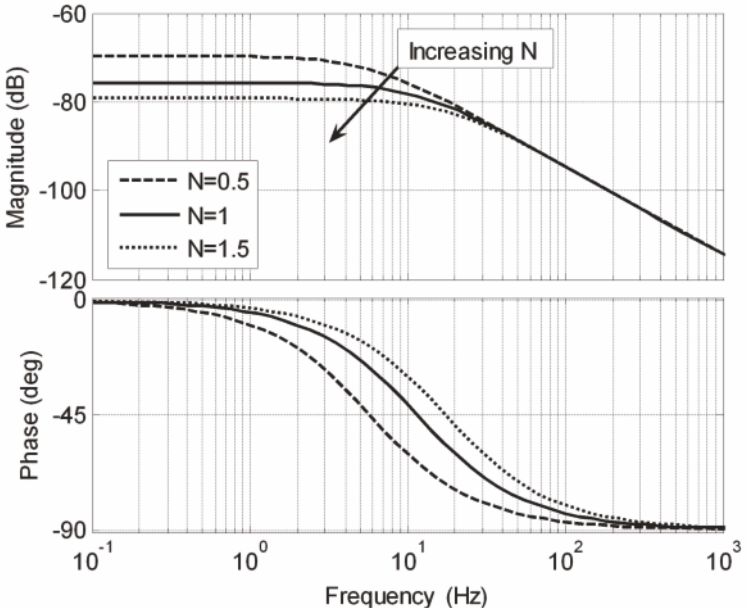

Figure 2.11 Magnitude and phase Bode plots of the frequency response associated with $G_\lambda(s)$ for different values of the vertical load (the nominal linearisation conditions are as in Table 2.4)

2.5.2 Double-corner Model Analysis

We now analyse the double-corner model introduced in Section 2.4. For this model we will be able to analytically study the system equilibrium points and to carry out the model linearisation explicitly. Further, the transfer function matrix will be obtained. Finally, the proposed dynamical models will be compared based on the analysis of their frequency responses.

2.5.2.1 Equilibrium Points

Once again, we are interested in the equilibrium points characterised by $\dot{\lambda}_i = 0$, $i = \{f, r\}$, *i.e.*, constant longitudinal slip $\lambda_i = \overline{\lambda}_i$, which in turn yields a constant deceleration $\dot{v} = \bar{v}$.

As mentioned in Section 2.4, we work on the first two equations of system (2.25) and consider v as a parameter. Therefore, the system dynamics we are interested in are given by

$$\begin{cases} \dot{\lambda_f} = -\frac{r}{Jv}\left(\Psi_f(\lambda_f, \lambda_r) - T_{b_f}\right), \\ \dot{\lambda_r} = -\frac{r}{Jv}\left(\Psi_r(\lambda_f, \lambda_r) - T_{b_r}\right), \end{cases} \tag{2.56}$$

where $\Psi_f(\lambda_f, \lambda_r)$ and $\Psi_r(\lambda_f, \lambda_r)$ are as in (2.26) and (2.27), respectively.

Figures 2.12(a) and 2.12(b) show a plot of the functions $\Psi_f(\cdot, \lambda_r)$ and $\Psi_r(\lambda_f, \cdot)$, respectively, obtained for different values of λ_r and λ_f. As it is apparent by inspecting these figures, the front wheel behaviour is substantially independent from that of the rear wheel, while the latter is strongly coupled to the front one.

This can be explained recalling the expression of $\Psi_f(\cdot, \lambda_r)$ and $\Psi_r(\lambda_f, \cdot)$ given in (2.26) and (2.27). As a matter of fact, as $\dot{v}$ is negative during braking, $\Psi_f(\cdot, \lambda_r)$ and $\Psi_r(\lambda_f, \cdot)$ are different in magnitude, as the term $\Delta_{F_z}\dot{v}$ is negative. This difference in magnitude makes $\Psi_r(\lambda_f, \cdot)$ much more sensitive to the variations in the wheel slip λ_f, which modifies both the numerical value and the shape of the function $\dot{v}$ in (2.24).

As such, the equilibrium points for each wheel have the form

$$\begin{aligned} \Psi_f(\overline{\lambda}_f, \overline{\lambda}_r) &= \overline{T}_{bf}, \\ \Psi_r(\overline{\lambda}_f, \overline{\lambda}_r) &= \overline{T}_{br}, \end{aligned} \tag{2.57}$$

and thus share the same structure with those analysed for the single-corner model, see Equation 2.31. Thus, the reasoning used in Section 2.5.1 to study the system equilibria for the single-corner model can be applied also in this case. In fact, for both the front and the rear wheels, conditions (2.57) can be pictorially described as in Figure 2.6 and similar conclusions can be drawn.

2.5.2.2 Model Linearisation

To linearise the double-corner model (2.56), let us define the variables $\delta\lambda_f = \lambda_f - \overline{\lambda}_f$, $\delta\lambda_r = \lambda_r - \overline{\lambda}_r$, $\delta T_{bf} = T_{bf} - \overline{T}_{bf}$ and $\delta T_{br} = T_{br} - \overline{T}_{br}$.

To perform the linearisation we work under the assumption of constant vehicle speed. This choice is motivated by the fact that with this assumption the linearisation procedure can be carried out analytically in a rather simple manner. Of course, the alternative linearisation method considered for the single-corner model in Section 2.5.1 (see in particular Equation 2.42) can be applied also to this case, but the computations are too complex to be analysed explicitly.

Thus, the Taylor expansion of the tyre–road friction coefficient has the form

$$\mu(\lambda_i) \approx \mu(\overline{\lambda}_i) + \mu_1(\overline{\lambda_i})\delta\lambda_i, \quad i = \{f, r\}, \tag{2.58}$$

where $\mu_1(\overline{\lambda})$ is as in (2.37). Further, to simplify the notation of the linearised equations, we introduce the following definition:

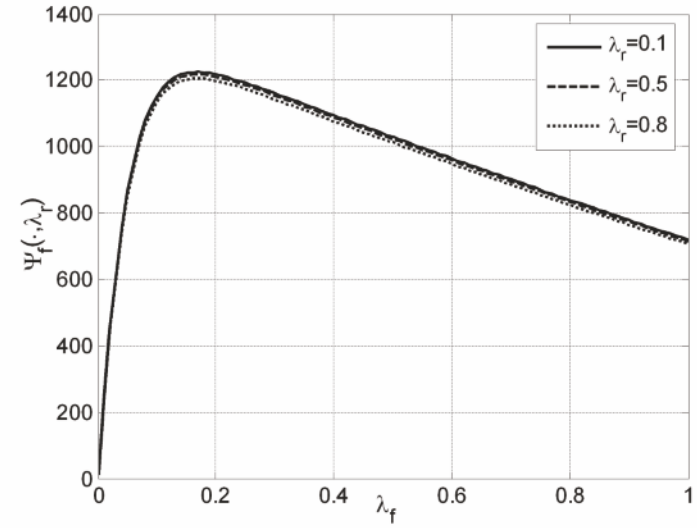

(a)

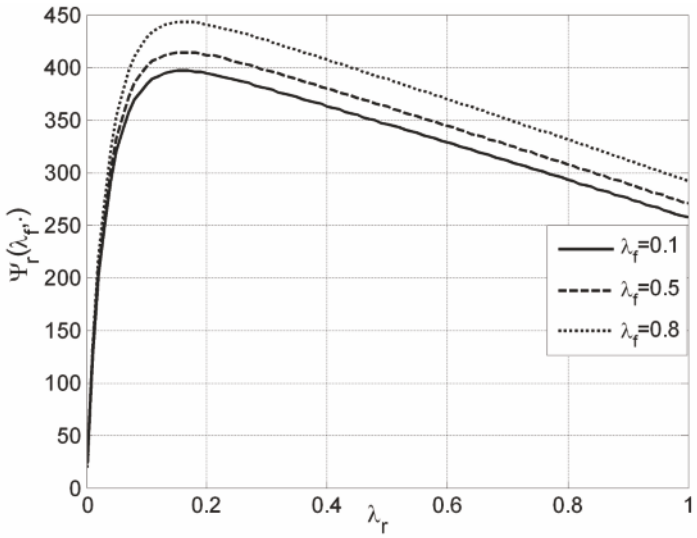

(b)

Figure 2.12 Plot of (a) $\Psi_f(\cdot, \lambda_r)$ for different values of λ_r: $\lambda_r = 0.1$ (*solid line*), $\lambda_r = 0.5$ (*dashed line*) and $\lambda_r = 0.8$ (*dotted line*) and (b) $\Psi_r(\lambda_f, \cdot)$ for different values of λ_f: $\lambda_f = 0.1$ (*solid line*), $\lambda_f = 0.5$ (*dashed line*) and $\lambda_f = 0.8$ (*dotted line*)

$$\delta\overline{\Psi}_{i,j} := \left.\frac{\partial \Psi_i(\lambda_i,\lambda_j)}{\partial \lambda_j}\right|_{\lambda_i=\overline{\lambda}_i,\lambda_j=\overline{\lambda}_j}, \quad i=\{f,r\}. \tag{2.59}$$

Thus, the linearised equations of the double-corner model (2.56) have the form

$$\begin{cases} \delta\dot{\lambda}_f = -\frac{r}{J\overline{v}}\left(\delta\overline{\Psi}_{f,f}\delta\lambda_f + \delta\overline{\Psi}_{f,r}\delta\lambda_r - \delta T_{b_f}\right), \\ \delta\dot{\lambda}_r = -\frac{r}{J\overline{v}}\left(\delta\overline{\Psi}_{r,f}\delta\lambda_f + \delta\overline{\Psi}_{r,r}\delta\lambda_r - \delta T_{b_r}\right), \end{cases} \tag{2.60}$$

where

$$\begin{aligned} \delta\overline{\Psi}_{f,f} = rW_f\mu_1(\overline{\lambda}_f) + \left[r\Delta_{F_z}\mu_1(\overline{\lambda}_f) - \frac{J}{r}\right]\dot{\overline{v}}_+ \\ + \left[r\Delta_{F_z}\mu(\overline{\lambda}_f) + \frac{J}{r}(1-\overline{\lambda}_f)\right]\dot{\overline{v}}_{+,f}, \end{aligned} \tag{2.61}$$

$$\delta\overline{\Psi}_{f,r} = \left[r\Delta_{F_z}\mu(\overline{\lambda}_f) + \frac{J}{r}(1-\overline{\lambda}_f)\right]\dot{\overline{v}}_{+,r}, \tag{2.62}$$

$$\delta\overline{\Psi}_{r,f} = \left[-r\Delta_{F_z}\mu(\overline{\lambda}_r) + \frac{J}{r}(1-\overline{\lambda}_r)\right]\dot{\overline{v}}_{+,f}, \tag{2.63}$$

$$\begin{aligned} \delta\overline{\Psi}_{r,r} = rW_r\mu_1(\overline{\lambda}_r) - \left[r\Delta_{F_z}\mu_1(\overline{\lambda}_r) + \frac{J}{r}\right]\dot{\overline{v}}_+ \\ - \left[r\Delta_{F_z}\mu(\overline{\lambda}_r) - \frac{J}{r}(1-\overline{\lambda}_r)\right]\dot{\overline{v}}_{+,r}, \end{aligned} \tag{2.64}$$

and

$$\dot{\overline{v}}_+ = \frac{W_f\mu(\overline{\lambda}_f) + W_r\mu(\overline{\lambda}_r)}{M - \Delta_{F_z}[\mu(\overline{\lambda}_f) - \mu(\overline{\lambda}_r)]}, \tag{2.65}$$

$$\dot{\overline{v}}_{+,f} = \frac{W_f\mu_1(\overline{\lambda}_f)}{M - \Delta_{F_z}[\mu(\overline{\lambda}_f) - \mu(\overline{\lambda}_r)]} + \Delta_{F_z}\mu_1(\overline{\lambda}_f)\frac{W_f\mu(\overline{\lambda}_f) + W_r\mu(\overline{\lambda}_r)}{\left(M - \Delta_{F_z}[\mu(\overline{\lambda}_f) - \mu(\overline{\lambda}_r)]\right)^2}, \tag{2.66}$$

$$\dot{\overline{v}}_{+,r} = \frac{W_r\mu_1(\overline{\lambda}_r)}{M - \Delta_{F_z}[\mu(\overline{\lambda}_f) - \mu(\overline{\lambda}_r)]} - \Delta_{F_z}\mu_1(\overline{\lambda}_r)\frac{W_f\mu(\overline{\lambda}_f) + W_r\mu(\overline{\lambda}_r)}{\left(M - \Delta_{F_z}[\mu(\overline{\lambda}_f) - \mu(\overline{\lambda}_r)]\right)^2}. \tag{2.67}$$

The expressions obtained are useful for deriving the transfer function matrix

$$G(s) = \begin{bmatrix} \delta\lambda_f \\ \delta\lambda_r \end{bmatrix} = \begin{bmatrix} G_{ff}(s) & G_{fr}(s) \\ G_{rf}(s) & G_{rr}(s) \end{bmatrix} \begin{bmatrix} \delta T_{bf} \\ \delta T_{br} \end{bmatrix}, \tag{2.68}$$

which describes the wheel slip dynamics of the double-corner model.

To compute the expression of the transfer function matrix in (2.68), consider that system (2.60) has the following second-order state space representation:

$$\begin{aligned} \dot{x}(t) &= Ax(t) + Bu(t), \\ y(t) &= Cx(t), \end{aligned} \tag{2.69}$$

where $x = [\delta\lambda_f \ \delta\lambda_r]^T$ and $u = [\delta T_{bf} \ \delta T_{br}]^T$, and

$$A = -\frac{r}{J\overline{v}} \begin{bmatrix} \delta\overline{\Psi}_{f,f} & \delta\overline{\Psi}_{f,r} \\ \delta\overline{\Psi}_{r,f} & \delta\overline{\Psi}_{r,r} \end{bmatrix},$$

$$B = \frac{r}{J\overline{v}} \begin{bmatrix} 1 & 0 \\ 0 & 1 \end{bmatrix},$$

$$C = \begin{bmatrix} 1 & 0 \\ 0 & 1 \end{bmatrix}.$$

Thus, computing $G(s) = C(sI - A)^{-1}B$, yields

$$G(s) = \frac{r/J\overline{v}}{D(s)} \begin{bmatrix} (s + \frac{r}{J\overline{v}}\delta\overline{\Psi}_{r,r}) & -\frac{r}{J\overline{v}}\delta\overline{\Psi}_{f,r} \\ -\frac{r}{J\overline{v}}\delta\overline{\Psi}_{r,f} & (s + \frac{r}{J\overline{v}}\delta\overline{\Psi}_{f,f}), \end{bmatrix}, \tag{2.70}$$

with

$$D(s) = s^2 + \frac{r}{J\overline{v}}(\delta\overline{\Psi}_{f,f} + \delta\overline{\Psi}_{r,r})s + \left[\frac{r}{J\overline{v}}\right]^2 \left(\delta\overline{\Psi}_{f,f}\delta\overline{\Psi}_{r,r} - \delta\overline{\Psi}_{f,r}\delta\overline{\Psi}_{r,f}\right). \tag{2.71}$$

2.5.2.3 Stability Analysis

Based on the transfer function matrix (2.70), the stability and minimum-phase properties of the linearised double-corner model can be easily analysed.

The linearised double-corner model with transfer function matrix (2.70) is asymptotically stable if and only if the coefficients of the denominator $D(s)$ in (2.71) are non-zero and have the same sign[4].

To work out this condition in a meaningful and readable manner, we proceed by assuming that the front wheel dynamics are independent of those of the rear wheel, *i.e.*, we disregard the dependence of $\Psi_f(\lambda_f, \lambda_r)$ from λ_r and set $\delta\overline{\Psi}_{f,r} = 0$. This assumption is motivated by the analysis carried out in

[4] For a second-order polynomial, this is a necessary and sufficient condition for its roots to have negative real part.

Section 2.4 (see also Figures 2.12(a) and 2.12(b)). Further, we perform the linearisation about $\overline{\lambda}_f = \overline{\lambda}_r = \overline{\lambda}$.

Under this assumption, one has asymptotic stability of the linearised model if and only if

$$\begin{cases} \delta\overline{\Psi}_{f,f} + \delta\overline{\Psi}_{r,r} > 0, \\ \delta\overline{\Psi}_{f,f}\delta\overline{\Psi}_{r,r} > 0. \end{cases} \tag{2.72}$$

In view of the above assumptions and of the expressions of $\delta\overline{\Psi}_{f,f}$ and $\delta\overline{\Psi}_{r,r}$ in (2.61) and (2.64), the first equation of (2.72) has the form

$$\begin{aligned} &\delta\overline{\Psi}_{f,f} + \delta\overline{\Psi}_{r,r} = r(W_f + W_r)\mu_1(\overline{\lambda}) - 2\frac{J}{r}\overline{v}_+ \\ &+ \frac{J}{r}(1-\overline{\lambda})[\overline{v}_{+,f} + \overline{v}_{+,r}] + r\Delta_{F_z}\mu(\overline{\lambda})[\overline{v}_{+,f} - \overline{v}_{+,r}] \\ &= r(W_f + W_r)\mu_1(\overline{\lambda})\left[1 + \frac{J}{r^2 M}\left(-2\frac{\mu(\overline{\lambda})}{\mu_1(\overline{\lambda})} + (1-\overline{\lambda})\right) + \frac{2\Delta_{F_z}\mu(\overline{\lambda})^2}{M^2}\right] > 0, \end{aligned}$$

which, considering that $J/(r^2 M) << 1$ reduces to $\mu_1(\overline{\lambda}) > 0$.

Analysing now the second condition (2.72), one obtains

$$\begin{aligned} &\delta\overline{\Psi}_{f,f}\delta\overline{\Psi}_{r,r} = r^2 W_f W_r \mu_1(\overline{\lambda})^2 + \left(\frac{J^2}{r^2} - r^2\Delta_{F_z}^2\mu_1(\overline{\lambda})^2\right)\overline{v}_+^2 \\ &+ \left(\frac{J^2}{r^2}(1-\overline{\lambda})^2 - r^2\Delta_{F_z}^2\mu(\overline{\lambda})^2\right)[\overline{v}_{+,f}\overline{v}_{+,r}] \\ &\cong r^2 W_f W_r \mu_1(\overline{\lambda})^2\left[1 - \frac{\Delta_{F_z}^2\mu(\overline{\lambda})^2}{M^2}\frac{(W_f + W_r)^2}{W_f W_r} - \frac{\Delta_{F_z}^2\mu(\overline{\lambda})^2}{M^2}\right] > 0, \end{aligned}$$

which, considering that the two negative terms in the square brackets are both $<< 1$, is trivially satisfied for all choices of the linearisation point.

This analysis shows that the linearised system with transfer function $G(s)$ is open-loop unstable if the equilibrium $(\overline{\lambda}_f, \overline{\lambda}_r)$ occurs beyond the peak of the curve $\mu(\lambda)$, thus yielding the same stability condition found for the single-corner model.

Further, it is interesting to note that the static gain of $G_{ff}(s)$ is given by

$$G_{ff}(0) = \frac{\delta\overline{\Psi}_{r,r}}{\left(\delta\overline{\Psi}_{f,f}\delta\overline{\Psi}_{r,r} - \delta\overline{\Psi}_{f,r}\delta\overline{\Psi}_{r,f}\right)} \cong \frac{1}{\delta\overline{\Psi}_{f,f}}, \tag{2.73}$$

while similarly that of $G_{rr}(s)$ has the form

$$G_{rr}(0) = \frac{\delta\overline{\Psi}_{f,f}}{\left(\delta\overline{\Psi}_{f,f}\delta\overline{\Psi}_{r,r} - \delta\overline{\Psi}_{f,r}\delta\overline{\Psi}_{r,f}\right)} \cong \frac{1}{\delta\overline{\Psi}_{r,r}}. \tag{2.74}$$

By analysing the expression of $\delta\overline{\Psi}_{f,f}$ in (2.61) and observing that $\overline{\dot{v}}_{+,r} > 0$ if and only if $\mu_1(\overline{\lambda}) > 0$ (see Equation 2.66), one has that the static gain of $G_{ff}(s)$ is positive if the linearisation point is before the peak of the friction curve (note that the same was true for the single-corner model, see Equation 2.54). To see that this holds also for $G_{rr}(s)$, consider the expression of $\delta\overline{\Psi}_{r,r}$ in (2.64), which can be rewritten as

$$\begin{aligned}\delta\overline{\Psi}_{r,r} &= rW_r\mu_1(\overline{\lambda}) - \frac{rW_r\Delta_{F_z}\mu(\overline{\lambda})\mu_1(\overline{\lambda})}{M} \\ &\quad - \frac{r(W_f+W_r)\Delta_{F_z}\mu(\overline{\lambda})\mu_1(\overline{\lambda})}{M}\left[1+\frac{\Delta_{F_z}\mu(\overline{\lambda})}{M}\right] \\ &\cong rW_r\mu_1(\overline{\lambda})\left[1-\frac{\Delta_{F_z}\mu(\overline{\lambda})}{M}\left(1+\frac{(W_f+W_r)}{W_r}\right)\right] \cong rW_r\mu_1(\overline{\lambda}).\end{aligned}$$

Finally, the zero of the transfer functions $G_{ff}(s)$ and $G_{rr}(s)$ has the form

$$s_z = -\frac{r}{J\overline{v}}\delta\overline{\Psi}_{i,i}, \quad i = \{f, r\}.$$

Thus, the zero is negative if and only if $\delta\overline{\Psi}_{i,i} > 0$ and this, as shown above, happens when $\mu_1(\overline{\lambda}) > 0$, thus again yielding results that are qualitatively equal to those obtained for the single-corner model.

Moving to the transfer functions $G_{ij}(s)$, $i = \{f, r\}$ of the coupling terms, one has that the static gain is given by

$$G_{ij}(0) = \frac{-\delta\overline{\Psi}_{i,j}}{\frac{r}{J\overline{v}}\left(\delta\overline{\Psi}_{i,i}\delta\overline{\Psi}_{j,j} - \delta\overline{\Psi}_{i,j}\delta\overline{\Psi}_{j,i}\right)} \cong \frac{-\delta\overline{\Psi}_{i,j}}{\frac{r}{J\overline{v}}\left(\delta\overline{\Psi}_{i,i}\delta\overline{\Psi}_{j,j}\right)}. \tag{2.75}$$

Thus, while the static gain of the direct transfer functions $G_{ff}(s)$ and $G_{rr}(s)$ is independent of $\overline{v}$ as it was for the single-corner model, see Equation 2.54, this is not true for the transfer functions of the coupling terms, whose static gain is inversely proportional to $\overline{v}$. Further, note that the static gain of the transfer function $G_{rf}(s)$ is positive for all linearisation points with $\mu_1(\overline{\lambda}) > 0$, as – see Equation 2.63 – one has that

$$\delta\overline{\Psi}_{r,f} \cong -r\Delta_{F_z}\mu(\overline{\lambda})\mu_1(\overline{\lambda})\frac{W_f}{m}. \tag{2.76}$$

Conversely, the static gain of the transfer function $G_{fr}(s)$ is negative for all linearisation points with $\mu_1(\overline{\lambda}) > 0$, as – see Equation 2.62 – one has that

$$\delta\overline{\Psi}_{f,r} \cong r\Delta_{F_z}\mu(\overline{\lambda})\mu_1(\overline{\lambda})\frac{W_r}{m}. \tag{2.77}$$

Finally, the high frequency gain for the direct terms $G_{ff}(s)$ and $G_{rr}(s)$ has the form

$$\lim_{s\to\infty} s\,G_{ii}(s) = \frac{r}{J\overline{v}}, \quad i = \{f, r\}, \tag{2.78}$$

as was the case for the single-corner model, see Equation 2.55, while for the coupling terms it is given by

$$\lim_{s\to\infty} s^2\,G_{ij}(s) = -\left[\frac{r}{J\overline{v}}\right]^2 \delta\overline{\Psi}_{i,j}, \quad i = \{f, r\}. \tag{2.79}$$

Table 2.5 Nominal linearisation conditions for the double-corner model

Variable	Steady-state value
$\overline{\lambda}_f$	0.05
$\overline{\lambda}_r$	0.07
$\overline{T}_{bf}$	859 Nm
$\overline{T}_{br}$	395 Nm
$\overline{v}$	25 m/s
$\dot{\overline{v}}$	-8.8 m/s^2
F_{zf}	3.193.2 N
F_{zr}	1221.5 N
Road conditions	Dry asphalt (see Table 2.1)

2.5.2.4 Numerical Sensitivity Analysis

For the double-corner model, the analysis is carried out for the equilibrium point characterised by the values given in Table 2.5, which reports the linearisation conditions for the double-corner model. To analyse the open-loop behaviour of the transfer function matrix (2.68), let us refer to Figures 2.13 and 2.14, where the magnitude and phase Bode plots of frequency responses associated with the transfer functions in (2.68) are plotted. Note further that to perform a comparison with the single-corner model, the transfer functions $G_{ff}(s)$ and $G_{rr}(s)$ are also compared with their single-corner counterparts. The latter have been obtained employing the steady-state values in Table 2.5.

- **Single-corner *versus* Double-corner Model**
  The comparison is done first of all by analysing the transfer functions $G_{ff}(s)$ and $G_{rr}(s)$ and their counterparts obtained with the single-corner model. As can be seen, the single-corner model and the double-corner model do not show significant differences. This is due to the fact that considering Equation 2.71 and assuming again to disregard the dependency of $\Psi_f(\lambda_f, \lambda_r)$ from λ_r, *i.e.*, setting $\delta\overline{\Psi}_{f,r} = 0$, one has that the denominator $D(s)$ in (2.71) takes the form

$$D(s) = (s + \frac{r}{J\overline{v}}\delta\overline{\Psi}_{f,f})(s + \frac{r}{J\overline{v}}\delta\overline{\Psi}_{r,r}). \tag{2.80}$$

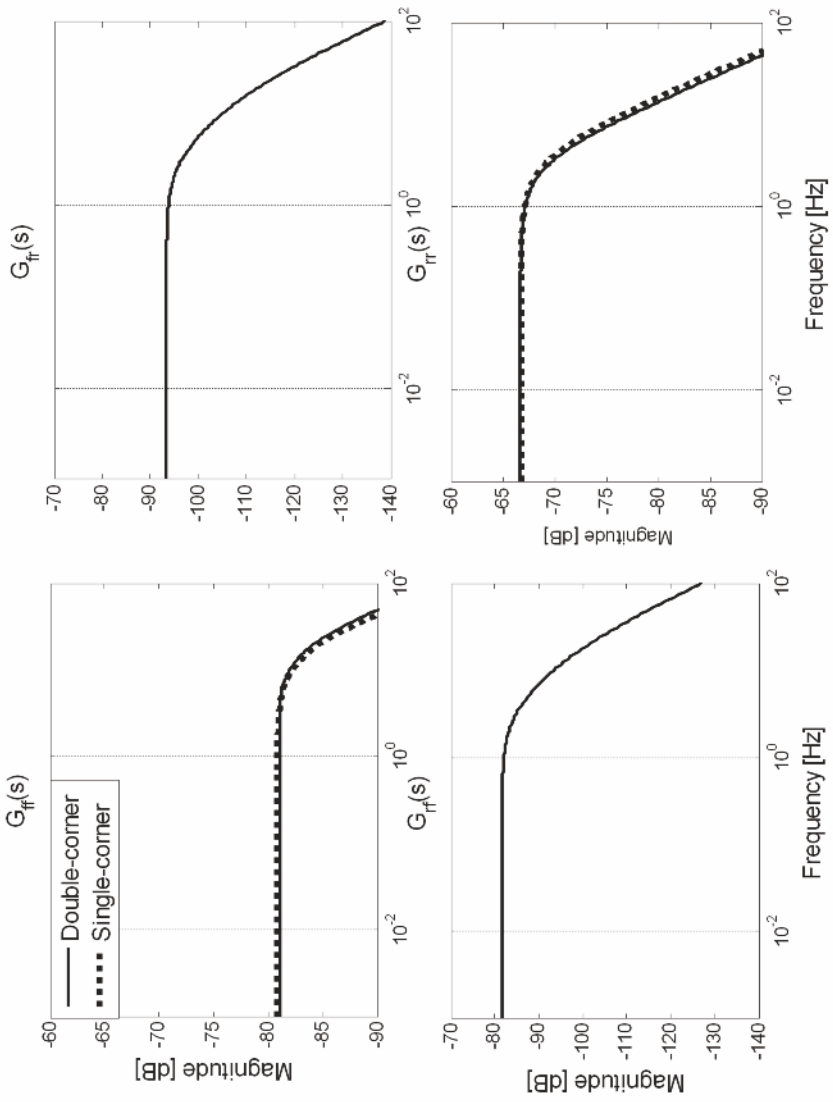

Figure 2.13 Magnitude Bode plots of the frequency response associated with the transfer function matrix (2.68)

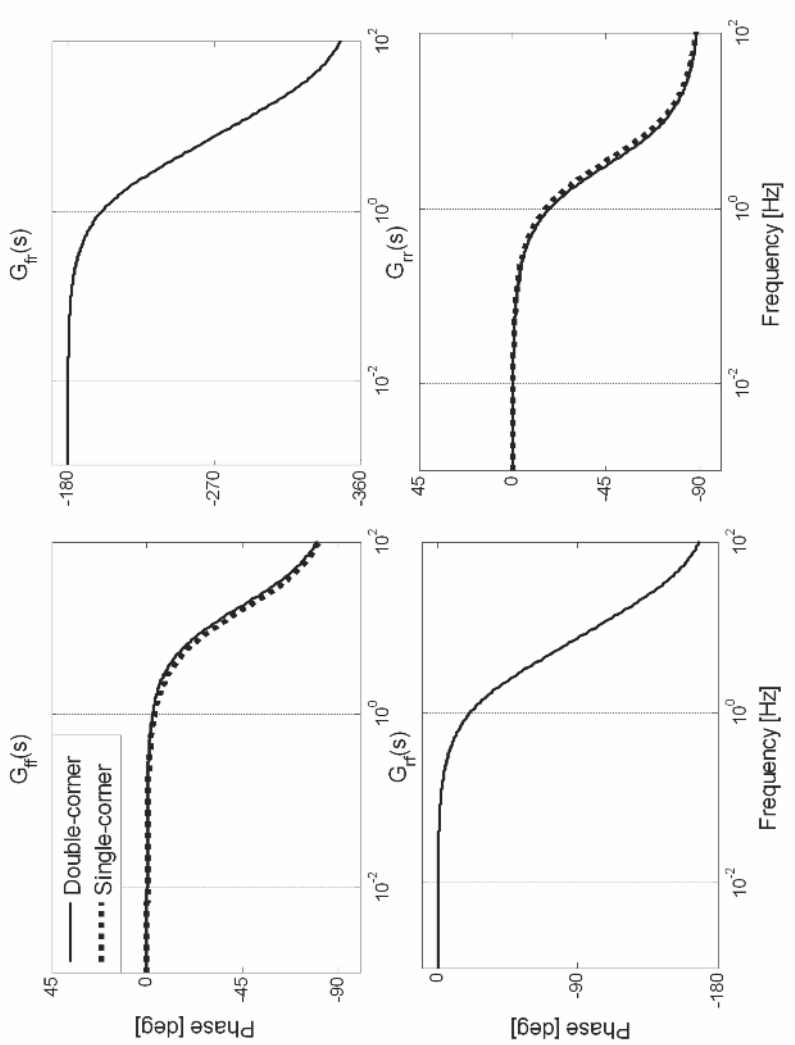

Figure 2.14 Phase Bode plots of the frequency response associated with the transfer function matrix (2.68)

Thus, under this assumption there is a cancellation between one of the poles and the zero of the direct terms, see Equation 2.70, and the double-corner model reduces in fact to the single-corner one. Actually, if no assumptions are made, the cancellation is not exact but nonetheless tends to cancel out the effects of the pole and of the zero, which indeed remain quite close. Further, coherently with the analysis carried out on the high-frequency gain, the single-corner and the double-corner model share the

same behaviour at high frequency. Due to this fact, the effects of longitudinal vehicle speed variations act as a frequency scaling on the transfer functions $G_{ff}(s)$ and $G_{rr}(s)$ of the double-corner model exactly in the same way as they do for the single-corner model, see Equations 2.55 and 2.78.

- **Coupling Terms**
  The most interesting feature of the double-corner model is its ability to describe the dynamic coupling between front and rear axles. As can be seen from Figure 2.13 the static gain of the coupling terms $G_{fr}(s)$ and $G_{rf}(s)$ is of the same magnitude as that of the *direct* transfer functions $G_{ff}(s)$ and $G_{rr}(s)$.
  Finally, the phase diagram in Figure 2.14 allows us to confirm the behaviour of the static gains of the coupling terms outlined in Equations 2.76 and 2.77. Specifically, the cross coupling term $G_{rf}(s)$ has negative static gain. This has the following intuitive physical interpretation: when a constant braking torque is applied to the front wheel, the front wheel slip λ_f increases (recall that λ is positive during braking) and this in turn causes the vehicle speed v to decrease. Hence, the effect on the rear axle (whose wheel speed ω_r is unaffected by the change on λ_f) is a decrease in the rear wheel slip as $\lambda_r = 1 - r\omega_r/v$. Note that this is in principle true also for the effect of the rear wheel on the front one, but because the effect of the rear wheel slip on the front one is very weak this is not evident.

2.6 Summary

In this chapter the adopted analytical description of the tyre–road contact forces was introduced and the dynamical models of the braking dynamics, which will serve as a basis in the control design phase, namely the single-corner and the double-corner models, were described.

Specifically, a complete analysis was carried out, both on the nonlinear models and on their linearised versions, so as to highlight the equilibrium points, their stability properties as a function of the model parameters and the frequency response characteristics.

These results constitute the necessary background on braking dynamics analysis and will serve as a basis for the next chapters where active braking controllers will be designed.

Part II
Braking Control Systems Design: Basic Solutions

This part of the book deals with the main aspects of both braking control and estimation. Specifically, the basic solutions to braking control systems design are introduced based on the two different types of considered actuators, starting with braking systems with continuous dynamics, and then moving to the case of braking systems with on/off dynamics. Finally, the fundamental problem of longitudinal wheel slip estimation is studied, which is inextricably linked with active braking controller design.

Chapter 3
Braking Control Systems Design: Actuators with Continuous Dynamics

3.1 Introduction

This chapter addresses the problem of braking control design based on actuators with continuous dynamics (see Section 1.3 for their dynamic description).

Of course, the actuator performance forces the engineer to design the braking control system accordingly. Here, for the case of an actuator with continuous dynamics we show how to design a wheel slip controller that can guarantee closed-loop stability and acceptable performance in all possible working conditions by solving a regulation problem. It will be also clear that, because the braking controller is a safety-oriented aid for the driver, it must be switched on and off according to the current manoeuvre. Thus, an appropriate activation and deactivation logic must be designed to accomplish this task.

Further, we investigate the wheel slip control problem starting from a double-corner model, *i.e.*, taking into account the load transfer phenomena. The analysis highlights the effects of dynamic coupling between front and rear axles and its impact on ABS systems design. This leads to the selection of an alternative controlled variable for the braking control of the rear wheel, which arises from the idea of interlocking the rear wheels with the front wheels to achieve a more favorable dynamic behaviour while maintaining a SISO approach to wheel slip control design.

3.2 Wheel Slip Control

In braking control systems, two output variables are usually considered for regulation purposes: wheel deceleration and wheel slip. The traditional controlled variable, which is still used in some ABS systems, is the wheel deceleration. This is due to the fact that it can be easily measured with a simple

wheel encoder (see Appendix B for a discussion on this topic). However, it can be dynamically critical if the road surface changes rapidly. On the other hand, the regulation of the wheel slip is very robust from the dynamical point of view, but the slip measurement is critical, since it requires the estimation of the speed of the vehicle (see Chapter 5 for more details on this issue). Noise sensitivity of slip control hence is a critical issue, especially at low speed.

Thus, the aim of this section is to analyse the merits and drawbacks of slip and deceleration control when both are set up as regulation problems. Further, having made it clear that wheel slip control is the most suitable choice for the design of braking controllers that are robust with respect to road surface variations, the design steps for the synthesis of a linear wheel slip controller will be presented and discussed.

To do this, we will adopt a frequency-domain approach, and start by studying the control problem considering the braking dynamics described by the single-corner model.

Within this context, and based on the analysis performed in Section 2.5.1, the regulation of the wheel slip has a straightforward graphical interpretation in the (λ, η) domain, as displayed in Figure 3.1, where the equilibrium manifold $\eta(\lambda)$ given in (2.34) is depicted in four different road conditions.

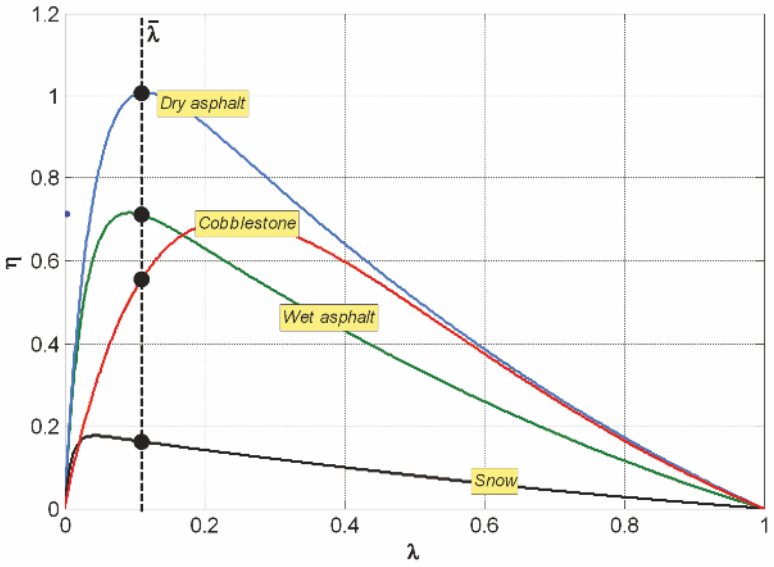

Figure 3.1 Graphical interpretation of slip control in the (λ, η) domain. The *vertical dashed line* represents the set-point $\overline{\lambda}$. The *dots* represent the equilibrium points, for different road conditions

Note that, whatever the value of $\overline{\lambda}$ ($0 \leq \overline{\lambda} \leq 1$), this regulation scheme guarantees the uniqueness of the equilibrium point.

Now, let us consider the transfer function model $G_\lambda(s)$ given in Equation 2.46, in a unitary negative feedback closed-loop with the simplest controller form, *i.e.*, a proportional controller with constant gain K. The closed-loop system is shown in Figure 3.2.

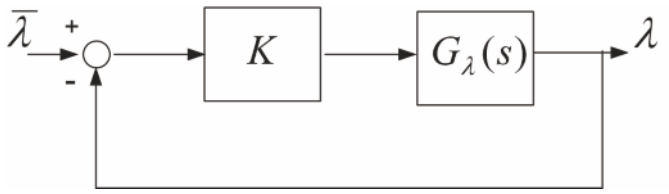

Figure 3.2 Wheel slip closed-loop system with a proportional controller

To analyse the dynamic properties of the slip control system, let us compute the characteristic polynomial $\chi_\lambda(s)$ of the closed-loop system, which, in view of the negative feedback, is given by

$$\chi_\lambda(s) = s + \frac{1}{\overline{v}} \left[\frac{\mu_1(\overline{\lambda}) F_z}{m} \left((1 - \overline{\lambda}) + \frac{mr^2}{J} \right) + K \frac{r}{J} \right].$$

Accordingly, the following stability condition can be derived (note that it does not depend on $\overline{v}$).

Stability Condition for Slip Control
The closed-loop stability condition for the slip control system shown in Figure 3.2 is given by

$$K > -\frac{\mu_1(\overline{\lambda}) F_z \, J}{m \, r} \left((1 - \overline{\lambda}) + \frac{mr^2}{J} \right). \tag{3.1}$$

This condition obviously always holds when $\mu_1(\overline{\lambda}) > 0$. However, also when $\mu_1(\overline{\lambda}) < 0$, since $|\mu_1(\overline{\lambda})|$ is bounded, it is always possible to find a value $\overline{K}$ such that for $K > \overline{K}$, the closed-loop system in Figure 3.2 is asymptotically stable in every working condition, namely for every value of $\overline{\lambda}$ and for every road condition (note from Figure 3.1 that, *e.g.*, on snow/icy roads, $\overline{\lambda} = 0.09$ corresponds to an open-loop unstable equilibrium, since $\mu_1(\overline{\lambda}) < 0$, but the closed-loop stability can be guaranteed).

Note that condition (3.1) has also an intuitive geometrical interpretation. To see this, note that the condition $K > \overline{K}$ can be graphically identified by first intersecting equilibrium manifold in the (λ, η) plane (see Figure 3.1) with the line of negative slope $\overline{K}$ cutting the λ axis in $\overline{\lambda}$. Note also that in doing so, the intersection between the equilibrium manifold in the (λ, η) plane

determines the actual equilibrium value of the wheel slip, say $\tilde{\lambda}_f$, which (as we are using a proportional controller) is in general different from the set-point value $\overline{\lambda}$. If K satisfies the bound in (3.1) for all values of $\overline{\lambda}$ and for all road conditions, then the closed-loop equilibrium is unique and it is locally asymptotically stable.

The performed analysis illustrates why slip control is an attractive approach in braking control systems:

- Given a set-point $\overline{\lambda}$, it guarantees the uniqueness of the equilibrium.
- The choice of $\overline{\lambda}$ is not critical; as a matter of fact, it is easy to find a value of $\overline{\lambda}$ (*e.g.*, $\overline{\lambda} = 0.09$, see Figure 3.1) that provides very good results (even if slightly sub-optimal) for every road condition. This feature is very appealing since it allows the use of a fixed structure controller, with no need for online identification and detection of the road conditions.
- With a fixed structure controller (*i.e.*, a fixed value of K), the asymptotic stability of the closed-loop is guaranteed for every value of $\overline{\lambda}$ and for every road condition.

The major flaw of slip control is that the measurement of the wheel slip is comparatively difficult and unreliable, especially at low speed. Hence, the sensitivity of wheel slip control to measurement errors is a key issue. Chapter 6 provides a control strategy able of alleviating the problems related to this issue.

3.3 Wheel Deceleration Control

If the controlled variable is the normalised linear wheel deceleration η, the corresponding set-point value is $\overline{\eta}$. Also this control strategy has a straightforward graphical interpretation in the (λ, η) domain, as displayed in Figure 3.3, which shows again the equilibrium manifolds $\eta(\lambda)$ in four different road conditions.

From Figure 3.3 it is immediately clear which is the first major drawback of deceleration control: the selection of the set-point $\overline{\eta}$ is very critical, and it is impossible to find a unique value of $\overline{\eta}$ that provides a good compromise in every road condition. If a large value of $\overline{\eta}$ is chosen (*e.g.*, $\overline{\eta} = 1$), deceleration control provides optimal performance on high-grip road, but on low-grip roads the wheel dynamics do not exhibit any equilibrium point. On the other hand, a low value of $\overline{\eta}$ (*e.g.*, $\overline{\eta} = 0.1$) can guarantee the existence of an equilibrium for every road condition, but it results in an over-conservative design for high-grip roads. As has already been remarked (see Section 2.5.1), note that the system always has (if any) two equilibrium points.

To analyse the dynamic properties of the deceleration control system, we consider the transfer function model $G_\eta(s)$ given in Equation 2.45 in a unitary

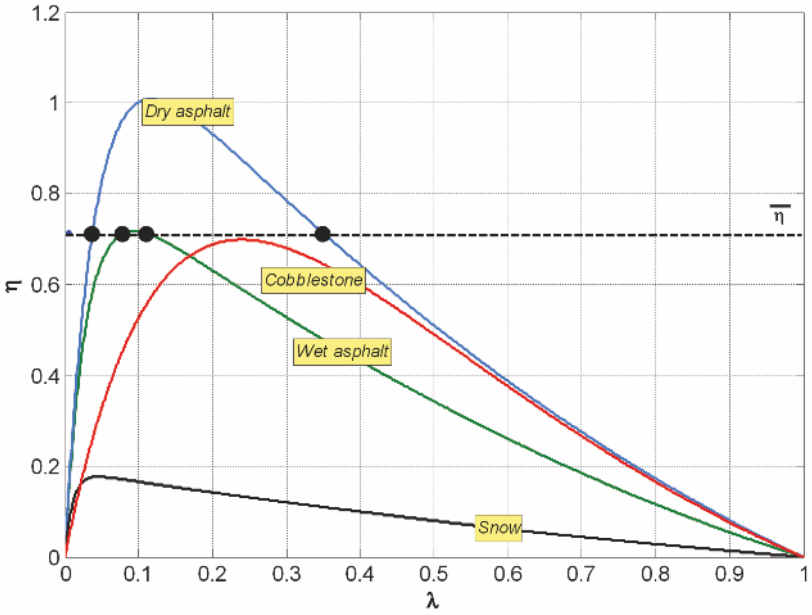

Figure 3.3 Graphical interpretation of deceleration control in the (λ, η) domain. The *horizontal dashed* line represents the set-point $\overline{\eta}$. The *dots* represent the equilibrium points, for different road conditions

negative feedback connection with a proportional controller with gain K, yielding the closed-loop system depicted in Figure 3.4.

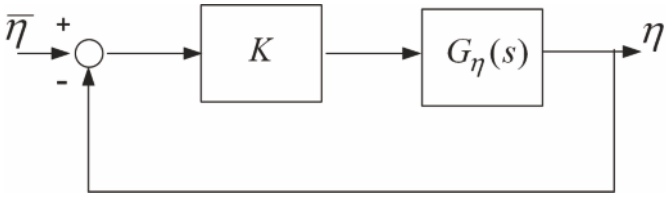

Figure 3.4 Wheel deceleration closed-loop system with a proportional controller

For this system, the characteristic polynomial $\chi_\eta(s)$ of the closed-loop system has the form

$$\chi_\eta(s) = \left(1 + K\frac{r}{Jg}\right)s + \frac{\mu_1(\overline{\lambda})F_z}{m\overline{v}}\left[(1-\overline{\lambda})\left(1 + K\frac{r}{Jg}\right) + \frac{mr^2}{J}\right].$$

Accordingly, the following stability condition can be derived (note that it does not depend on $\overline{v}$).

Stability Condition for Deceleration Control

The closed-loop stability condition for the deceleration control shown in Figure 3.4 is given by

$$\mu_1(\overline{\lambda}) \left[(1 - \overline{\lambda}) \left(1 + K \frac{r}{Jg} \right) + \frac{mr^2}{J} \right] > 0.$$

Clearly, it is not possible to find a fixed value of K that provides stability for every value of $\overline{\lambda}$ and for every road condition, since $\mu_1(\overline{\lambda})$ can be either positive or negative, depending on the value of $\overline{\lambda}$. Notice that if, *e.g.*, $K > 0$, the closed-loop system in Figure 3.2 can be made asymptotically stable for choices of $\overline{\lambda}$ before the friction curve peak, but it becomes unstable for choices of $\overline{\lambda}$ beyond the peak. Henceforth, one of the two equilibrium points is always unstable.

This analysis reveals the main limits of deceleration control:

- The choice of $\overline{\eta}$ is very critical; henceforth, it must be adapted online by means of an estimation algorithm which allows to detect the current road conditions.
- With a fixed structure controller (*i.e.*, with a fixed value of K), the asymptotic stability of the closed-loop linearised system is not guaranteed for all choices of $\overline{\lambda}$, also for a fixed road condition (this result can be extended from a simple proportional controller to every linear time-invariant controller).
- For wheel slip values beyond the peak of the friction curve the open-loop system is non-minimum phase (see Section 2.5.1 and the transfer function $G_\eta(s)$ in (2.45)) and this significantly limits the achievable closed-loop performance.

Due to these major drawbacks, deceleration control has never been implemented as a classical regulation loop for ABS in practice. Rather, complex rule-based heuristics based on a set of adjustable thresholds on η and its derivative have been used (see, *e.g.*, [88, 124]).

However, it is important to recall that deceleration-based algorithms have the appealing feature of requiring only the measurement of the wheel deceleration (no vehicle speed estimation is required). The wheel deceleration can be measured in a very reliable and straightforward manner with low cost sensors, the noise affecting the measure of η is almost stationary, and the variance of this noise can be *a priori* designed by properly choosing the precision of the wheel encoder (see also Appendix B).

Notice that deceleration control can be particularly appealing when the considered vehicle is such that its main dynamic limit during braking is not

due to the tyre–road friction but rather to the rollover condition, *e.g.*, the so-called *wheelie* phenomenon (that is the uplift of the rear wheel when braking on high-grip roads) in two-wheeled vehicles, which is mainly due to the large ratio between the height of the centre of mass and the wheelbase.

As has already been mentioned, the reader is referred to Chapter 6 for the illustration of a control strategy capable of properly *mixing* the benefits and drawbacks of slip and deceleration control and which leads to optmised performance of the resulting braking control system.

3.4 Linear Wheel Slip Controller Design

For the design of a linear wheel slip controller, we work on the transfer function model $G_\lambda(s)$, which is repeated here to ease readability

$$G_\lambda(s) = \frac{r}{J\overline{v}} \frac{1}{s + \frac{\mu_1(\bar{\lambda})F_z}{m\overline{v}} \left((1-\bar{\lambda}) + \frac{mr^2}{J}\right)}. \tag{3.2}$$

Further, as we are interested in the synthesis of a single controller capable of providing both closed-loop stability and acceptable performance in all working conditions, first of all we need to define the linearisation conditions based on which we can evaluate $G_\lambda(s)$ to serve as a basis for controller synthesis.

To do this, recall that the pole of the system can be written as

$$s_p = -\mu_1(\bar{\lambda}) \frac{Ng}{\overline{v}} \left((1-\bar{\lambda}) + \frac{mr^2}{J}\right), \tag{3.3}$$

thereby showing that the pole location depends on the vehicle speed v, on the vertical load distribution N, see also Equation 2.53, and on the road conditions.

Thus, to account for the load variations at the front and rear wheels (the former becomes more loaded during braking due to load transfer while the opposite is true for the latter) it is wise to tune the controllers for the front axle in a different way with respect to those that regulate the rear wheels.

Further, one needs to linearise the model around an open-loop unstable equilibrium point, so as to work on the *worst* case with respect to the road friction conditions. Thus, to investigate which is the most appropriate operating point in which to evaluate $G_\lambda(s)$, Figure 3.5 shows a plot of the system pole angular frequency as a function of λ for $N = 1.5$ (*i.e.*, in a setting compatible with the front wheel load) normalised with respect to the vehicle speed to capture the effects of load transfer and friction conditions only. To improve readability, and coherently with the aim of defining a worst-case setting, Figure 3.5 shows the pole angular frequency only for the open-loop

unstable equilibrium points (in the case where the real pole is negative, its angular frequency has been clipped to zero).

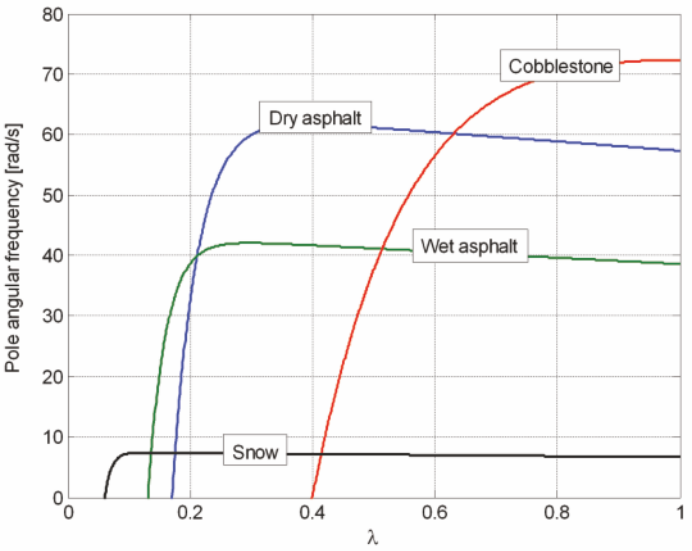

Figure 3.5 Angular frequency of the open-loop pole (3.3) normalised with respect to $\overline{v}$ for $N = 1.5$

By inspecting Figure 3.5 the following operating point for linearisation is considered. For the front wheel the worst-case situation considered for linearisation happens on dry asphalt, where the large value of N (see also Figure 2.11), causes the pole to move toward higher frequencies. Thus, on dry asphalt, for $\lambda = 0.62$ we obtain a pole $s_p = 60/\overline{v}$. Note that this is not the worst-case condition in general; by inspecting Figure 3.5 one may see that the pole location which is at the largest distance from the imaginary axis is found for $\lambda = 0.85$ on cobblestone. However, this situation, that is a very large value of the wheel slip on cobblestone, is much less likely to occur in practice. As such, choosing such a condition as a basis for controller design would be overly conservative. Of course, this choice is problem-dependent, and must be carefully evaluated according to the specific situation. On the other hand, whichever condition is chosen, the control designer will have to always check that basic closed-loop properties, such as asymptotic stability of the closed-loop system, are guaranteed in all admissible working conditions, possibly with a loss of dynamic performance with respect to the nominal case chosen for control design. A similar rationale may be applied to fix the linearisation point for the rear wheel if needed.

Based on these considerations, for controller design we will work with the transfer function $G_\lambda(s)$ given by

$$G_\lambda(s) = \frac{0.3/\overline{v}}{s - 60/\overline{v}} = \frac{\rho}{s + \gamma}, \tag{3.4}$$

with $\rho > 0$ and $\overline{v} > 0$.

Before moving to the design of a dynamic controller, let us recall that we have shown that with an appropriate choice of the controller gain value, a proportional controller which guarantees closed-loop stability for all working conditions can be found.

However, besides guaranteeing closed-loop stability, one usually needs to satisfy also performance specifications, which call for the design of a dynamic controller. The equilibria of the system to be controlled being open-loop unstable in some operating conditions of interest, there are two main approaches to the design of a performance-oriented controller. One choice may be that of designing first an internal feedback loop with the only aim of stabilising the closed-loop system in all operating conditions (note that this can be done, for example, with the simple proportional controller discussed previously) and then design an external control loop whose aim is to ensure the satisfaction of performance requirements and disturbance rejection properties. This approach allows one to work on a pre-stabilised system dynamics, which indeed poses less limitations on the achievable performance levels (for a detailed and advanced discussion on the limitations on closed-loop performance posed by right half plane poles and/or zeros the reader may refer to, *e.g.*, [98]).

The other option is that of designing a single controller which deals with both stabilisation and performance specifications. As in the considered application this second approach allows us to highlight some interesting tuning rules, in the following the design will be approached accordingly.

Thus, the first attempt to ensure, say, asymptotic tracking of a constant set-point (which is usually the first performance specification that one needs to fulfil) would lead to consider an integral controller, *i.e.*,

$$R_I(s) = \frac{K}{s}. \tag{3.5}$$

Consider, as an example, working on the transfer function model $G_\lambda(s)$ in (3.4) and employing the integral controller (3.5).

Assuming again unitary negative feedback, it is easy to see that the characteristic polynomial is given by

$$\chi_{\lambda(s),I} = s^2 + \gamma\, s + K\rho. \tag{3.6}$$

Thus, it is apparent that, in the case $\gamma < 0$, *i.e.*, if $G_\lambda(s)$ is open-loop unstable, no matter which value of K is chosen, the closed-loop system will never be asymptotically stable (recall that, the characteristic polynomial being a

second-order one, the necessary and sufficient condition for its roots to have negative real part is that all its coefficients are non-zero and have the same sign).

Bearing this in mind, let us move to consider a PI controller structure, *i.e.*,

$$R_{PI}(s) = K\frac{(\tau\, s + 1)}{s}, \tag{3.7}$$

with $\tau > 0$. With this controller, the characteristic polynomial (assuming again unitary negative feedback) is given by

$$\chi_{\lambda(s),PI} = s^2 + (K\rho\tau + \gamma)s + K\rho. \tag{3.8}$$

In this case, because $\rho > 0$ and $\tau > 0$, if K is chosen such that

$$K > -\frac{\gamma}{\rho\tau}, \tag{3.9}$$

then the closed-loop system will be asymptotically stable. Note that with a PI controller structure we obtained a closed-loop stability condition that is fully analogous to the one obtained for the proportional controller (see inequality (3.1)), with the additional degree of freedom offered by the time constant τ of the controller zero, which can be used, together with the controller gain K to guarantee that, besides closed-loop stability, other performance specifications are met. Substituting the full expressions for γ and ρ, see Equation 3.2, in (3.9), one obtains

$$K > -\mu_1(\bar{\lambda})\frac{NJg}{\tau r}\left((1-\bar{\lambda}) + \frac{mr^2}{J}\right), \tag{3.10}$$

which notably does not depend on the considered speed value $\overline{v}$ (recall that the same was true for condition (3.1) obtained based on the proportional controller). However, in practice a PI controller might not be enough to ensure that all desired performance specifications are met. Thus, as final analysis step, we consider a PID controller architecture complemented with a first-order filter to achieve a causal approximation of the ideal derivative term, *i.e.*,

$$R_{PID}(s) = K\frac{(\tau_1\, s + 1)(\tau_2\, s + 1)}{s(Ts + 1)}, \tag{3.11}$$

with $\tau_1 > 0$, $\tau_2 > 0$ and $T > 0$. This controller, with unitary negative feedback, yields the characteristic polynomial

$$\chi_{\lambda(s),PID} = T\, s^3 + (K\rho\tau_1\tau_2 + T\gamma + 1)s^2 + [\gamma + K\rho(\tau_1 + \tau_2)]s + K\rho. \tag{3.12}$$

Recalling that γ is the angular frequency of the system pole and letting $\gamma := 1/T_p$, if the real pole of the controller is chosen to be sufficiently fast, *i.e.*, if $T << |T_p|$, one has that $T\gamma \approx 0$. Let us consider this simplification, which

constitutes a tuning rule on its own, and recall that a necessary condition for the closed-loop stability of the considered third-order system is given by the coefficients of the characteristic polynomial (3.12) being all non-zero and with the same sign.

Based on these considerations, one obtains that the controller parameters must satisfy the following inequality:

$$K > -\frac{\gamma}{\rho(\tau_1+\tau_2)} = -\mu_1(\bar{\lambda})\frac{NJg}{r(\tau_1+\tau_2)}\left((1-\bar{\lambda})+\frac{mr^2}{J}\right). \tag{3.13}$$

Again, we have found a speed-independent stability condition, which can be satisfied acting on the larger number of controller parameters offered by the PID architecture.

Further, resorting to Routh's stability criterion (see, *e.g.*, [5]), one can investigate the additional conditions on the controller parameters that must be satisfied to fulfil the necessary and sufficient condition for closed-loop stability. Specifically, by constructing the Routh's table and recalling the assumption that $T\gamma \approx 0$, one finds that the only non-trivial additional condition on the controller parameters has the form

$$K > \frac{T-(\tau_1+\tau_2)}{\rho(\tau_1+\tau_2)\tau_1\tau_2}. \tag{3.14}$$

3.5 Effects of Actuator Dynamics

To move toward a more realistic situation consider, as an example, the transfer function model $G_\lambda(s)$ in (3.4) with, *e.g.*, $\overline{v} = 10$ m/s, and a proportional controller with gain $K = 1000$. It is easy to see that such a controller ensures closed-loop stability. However, $G_\lambda(s)$ is not a complete representation of the dynamics to be controlled. As a matter of fact, one has to consider the actuator dynamics. In this case, we assume that we are dealing with the EMB actuator servo-controlled dynamics $G_{\text{caliper}}(s)$ given in (1.4), which is a first-order linear time-invariant system with a pole at $\omega_{\text{act}} = 70$ rad/s and a pure delay $\tau = 10$ ms.

Bearing this in mind, the overall system dynamics to be controlled are given by

$$D(s) = G_{\text{caliper}}(s)G_\lambda(s). \tag{3.15}$$

It is now interesting to investigate how the proportional controller with gain $K = 1000$ that we assumed to have designed considering only the transfer function model $G_\lambda(s)$ in (3.4) with $\overline{v} = 10$ m/s behaves if we consider the full dynamics (3.15). It is clear that the choice of a proportional controller is a simplistic one, but the considerations remain unaltered for more complex

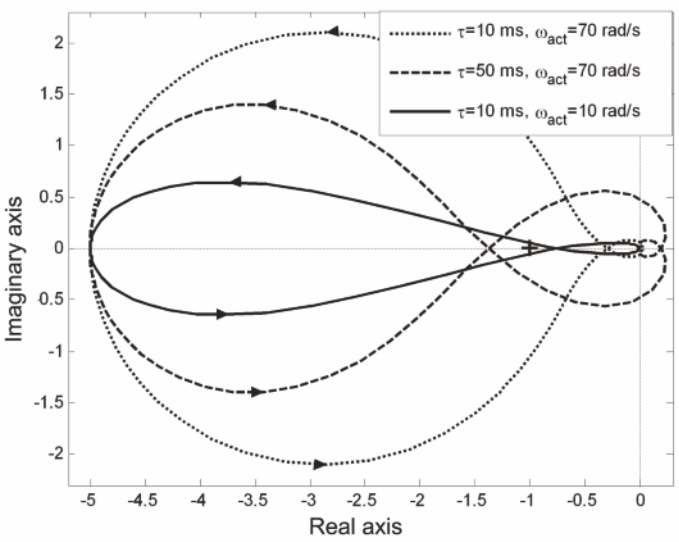

Figure 3.6 Nyquist diagram of the loop transfer function $L_\lambda(s)$ for $\tau = 10$ m/s and $\omega_{\rm act} = 70$ rad/s (*dotted line*), $\tau = 50$ m/s and $\omega_{\rm act} = 70$ rad/s (*dashed line*) and $\tau = 10$ m/s and $\omega_{\rm act} = 10$ rad/s (*solid line*)

controller structures. Such a simple choice is thus motivated by its ease of tractability.

For a pictorial representation of the considered situation, the reader is referred to Figure 3.6, which shows the Nyquist diagram of the loop transfer function

$$L_\lambda(s) = K\, D(s), \tag{3.16}$$

where $D(s)$ is as in (3.15) (and $K = 1000$), for different combinations of the actuator bandwidth and of the transmission delay.

Namely, the following situations are considered:

- the nominal case, *i.e.*, $\tau = 10$ ms and $\omega_{act} = 70$ rad/s (dotted line in Figure 3.6);
- a situation with a much larger transmission delay, *i.e.*, $\tau = 50$ ms and $\omega_{act} = 70$ rad/s (dashed line in Figure 3.6); and
- a situation with a much narrower actuator bandwidth, *i.e.*, $\tau = 10$ ms and $\omega_{act} = 10$ rad/s (solid line in Figure 3.6).

By inspecting Figure 3.6 it is clear that even though the controller gain chosen for the open-loop system $G_\lambda(s)$ still ensures stability for the nominal case of $\tau = 10$ ms and $\omega_{act} = 70$ rad/s, the same does not hold for the cases of a larger delay and of a narrower actuator bandwidth. Specifically, to cope with such modified situations one would in principle have to decrease the controller gain in order to ensure closed-loop stability, up to the point where

it would be impossible to fulfill condition (3.1) which ensures closed-loop stability for $G_\lambda(s)$ in all possible working conditions.

The message here is that one must always carefully evaluate all the system characteristics before moving to the controller design and investigate how and if they pose substantial limitations to the achievable closed-loop performance. If this is the case, then one may want to reconsider the vehicle layout or, if this is not possible, to revise the specifications and requirements for the closed-loop system.

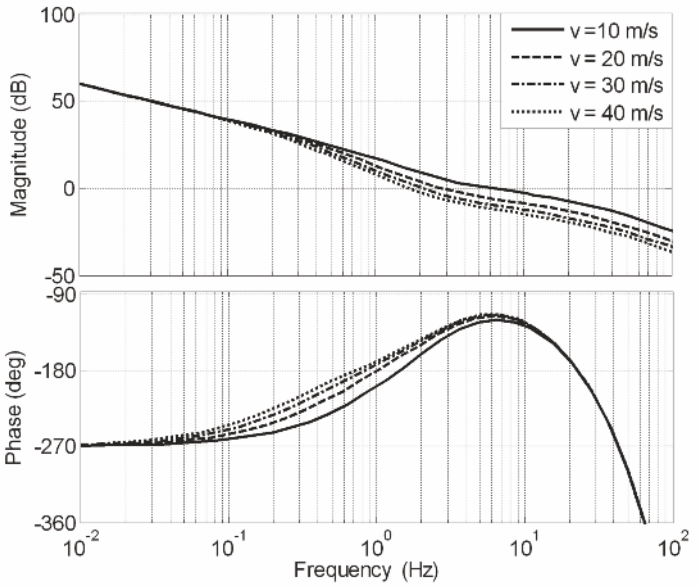

Figure 3.7 Magnitude and phase Bode diagrams of the frequency response associated with the loop transfer function $L_{1\lambda}(s)$ for $\overline{v} = 10$ m/s (*solid line*), $\overline{v} = 20$ m/s (*dashed line*), $\overline{v} = 30$ m/s (*dash-dotted line*) and $\overline{v} = 40$ m/s (*dotted line*)

3.6 Performance Analysis: a Numerical Example

We now design a slip controller that can achieve good dynamic performance, which, given the considered nominal actuator dynamics and transmission delay (*i.e.*, $\omega_{act} = 70$ rad/s and $\tau = 10$ ms), can be defined as: ensure asymptotic tracking of a constant wheel slip set-point and achieve a closed-loop bandwidth between approximately 1 and 10 Hz for all admissible speed values.

Based on the previous analysis, a PID controller architecture that satisfies the desired requirements can be devised. Note that besides fulfilling the stability conditions discussed in the previous section one has to consider the phase loss due to the delay and to the actuator dynamics.

In particular, the following PID controller can be employed:

$$R_\lambda(s) = 12000 \frac{(1 + \frac{1}{20}s)^2}{s(1 + \frac{1}{500}s)}. \tag{3.17}$$

Note that the controller (3.17) is not intended as the best possible tuning for the considered situation, but is given as an example of a simple controller architecture that achieves the desired performance levels. Each specific practical situation will lead to a more detailed list of requirements, which in turn will require a different tuning of the controller parameters.

To visually inspect the loop transfer function obtained with the controller (3.17), *i.e.*,

$$L_{1\lambda}(s) = R_\lambda(s)\, D(s), \tag{3.18}$$

the reader is referred to Figure 3.7, which shows the magnitude and phase Bode diagrams of the frequency response associated with $L_{1\lambda}(s)$ for different values of the vehicle speed. As can be seen the closed-loop bandwidth does indeed vary according to the vehicle speed value $\overline{v}$ used to evaluate the system dynamics $G_\lambda(s)$ in (3.4); specifically, the closed-loop dynamics are faster as speed decreases. Of course, no stability property of the closed-loop linearised system can be inferred from the Bode diagrams, as the loop transfer function has a positive pole.

The fact that the system dynamics become faster as speed decreases, coupled with the presence of a pure delay, makes it impossible to ensure closed-loop stability for very low values of $\overline{v}$.

To visually inspect this issue consider Figure 3.8, which shows the magnitude and phase Bode diagrams of the frequency response associated with the loop transfer function

$$L_{2\lambda}(s) = R_\lambda(s) D^{\mathrm{st}}(s),$$

where

$$D^{st}(s) = G_{\mathrm{caliper}}(s) G^{\mathrm{st}}_\lambda(s)$$

is the system dynamics obtained considering an open-loop stable equilibrium, that is

$$G^{\mathrm{st}}_\lambda(s) = \frac{0.3/\overline{v}}{s + 60/\overline{v}},$$

for $\overline{v} = 40$ m/s and $\overline{v} = 2$ m/s. As the loop transfer function has no poles with positive real part and the cut-off frequency is well-defined, the closed-loop stability can now be inferred *via* the Bode criterion. By inspecting Figure 3.8 one notes that for $\overline{v} = 2$ m/s the closed-loop system is unstable. Note that this is not due to the particular controller tuning; any controller tuning will

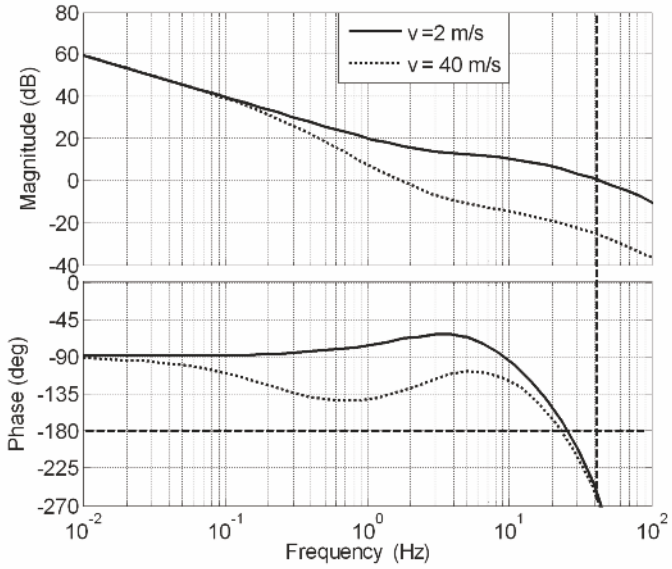

Figure 3.8 Magnitude and phase Bode diagrams of the frequency response associated with the loop transfer function $L_{2\lambda}(s)$ for $\overline{v} = 40$ m/s (*dotted line*) and $\overline{v} = 2$ m/s (*solid line*)

lead to a different minimum value of the speed which compromises closed-loop stability, but such a value will always exist.

Moreover, from a practical viewpoint one must also consider that at very low speed the wheel encoders used to measure the wheel speed become less reliable, so that the available wheel speed measurement cannot be safely employed to estimate the vehicle speed needed to compute the wheel slip. For a better analysis of these issues the reader is referred to Appendix B and to Chapter 5, which discuss the processing issues of the wheel encoders signal and the speed estimation problem, respectively.

In view of these problems, in practical applications the braking control system needs to be complemented with a deactivation logic that switches to an open-loop control strategy to manage the last part of the braking phase associated with very low values of the vehicle speed. The design of such a logic is addressed in the next section.

3.7 Activation and Deactivation Logic

The last design step, crucial for moving toward a real vehicle implementation, is to devise a safe and reliable activation and deactivation logic. As a matter

of fact, an active braking controller is a safety system, hence it is not active during normal vehicle operations but it has to be turned on when a panic stop occurs.

The first step is then to single out which signals better describe the current safety level on board as far as braking is concerned. Further, we need to devise an activation and deactivation logic based on these signals and take care that a bumpless transfer is guaranteed between manual and automatic operational modes.

To this end, the first step is to implement the wheel slip controllers with anti-windup architecture and with the structure shown in Figure 3.9, which ensures that a reliable controller output is available also when in manual mode, and that a bumpless transfer from manual to automatic mode is ensured upon the controller activation. The anti-windup implementation of the integral controller action is also necessary to cope with actuator constraints, which are of course to be taken into account in the considered application (see also Section 1.3).

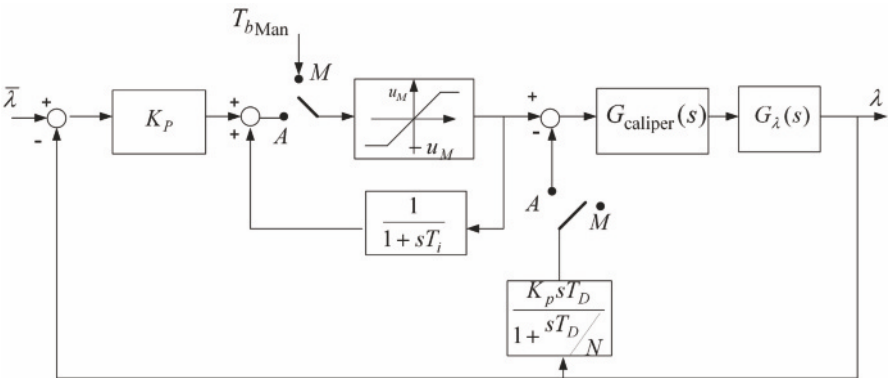

Figure 3.9 Schematic view of the implementation of a wheel slip PID controller which ensures a bumpless transfer from manual to automatic mode

Moreover, in the considered system, besides switching from manual to automatic mode, one has to monitor the value of the vehicle speed. In fact, in view of the analysis performed, when the value of the vehicle speed goes below a certain threshold, specific braking strategies must be devised in order to take the vehicle to a complete stop. Based on these considerations, the activation and deactivation logic is governed by the finite state machine (FSM) shown in Figure 3.10. We now analyse the conditions based on which the transitions between the states are activated.

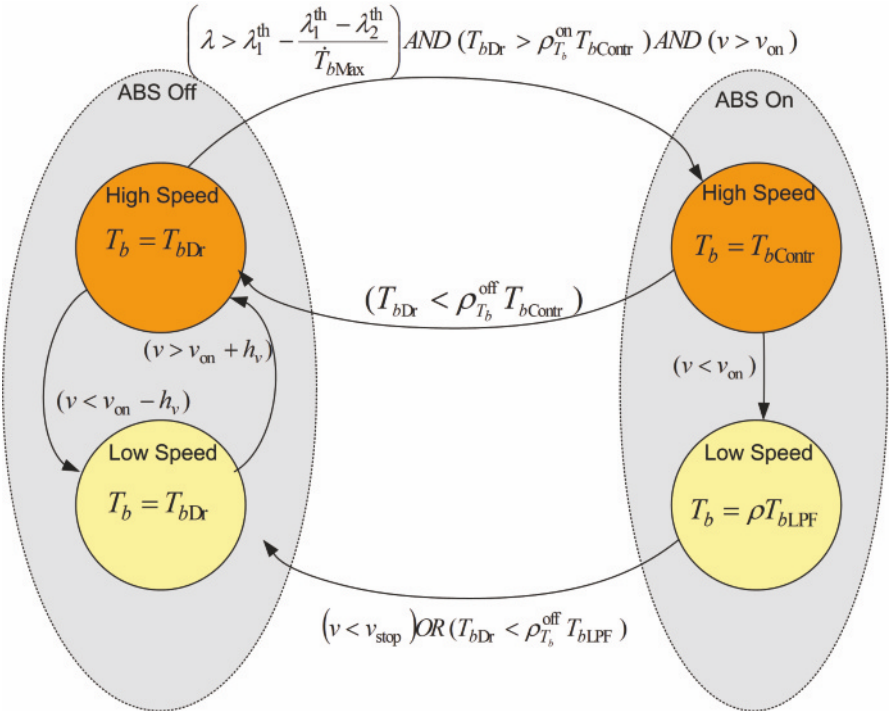

Figure 3.10 FSM representation of the activation and deactivation logic

3.7.1 Activation Conditions

When a braking manoeuvre takes place, the ABS is activated if the following condition holds (see also Figure 3.10 and Table 3.1):

$$\left(\lambda > \lambda_1^{\text{th}} - \frac{\lambda_1^{\text{th}} - \lambda_2^{\text{th}}}{\dot{T}_{b\text{Max}}} \dot{T}_b\right) \text{ AND } \left(T_{b\text{Dr}} > \rho_{T_b}^{\text{on}} T_{b\text{Contr}}\right) \text{ AND } (v > v_{\text{on}}) . \tag{3.19}$$

Thus, the activation is based on the wheel slip λ, the braking torque T_b and the vehicle speed v.

Specifically, the threshold on λ is modulated according to the braking intensity, described *via* the braking torque derivative $\dot{T}_b$. The threshold λ_1^{th} is employed in the case $\dot{T}_b = 0$, while a lower threshold value λ_2^{th} is used in the case when a hard braking manoeuvre occurs, *i.e.,* $\dot{T}_b = \dot{T}_{\text{bMax}}$. The first condition of (3.19) is simply a linear interpolation of these extreme conditions, which allows us to handle all the intermediate braking intensities.

However, note that an activation based only on this condition is not completely safe. In fact, the wheel slip λ is a noisy signal, and one needs to avoid that the controller is switched on due to possibly large measurement errors.

This is achieved by considering also the value of the braking torque, as shown by the second condition of (3.19), where $T_{b\mathrm{Dr}}$ is the braking torque requested by the driver, $T_{b\mathrm{Contr}}$ is the braking torque that the controller would apply if active (recall the the chosen controller architecture makes the control output available also in manual mode) and the parameter $\rho_{T_b}^{\mathrm{on}} > 1$.

Finally, as the controller is not guaranteed to ensure closed-loop stability at very low speed values, the automatic mode has to be switched on only if the speed value is sufficiently large, *i.e.*, if $v > v_{\mathrm{on}}$, where v_{on} is a properly defined threshold.

3.7.2 De-activation Conditions

When the braking manoeuvre is completed, the controller must be switched off so that the full control of the vehicle returns to the driver. Hence, an automatic to manual switch must occur when the driver releases the brake pedal. Thus, if the de-activation occurs at $v > v_{\mathrm{on}}$, it is allowed when the following condition holds (see again Figure 3.10):

$$T_{b\mathrm{Dr}} < \rho_{T_b}^{\mathrm{off}} T_{b\mathrm{Contr}}, \qquad \rho_{T_b}^{\mathrm{off}} < 1.$$

To switch off the controller at low speed, note that if the condition $v \leq v_{\mathrm{on}}$ occurs when a panic stop is still going on, then it is not safe to give back the control to the driver immediately. Hence, an additional braking logic has to be devised in order to take the vehicle to a complete stop automatically.

One solution is to complete the braking manoeuvre commanding the actuator to apply a constant braking torque, such that

$$T_b = \rho\, T_{b\mathrm{LPF}}, \qquad \rho < 1,$$

where $T_{b\mathrm{LPF}}$ is a low pass filtered version of the last value of the braking torque requested by the controller.

Then, once the vehicle has stopped or if the driver has released the brake pedal, *i.e.*, if

$$(v < v_{\mathrm{stop}})\,\mathrm{OR}\,(T_{b\mathrm{Dr}} < \rho_{T_b}^{\mathrm{off}}\, T_{b\mathrm{LPF}}),$$

then the ABS can be switched off (see the transition between the ABS on and off states associated with the low speed condition in Figure 3.10).

Figures 3.11(a) and 3.11(b) and Figures 3.12(a) and 3.12(b) show the closed-loop behaviour of the wheel slip and braking torque when the controller endowed with the activation logic is employed.

Specifically, Figures 3.11(a) and 3.11(b) show the results on dry asphalt, whereas Figures 3.12(a) and 3.12(b) those on snow. These figures show that the controller allows one to perform a safe braking manoeuvre and that the activation and deactivation logic guarantees a bumpless transfer between

Table 3.1 Description of the parameters employed in the activation and deactivation logic

Parameter	Value	Constraints	Meaning
$\rho_{T_b}^{\text{off}}$	0.9	< 1	Safety scaling between $T_{b\text{Dr}}$ and $T_{b\text{Contr}}$ to determine if the controller can be switched off at low speed
$\rho_{T_b}^{\text{on}}$	1.02	> 1	Scaling between $T_{b\text{Dr}}$ and $T_{b\text{Contr}}$ to activate the controller
ρ	0.97	< 1	Controller torque scaling factor for $v < v_{\text{on}}$
λ_1^{th}	0.2	$> \lambda_2^{\text{th}}$	Activation threshold for constant T_b
λ_2^{th}	0.1	> 0	Activation threshold for $\dot{T}_b = \dot{T}_{b\text{Max}}$
$\dot{T}_{b\text{Max}}$	5 kNm/s	> 0	Actuator rate limit
v_{on}	2.5 m/s	> 0	Speed threshold above which $T_{b\text{Contr}}$ is reliable
v_{stop}	0.05 m/s	$0 < v_{\text{stop}} \leq v_{\text{on}}$	Speed threshold below which the vehicle is considered still
h_v	0.5 m/s	> 0	Hysteresis on v_{on} to avoid chattering between the two manual ABS-OFF states

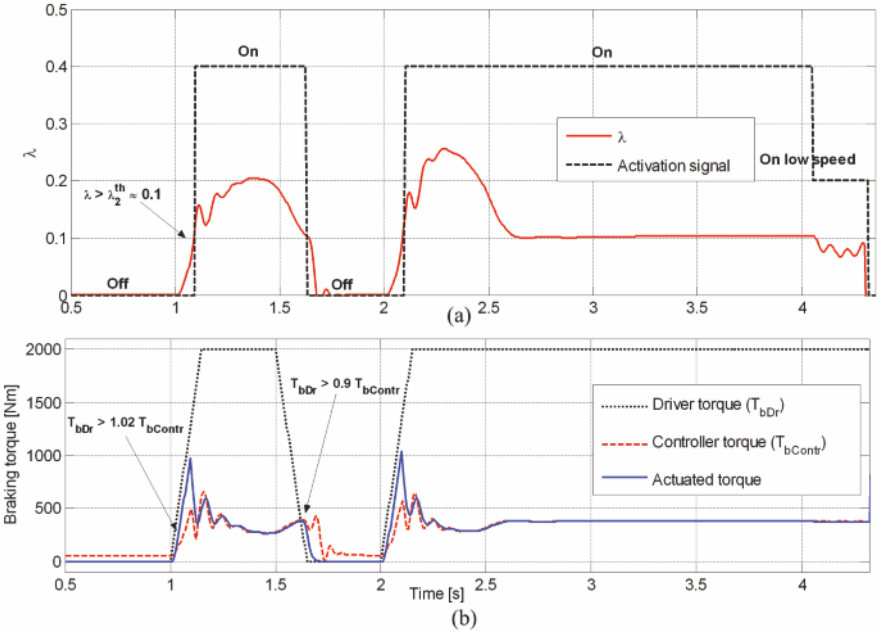

Figure 3.11 Activation logic behaviour for repeated braking manoeuvres on dry asphalt road with initial speed $v_0 = 100$ km/h; (a): plot of the longitudinal wheel slip (*solid line*) and activation signal (*dashed line*); (b): braking torque

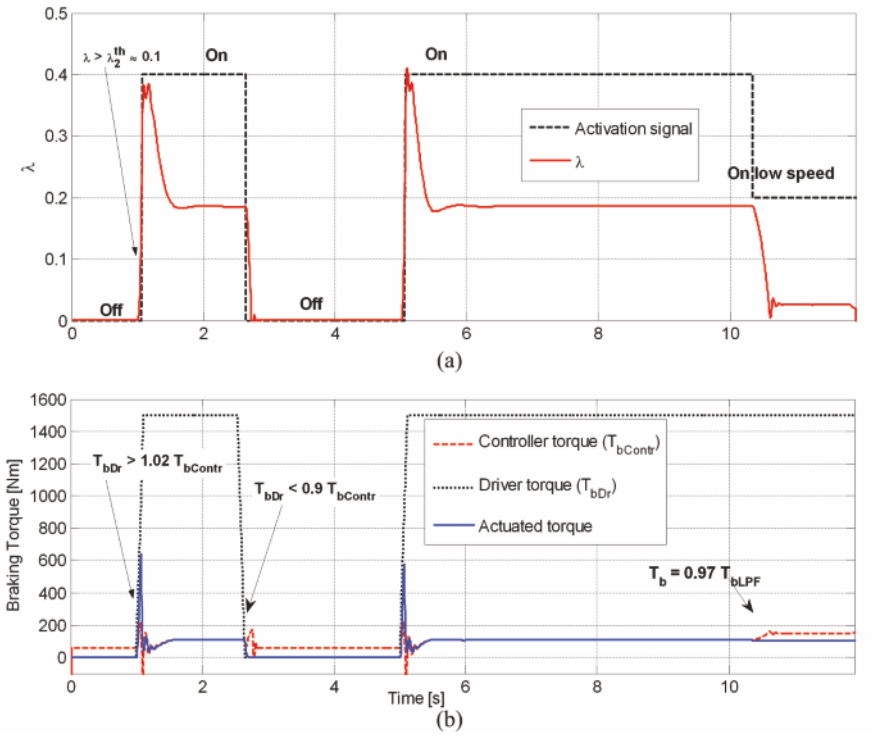

Figure 3.12 Activation logic behaviour for repeated braking manoeuvres on snowy road with initial speed $v_0 = 100$ km/h; (a): plot of the longitudinal wheel slip (*solid line*) and activation signal (*dashed line*); (b): braking torque

manual and automatic mode, and the controller state is correctly reset on deactivation, so that the subsequent braking manoeuvre can be safely handled. Finally, good performance and safety are ensured independently of the road condition.

In the simulations considered, the activation logic was implemented with the numerical values given in Table 3.1.

3.8 Slip Controller Analysis Based on the Double-corner Model

This section is devoted to investigating the wheel slip control problem starting from a double-corner model. Specifically, we first analyse the closed-loop stability properties obtained with a slip controller acting on both the front and the rear wheels. Further, we discuss an alternative control strategy that interlocks the rear wheels with the front ones, and allows one on the one

hand to achieve coupling minimisation while maintaining a SISO approach to wheel slip control and on the other hand to employ a control strategy that does not need the rear wheel slip measurement.

Finally, we briefly discuss the problem of adapting a wheel slip control system to the case of braking on curves, showing that the approaches discussed in this book still apply if the current manoeuvre does not compromise the vehicle stability, provided that a set-point adaptation strategy is available.

3.8.1 Closed-loop Stability Analysis

Similarly to what was done at the beginning of this chapter on the single-corner model, we now analyse the closed-loop stability of the wheel slip control applied to the double-corner model given in system (2.25).

Specifically, to perform the analysis it is assumed that the longitudinal dynamics of the vehicle (expressed by the state variable v) are significantly slower than the rotational dynamics of the wheels (expressed by the state variables λ_i or ω_i, $i = \{f, r\}$) due to the differences in inertia. Under this assumption, the third equation (centre of mass dynamics) in (2.25) is neglected, and the model reduces to a second-order model of the wheels dynamics only where v is treated as a varying parameter.

Further, as it was done for the single-corner model, we concentrate for simplicity on a proportional controller. This choice allows us to draw general conclusions, which hold also with a more complex linear time-invariant controller.

Finally, based on the analysis carried out in Chapter 2 (see also Figures 2.12(a) and 2.12(b)), which revealed that the front wheel behaviour is substantially independent from that of the rear wheel, while the latter is strongly coupled to the front one, in the following we disregard the dependence of $\Psi_f(\lambda_f, \lambda_r)$, see Equation 2.26, on λ_r and adopt the notation $\Psi_f(\lambda_f)$.

Accordingly, the control laws obtained with a proportional controller applied to each wheel have the form

$$\begin{aligned} T_{b_f} &= k_f(\overline{\lambda}_f - \lambda_f), \\ T_{b_r} &= k_r(\overline{\lambda}_r - \lambda_r), \end{aligned} \tag{3.20}$$

where $\overline{\lambda}_f$ and $\overline{\lambda}_r$ are the set-point values for the front and rear wheel slip, respectively, and k_f, k_r are positive constants. Hence, the closed-loop dynamics become

$$\begin{aligned} \dot{\lambda_f} &= -\frac{r}{Jv}\left[\Psi_f(\lambda_f) - k_f(\overline{\lambda}_f - \lambda_f)\right], \\ \dot{\lambda_r} &= -\frac{r}{Jv}\left[\Psi_r(\lambda_f, \lambda_r) - k_r(\overline{\lambda}_r - \lambda_r)\right]. \end{aligned} \tag{3.21}$$

For the closed-loop system (3.21), we can state the following:

Proposition 3.1. *Consider the closed-loop system described by* (3.21) *with* $v > 0$ *and let the wheel slip set-point values be* $\overline{\lambda}_i \in (0,1)$, $i = \{r, f\}$. *Then, there exist positive gain values* $\overline{k}_f$ *and* $\overline{k}_r$ *such that, for any* $k_f > \overline{k}_f$ *and* $k_r > \overline{k}_r$, *the closed-loop system admits a unique locally asymptotically stable equilibrium for all initial conditions* $\lambda_f(0), \lambda_r(0) \in (0,1)$, *for all choices of* $\overline{\lambda}_f$ *and* $\overline{\lambda}_r$ *and for all road conditions.*

Proof. Fix the set-point values $\overline{\lambda}_f, \overline{\lambda}_r \in (0,1)$. As a proportional controller does not guarantee that the wheel slip of the closed-loop system will converge to $\overline{\lambda}_f, \overline{\lambda}_r$, let $(\tilde{\lambda}_f, \tilde{\lambda}_r)$ be an equilibrium of system (3.21) associated with $\overline{\lambda}_f, \overline{\lambda}_r$, *i.e.*,

$$\begin{cases} \Psi_f(\tilde{\lambda}_f) = k_f(\overline{\lambda}_f - \tilde{\lambda}_f), \\ \Psi_r(\tilde{\lambda}_f, \tilde{\lambda}_r) = k_r(\overline{\lambda}_r - \tilde{\lambda}_r). \end{cases} \tag{3.22}$$

As a preliminary step, we re-write system (3.21) in a form that is more useful for analysing the stability properties of $(\tilde{\lambda}_f, \tilde{\lambda}_r)$.

We start from the equation governing λ_r, which can be expressed in the form

$$\begin{aligned} \dot{\lambda_r} &= -\frac{r}{Jv}\Big\{k_r(\lambda_r - \tilde{\lambda}_r) + \Psi_r(\tilde{\lambda}_f, \lambda_r) - k_r(\overline{\lambda}_r - \tilde{\lambda}_r) \\ &\quad + \Psi_r(\lambda_f, \lambda_r) - \Psi_r(\tilde{\lambda}_f, \lambda_r)\Big\} \\ &= -\frac{r}{Jv}\Big\{(\lambda_r - \tilde{\lambda}_r)\Big[k_r + \frac{\Psi_r(\tilde{\lambda}_f, \lambda_r) - \Psi_r(\tilde{\lambda}_f, \tilde{\lambda}_r)}{\lambda_r - \tilde{\lambda}_r}\Big] \\ &\quad + \Psi_r(\lambda_f, \lambda_r) - \Psi_r(\tilde{\lambda}_f, \lambda_r)\Big\}, \end{aligned}$$

where the first equality is obtained by adding and subtracting $k_r\tilde{\lambda}_r$ and $\Psi_r(\tilde{\lambda}_f, \lambda_r)$ to the expression within the brackets in (3.21), whereas the second equality is obtained using the equilibrium condition (3.22).

A similar procedure applied to the equation governing λ_f in (3.21) leads to the following equivalent form for the closed-loop system equations:

$$\begin{aligned} \dot{\lambda_f} &= -\frac{r}{Jv}\Big[k_f + \alpha_f(\lambda_f)\Big](\lambda_f - \tilde{\lambda}_f), \\ \dot{\lambda_r} &= -\frac{r}{Jv}\Big[k_r + \alpha_r(\lambda_r)\Big](\lambda_r - \tilde{\lambda}_r) + \gamma(\lambda_f, \lambda_r), \end{aligned} \tag{3.23}$$

where

$$\alpha_f(\lambda_f) = \frac{\Psi_f(\lambda_f) - \Psi_f(\tilde{\lambda}_f)}{\lambda_f - \tilde{\lambda}_f},$$

$$\alpha_r(\lambda_r) = \frac{\Psi_r(\tilde{\lambda}_f, \lambda_r) - \Psi_r(\tilde{\lambda}_f, \tilde{\lambda}_r)}{\lambda_r - \tilde{\lambda}_r},$$

and

$$\gamma(\lambda_f, \lambda_r) = -\frac{r}{Jv}[\Psi_r(\lambda_f, \lambda_r) - \Psi_r(\tilde{\lambda}_f, \lambda_r)].$$

Note that the system under study is made of a cascade connection of two subsystems where λ_f evolves independently of λ_r and this affects the dynamics of λ_r through the additive term $\gamma(\lambda_f, \lambda_r)$, which vanishes when λ_f is at the equilibrium, *i.e.*, $\gamma(\tilde{\lambda}_f, \lambda_r) = 0$, $\forall \lambda_r$. Also, $\alpha_f(\lambda_f)$ represents the slope of the straight line intersecting the curve $\Psi_f(\cdot)$ in the two points of coordinates λ_f and $\tilde{\lambda}_f$. Thus, $\alpha_f(\lambda_f)$ is lower bounded by the negative steepest slope of the curve $\Psi_f(\cdot)$ obtained for different road conditions. A similar geometric interpretation holds for $\alpha_r(\lambda_r)$.

It is next shown that, for $i \in \{f, r\}$, if k_i is large enough, then the equilibrium $\tilde{\lambda}_i$ of the subsystem

$$\dot{\lambda_i} = -\frac{r}{Jv}\Big[k_i + \alpha_i(\lambda_i)\Big](\lambda_i - \tilde{\lambda}_i) \tag{3.24}$$

is globally exponentially stable (GES) and, hence, also globally asymptotically stable (GAS). Note that subsystem (3.24) with $i = r$ is obtained from the cascade system (3.23) by removing the interconnection term $\gamma(\lambda_f, \lambda_r)$ and setting λ_f at the equilibrium.

Consider the candidate Lyapunov function

$$V(\lambda_i) = \frac{(\lambda_i - \tilde{\lambda}_i)^2}{2},$$

which, by construction, is positive definite ($V(\lambda_i) > 0$ for all $\lambda_i \neq \tilde{\lambda}_i$, and $V(\tilde{\lambda}_i) = 0$) and is radially unbounded. The time derivative of V along the subsystem trajectories is

$$\dot{V}(\lambda_i) = (\lambda_i - \tilde{\lambda}_i)\dot{\lambda}_i = -\frac{r}{Jv}\Big[k_i + \alpha_i(\lambda_i)\Big](\lambda_i - \tilde{\lambda}_i)^2.$$

Thus, recalling the definition of $\alpha_f(\lambda_f)$ and $\alpha_r(\lambda_r)$, if

$$k_f > \bar{k}_f = -\min_{\vartheta, \lambda_f, \lambda'_f} \frac{\Psi_f(\lambda_f) - \Psi_f(\lambda'_f)}{\lambda_f - \lambda'_f}, \tag{3.25}$$

$$k_r > \bar{k}_r = -\min_{\vartheta, \lambda_r, \lambda'_r, \lambda'_f} \frac{\Psi_r(\lambda'_f, \lambda_r) - \Psi_r(\lambda'_f, \lambda'_r)}{\lambda_r - \lambda'_r}, \tag{3.26}$$

one obtains that $\dot{V}(\lambda_i) < -c_i(\lambda_i - \tilde{\lambda}_i)^2$, with $c_i > 0$, which concludes the proof that the equilibrium $\tilde{\lambda}_i$ of subsystem (3.24) is GES (see also Appendix A). The stability properties of the equilibria of two nonlinear subsystems ensure that, once the cascade interconnection of the two is active, the closed-loop system admits a unique equilibrium point that is locally asymptotically stable (see *e.g.*, [44]).

□

Note that, in the case of nonlinear systems, the global asymptotic stability of the equilibrium of each of the two subsystems is not enough to infer the same property for the equilibrium of the interconnection, while this is instead true for the cascade connections of linear systems, see, *e.g.*, [35].

Note further that a solution to the equilibrium conditions (3.22) always exists for all gain values $k_f, k_r > 0$ and it can be graphically identified by first intersecting $\Psi_f(\lambda_f)$ in Figure 2.12(a) with the line of negative slope $-k_f$ cutting the λ_f axis in $\overline{\lambda}_f$ to determine $\tilde{\lambda}_f$, and then intersecting $\Psi_r(\tilde{\lambda}_f, \lambda_r)$ in Figure 2.12(b) with the line of negative slope $-k_r$ cutting the λ_r axis in $\overline{\lambda}_r$ to determine $\tilde{\lambda}_r$. If k_f and k_r satisfy the bound for the global asymptotic stability to hold, the equilibrium is unique. Note also that, as we are using a proportional controller, the values $\tilde{\lambda}_f$ and $\tilde{\lambda}_r$ are in general different from the set-point values $\overline{\lambda}_f$ and $\overline{\lambda}_r$. From the equilibrium conditions (3.22), however, it is clear that $\tilde{\lambda}_f$ and $\tilde{\lambda}_r$ can be made close to $\overline{\lambda}_f$ and $\overline{\lambda}_r$ if the controller gains k_r and k_f are sufficiently large.

Finally, it is worth pointing out that the condition obtained on the controller gains is similar to that given for the single-corner model in Section 3.2, where it was shown that the gain must be larger than the steepest negative slope of the friction curve for all road conditions to ensure *local* stability. Proposition 3.1 thus extends the results obtained on the single-corner model to the double-corner one, and from a linear to a nonlinear analysis setting.

3.8.2 Controlling the Rear Wheel: Slip versus Relative Slip Control

The double-corner model analysis has shown that stability can indeed be guaranteed with results that are fully analogous to those obtained with the single-corner model. The dynamic analysis carried out in Section 2.5.2 warned us that a dynamic coupling is present between front and rear wheel, which can be more or less significant according to the specific vehicle characteristics. In general, it cannot be neglected in vehicles that experience a very large load transfer between front and rear axles during braking, such as two-wheeled vehicles.

As an example, consider Figure 3.13, which shows the typical behaviour of the longitudinal force F_x as a function of the wheel slip at the front and rear wheels in a vehicle with large load transfer. As discussed in Section 2.2, the longitudinal force scales with the vertical load F_z and also the peak value shifts forward in λ as F_z increases due to the non-exact proportionality between F_z and F_x. So, assuming that one wants to control the wheel slip of both wheels at the value $\overline{\lambda}$ shown in Figure 3.13, the control problem at the rear wheel is difficult to be handled in open-loop by the driver, as $\overline{\lambda}$ is

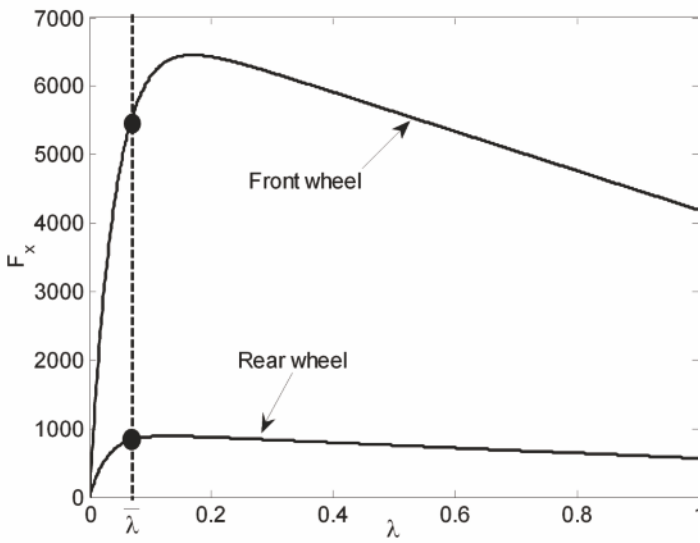

Figure 3.13 Longitudinal force as a function of the wheel slip at the front and rear wheels in a vehicle with large load transfer

very close to the peak of the friction curve, while this is not true for the front wheel.

As such, especially with two-wheeled vehicles, in the situation depicted in Figure 3.13 one would have the front wheel slip left in open-loop to be regulated by the driver, whereas the rear wheel slip should be regulated in closed-loop by an active controller.

Based on the above considerations, the idea is to devise an alternative control strategy for the rear wheel. The solution that we propose is that of considering an alternative control variable for the rear wheel, based on the idea of interlocking the rear wheels with the front ones with the aim of guaranteeing the same wheel slip on both axles.

Specifically, the controlled variable for the rear wheel is the speed difference between front and rear wheel, *i.e.*,

$$\omega_f - \omega_r, \tag{3.27}$$

which can be linked to slip control by means of the following equality:

$$\omega_f - \omega_r = \frac{v}{r}(\lambda_f - \lambda_r). \tag{3.28}$$

Hence, if we achieve $\omega_f - \omega_r = 0$, this implies that also the wheel slip at front and rear wheels will be the same. This is why we will refer to this approach as *relative slip control*.

Formulating the rear wheel control problem as that of regulating to zero the relative slip offers significant advantages with respect to controlling the rear wheel slip. First of all, feedback based on (3.27) does not require a measurement of the wheel slip. This is a particularly important feature in two-wheeled vehicles, where slip estimation is more critical than in cars, due to the larger load transfer. Thus, in the case where the front wheel slip is regulated by the driver, relative slip control at the rear wheel can be implemented by simply having two wheel encoders, which provide a cheap and robust measurement.

Further, from a dynamic viewpoint, Equation 3.28 reveals that the dependence on the forward speed obtained using the relative slip is different from the one obtained using the wheel slip as controlled variable.

Specifically, to compute the transfer function $G_{\omega_r-\omega_r}(s)$ from the rear braking torque δT_{br} to $\delta(\omega_f - \omega_r)$ of the double-corner model, the second-order state space representation employed in Section 2.5.2 can be used again with only the modification of the C matrix, which in view of (3.28) takes the form

$$C = \begin{bmatrix} 1 & 0 \\ -\frac{\overline{v}}{r} & \frac{\overline{v}}{r} \end{bmatrix}.$$

Thus, if we assume again, as was done in Section 2.5.2, that we can disregard the dependence of $\Psi_f(\lambda_f, \lambda_r)$ from λ_r and set $\delta\overline{\Psi}_{f,r} = 0$, the transfer function $G_{\omega_r-\omega_r}(s)$ is given by

$$G_{\omega_r-\omega_r}(s) = \frac{1}{J}\frac{s + \frac{r}{J\overline{v}}\delta\overline{\Psi}_{f,f}}{D(s)}, \tag{3.29}$$

where $D(s)$ is as in (2.71). Hence, the dependence of $G_{\omega_r-\omega_r}(s)$ on $\overline{v}$ is significantly different from that of $G_{rr}(s)$. Specifically, the static gain is given by

$$G_{\omega_r-\omega_r}(0) \cong \frac{\overline{v}J/r}{\delta\overline{\Psi}_{r,r}}, \tag{3.30}$$

thus proportional to the vehicle speed, while that of $G_{rr}(s)$ was independent of $\overline{v}$, see Equation 2.74. The high frequency gain, instead, is given by

$$\lim_{s\to\infty} s\, G_{\omega_r-\omega_r}(s) = \frac{1}{J}, \tag{3.31}$$

thus independent of $\overline{v}$, while that of $G_{rr}(s)$ was inversely proportional to $\overline{v}$, see Equation 2.78.

Figures 3.14(a) and 3.14(b) show a comparison between the Bode plots of the frequency responses associated with $G_{rr}(s)$ and with $G_{\omega_r-\omega_r}(s)$ obtained employing the double-corner model (see Section 2.4) with $\overline{\lambda_r} = 0.05$, $\overline{v} = 25$ m/s and on dry asphalt for different vehicle speed values, which visually confirm the different dynamic behaviour just analysed. Based on these results,

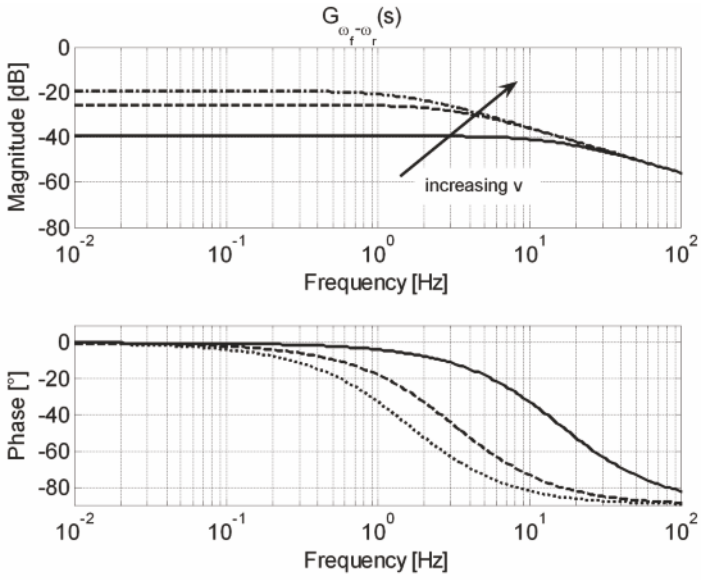

(a)

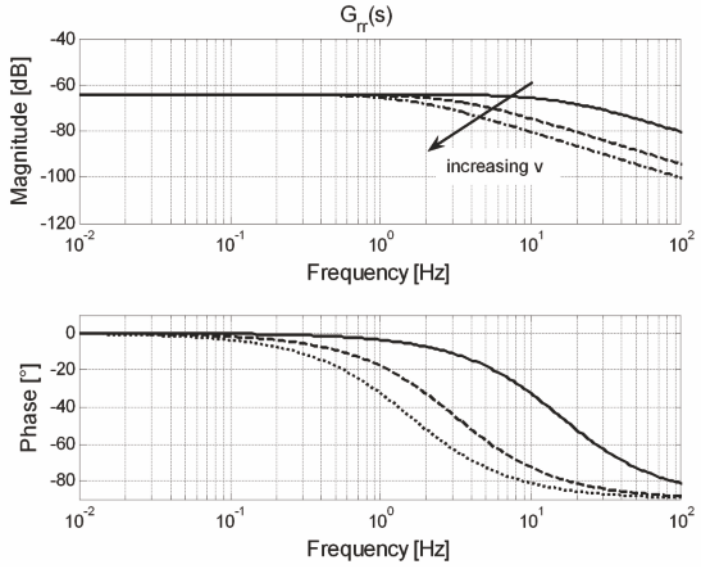

(b)

Figure 3.14 Magnitude and phase Bode plots of the frequency responses associated with $G_{\omega_f-\omega_r}(s)$ (a) and $G_{rr}(s)$ (b) for different vehicle speed values: $\overline{v} = 25$ m/s (*solid line*), $\overline{v} = 15$ m/s (*dashed line*) and $\overline{v} = 5$ m/s (*dash-dotted line*)

a simple and fixed structure PID controller has been designed to regulate the relative slip at the rear wheel.

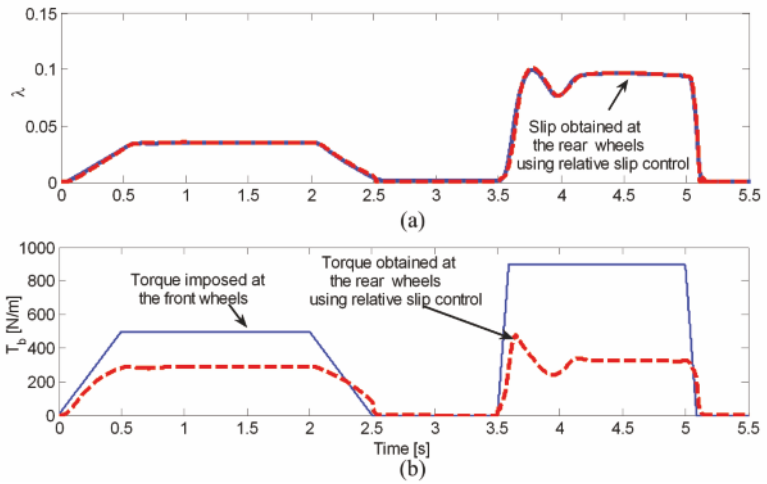

Figure 3.15 Plot of the wheel slip (a) and braking torque (b) in two braking manoeuvres with no control on the front wheel (dry asphalt and initial speed $v_0 = 100$ km/h)

Figures 3.15(a) and 3.15(b) show the rear wheel slip behaviour when the front wheel is in open-loop (the braking torque is imposed by the driver), and the rear wheel is controller using the relative slip as controlled variable, showing a good dynamic behaviour.

Finally, Figures 3.16(a) and 3.16(b) show the closed-loop behaviour of the wheel slip when a closed-loop slip controller (a simple PID controller of the type discussed in Section 3.4) acts on the front wheels and the rear wheels are regulated *via* relative slip control. In this case, when all the four wheels are controlled at the same time, the effects of dynamic coupling are more significant. However, the proposed control approach allows us to achieve a very good closed-loop performance with a SISO approach and two linear and fixed structure controllers.

3.8.3 Wheel Slip Control on Curves

Up to now we have always considered the wheel slip control problem under the assumption of negligible tyre sideslip angles, that is when the tyre–road contact forces are dominated by the longitudinal component.

When braking on a curve with non-negligible tyre sideslip angles, instead, one has to handle the trade-off between longitudinal and lateral forces (see

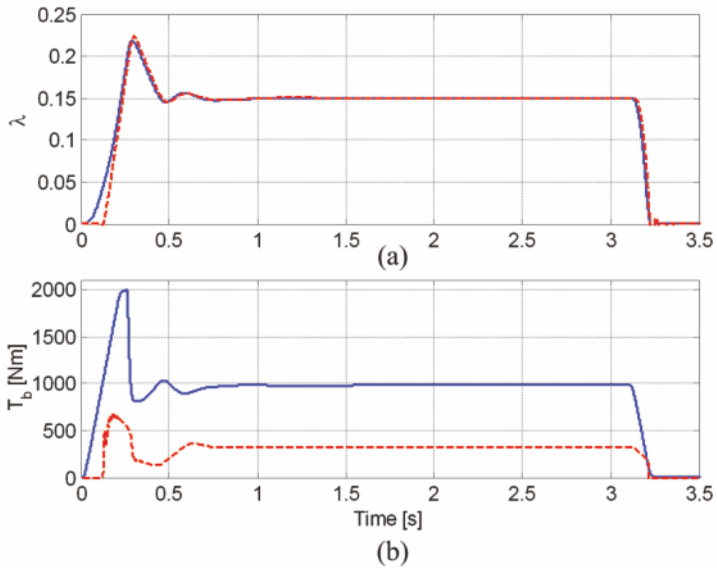

Figure 3.16 Plot of the wheel slip (a) and braking torque (b) in a hard braking manoeuvre on dry asphalt with front wheel slip control and rear wheels relative slip control. Front wheels (*solid line*) and rear wheel (*dashed line*)

Figures 2.2(a) and 2.2(b)). When on a curve, in fact, the largest amount of longitudinal force for transferring the braking torque to the ground is limited by the lateral force which is needed for negotiating the curve.

Thus, if the braking occurs in a curve manoeuvre where the vehicle is not subject to stability problems, that is when the ESC controller is not active, a wheel slip controller can be used by adapting the longitudinal slip set-point value $\overline{\lambda}$ to the curve condition. In four-wheeled vehicles this can be done by letting the set-point be a function of the steering angle (a variable commonly measured on all cars equipped with ESC systems), whereas in two-wheeled vehicles the set-point should be adapted as a function of the roll angle (see, *e.g.*, [108] and the references therein for a more detailed discussion on this topic). Besides the set-point adaptation, then, a wheel slip controller of the type discussed in this book is needed to handle the braking manoeuvre.

In the case of stability problems, instead, which in general occur when large values of the vehicle sideslip angle (*i.e.*, the angle between the chassis longitudinal axis and the velocity vector of the centre of mass) are reached, the ESC controller is activated. Some modern ESC controllers have a supervisory control logic that translates the yawing moment needed to recover stability into different wheel slip set-points commanded to each wheel and that are tracked by means of a slip controller of the type discussed in this book.

Other ESC controllers, instead, do not have this supervisory unit and directly act on the brakes to achieve the desired yawing moment, thus overriding the wheel slip control loop.

3.9 Summary

This chapter showed how to design braking controllers based on actuators with continuous dynamics.

Specifically, we first highlighted the advantages of controlling the wheel slip rather than the wheel deceleration, and discussed how to solve the slip control problem employing a linearised model of the single-corner dynamics. The tuning phase of different simple linear controllers was analysed in detail, providing the tuning rules to ensure closed-loop stability.

Further, the need for an activation and deactivation logic was motivated and a possible solution was outlined.

Finally, an analysis of the wheel slip control problem based on the double-corner model was presented, and its closed-loop stability properties were analysed.

Further, a control strategy based on the idea of interlocking the rear wheels with the front ones was presented, which imposes the same wheel slip behaviour on both axles and which is particularly interesting for vehicles presenting a large load transfer during braking.

Note finally that the stability proof carried out in Proposition 3.1 for the slip controller applied to the double-corner model could be extended to show that the stability of the equilibrium of the closed-loop system is indeed global and not only local. To do this, however, advanced concepts of nonlinear analysis are needed, which we believe go beyond the scope of this book and do not add crucial information to the specific problem. The interested reader can find the full proof in [115], together with some references to the related theoretical tools.

Chapter 4
Braking Control Systems Design: Actuators with Discrete Dynamics

4.1 Introduction

As discussed in the previous chapters, the design of automatic braking control systems is highly dependent on the braking system characteristics and actuator performance. This chapter addresses the problem of designing an ABS controller based on a hydraulic actuator system with on/off dynamics, which is capable of providing only three control actions: namely, one can only *increase*, *hold* and *decrease* the brake pressure.

Clearly, the control objectives must be traded off with the braking system capabilities. Accordingly, the aim of the control system will be that of maintaining the wheel slip around acceptable values, thus avoiding wheel locking, abandoning the goal of regulating it around a constant single value as was done in the preceding chapter for the case of a braking system with continuous dynamics.

To solve this problem, we will design a switching controller that yields closed-loop dynamics that converge to an asymptotically stable limit cycle.

For this control system, we provide necessary conditions for the limit cycle existence, which come from a detailed analysis of the state plane trajectories of the resulting braking dynamics. Further, the limit cycle stability properties are formally proved *via* a Poincaré map analysis (the interested reader may refer to Section A.2.2 for an introduction to the analysis tools used in this chapter).

An analysis of the effect of the actuator performance on the closed-loop system is also provided, which helps highlighting the features of the controller under study.

We underline that the main purpose of this analysis is to provide a system-theoretic framework to characterise the performance of standard ABS systems rather than on focusing on the design of a new ABS control algorithm.

Finally, the chapter provides a discussion on the link between the two braking technologies considered, which aims at pointing out that the control

engineer will have to carefully analyse the actuator dynamic capabilities in order to devise the most appropriate control approach for braking systems design.

The presentation of this topic is organised as follows. In Section 4.2 the braking and actuator dynamics are described and discussed. The state plane trajectories are shown and the considered ABS controller is introduced. In Section 4.3 the necessary conditions for the limit cycle existence are presented and the limit cycle properties in terms of amplitude and period are derived. Then, in Section 4.4 the construction of the Poincaré map is outlined, and the cycle asymptotic stability is assessed. Further, an analysis of the effect of the actuator rate limit on the closed-loop trajectories is presented and the chapter is concluded with a comparison of braking technologies considered.

4.2 Problem Setting

The model of the braking dynamics considered in this chapter is the single-corner model (see Section 2.3), coupled with the HAB discussed in Section 1.3.

Specifically, the connection between the wheel dynamics (2.29) and the hydraulic actuator dynamics introduced in (1.2) yields the second-order system

$$\begin{cases} \dot{\lambda} = -\frac{1-\lambda}{J\omega}\left(\Psi(\lambda) - T_b\right), \\ \dot{T}_b = u, \end{cases} \tag{4.1}$$

where $\omega > 0$, $u = \{-k, 0, k\}$ and (see also Equation 2.30)

$$\Psi(\lambda) = \left(r + \frac{J}{rm}(1-\lambda)\right) F_z \mu(\lambda). \tag{4.2}$$

Recall (see Section 1.3) that according to the value of the control variable u, we have three possible closed-loop dynamics, where $u = -k$ corresponds to the *decrease* control action, $u = 0$ corresponds to the *hold* control action and $u = k$ corresponds to the *increase* control action. The nominal value for k in this chapter will be $k = 5$ kNm/s.

We now study the closed-loop trajectories with the aim of gathering information for the design of a switching control law that yields a limit cycle in the closed-loop system. To this end, Figure 4.1(a) shows the closed-loop trajectories in the state plane (λ, T_b) when $u = k$, Figure 4.1(b) the closed-loop trajectories in the state plane (λ, T_b) when $u = 0$ and Figure 4.1(c) the closed-loop trajectories in the state plane (λ, T_b) when $u = -k$. These results were obtained for a static value of the vertical load $F_z = mg$, for $v = 30$ m/s and on a dry asphalt road.

The dashed line in these figures is the curve defined by the expression of the equilibrium points for the open-loop single-corner model, *i.e.*,

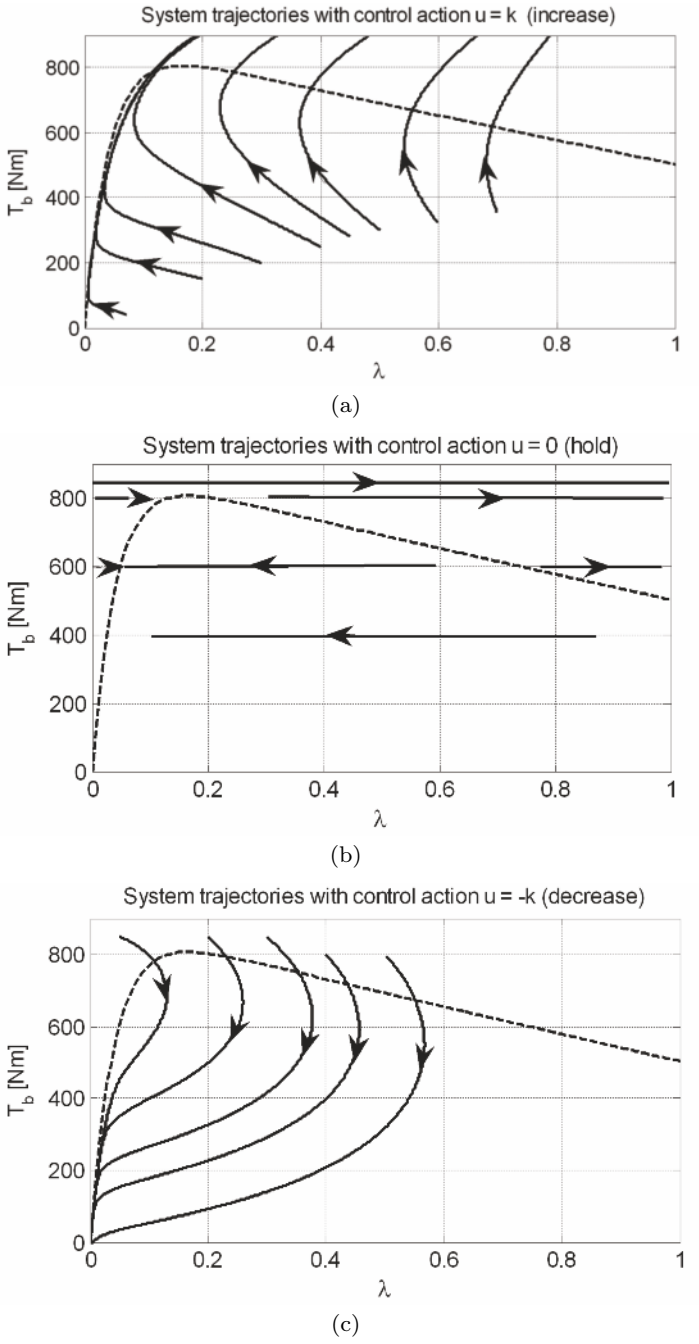

Figure 4.1 Closed-loop trajectories in the state plane (λ, T_b) when $u = k$ (a), $u = 0$ (b) and $u = -k$ (c)

$$T_b(\lambda) = \Psi(\lambda), \tag{4.3}$$

where $\Psi(\lambda)$ is as in (4.2).

According to the trajectories analysis, we can devise an appropriate switching logic to induce a limit cycle on the wheel slip. To this end, as depicted in Figure 4.2(a), we select a box in the state plane; the idea is to use the boundaries of the box as switching surfaces and to select the control actions according to the finite state machine (FSM) shown in Figure 4.2(b). Specifically, Figure 4.2(b) shows that the hybrid controller is composed of four discrete states $q = \{0, 1, 2, 3\}$, each of which has an associated control action, that is $u = \{k, 0, -k\}$. The transitions between these discrete states take place when the closed-loop system trajectory *hits* the switching surfaces.

We define the switching manifolds as follows (see Figure 4.2(a)):

$$\Sigma_0 = \{(\lambda, T_b) \,:\, H_0(\lambda, T_b) := T_b - T_{b\text{Max}} = 0\}, \tag{4.4}$$

$$\Sigma_1 = \{(\lambda, T_b) \,:\, H_1(\lambda, T_b) := \lambda - \lambda_{\text{Max}} = 0\}, \tag{4.5}$$

$$\Sigma_2 = \{(\lambda, T_b) \,:\, H_2(\lambda, T_b) := T_b - T_{b\text{Min}} = 0\}, \tag{4.6}$$

$$\Sigma_3 = \{(\lambda, T_b) \,:\, H_3(\lambda, T_b) := \lambda - \lambda_{\text{Min}} = 0\}. \tag{4.7}$$

A detailed discussion on the relative position between the box and the equilibrium curve $\Psi(\lambda)$ given in Equation 4.2 is postponed to Section 4.3, as it is closely related to the existence of the limit cycle.

By analysing Figure 4.2(b), where the FSM representation of the hybrid controller is depicted, one can see that we employ the braking torque T_b and the wheel slip λ as switching variables and that the switching manifolds change according to the current discrete controller state $q = \{0, 1, 2, 3\}$. Moreover note that because of the specific application, we can assume that (in normal operating conditions) the controller – upon activation – enters the state $q = 0$ associated with the *increase* control action. This is due to the fact that, when the braking manoeuvre begins, the controller is usually activated when the wheel slip λ reaches a predefined threshold value, lower than λ_{Min}. In the following simulations, for simplicity, we assume that the braking manoeuvre starts with $\lambda = 0$ and $T_b = 0$.

Finally, it is worth noticing that when the closed-loop system evolves in the discrete states $q = 1$ and $q = 3$, the control action is $u = 0$. Hence, the dynamics given in (4.1) reduce to a first-order system and the closed-loop trajectories in these discrete states *slide* along the switching manifold.

From the application viewpoint, the controller needs a measure of the longitudinal wheel slip λ and of the braking torque T_b (which can be derived *via* a pressure measurement by means of Equation 1.1). Chapter 5 will discuss the problem of wheel slip estimation in detail. What can be said here is that the considered controller provides robustness features to measurement errors, as the thresholds can be properly tuned based on the confidence on the quality of the available estimates of the controlled variables. Finally, note that the ABS controller depicted in Figure 4.2(b) is representative of the heart of

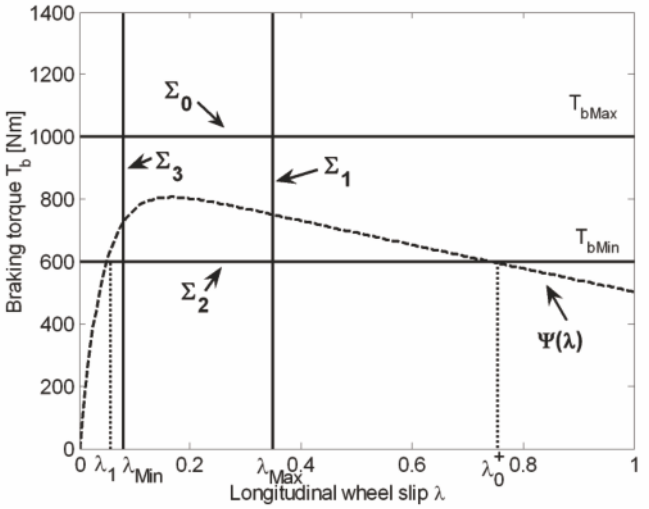

(a)

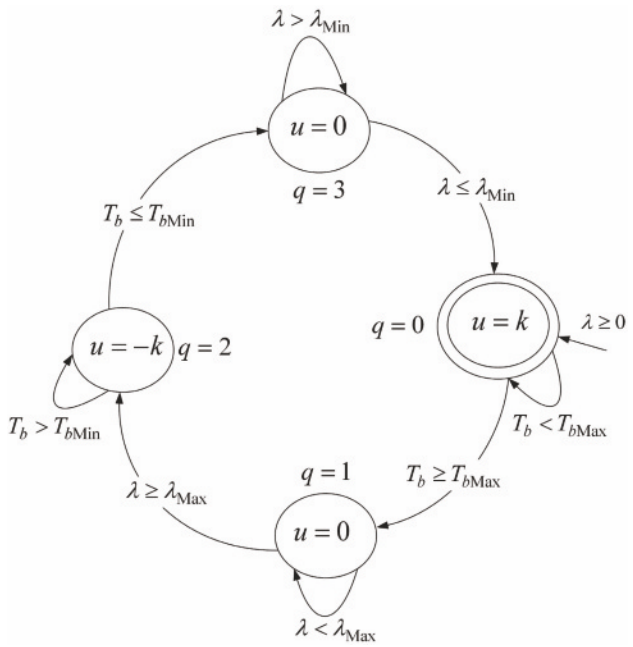

(b)

Figure 4.2 Switching logic shown in the state plane (λ, T_b) (a) and FSM description of the braking controller (b)

the switching logic actually implemented on current hydraulic ABS systems, even though it offers a simplified description of the whole set of rules actually employed. An industrial implementation of such control logic, in fact, must handle all possible exceptions to normal functioning and this causes a huge increase in the set of the needed logic rules. In particular, it is worth mentioning that as the braking pressure is not always available for measurement, the threshold on the braking torque T_b might be replaced with thresholds on the wheel deceleration (see, *e.g.*, [27, 74]). Moreover, some vehicles might be equipped with some sort of tyre–road friction monitoring system; if this is the case, the threshold values $T_{b\mathrm{Min}}$ and $T_{b\mathrm{Max}}$ can be adapted online according to the current road conditions. We discuss the controller in Figure 4.2(b) because it is representative of the actual functioning of current industrial ABS controllers while consisting only of a few discrete states, thereby allowing us to provide a sound formal analysis in a simple yet realistic framework.

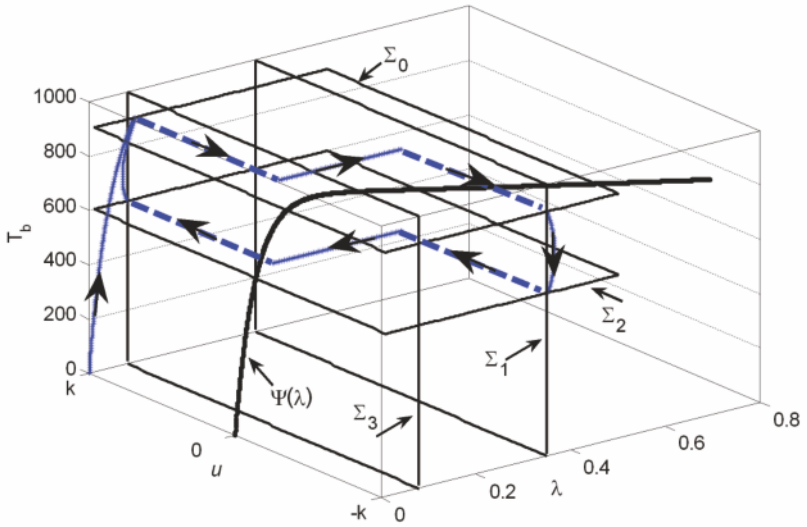

Figure 4.3 Simulated closed-loop trajectory of system (4.1) with the given control logic in the *hybrid* state space (T_b, λ, u)

4.3 Existence and Stability of Limit Cycles

We now investigate the existence and stability properties of the limit cycle exhibited by the closed-loop braking system. We start by analysing the be-

haviour of the closed-loop system obtained with the considered controller and then give appropriate necessary conditions for the limit cycle existence.

The main features of the limit cycle are obtained by solving the associated boundary value problem (BVP), *i.e.*, by solving the nonlinear differential equations defining system (4.1) over a specified time interval with appropriate initial and final conditions.

For the definition of a limit cycle and a discussion on its stability properties the interested reader is referred to Appendix A for a brief introduction and to the references given therein for a more detailed presentation of the related topics. It is worth mentioning that the considered closed-loop system is within the class of *non-smooth* systems, *i.e.*, its dynamics are not fully continuous, as the control action switches according to the FSM representing the braking controller. For the analysis carried out in this chapter, the material presented Appendix A for the case of continuous systems still applies. For a thorough review of the existing results concerning the nonlinear dynamic analysis of non-smooth and hybrid systems, the interested reader may refer to [22, 50, 126].

Moving now to the considered case, Figure 4.3 shows a representative simulation of the closed-loop system (4.1) with the control logic given in Figure 4.2(b) and with the threshold values $T_{b\mathrm{Min}} = 600$ Nm, $T_{b\mathrm{Max}} = 900$ Nm, $\lambda_{\mathrm{Min}} = 0.08$ and $\lambda_{\mathrm{Max}} = 0.35$, on dry asphalt. In particular, Figure 4.3 shows the closed-loop system trajectory in the three-dimensional hybrid state space (T_b, λ, u), where also the discrete control action $u \in \{k, 0, -k\}$ is regarded as an additional state of the system. The dashed lines connecting the segments of the periodic orbit in Figure 4.3 represent the *jumps* of the closed-loop system among the different discrete states of the controller. These simulation results demonstrate that the proposed control logic can indeed induce a periodic behaviour in the wheel slip and in the braking torque. Nonetheless, we still need to analyse under which conditions the existence of the limit cycle is ensured and what the other possible closed-loop dynamics are when the desired periodic solution does not exist.

To investigate under which conditions the proposed control logic induces a limit cycle behaviour in the wheel slip, refer to Figures 4.3 and 4.4; in the latter a pictorial representation of the closed-loop trajectories (plotted in Figure 4.3) is displayed. According to the hybrid controller behaviour depicted in Figure 4.2(b) the limit cycle of interest is composed of the four different segments shown in Figure 4.4.

1. When the braking manoeuvre begins, the FSM is in the discrete state $q = 0$. The system then evolves with the dynamics given by system (4.1) for $u = k$. Accordingly, the first switching occurs when the switching manifold Σ_0 is crossed at the point labelled as

$$\bar{x} = (T_{b\mathrm{Max}}, \bar{\lambda}). \tag{4.8}$$

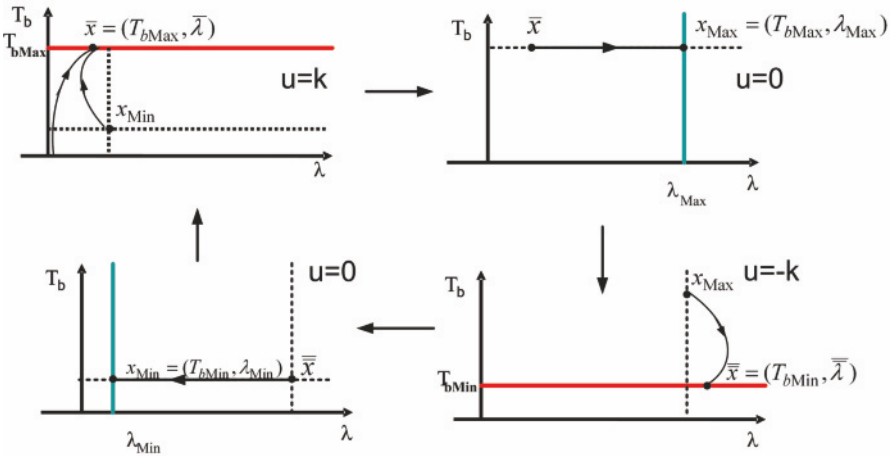

Figure 4.4 Pictorial representation of the limit cycle behaviour in terms of itinerary and initial conditions

2. The system then switches to the discrete state $q = 1$ where $u = 0$, and starting from this initial condition evolves in this discrete state until hitting Σ_1 at the point

$$x_{\text{Max}} = (T_{b\text{Max}}, \lambda_{\text{Max}}). \tag{4.9}$$

3. Now, the system switches again, this time to the discrete state $q = 2$, and starting from x_{Max} it remains in this state until crossing the switching manifold Σ_2. Again, the switching occurs at a specific point, labelled (see also Figure 4.4)

$$\bar{\bar{x}} = (T_{b\text{Min}}, \bar{\bar{\lambda}}). \tag{4.10}$$

4. Finally, the system switches to the discrete state $q = 3$ until, at the point

$$x_{\text{Min}} = (T_{b\text{Min}}, \lambda_{\text{Min}}), \tag{4.11}$$

it crosses Σ_3 when the discrete state $q = 0$ is entered again and the cycle is repeated.

Note that both $\bar{\lambda}$ and $\bar{\bar{\lambda}}$ are functions of the system parameter k, which defines the curvature of the vector field when the system is in the states $q = 0$ and $q = 2$. Furthermore, while $\bar{\bar{\lambda}}$ affects the limit cycle existence, $\bar{\lambda}$ only affects the itinerary of the limit cycle. In fact, if $\bar{\lambda} > \lambda_{\text{Max}}$, the point $(T_{b\text{Max}}, \lambda_{\text{Max}})$ does not belong to the limit cycle, but the limit cycle itself might still exist.

Now let $\Phi(t, [\lambda(0), T_b(0); q = i]), i = 0, \ldots, 3$ define the system trajectory forward in time[1]. In the following, we use the terminology *forward trajectory.*

Thus, if the limit cycle described above exists, the following conditions must be satisfied.

1. There must be no intersection between the switching manifold Σ_0 and the manifold $\Psi(\lambda)$ (see Figure 4.2(a)), *i.e.*,
$$\Sigma_0 \cap \Psi(\lambda) = \emptyset. \tag{4.12}$$
2. The switching manifold Σ_2 must intersect the equilibrium manifold $\Psi(\lambda)$, *i.e.*,
$$\Sigma_2 \cap \Psi(\lambda) \neq \emptyset. \tag{4.13}$$
Note that if an intersection exists between the two manifolds, then, recalling Equation 2.30 (see also Figure 4.2(a)) if $T_{b\text{Min}} < \Psi(\lambda = 1)$ the intersection is constituted by a single point, while, if $T_{b\text{Min}} \geq \Psi(\lambda = 1)$ it is constituted by two points.
3. If $T_{b\text{Min}} \geq \Psi(\lambda = 1)$, *i.e.,* two points of intersections exist between Σ_2 and $\Psi(\lambda)$, that is
$$\Sigma_2 \cap \Psi(\lambda) = \{(T_{b\text{Min}}, \lambda_1), (T_{b\text{Min}}, \lambda_0^+)\}, \tag{4.14}$$
with
$$\lambda_1 < \lambda_0^+, \tag{4.15}$$
then the intersection between the system forward trajectory
$$\Phi(t, [\lambda_{\text{Max}}, T_{b\text{Max}}; q = 2])$$
and Σ_2 must occur at a point $(T_{b\text{Min}}, \overline{\overline{\lambda}})$ such that
$$\overline{\overline{\lambda}} < \lambda_0^+. \tag{4.16}$$

Clearly, if condition (4.12) were not satisfied, then the closed-loop trajectory would intersect $\Psi(\lambda)$ when evolving in the discrete state $q = 0$ with $u = 0$. When $u = 0$, the isocline is a set of equilibrium points for the closed-loop dynamics. Hence, the system trajectory *hits* the point of intersection with this curve and remains at the equilibrium with no limit cycle occurring. This case is depicted in Figures 4.5(a) and 4.5(b), where the trajectory and the time histories of the closed-loop system are shown for threshold values $T_{b\text{Min}} = 600$ Nm, $T_{b\text{Max}} = 750$ Nm, $\lambda_{\text{Min}} = 0.08$ and $\lambda_{\text{Max}} = 0.35$, on dry asphalt. Note that when condition (4.12) is violated the closed-loop behaviour of the system resembles that of a modulating controller, and we are able

[1] For a generic dynamical system with state $x \in \mathbb{R}^n$, the trajectory forward in time is defined as $\Phi(t - t_0, x(t_0))$, where t_0 is the initial time and $x(t_0)$ the initial conditions, see, *e.g.*, [126].

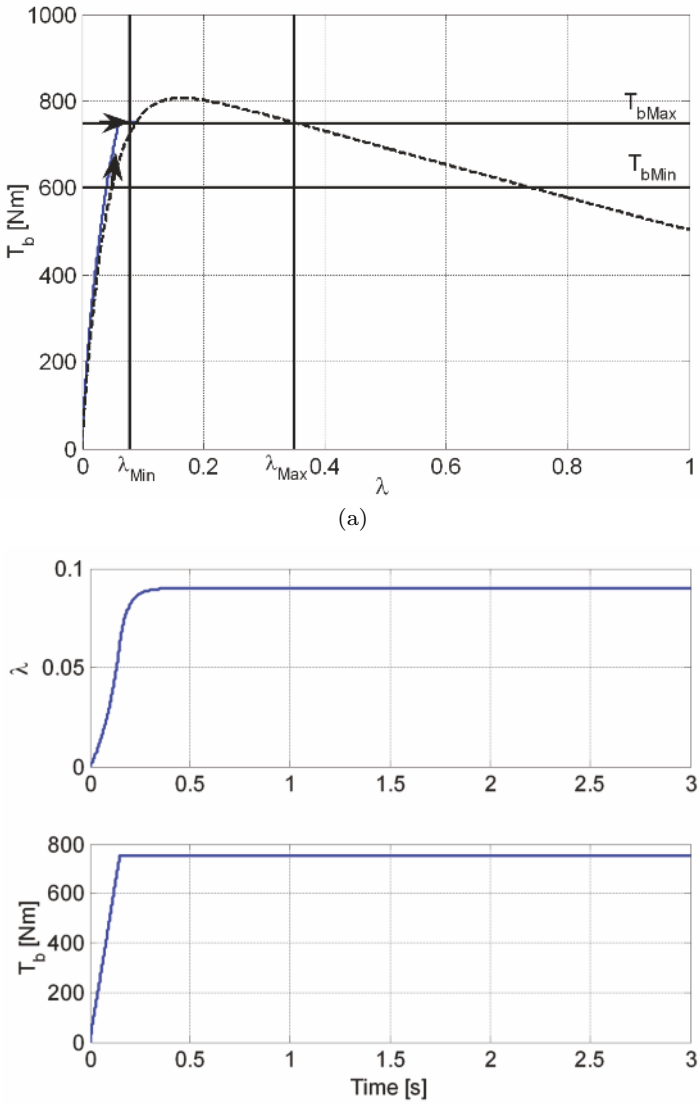

Figure 4.5 Closed-loop trajectory (a) and time histories of slip and braking torque (b) of system (4.1) with the given control logic when the necessary condition (4.12) for the limit cycle existence is violated

to track a constant wheel slip value that corresponds to the abscissa of the intersection between the manifolds Σ_0 and $\Psi(\lambda)$. Hence, even though the desired limit cycle does not exist, from the application point of view this kind of solution can be regarded as acceptable, as the braking manoeuvre is still handled in a safe way.

Condition (4.13) guarantees that when the discrete controller switches between $q = 2$ and $q = 3$, the system trajectory (which in this case is the wheel dynamics only, as Σ_2 is a sliding surface) evolves along decreasing values of λ. In the case $\Sigma_2 \cap \Psi(\lambda) = \emptyset$, in fact, the system trajectory after such switching would be such that λ increases (see Figure 4.1(b)) and wheel locking would then occur. The effect of violating this condition is shown in Figures 4.6(a) and 4.6(b), where the trajectory and the time histories of the closed-loop system are shown, for threshold values $T_{b\text{Min}} = 850$ Nm, $T_{b\text{Max}} = 950$ Nm, $\lambda_{\text{Min}} = 0.08$ and $\lambda_{\text{Max}} = 0.35$, on dry asphalt. Note that when condition (4.13) is not fulfilled, after the switching between $q = 2$ and $q = 3$ occurs the system trajectory evolves along increasing values of λ, and this causes the wheel slip to lock.

Similarly, if the condition $\overline{\overline{\lambda}} < \lambda_0^+$ in (4.16) were violated, then when the system switched between $q = 2$ and $q = 3$ the system trajectory would again evolve along increasing values of λ, thereby causing the system to move toward $\lambda = 1$ (see also Figure 4.1(b)). Again, this means that no limit cycle exists and the braking manoeuvre ends with the locking of the wheel. A simulation of the violation of this condition is shown in Figures 4.7(a) and 4.7(b), for threshold values $T_{b\text{Min}} = 700$ Nm, $T_{b\text{Max}} = 950$ Nm, $\lambda_{\text{Min}} = 0.08$, $\lambda_{\text{Max}} = 0.35$ and $k = 1$ kNm/s, again on dry asphalt.

Assume now that conditions (4.12-4.16) are satisfied. Then, according to the limit cycle itinerary described above and to the definitions of the switching points given in Equations 4.8-4.11, we can explicitly define the switching instants (we assume $t_0 = 0$) as

$$t_1 = \{t : \Phi(t_1, [x_{\text{Min}}; q = 0]) \cap \Sigma_0 = \{\overline{x}\}\}, \tag{4.17}$$

$$t_2 = \{t : \Phi(t_2 - t_1, [\bar{x}; q = 1]) \cap \Sigma_1 = \{x_{\text{Max}}\}\}, \tag{4.18}$$

$$t_3 = \left\{t : \Phi(t_3 - t_2, [x_{\text{Max}}; q = 2]) \cap \Sigma_2 = \{\overline{\overline{x}}\}\right\}, \tag{4.19}$$

$$t_4 = \left\{t : \Phi(t_4 - t_3, [\overline{\overline{x}}; q = 3]) \cap \Sigma_3 = \{x_{\text{Min}}\}\right\}. \tag{4.20}$$

Once all the system parameters have been fixed, conditions (4.17-4.20) together with (4.8-4.11) can be seen as a BVP that can be solved numerically for the unknowns $\overline{\lambda}$, $\overline{\overline{\lambda}}$, $\Delta_0 = t_1$, $\Delta_1 = t_2 - t_1$, $\Delta_2 = t_3 - t_2$ and $\Delta_3 = t_4 - t_3$. Setting the threshold values $T_{b\text{Min}} = 600$ Nm, $T_{b\text{Max}} = 900$ Nm, $\lambda_{\text{Min}} = 0.08$ and $\lambda_{\text{Max}} = 0.35$, as depicted in Figure 4.2(a), considering dry asphalt road and simulating the single-corner model with the numerical values given in Table 2.2 we obtain the solution $\overline{\lambda} = 0.093$, $\overline{\overline{\lambda}} = 0.352$, $\Delta_0 = 0.072$, $\Delta_1 = 0.25$, $\Delta_2 = 0.052$ and $\Delta_3 = 0.22$.

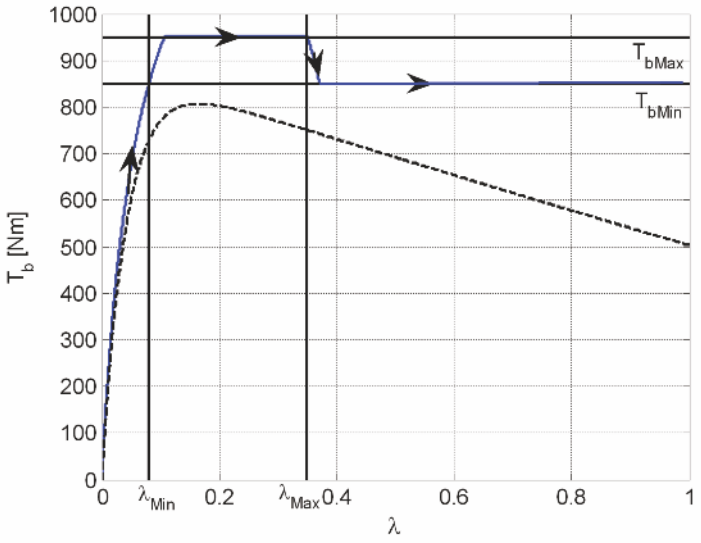

(a)

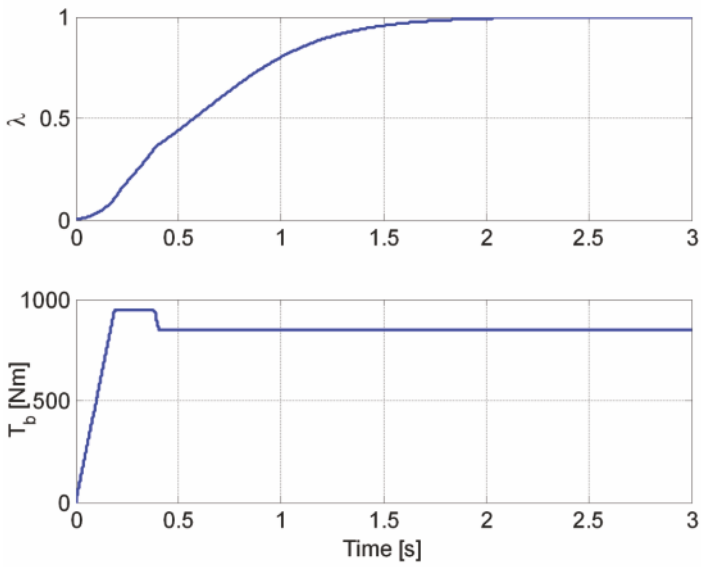

(b)

Figure 4.6 Closed-loop trajectory (a) and time histories of wheel slip and braking torque (b) of system (4.1) with the given control logic when condition (4.13) for the limit cycle existence is violated

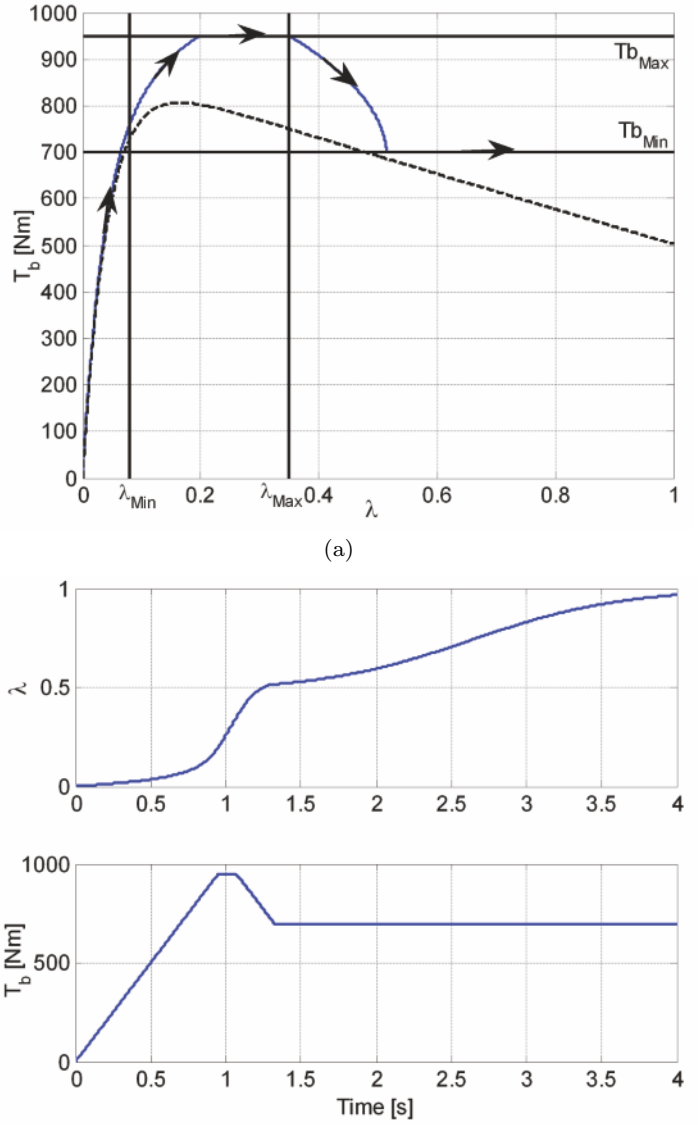

Figure 4.7 Closed-loop trajectory (a) and time histories of wheel slip and braking torque (b) of system (4.1) with the given control logic when condition (4.16) for the limit cycle existence is violated

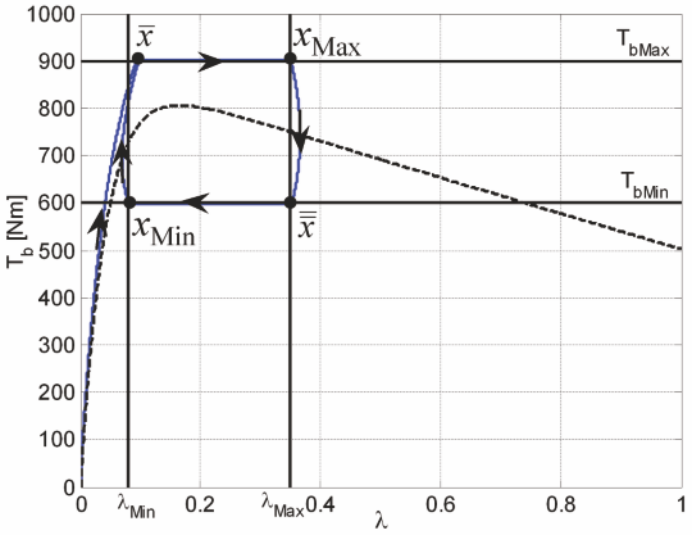

Figure 4.8 Plot of the closed-loop system trajectory in the state plane (λ, T_b) obtained as the solution of the BVP

The resulting closed-loop behaviour is depicted in Figure 4.8, where the limit cycle is shown in the state plane (λ, T_b). From the numerical solution of the BVP we can also extract quantitative informations about the cycle amplitude and period. Specifically, the period is given by

$$T = \sum_{i=0}^{3} \Delta_i = 0.594\,\text{s}.$$

As for the amplitude, it is clear that, in the vertical direction, the cycle amplitude is *a priori* fixed from the choice of the thresholds $T_{b\text{Min}}$ and $T_{b\text{Max}}$. Hence, the only interesting amplitude value is that on the longitudinal direction, which we refer to as to the cycle λ-amplitude.

To compute this value numerically, we evaluate the closed-loop system forward trajectory in the states $q = 0$ and $q = 2$ until the time instant at which the event $\dot{\lambda} = 0$ occurs. Hence, the cycle λ-amplitude is computed as

$$A_\lambda = \underline{\lambda} - \underline{\underline{\lambda}} = 0.295,$$

where $\underline{\lambda}$ and $\underline{\underline{\lambda}}$ are defined as

$$\underline{\lambda} := \Gamma_\lambda[\Phi(t_3 - t_2, [x_{\text{Max}}; q = 2]) \cap \Psi(\lambda)] \tag{4.21}$$

and

$$\underline{\underline{\lambda}} := \Gamma_\lambda[\Phi(t_1, [x_{\text{Min}}; q = 0]) \cap \Psi(\lambda)], \tag{4.22}$$

with $\Gamma_\lambda : \mathbb{R} \times \mathbb{R} \to \mathbb{R}$ being a map such that $\Gamma_\lambda(x, y) = x$, *i.e.*, a map that returns the abscissas of the intersections described in (4.21) and (4.22).

Thus, the existence of the limit cycle has been proved and its nominal amplitude and period computed. The next issue, which will be addressed in the next section, is to investigate its stability. To do this, we will employ some of the analysis tools presented in Appendix A.

Before moving to the stability analysis, it is worth mentioning that up to now a single tyre–road friction condition has been considered, that is dry asphalt road. Actually, the controller considered herein must be tuned by fixing the threshold values for both the wheel slip and the braking torque so that the necessary conditions (4.12)-(4.16) are satisfied. Hence, to devise a controller that can ensure the limit cycle existence on all road surfaces, and in view of the fact that a change in the road condition affects the curve $\Psi(\lambda)$ (see Equation 4.2), a trade-off in these values must be found. Nonetheless, as $\Psi(\lambda)$ can be analytically computed, the considered control approach allows an easy tuning of such values so as to define a *fixed-structure* control law that works on all different (a priori unknown) road conditions.

4.4 Limit Cycle Stability Analysis

To prove asymptotic stability of the limit cycle exhibited by system (4.1) in closed-loop with the hybrid control law given in Figure 4.2(b) we need to construct an appropriate *Poincaré map* (see Section A.2.2). In particular, we choose a plane $\Pi := \{(\lambda, T_b) \,|\, \bar{\lambda} \leq \lambda \leq \lambda_{\text{Max}}\}$ as a suitable Poincaré section, which is transversal to the system flow associated with the discrete controller state $q = 1$; that is, as time evolves, the closed-loop system trajectory intersects Π transversally.

Let x_n be the nth intersection of the system trajectory with the section Π. Also, let $x^* = (\lambda^*, T_b^*) \in \Pi$ be the point at which the limit cycle crosses the Poincaré section. Then, it is possible to construct a local mapping $P : \Pi \mapsto \Pi$ in a neighbourhood of x^* from one intersection x_n to the next x_{n+1}. Specifically, we have

$$x_{n+1} = P(x_n), \qquad x_n \in \mathcal{B}_r(x^*) \cap \Pi,$$

where $\mathcal{B}_r(x^*)$ is a ball of centre x^* and radius r.

Referring to Figure 4.9, we can see that for threshold values $T_{b\text{Min}} = 700$ Nm, $T_{b\text{Max}} = 1000$ Nm, $\lambda_{\text{Min}} = 0.08$, $\lambda_{\text{Max}} = 0.35$, with $\Pi := \{(\lambda, T_b) \,|\, \lambda = 0.2\}$ and considering again a dry asphalt road, if we select two initial conditions x_0^- and x_0^+ both belonging to $\mathcal{B}_r(x^*) \cap \Pi$, the system trajectories starting from any of these two initial conditions evolve on a sliding surface (see also Figure 4.1(b)) which is parallel to that of the steady-state system flow in $q = 1$. Nonetheless, as the first switching manifold is Σ_1, both

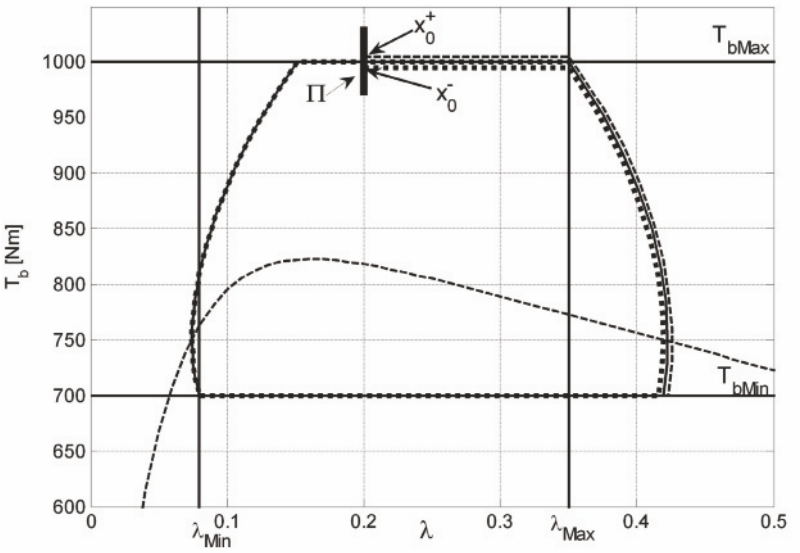

Figure 4.9 Plot of the closed-loop system trajectory in the state plane (λ, T_b) with the Poincaré section for the initial conditions x_0^- (*dotted line*) and x_0^+ (*dashed line*) in a neighbourhood of the fixed point x^*

these perturbed trajectories switch with the same value of $\lambda = \lambda_{\text{Max}}$. Then, when the second switching manifold Σ_2 is encountered, both trajectories again evolve on a sliding surface, which annihilates the initial perturbation.

From here onwards, the two trajectories are indistinguishable and coincide with the nominal one (solid line in Figure 4.9), *i.e.*,

$$P(x_n) = x^* \qquad \forall\, x_n \in \mathcal{B}_r(x^*) \cap \Pi. \tag{4.23}$$

From the above discussion and from Equation 4.23 it is clear that the only eigenvalue γ_F of the Jacobian of the Poincaré map is $\gamma_F = 0$ and this guarantees (see also Section A.2.2) that the limit cycle is not only *asymptotically stable* but it is also characterised by *dead beat* convergence, in the sense that the cycle starting from a perturbed initial condition is indistinguishable from the nominal one already at its first intersection with the plane Π and not only asymptotically.

4.5 Effects of the Actuator Rate-limit Variation

It is interesting to further investigate the effect of the actuator rate-limit k on the closed-loop trajectories. First of all, it is worth noting that there

exists a critical value for k that can cause the violation of the necessary condition (4.16) for the limit cycle existence.

In fact, as has already been mentioned, the parameter k is responsible for the *curvature* of the vector field when the system is in the states $q = 0$ and $q = 2$. Accordingly, a low value of k can make the system switch from $q = 0$ to $q = 1$ when $\lambda > \lambda_{\text{Max}}$, hence the pair $(T_{b\text{Max}}, \lambda_{\text{Max}})$ does not belong to the limit cycle. This, however, only modifies the cycle itinerary, but does not prevent its existence. On the other hand, a critical value of k exists such that when the switching from $q = 2$ to $q = 3$ occurs after the *decrease* control action has been applied, condition (4.16) is violated and wheel locking occurs.

To highlight the effects of k on the tuning of the different thresholds used in the algorithm, it is interesting to derive analytical bounds that allow us to capture the parameter effects on the closed-loop trajectories. To this end, consider the closed-loop system dynamics in the discrete state $q = 2$, which have the form

$$\begin{cases} \dot{\lambda} = -\frac{1-\lambda}{J\omega} \left(\Psi(\lambda) - T_b\right), \\ \dot{T}_b = -k. \end{cases} \tag{4.24}$$

To derive an analytical bound on the wheel slip evolution in time in $q = 2$, note first that when the switching from $q = 1$ to $q = 2$ occurs, the braking torque is such that $T_b = T_{b\text{Max}}$ (recall that $T_b = T_{b\text{Max}}$ for the entire system evolution in $q = 1$, where the *hold* control action is applied). Thus, the evolution in time of the braking torque in $q = 2$ is described as $T_{b\text{Max}} - k\,t$. Further, one must note that the function $\Psi(\lambda)$ is bounded, as it satisfies $0 \leq \Psi(\lambda) \leq \Psi_{\text{Max}}$, where $\Psi_{\text{Max}} = \max_\lambda \Psi(\lambda)$.

Due to these considerations and recalling that $\lambda \in [0, 1]$, it holds that

$$0 \leq \dot{\lambda} \leq \Psi_{\text{Max}} + (T_{b\text{Max}} - k\,t). \tag{4.25}$$

Further, as λ is non-negative, the same bound holds if we integrate (4.25) with respect to time; this yields

$$\lambda(0) \leq \lambda(t) \leq \lambda(0) + \Psi_{\text{Max}}\,t + T_{b\text{Max}}\,t - k\frac{t^2}{2}. \tag{4.26}$$

We are now interested in finding the time instant $\bar{t}$ when the switching from $q = 2$ to $q = 3$ occurs; that is

$$\bar{t} : T_b = T_{b\text{Max}} - k\,t = T_{b\text{Min}} \rightarrow \bar{t} = \frac{T_{b\text{Max}} - T_{b\text{Min}}}{k} > 0.$$

Substituting this expression into the right-hand side of (4.26) and noticing that $\lambda(0) = \lambda_{\text{Max}}$ yields

$$\lambda(t) \leq \lambda_{\text{Max}} + (\Psi_{Max} + T_{b\text{Max}})\frac{(T_{b\text{Max}} - T_{b\text{Min}})}{k} - \frac{(T_{b\text{Max}} - T_{b\text{Min}})^2}{2k} \tag{4.27}$$

$$= \lambda_{\text{Max}} + \left[(\Psi_{Max} + T_{b\text{Max}}) - \frac{(T_{b\text{Max}} - T_{b\text{Min}})}{2} \right] \frac{(T_{b\text{Max}} - T_{b\text{Min}})}{k}.$$

The above relation allows us to capture the fact that if $k \to 0$ (*i.e.*, if no braking torque is applied) we obtain $\lambda(t) \to 1$, *i.e.*, wheel locking occurs. In fact, if this is the case the trajectories are of the form depicted in Figure 4.1(b). On the other hand, if $k \to +\infty$ (*i.e.*, if we have an infinitely large actuator rate-limit) we have $\lambda(t) \to \lambda(0)$, *i.e.*, the system trajectory would evolve exactly along Σ_1 (and thus the limit cycle would coincide with the box defined in the state space by the curves Σ_i, see Figure 4.2(a)).

Finally, from (4.27), if we let

$$\lambda_{\text{Max}} + \left[(\Psi_{\text{Max}} + T_{b\text{Max}}) - \frac{(T_{b\text{Max}} - T_{b\text{Min}})}{2} \right] \frac{(T_{b\text{Max}} - T_{b\text{Min}})}{k} = \lambda_0^+, \quad (4.28)$$

we can solve for k to find out the effect of k on the necessary condition (4.16). Namely, for condition (4.16) to hold, the following inequality must be fulfilled:

$$k \geq \left[(\Psi_{\text{Max}} + T_{b\text{Max}}) - \frac{(T_{b\text{Max}} - T_{b\text{Min}})}{2} \right] \frac{(T_{bMax} - T_{b\text{Min}})}{\lambda_0^+ - \lambda_{\text{Max}}}. \quad (4.29)$$

Equation 4.29 shows that it is possible to obtain a periodic behaviour in the wheel slip also with a low value of k by simply lowering the threshold $T_b = T_{b\text{Min}}$. In so doing, when the system switches from $q = 1$ to $q = 2$ the necessary condition (4.16) holds and the limit cycle is induced on the wheel slip. In fact, a lower value of k means that the curvature of the vector field will be larger, and thus $\lambda(t)$ will reach values that grow larger than λ_{Max} as k decreases. However, by lowering the value $T_{b\text{Min}}$ one may allow the system trajectory to switch to $q = 2$ when condition (4.16) holds. As a matter of fact, if the value of $T_{b\text{Min}}$ is low enough so that no intersections exist between Σ_2 and $\Psi(\lambda)$ other than λ_1, then condition (4.16) does not apply, and the trajectories – when hitting Σ_2 – will certainly evolve toward lower values of λ (see again Figure 4.1(b)).

The same kind of reasoning can be applied to see the effect of k in enforcing the condition that $(T_{b\text{Max}}, \lambda_{\text{Max}})$ belongs to the limit cycle. In this case, one needs to find a bound on the closed-loop system dynamics associated to the discrete state $q = 0$. Note that, in this case, the time instant that defines the switching we are interested in is

$$\bar{t} : T_b = T_{b\text{Min}} + k\,t = T_{b\text{Max}} \to \bar{t} = \frac{T_{b\text{Max}} - T_{b\text{Min}}}{k} > 0.$$

A simple computation in this case (note that now $\lambda(0) = \lambda_{Min}$) yields

$$\lambda(t) \leq \lambda_{\text{Min}} + \left[(\Psi_{\text{Max}} + T_{b\text{Max}}) + \frac{(T_{b\text{Max}} - T_{b\text{Min}})}{2} \right] \frac{(T_{b\text{Max}} - T_{b\text{Min}})}{k}. \quad (4.30)$$

Hence, to guarantee that $(T_{b\mathrm{Max}}, \lambda_{\mathrm{Max}})$ belongs to the limit cycle one needs

$$k \geq \left[(\Psi_{\mathrm{Max}} + T_{b\mathrm{Max}}) + \frac{(T_{b\mathrm{Max}} - T_{b\mathrm{Min}})}{2} \right] \frac{(T_{b\mathrm{Max}} - T_{b\mathrm{Min}})}{\lambda_{\mathrm{Max}} - \lambda_{\mathrm{Min}}}. \tag{4.31}$$

If, for a fixed value of k, one wants to ensure that $(T_{b\mathrm{Max}}, \lambda_{\mathrm{Max}})$ belongs to the limit cycle then Equation 4.31 shows that it suffices to choose a smaller value for the threshold $T_b = T_{b\mathrm{Max}}$ — taking care that this satisfies $\Sigma_0 \cap \Psi(\lambda) = \emptyset$ — so that, when the switching manifold Σ_0 is hit, $\bar{\lambda} \leq \lambda_{\mathrm{Max}}$.

4.6 Summary of the Actuators' Performance

After having presented two different approaches for braking control design, which are based on the two possible classes of braking actuators, it is interesting to show that the two are indeed deeply linked to each other.

As a matter of fact, the control logic that we have just discussed for the case of discrete actuator dynamics is based on the thresholds on the wheel slip and braking torque, which define a *box* in the state space of the closed-loop system.

It is clear, then, that if we let the box shrink — in the limit to a single point — then we are practically achieving the regulation of the wheel slip to a fixed set-point value, which is exactly what we did in Section 3.1 to design the slip controller based on continuous actuator dynamics.

To see this, refer to Figure 4.10(a) and Figure 4.10(b), which show the closed-loop trajectory and the time histories of the wheel slip and of the braking torque in a simulation carried out on dry asphalt, with threshold values $T_{b\mathrm{Min}} = 790$ Nm, $T_{b\mathrm{Max}} = 810$ Nm, $\lambda_{\mathrm{Min}} = 0.14$, $\lambda_{\mathrm{Max}} = 0.145$ and $k = 5$ kNm/s. These results show that, indeed, the obtained closed-loop behaviour resembles that achieved *via* regulation of the wheel slip at a constant value.

From the technological point of view, the possibility of reducing the box size implies the ability of the braking system to switch between the three possible actions assumed in the discrete case, *i.e.*, increase, hold and decrease, fast enough to allow the switching to take place. Should such an assumption be fulfilled, then one may say that the discrete braking actuator can in fact be modulated in a pulse-width-modulation (PWM) fashion and can therefore be regarded as a continuous actuator for control purposes.

This shows the link between the two technologies considered in this book, which constitute the two limiting situations in which one can operate. In practice, each braking system will have to be analysed in order to select the best control approach based on its dynamic characteristic and on the final performance levels that are expected for the considered application.

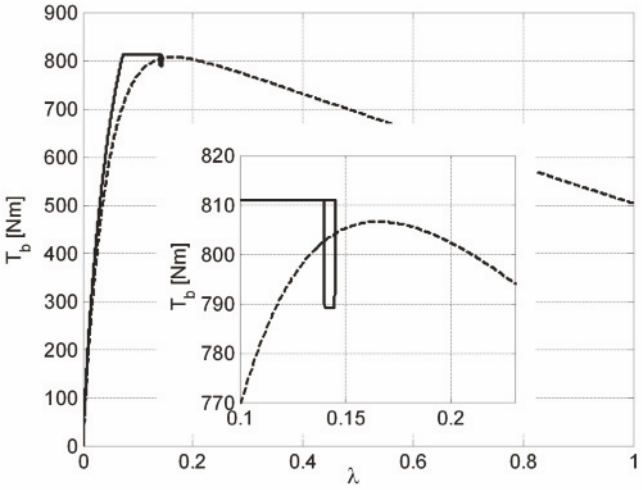

(a)

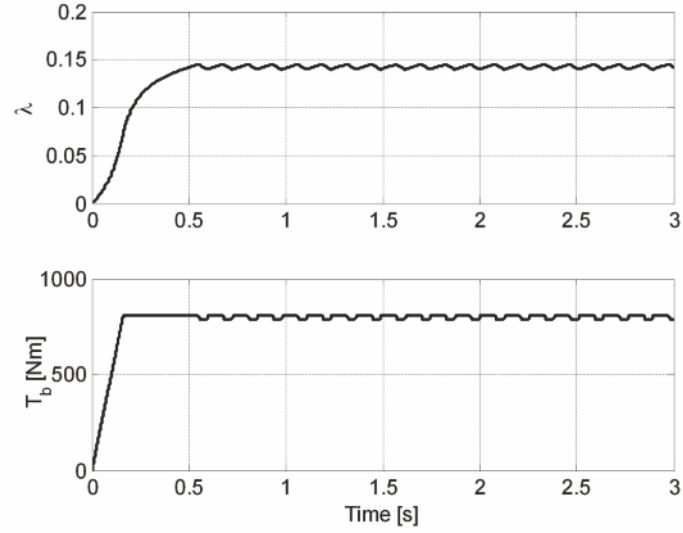

(b)

Figure 4.10 Closed-loop trajectory (a) and time histories of wheel slip and braking toque (b) of system (4.1) with the given control logic with threshold values $T_{b\mathrm{Min}} = 790$ Nm, $T_{b\mathrm{Max}} = 810$ Nm, $\lambda_{\mathrm{Min}} = 0.14$, $\lambda_{\mathrm{Max}} = 0.145$ and $k = 5$ kNm/s

4.7 Summary

This chapter discussed in detail how to cope with an actuator with discrete dynamics for the design of ABS systems. Specifically, the existence and asymptotic stability of a limit cycle induced by an appropriate braking controller was studied. Based on a detailed analysis of the state plane trajectories of the braking dynamics we have given necessary conditions for the limit cycle existence. Moreover, we have proved the limit cycle existence by showing that the related BVP admits a solution and assessed its asymptotic stability properties *via* Poincaré map analysis. For a more detailed presentation of the robustness properties of the proposed controller, in the face of both measurement errors and variations in the tyre–road conditions, the interested reader is referred to [112].

In the scientific literature, some results on the study of the wheel slip dynamics based on nonlinear dynamics' theoretical tools can be found in [67] and [68]; in these works, though, the analysis concentrated on vehicle traction and braking dynamics and was not related to any particular controller architecture. Other works focused on the study of rule-based ABS systems are [26,49,70,74], each of which considers a different number of discrete states in the ABS controller. In particular, in [49] an ABS controller with four discrete states is studied, and switching between the different states is governed by wheel deceleration thresholds and the elapsed time intervals spent in the different states. The structure of the hybrid controller in [49] is similar to that discussed in this chapter, even if it is based on a simplified tyre–road model, which is a piecewise linear approximation of the one considered herein. The tuning of the threshold values is made by analysing the quarter car dynamics, even if no formal existence and stability analysis of the closed-loop trajectories are given. Recently, [74] presented a five-state controller, where the threshold values are based on wheel deceleration, and the stability analysis was performed *via* Poincaré maps and notions from hybrid systems theory. From the industrial viewpoint, rule-based ABS were introduced on commercial cars by Bosch [87] and a qualitative description of such algorithms is provided in [45].

Chapter 5
Longitudinal Wheel Slip Estimation

5.1 Introduction

As has become clear in the previous chapters of this book, the problem of estimating the longitudinal wheel slip is crucial for an effective design of ABS, TCS and ESC control systems, especially in the case when the control problem is formulated as the regulation of the wheel slip itself.

To obtain an accurate estimate of the longitudinal wheel slip one first of all needs to correctly process the wheel speed sensor measurements in order to obtain an estimate of the wheel speed. This topic is discussed in detail in Appendix B, where the two main algorithms employed for this task are discussed and their advantages and disadvantages outlined.

Further, according to the wheel slip definition, see Equation 2.3, one needs to estimate the longitudinal vehicle speed. In fact, this variable can be directly measured only by means of optical sensors, which are expensive and fragile and hence used only for prototyping purposes.

The crucial difference in setting up a speed estimation algorithm for ABS and TCS control systems is that in the former case all wheels are in general subject to braking torque (and thus to a non-zero wheel slip), whereas in the latter only the driving wheels transmit the traction torque to the ground, and thus two of the wheel speeds in fact evolve in almost free rolling (thus with no – or with negligible – wheel slip) and can hence be used estimate the vehicle speed.

This is also true for braking systems for two-wheeled vehicles where only the front wheel brake is used. In this case, the rear wheel speed provides a reasonable estimate of the vehicle speed.

Thus, the availability or lack of free rolling wheels makes a crucial difference in the speed estimation problem.

To demonstrate the need for a reliable estimate of the vehicle speed during braking, this chapter studies first the interaction between speed estimation and braking control, showing that feeding a slip controller with a coarse esti-

mation of the controlled variable can substantially alter its dynamic properties. Specifically, we analyse what happens to the closed-loop system stability properties when one controls the wheel slip of a vehicle using the simple *fastest wheel* algorithm to estimate the vehicle speed, that is by using as estimate – at each time instant – the speed of the wheel with the lowest slip. This analysis, carried out based on the double-corner model, reveals that such a coarse estimation coupled with a slip controller can lead to closed-loop instability, thus confirming the need of an accurate estimation algorithm. The results obtained suggest that the slip controller and the speed estimation algorithm – which might be developed separately and by different teams in current practice – should be carefully designed through a coordinated effort.

Based on this, a data-based approach to the estimation problem in the ABS case is provided, yielding an algorithm for vehicle speed estimation, which is based only on the four wheel rotational speeds and longitudinal vehicle acceleration measurements. Four wheel encoders and a one-axis accelerometer, in fact, are standard sensors on cars equipped with modern ABS control systems.

5.2 Interaction Between Braking Control and Speed Estimation

The discussion provided in Chapter 3 has shown that under perfect speed knowledge a slip controller can be designed, which guarantees the existence of a unique equilibrium that is locally asymptotically stable for all choices of the set-point at the front and rear wheels and for all road conditions, both for the single-corner and for the double-corner models.

Consider now the case when the vehicle speed is estimated as the fastest wheel speed. Even though this estimation may appear quite crude, it is in fact still used in practice, as it does not need any additional sensor to the wheel encoders.

Formally, considering the double-corner model the vehicle speed is estimated as

$$\hat{v} = \max\{\omega_f, \omega_r\} r. \tag{5.1}$$

Correspondingly, given the definition of the wheel slip in Equation 2.5, the estimate of the front wheel slip $\hat{\lambda}_f$ has the form

$$\begin{aligned} \hat{\lambda}_f &= 1 - \frac{\omega_f}{\omega_f} = 0 && \text{if } \omega_f \geq \omega_r \Leftrightarrow \lambda_f \leq \lambda_r, \\ \hat{\lambda}_f &= 1 - \frac{\omega_f}{\omega_r} = \frac{\lambda_f - \lambda_r}{1 - \lambda_r} && \text{if } \omega_f < \omega_r \Leftrightarrow \lambda_f > \lambda_r. \end{aligned} \tag{5.2}$$

Analogous expressions hold for the rear slip estimate $\hat{\lambda}_r$.

Based on the double-corner model (2.56), we now show that when a slip controller is fed by the vehicle speed estimate (5.1) stability is lost. To concentrate on the core of the problem and to provide insightful results, for analysis purposes a simple proportional feedback controller is considered. Needless to say, the performance of proportional controllers can be improved by higher-order control architectures, but the basic results and conclusions remain unchanged. Once again, we assume that the dependence of $\Psi_f(\lambda_f, \lambda_r)$ from λ_r can be neglected and adopt the notation $\Psi_f(\lambda_f)$.

As shown in Proposition 3.1 (see Section 3.8.1), in the case of perfect knowledge of the vehicle speed v, the closed-loop system equilibrium can be stabilised by a proportional controller, provided that the controller gains are chosen to be large enough.

Recall that in the case where an error-free measure of the controlled variables λ_i, $i = \{r, f\}$ is available letting

$$\begin{aligned} T_{b_f} &= k_f(\overline{\lambda}_f - \lambda_f), \\ T_{b_r} &= k_r(\overline{\lambda}_r - \lambda_r), \end{aligned} \tag{5.3}$$

where $\overline{\lambda}_f$ and $\overline{\lambda}_r$ are the set-point values for the front and rear wheel slip, respectively, and k_f, k_r are the positive controller gains, the closed-loop dynamics become

$$\begin{aligned} \dot{\lambda}_f &= -\frac{r}{Jv}\left[\Psi_f(\lambda_f) - k_f(\overline{\lambda}_f - \lambda_f)\right], \\ \dot{\lambda}_r &= -\frac{r}{Jv}\left[\Psi_r(\lambda_f, \lambda_r) - k_r(\overline{\lambda}_r - \lambda_r)\right]. \end{aligned} \tag{5.4}$$

For the closed-loop system (5.4), fixing the set-point values to $\overline{\lambda}_f, \overline{\lambda}_r \in (0, 1)$, and letting $(\tilde{\lambda}_f, \tilde{\lambda}_r)$ be an equilibrium of system (5.4) associated with $\overline{\lambda}_f, \overline{\lambda}_r$, one has the following equilibrium condition:

$$\begin{cases} \Psi_f(\tilde{\lambda}_f) = k_f(\overline{\lambda}_f - \tilde{\lambda}_f) \\ \Psi_r(\tilde{\lambda}_f, \tilde{\lambda}_r) = k_r(\overline{\lambda}_r - \tilde{\lambda}_r). \end{cases} \tag{5.5}$$

Now, if the proportional controller (5.3) is used with λ_i replaced by $\hat{\lambda}_i$ $i = \{f, r\}$ computed as in (5.2), the closed-loop system dynamics are still continuous but have two different expressions according to the region of the state space within which the system state is at any time instant, determined according to the wheel that is currently used to estimate the vehicle speed.

Specifically, the system dynamics have the following form.

Region I ($\lambda_f \leq \lambda_r$)**:**

$$\dot{\lambda}_f = -\frac{r}{Jv}\left(\Psi_f(\lambda_f) - k_f\overline{\lambda}_f\right), \tag{5.6}$$

$$\dot{\lambda}_r = -\frac{r}{Jv}\left(\Psi_r(\lambda_f, \lambda_r) - k_r\left[\overline{\lambda}_r - \frac{\lambda_r - \lambda_f}{1-\lambda_f}\right]\right).$$

Region II ($\lambda_f > \lambda_r$)**:**

$$\begin{aligned}\dot{\lambda}_f &= -\frac{r}{Jv}\left(\Psi_f(\lambda_f) - k_f\left[\overline{\lambda}_f - \frac{\lambda_f - \lambda_r}{1-\lambda_r}\right]\right),\\ \dot{\lambda}_r &= -\frac{r}{Jv}\left(\Psi_r(\lambda_f, \lambda_r) - k_r\overline{\lambda}_r\right).\end{aligned} \tag{5.7}$$

In the following proposition we analyse the behaviour of the system described by (5.6) and (5.7), when the gains of the wheel slip controller are chosen to be large enough to satisfy the stability condition worked out for the stability of the double-corner model in the case of perfect speed knowledge (see again Proposition 3.1 in Section 3.8.1). This choice is motivated by two different reasons. First of all, the spirit of this analysis is that of showing how the results that one has found assuming perfect knowledge of the vehicle speed coupled with a bad speed estimate can cease to hold. Secondly, this is due to the fact that considering the common set-point values for the application at hand, that is $\overline{\lambda} \in [0.1, 0.25]$, one finds that the values of the the front and rear wheel slip associated with the equilibrium points in (5.5) that correspond to low values of the gains k_f and k_r would be extremely low, and thus unappropriate for safely managing a braking manoeuvre. Thus, the only situation of potentially practical interest is that investigated in the next proposition.

Proposition 5.1. *Consider the closed-loop system described by* (5.6) *and* (5.7) *with* $k_f > \max_{\lambda_f} \Psi_f(\lambda_f)$ *and* $k_r > \max_{\lambda_f,\lambda_r} \Psi_r(\lambda_f, \lambda_r)$*. Then, there exist set-point values* $\overline{\lambda}_i \in (0,1), i = \{r, f\}$ *such that, for all initial conditions* $\lambda_f(0)$*,* $\lambda_r(0) \in (0,1)$ *the wheels lock, that is* $\lambda_i \to 1\,, i = \{r, f\}$*.*

Proof. Given the bounds on the controller gains, we can choose $\overline{\lambda}_i \in (0,1), i = \{r, f\}$ so as to satisfy

$$\begin{aligned}&\Psi_f(\lambda_f) - k_f\overline{\lambda}_f < 0,\ \forall\lambda_f,\\ &\Psi_r(\lambda_f, \lambda_r) - k_r\overline{\lambda}_r < 0,\ \forall\lambda_f, \lambda_r.\end{aligned} \tag{5.8}$$

In the closed-loop system evolution, three different situations may occur.

1. The state of the system remains in Region I from some time $\bar{t} \geq 0$ on, *i.e.*, $\lambda_f(t) \leq \lambda_r(t)$, $t \geq \bar{t}$.
2. The state of the system remains in Region II from some time $\bar{t} \geq 0$ on, *i.e.*, $\lambda_f(t) > \lambda_r(t)$, $t \geq \bar{t}$.
3. The state of the system keeps switching between Region I and Region II.

Let us start considering case 1. By the first equations in (5.6) and (5.8), within Region I, we have both $\dot{\lambda}_f > 0$ and $\lambda_r > \lambda_f$. Thus, as time grows,

$\lambda_f \to 1$, so that the front wheel locks and, as $\lambda_r > \lambda_f$, also $\lambda_r \to 1$. The same reasoning applies to case 2.

As for case 3, we shall prove by contradiction that it cannot actually occur. For this purpose, we start by observing that the time derivative of $\Delta\lambda = \lambda_f - \lambda_r$ for $\lambda_f = \lambda_r = \lambda$ is given by

$$\dot{\Delta\lambda} = -\frac{r}{Jv}\Big[r(W_f - W_r - 2\Delta_{F_z}\dot{v})\mu(\lambda) - k_f\overline{\lambda}_f + k_r\overline{\lambda}_r\Big], \tag{5.9}$$

which is obtained based on (5.6) and the definitions of $\Psi_f(\cdot)$ and $\Psi_r(\cdot,\cdot)$ given in (2.26) and (2.27). Thus, on the boundary between Region I and Region II, $\dot{\Delta\lambda}$ is zero for those values of $\lambda_f = \lambda_r = \lambda$ satisfying the equation

$$\mu(\lambda) = \frac{k_f\overline{\lambda}_f - k_r\overline{\lambda}_r}{r(W_f - W_r - 2\Delta_{F_z}\dot{v})}.$$

Recalling the expression for $\mu(\cdot)$ in (2.13), we then have that there is a single value, say $\overline{\lambda}$, such that $\dot{\Delta\lambda}(t) = 0$ when $\lambda_f(t) = \lambda_r(t) = \overline{\lambda}$.

Assume now by contradiction that there exists a sequence of time instants $\{t_k\}_{k\geq 0}$, with $t_{k+1} > t_k \geq 0$, $k \geq 0$, such that $\lambda_f(t) > \lambda_r(t)$, $t \in (t_{2h}, t_{2h+1})$, and $\lambda_f(t) \leq \lambda_r(t)$, $t \in (t_{2h+1}, t_{2h+2})$ with $h \geq 0$, that is a sequence of time instants at each of which successive switchings between Region I and Region II occur. Set $\lambda_k := \lambda_f(t_k) = \lambda_r(t_k)$. We next show that from this assumption it follows that

$$\lambda_{k+1} > \lambda_k,\ k \geq 0. \tag{5.10}$$

Note that (5.10) implies that there exists a sequence $\{\lambda_k\}$ of increasing values of λ such that $\dot{\Delta\lambda}$ in (5.9) keeps changing sign. Because of the continuity of $\dot{\Delta\lambda}$ as a function of λ, this contradicts the fact that $\dot{\Delta\lambda} = 0$ on a single point ($\lambda_f = \lambda_r = \breve{\lambda}$) of the boundary between Region I and Region II, thus concluding the proof of the proposition.

As a matter of fact, for the state to commute at time t_{2h} from Region I where $\lambda_f - \lambda_r \leq 0$ to Region II where $\lambda_f - \lambda_r > 0$, it should hold that $\lambda_f(t_{2h}) = \lambda_r(t_{2h}) = \lambda_{2h}$ and $\dot{\Delta\lambda}(t_{2h}) > 0$. By a similar reasoning, it is easily seen that for the state to commute at time $t_{2h+1} > t_{2h}$ back from Region II to Region I, $\lambda_f(t_{2h+1}) = \lambda_r(t_{2h+1}) = \lambda_{2h+1}$ and $\dot{\Delta\lambda}(t_{2h+1}) \leq 0$. Thus, $\lambda_{2h+1} \neq \lambda_{2h}$ because of the different sign of $\dot{\Delta\lambda}$ on the boundary at $\lambda_f = \lambda_r = \lambda_{2h}$ and $\lambda_f = \lambda_r = \lambda_{2h+1}$. Moreover, we know that $\lambda_{2h+1} \geq \lambda_{2h}$, since we have $\dot{\lambda}_f > 0$ within Region I, $\dot{\lambda}_r > 0$ within Region II, and both $\dot{\lambda}_f > 0$ and $\dot{\lambda}_r > 0$ on the boundary between Region I and Region II (this is a consequence of (5.8) and of the continuity of the vector field (5.6) and (5.7)).

Thus, from $\lambda_{2h+1} \geq \lambda_{2h}$ and $\lambda_{2h+1} \neq \lambda_{2h}$, it follows that $\lambda_{2h+1} > \lambda_{2h}$. In a perfectly analogous way it can be shown that $\lambda_{2h+2} > \lambda_{2h+1}$, so that (5.10) is finally proved and hence the thesis follows.

□

5.3 A Solution for Vehicle Speed Estimation

The problem of vehicle speed estimation with four-wheeled vehicles has traditionally been tackled by pursuing three different kinds of approaches: devising algorithms based on intuitive procedures linked to the physics of the considered problem (a basic example of these is the fastest wheel speed discussed in the previous section), setting up genuine black-box approaches based on input/output data and stating model-based filtering problems solved *via* classical identification techniques and observer design methods (see Section 5.5 for a list of references and a brief description of the different existing approaches).

The rest of the section illustrates a solution to the vehicle speed estimation problem coming from the first family of algorithms described above, which offers a more accurate and refined solution than the fastest wheel speed but retains the intuitive nature of that approach. The estimation algorithm allows highlighting some of the data processing problems involved in the considered application which are almost independent of the chosen estimation approach; further, it is easy to implement on board of commercial ECUs, it makes use of standard sensors only (four wheel encoders and a longitudinal accelerometer) and it represents a good compromise between estimation accuracy, computational complexity and physical insight.

The main idea of the algorithm is to estimate the vehicle speed differently according to the current vehicle status, so as to account for the different motion conditions. Specifically, the *status* of the vehicle is represented by a four-valued variable $S(t)$, which is used to model the condition in which the vehicle speed is very low, the acceleration condition, the constant or soft braking condition and, finally, the strong braking condition.

Once the vehicle status has been reconstructed from the measured signals *via* appropriate data processing, the estimated vehicle speed is computed based on the following observations: when the vehicle has very low or constant speed, the estimated vehicle speed can be obtained as the average of the four wheel speeds, as basically the slip is equal to zero for all wheels. When the car accelerates, instead, as the driving wheels have a non-null longitudinal slip due to traction force, the estimated vehicle speed must be obtained as the average of the non-driving wheels. Not surprisingly, the braking condition is the most critical, and it requires an appropriate integration procedure of the accelerometer signal. In the following, the computation of the vehicle status and the speed estimation in each of the four cases outlined above will be formally specified.

Overall, the estimation approach is composed of the following:

Input (Measured) Signals

- $v_i(t)$, $i = 1, \ldots, 4$: four wheel linear speeds at the tyre–road contact point; and
- $a_x(t)$: longitudinal vehicle acceleration.

All the signals are assumed to derive from measurements coming from properly calibrated sensors. For a thorough discussion on wheel encoder processing the reader is referred to Appendix B. The accelerometer needs to be calibrated by adjusting the sensor gain and removing the offset.

Input (Internally Computed) Signals
At each sampling instant, the following auxiliary signals are computed:

- $\bar{v}(t) = \frac{1}{4}\sum_{i=1}^{4} v_i(t)$: average of the four wheel speeds;
- $\bar{v}_{\mathrm{ND}}(t) = \frac{1}{2}\sum_{i=1}^{2} v_i(t)$: average of the two non-driving wheel speeds; and
- $a_{x\mathrm{FIL}}(t) = F(z)a_x(t)$: filtered version of the longitudinal acceleration – the filter $F(z)$ is a digital FIR low pass filter.

Output Signal

- $\hat{v}_x$: estimated longitudinal vehicle speed.

Estimation Algorithm

The algorithm behaviour changes according to the *status* of the vehicle, which is represented by the four-valued variable $S(t)$. Specifically:

- $S(t) = -2$ means that the vehicle speed is very low;
- $S(t) = -1$ means that the vehicle is accelerating;
- $S(t) = 0$ means that the vehicle has constant speed or is softly braking; and
- $S(t) = 1$ means that the vehicle is braking.

The vehicle status $S(t)$ is computed as follows:
$S(t) = -2$ if

$$\begin{cases} S(t-1) = -2 \quad \text{AND} \quad \bar{v}(t) \leq v_{\mathrm{Min}} + h_v \\ \text{OR} \\ S(t-1) \neq -2 \quad \text{AND} \quad \bar{v}(t) \leq v_{\mathrm{Min}}. \end{cases}$$

$S(t) = -1$ if

$$\begin{cases} S(t-1) = -2 \quad \text{AND} \quad (a_{x\mathrm{FIL}}(t) \geq \delta \quad \text{AND} \quad \bar{v}(t) > v_{\mathrm{Min}} + h_v) \\ \text{OR} \\ S(t-1) \neq -2 \quad \text{AND} \quad (a_{x\mathrm{FIL}}(t) \geq \delta \quad \text{AND} \quad \bar{v}(t) > v_{\mathrm{Min}})\,. \end{cases}$$

$S(t) = 0$ if

$$\begin{cases} S(t-1) = -2 \quad \text{AND} \quad (-\beta \leq a_{x\mathrm{FIL}}(t) < \delta \quad \text{AND} \quad \bar{v}(t) > v_{\mathrm{Min}} + h_v) \\ \text{OR} \\ S(t-1) = 1 \quad \text{AND} \quad (-\beta + h_a \leq a_{x\mathrm{FIL}}(t) < \delta \quad \text{AND} \quad \bar{v}(t) > v_{\mathrm{Min}}) \\ \text{OR} \\ S(t-1) = \{0, -1\} \quad \text{AND} \quad (-\beta \leq a_{x\mathrm{FIL}}(t) < \delta \quad \text{AND} \quad \bar{v}(t) > v_{\mathrm{Min}}.) \end{cases}$$

$S(t) = 1$ if

$$\begin{cases} S(t-1) = -2 \quad \text{AND} \quad (a_{x\text{FIL}}(t) < -\beta \quad \text{AND} \quad \bar{v}(t) > v_{\text{Min}} + h_v) \\ \text{OR} \\ S(t-1) = 1 \quad \text{AND} \quad (a_{x\text{FIL}}(t) < -\beta + h_a \quad \text{AND} \quad \bar{v}(t) > v_{\text{Min}}) \\ \text{OR} \\ S(t-1) = \{0, -1\} \quad \text{AND} \, (a_{x\text{FIL}}(t) < -\beta \quad \text{AND} \quad \bar{v}(t) > v_{\text{Min}}) \, . \end{cases}$$

The longitudinal vehicle speed is estimated as follows:

$$\begin{aligned} &\text{if} \quad S(t) = -2 \text{ OR } S(t) = 0 \rightarrow \hat{v}_x(t) = \bar{v}(t), \\ &\text{if} \quad S(t) = -1 \rightarrow \hat{v}_x(t) = \bar{v}_{\text{ND}}(t), \\ &\text{if} \quad S(t) = 1, \end{aligned}$$

$$\hat{v}_x(t) = \hat{v}_x(t-1) + a_x(t)T, \quad \forall t \geq \bar{t}, \tag{5.11}$$

where T is the sampling time, $\bar{t}$ is such that $S(\bar{t} - 1) = 0$ and $S(t) = 1$ for $t \geq \bar{t}$ and

$$\hat{v}_x(\bar{t} - 1) = \hat{v}_x(\bar{t} - 2) + a_x(\bar{t} - 1)T, \quad \forall t \in [\bar{t} - M + 1, \bar{t}), \tag{5.12}$$

with $\hat{v}_x(\bar{t} - M) = \bar{v}(\bar{t} - M)$.

Comments and Additional Aspects

It is worth noting that as the braking condition is the most critical, since all four wheels are slipping, the speed estimation is carried out *via* an *open-loop* integration procedure of the accelerometer signal, augmented with a backward integration phase, see Equation 5.12, to cope with initialisation errors due to a delayed detection of the braking condition caused by the use of a filtered acceleration signal.

However, one must filter the longitudinal acceleration for computing the vehicle status due to the need of preventing chattering between different states due to the measurement noise affecting the signal $a_x(t)$. Therefore, the rationale behind the backward integration phase is as follows: it is assumed that $\bar{t}$ is the last time instant when a switch of the vehicle status $S(t)$ took place from 0 to 1 (which is the natural transition from soft to strong braking), namely that $S(\bar{t} - 1) = 0$ and $S(t) = 1$, $t = \bar{t}, \bar{t} + 1, \bar{t} + 2, \ldots$ In this phase the speed estimation $\hat{v}_x(t)$ is computed according to the discrete time integration of the vehicle acceleration given in Equation 5.11. This integration rule, however, is itself recursive, and it must be initialised at $t = \bar{t}$. Even if a natural initialisation could in principle be given by

$$\hat{v}_x(\bar{t} - 1) = \bar{v}(\bar{t} - 1),$$

under the assumption that $S(\bar{t} - 1) = 0$, such a choice would lead to an error due to the delay in the identification of the braking phase introduced both

by the use of thresholds to detect the braking phase itself and by the use of the filtered version of the vehicle acceleration for determining the vehicle current status. Accordingly, for the initialization of the recursion (5.11), the additional vehicle integration given in Equation 5.12 is used, which is back-propagated for M samples up to the time instant $\bar{t} - M + 1$, assuming that $\hat{v}_x(\bar{t} - M) = \bar{v}(\bar{t} - M)$.

For a correct operation of the algorithm, the different parameters need to be correctly tuned, and this has to be done based on the analysis of the measured data. Specifically, β is the threshold set on the filtered version of the vehicle deceleration $a_{x\mathrm{FIL}}(t)$ for identifying a braking manoeuvre. The constants v_{Min} and δ are thresholds – to be properly tuned according to the specific vehicle characteristics – to detect the low speed status and the acceleration status, respectively. The additional hysteresis thresholds on the acceleration h_a and on the wheel speed h_v were introduced to avoid chattering phenomena.

In the above description of the algorithm, all input signals are assumed to be correct and available at each sampling instant. A deployable implementation should take care of, for instance, outliers detection and removal. To this purpose, when the four wheel signals are obtained as inputs, an *a posteriori* check of $\bar{v}(t)$ (and $\bar{v}_{\mathrm{ND}}(t)$) is performed. To avoid an outlier wheel measurement, the four wheel speeds $v_i(t)$ are re-checked immediately after $\bar{v}(t)$ is computed as follows:

$$\frac{|\bar{v}(t) - v_i(t)|}{|\bar{v}(t)|} < e_r, \tag{5.13}$$

where the value of the threshold e_r is to be defined according to the noise level in the wheel speed measurements and to the application-specific safety requirements. If one – or more – wheel speeds do not pass this consistency test they are discarded, and $\bar{v}(t)$ is re-computed as the average of the reduced set of wheel speeds.

Another issue to be considered when deploying a final version of the algorithm is the inclusion of a feasibility check of the output provided during the open-loop integration phase. To guarantee the estimation convergence, one may notice that during braking phases (*i.e.*, when the algorithm relies on the open-loop integration of the accelerometer signal), the estimated speed must be monotonically decreasing.

Accordingly, if $S(t) = 1$ and

$$\hat{v}_x(t) - \hat{v}_x(t-1) > e_a, \tag{5.14}$$

e_a being a properly tuned threshold, the algorithm should detect the inconsistency. As a back-up strategy, one may let $\hat{v}_x(t) = \hat{v}_x(t-1)$ – if the vehicle deceleration rate has kept nearly constant in the last few samples – or let $\hat{v}_x(t)$ be a scaled version of the current fastest wheel speed, with the scaling

factor that can be made proportional to the current vehicle deceleration, so as to account for the fact that the wheel slip in general increases with the deceleration.

Table 5.1 Parameters employed in estimation algorithm implementation

Parameter	Value	Meaning
T_s	5ms	Sampling time
v_{Min}	2.5 m/s	Speed threshold to identify the low speed status $S = -2$
δ	0.1 m/s^2	Acceleration threshold to identify the acceleration status $S = -1$
β	0.8 m/s^2	Acceleration threshold to identify the braking status $S = 1$
h_v	0.2 m/s	Hysteresis on the speed threshold v_{Min} to avoid chattering between different states
h_a	0.1 m/s^2	Hysteresis on the acceleration threshold β to avoid chattering between different states
M	50 samples	Back-propagation window length
e_r	0.05	Speed threshold for the outlier check (5.13)
e_a	0.3 m/s	Speed threshold for the consistency check (5.14)

5.4 Performance Evaluation of the Estimation Algorithm

To investigate the results that can be obtained *via* the estimation algorithm described in the previous section, some experimental results are now discussed. The test drives used for collecting the experimental data on the basis of which the following results were carried out on two different road conditions, *i.e.*, a high-grip asphalt road and a low-grip gravel road. All the braking manoeuvres took place in a straight line.

The algorithm performance is tested against the fastest wheel algorithm, which estimates the vehicle speed as in (5.1), *i.e.*, selecting the wheel with the lowest longitudinal slip.

The parameter values used for the algorithm implementation are reported in Table 5.1 where their meaning is also recalled. To evaluate the estimation algorithm performance a one-axis optical sensor for measuring the actual longitudinal vehicle speed $v(t)$ was installed on the test vehicle.

Figures 5.1 and 5.2 show (a few seconds' zoom out of a 2 min test drive) the results of the estimation algorithm on high-grip and low-grip road, respectively. Namely, the figures show both the estimated vehicle speed and the estimated wheel slip, each with the pertaining estimation error. For com-

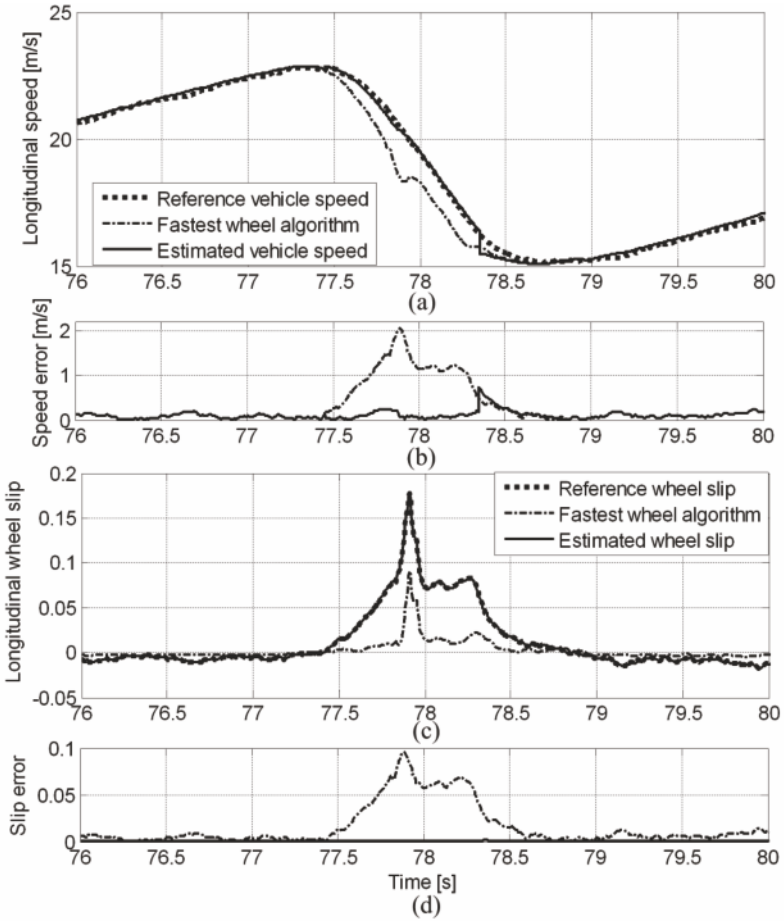

Figure 5.1 Time histories of: (a) vehicle speed, (b) speed estimation error, (c) wheel slip and (d) slip estimation error on a high-grip road. Reference signals (*dotted line*), estimated signals with the proposed algorithm (*solid line*), and estimated signals with the *fastest-wheel* algorithm (*dash-dotted line*)

parison purposes, Figures 5.1 and 5.2 also show the reference vehicle speed and the estimation results obtained *via* the *fastest-wheel* algorithm.

The maximum and the average speed estimation errors, say $e_{v_{\mathrm{Max}}}$ and $e_{v_{\mathrm{Avg}}}$ (these values were computed over the whole 2 min test drive) are very small: $e_{v_{\mathrm{Max}}} = 0.270$ m/s and $e_{v_{\mathrm{Avg}}} = 0.040$ m/s on high-grip asphalt road and $e_{v_{\mathrm{Max}}} = 0.364$ m/s and $e_{v_{\mathrm{Avg}}} = 0.077$ m/s on low-grip off-road. If compared with the simple *fastest-wheel* benchmark, both $e_{v_{\mathrm{Max}}}$ and $e_{v_{\mathrm{Avg}}}$ obtained with the discussed estimation algorithm are about one order of magnitude smaller on both road conditions.

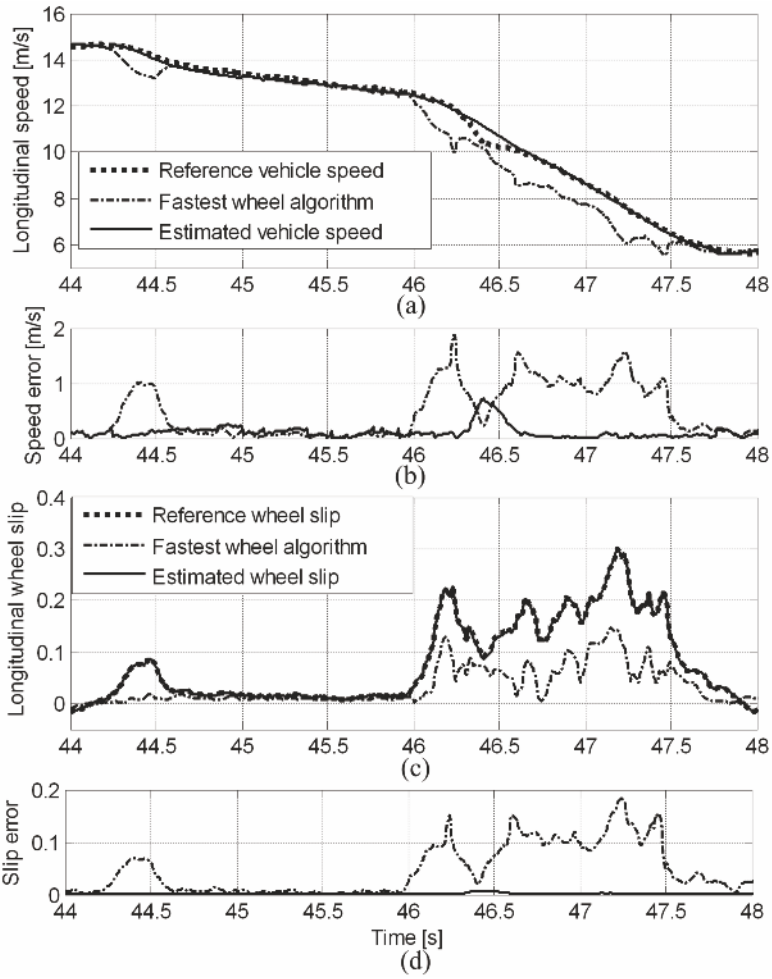

Figure 5.2 Time histories of: (a) vehicle speed, (b) speed estimation error, (c) wheel slip and (d) slip estimation error on a low-grip road: reference signals (*dotted line*), estimated signals with the proposed algorithm (*solid line*), and estimated signals with the *fastest-wheel* algorithm (*dash-dotted line*)

The maximum and average slip estimation errors, say $e_{\lambda\mathrm{Max}}$ and $e_{\lambda\mathrm{Avg}}$, are $e_{\lambda\mathrm{Max}} = 2.48\%$ and $e_{\lambda\mathrm{Avg}} = 0.47\%$ on high-grip road and $e_{\lambda\mathrm{Max}} = 3.55\%$ and $e_{\lambda\mathrm{Avg}} = 0.58\%$ on low-grip road.

Such orders of magnitude can be considered adequate for the estimation algorithm to be used in combination with slip-based ABS/TCS control systems.

5.5 Summary

In this chapter, the problem of wheel slip estimation has been considered. In particular, the interactions between wheel slip estimation and slip control have been investigated, revealing that care must be taken in evaluating the quality of the estimates with respect to the braking controller considered.

A solution to wheel slip estimation has been proposed, describing an algorithm based on the signals coming from wheel encoders and a longitudinal acceleration sensor to estimate the vehicle speed. The algorithm has been described based on four-wheeled vehicle dynamics. The results can be extended also to two-wheeled vehicles, even though the differences in some aspects of the dynamic behaviour might call for some adaptations and modifications of the proposed approach.

As mentioned in Section 5.3, the scientific literature offers several solutions to wheel speed and wheel slip estimation for four-wheeled vehicles. Some of these, such as [37], are based on the assumption that the braking control algorithm is of the type discussed in Chapter 4, thus yielding an oscillatory behaviour of the wheel slip, and the resulting algorithm relies on the detection of the fast alternation of minima and maxima in the wheel speed signal. In [29], an adaptive estimation method for the wheel slip is proposed based on a linear approximation of the tyre–road friction relation and the use of least squares identification techniques. Others approaches are model-based: in [123], the estimation of the vehicle speed is derived from a Kalman filter used in combination with a set of fuzzy rules for dynamically adapting the filter coefficients. Similar approaches are presented in [47, 48, 96], where the fuzzy logic is used to tune the estimator weights by selecting the most reliable measures among the available ones at each time instant. In [85] and [86] a nine-degrees of freedom vehicle model is used, on the basis of which an extended Kalman filter is built to estimate vehicle speed, braking forces, wheel slip and vehicle sideslip angle. Further, [2, 34, 128] propose to estimate the vehicle speed *via* nonlinear observers, possibly combined with a dynamic description of the tyre–road friction based on a Lu–Gre friction model.

Part III
Braking Control Systems Design: Advanced Solutions

This part of the book presents some advanced and research-oriented solutions both to active braking control systems design and to the problem of real-time estimation of tyre–road friction conditions. Specifically, we start by presenting the mixed slip-deceleration control approach, which is an effective control solution based on linearised models of the braking dynamics. Further, we also discuss a nonlinear approach for slip control grounded on Lyapunov-based synthesis methods, which provides significant advantages in terms of closed-loop behaviour. Finally, the problem of estimating the tyre–road friction conditions is considered, and an online estimation method based on linear identification techniques is proposed, together with a method to directly estimate the contact forces from sensors inserted in the tyre itself.

Chapter 6
Mixed Slip and Deceleration Control

6.1 Introduction

As has been discussed in the previous chapters (see in particular Chapter 3), in braking control systems, two output variables are usually considered for regulation purposes: wheel deceleration and wheel slip. Deceleration control and slip control are mostly viewed as alternative strategies; when deceleration and slip are both used, the typical approach is to regulate one variable and to keep the other variable within pre-defined thresholds.

In this chapter a braking control strategy that makes use of both wheel slip and wheel deceleration is presented and analysed. It is based on the idea of designing the braking controller as a classical feedback regulation loop, where the regulated variable is a convex combination of the wheel slip and the wheel deceleration. Accordingly, this control approach is concisely named *mixed slip-deceleration* (MSD) control. MSD is effective and flexible; it inherits all the attractive dynamical features of slip control, while strongly alleviating the detrimental effects of poor slip measurement. Moreover, by simply changing the design parameter that governs the relative weighting between slip and deceleration in forming the convex combination it is possible to emphasise different characteristics of the controller, according to different working conditions.

6.2 Mixed Slip-deceleration Control

The general structure of the proposed MSD control scheme is outlined in Figure 6.1. The transfer functions $G_\eta(s)$ and $G_\lambda(s)$ describing the linearised dynamics between wheel slip and braking torque and normalised wheel deceleration and braking torque, respectively, have been derived in (2.45) and (2.46) and are reported here for completeness

$$G_\eta(s) = \frac{\frac{r}{Jg}\left(s + \frac{\mu_1(\overline{\lambda})F_z}{m\overline{v}}(1-\overline{\lambda})\right)}{s + \frac{\mu_1(\overline{\lambda})F_z}{m\overline{v}}\left((1-\overline{\lambda}) + \frac{mr^2}{J}\right)}, \tag{6.1}$$

$$G_\lambda(s) = \frac{\frac{r}{Jv}}{s + \frac{\mu_1(\overline{\lambda})F_z}{m\overline{v}}\left((1-\overline{\lambda}) + \frac{mr^2}{J}\right)}. \tag{6.2}$$

By inspecting Figure 6.1, it is worth noticing that the noises on the deceleration and slip, d_η and d_λ respectively, are explicitly embedded in the control scheme. As in a classical control scheme, note that d_η and d_λ can represent both measurement noises and external disturbances acting on the system. In the rest of the chapter the notions of disturbance and measurement noise will be treated without explicit distinction. In practice, the emphasis here is on the measurement noise as this is the most critical aspect of slip control, since the accurate measurement of λ is well known to be rather challenging and critical (see Chapter 5).

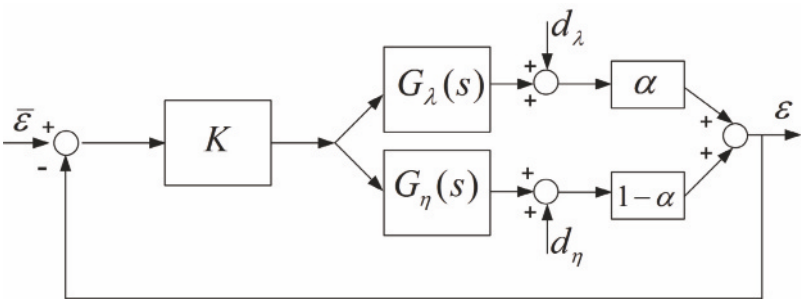

Figure 6.1 General scheme of the MSD controller

The basic idea of MSD control is to define an output controlled variable ε, which is the convex combination of the wheel normalised deceleration η and of the wheel slip λ, namely

$$\varepsilon = \alpha\lambda + (1-\alpha)\eta, \qquad \alpha \in [0,1], \tag{6.3}$$

and to regulate this variable to a set-point constant value $\overline{\varepsilon}$ given by

$$\overline{\varepsilon} = \alpha\overline{\lambda} + (1-\alpha)\overline{\eta}. \tag{6.4}$$

Note that the set-point $\overline{\varepsilon}$ itself can be interpreted as a convex combination of the set-points for wheel slip and wheel deceleration.

As was done in Chapter 3 for the case of wheel slip control, in order to focus on the heart of the control problem and to provide simple and insightful results, for analysis purposes a simple proportional controller is initially considered. Needless to say, the performance of the proportional controller

can be improved by employing a higher-order control architecture, but the basic results and conclusions remain unchanged, as will be shown later in this chapter.

It is interesting to notice that the MSD controller has the distinctive feature of embedding, as *extremal* cases, the slip controller ($\alpha = 1$) and the deceleration controller ($\alpha = 0$), which have been discussed in Sections 3.2 and 3.3. Now, the dynamic properties of the MSD controller will be studied.

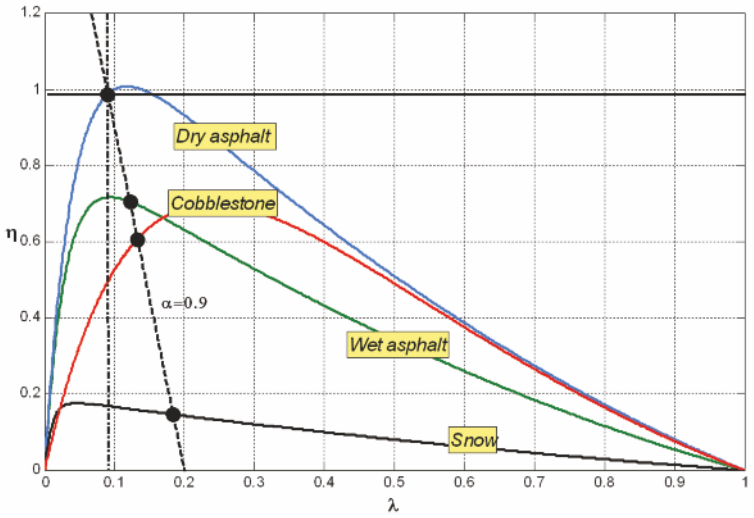

Figure 6.2 Equilibrium points for the MSD control in the (λ, η) plane with $\alpha = 0.9$ and $F_z = mg$

Figure 6.2 shows the equilibrium manifold in the (λ, η) plane given in Equation 2.34 for different road conditions, together with the corresponding graphical interpretation of the set-point $\bar{\varepsilon}$ given in (6.4) for $\alpha = 0.9$. The intersection points between the two curves represent the feasible equilibrium points for the closed-loop system.

By inspecting Figure 6.2 and recalling the expression of the equilibrium manifold for the wheel deceleration η as a function of λ in (2.34) and the expression of the set-point equation $\bar{\varepsilon}$ in (6.4), one may notice that the system equilibria are affected by the following four different factors.

1. The load transfer, represented by the term F_z/mg which is the ratio between the real vertical load F_z and its static value mg (see also Section 2.5). This factor, however, does not affect the qualitative properties of the equilibrium points. In fact, the the steady-state relationship between η and λ has the form

$$\eta(\lambda) = \frac{F_z}{mg}(1 - \lambda)\mu(\lambda).$$

Hence, the dynamic load transfer effect acts in the same way as a scaling factor in the tyre-road friction characteristic.

2. The tyre–road friction condition described by $\mu(\lambda)$, according to which the equilibrium point may vary (see Figure 6.2).
3. The set-point $\overline{\varepsilon}$. A change in the set-point corresponds to a rigid translation of the line $\overline{\varepsilon}(\eta, \lambda)$ (dashed line in Figure 6.2) which changes the equilibrium point and can affect its uniqueness.
4. The coefficient α, which determines the slope of the line $\overline{\varepsilon}(\eta, \lambda)$ in the (λ, η) plane (dashed line in Figure 6.2). This is the distinctive feature of the MSD control approach. In fact, for $\alpha = 1$ (vertical dash-dotted line in Figure 6.2) we have a genuine *slip control*. In this case, for any $\overline{\varepsilon} \in [0, 1]$ there always exists a unique equilibrium for all road conditions. On the other hand, for $\alpha = 0$ (horizontal solid line in Figure 6.2) we have a *deceleration control*; in this case there exist some values of the set-point for which two equilibria exist on some road conditions and none on other road conditions (see also Sections 3.2 and 3.3). For continuity, these two extremal conditions must be separated by a *threshold* (or lower bound) on α, located between 0 and 1, above which the equilibrium uniqueness is guaranteed. It will be shown that a good trade-off between slip and deceleration control is obtained for values of $\alpha \in [0.8, 1]$. Hence, the existence and uniqueness of the equilibrium points are deeply interlaced with the choice of this parameter, as will be further discussed in the following.

6.2.1 Analysis of the Open-loop Dynamics

From the dynamical viewpoint, the open-loop transfer function $G_\varepsilon(s)$ from δT_b to $\delta\varepsilon$ can be computed combining the transfer functions $G_\eta(s)$ and $G_\lambda(s)$ *via* the convex combination defined by (6.3).

Specifically, it has the form

$$\begin{aligned} G_\varepsilon(s) &= \frac{r}{J} \frac{\frac{1-\alpha}{g}\left[s + \frac{\mu_1(\overline{\lambda})F_z}{m\overline{v}}(1-\overline{\lambda})\right] + \frac{\alpha}{\overline{v}}}{s + \frac{\mu_1(\overline{\lambda})F_z}{m\overline{v}}\left((1-\overline{\lambda}) + \frac{mr^2}{J}\right)} \\ &= \frac{(1-\alpha)r}{Jg} \frac{s + \left(\frac{\mu_1(\overline{\lambda})F_z}{m\overline{v}}(1-\overline{\lambda}) + \frac{g}{\overline{v}}\frac{\alpha}{1-\alpha}\right)}{s + \frac{\mu_1(\overline{\lambda})F_z}{m\overline{v}}\left((1-\overline{\lambda}) + \frac{mr^2}{J}\right)}. \end{aligned} \tag{6.5}$$

By analysing (6.5), the stability properties of the linearised system having the braking torque as input and ε as output can be easily studied.

Specifically, note that the linearised single-corner model with transfer function $G_\varepsilon(s)$ is asymptotically stable if and only if

$$\frac{\mu_1(\overline{\lambda})F_z}{m\overline{v}}\left((1-\overline{\lambda})+\frac{mr^2}{J}\right)>0,$$

which, as both summands in the brackets are positive, reduces to $\mu_1(\overline{\lambda})>0$. Hence, $G_\varepsilon(s)$ has a real positive pole if the equilibrium wheel slip value $\overline{\lambda}$ occurs beyond the peak of the curve $\mu(\lambda)$, which is the same result found in Chapter 3 for $G_\lambda(s)$ and $G_\eta(s)$.

Further, it is interesting to investigate the position of the (real) zero of $G_\varepsilon(s)$ as a function of the parameter α. Specifically, the zero of $G_\varepsilon(s)$ is negative if and only if

$$\frac{\mu_1(\overline{\lambda})F_z}{m\overline{v}}(1-\overline{\lambda})+\frac{g}{\overline{v}}\frac{\alpha}{1-\alpha}>0.$$

Thus, if $\mu_1(\overline{\lambda})>0$ the zero is negative for all possible values of $\alpha\in[0,1)$, whereas, if $\mu_1(\overline{\lambda})<0$, to have a negative zero one needs

$$\frac{\alpha}{(1-\alpha)}>-\frac{\mu_1(\overline{\lambda})F_z}{mg}\left(1-\overline{\lambda}\right).$$

Thus, it is always possible to find a value of α, say $\overline{\alpha}$, such that, for $\overline{\alpha}<\alpha<1$, the zero of $G_\varepsilon(s)$ is negative (in practice, $\overline{\alpha}\cong 0.3$ is enough to guarantee this in every road condition and for every value of $\overline{\lambda}$).

6.2.2 Closed-loop Stability for MSD Control

Consider now the MSD closed-loop system shown in Figure 6.1. In this case, the characteristic polynomial $\chi_\varepsilon(s,\alpha)$ is given by

$$\begin{aligned}\chi_\varepsilon(s,\alpha)=&\,s\left[1+\frac{Kr}{Jg}(1-\alpha)\right]\\&+\frac{1}{\overline{v}}\left[\frac{\mu_1(\overline{\lambda})F_z}{m}\left((1-\overline{\lambda})\left(1+\frac{Kr}{Jg}(1-\alpha)\right)+\frac{mr^2}{J}\right)+\alpha\frac{Kr}{J}\right].\end{aligned}$$

Accordingly, the following stability condition can be determined (note that, as was the case also for slip and deceleration control, see Sections 3.2 and 3.3), it does not depend on $\overline{v}$)

$$\frac{\mu_1(\overline{\lambda})F_z}{m}\left((1-\overline{\lambda})\left(1+K\frac{r}{Jg}(1-\alpha)\right)+\frac{mr^2}{J}\right)+K\alpha\frac{r}{J}>0.$$

Note that for a fixed value of $\alpha\in(0,1)$ and for large values of K this condition can be simplified as follows:

$$(1-\alpha)\frac{\mu_1(\overline{\lambda})F_z}{mg}(1-\overline{\lambda})+\alpha>0.$$

From the above condition it can be easily shown that if $\mu_1(\overline{\lambda})>0$ the condition is fulfilled for all feasible values of α, while to ensure closed-loop stability for wheel slip values beyond the peak of the friction curve (*i.e.*, when $\mu_1(\overline{\lambda})<0$), one needs to choose the value of the parameter α such that $\alpha_{\text{Min}}<\alpha\leq 1$, where

$$\alpha_{\text{Min}}=\max_{\overline{\lambda},\vartheta_r}\left\{\frac{\mu_1(\overline{\lambda};\vartheta_r)(\overline{\lambda}-1)\frac{F_z}{mg}}{1+\mu_1(\overline{\lambda};\vartheta_r)(\overline{\lambda}-1)\frac{F_z}{mg}}\right\}. \tag{6.6}$$

If α is fixed based on (6.6) it is always possible to find a value $\overline{K}$ such that, for $K>\overline{K}$, the closed-loop system is asymptotically stable in every working condition (namely for every value of $\overline{\lambda}$ and for every road condition, represented in (6.6) by the parameters ϑ_r which define the different tyre–road friction conditions in the model given in (2.13)).

Given the previous stability results for slip control and deceleration control, condition (6.6) was somehow to be expected; we have seen in Chapter 3 that for $\alpha=1$ (wheel slip control) stability can be always guaranteed, whereas for $\alpha=0$ (wheel deceleration control) it is impossible to find a unique stabilising proportional controller. For continuity, these two extremal conditions must be separated by a *threshold* on α, located between 0 and 1. Expression (6.6) is interesting since it provides, in a simple closed-form, the analytic expression of this threshold α_{Min}.

Note that the lower bound (6.6) is computed as the worst case with respect to both the equilibrium point $\overline{\lambda}$ and the road conditions modelled *via* ϑ_r. In Figure 6.3 the expression

$$\frac{\mu_1(\overline{\lambda};\vartheta_r)(\overline{\lambda}-1)\frac{F_z}{mg}}{1+\mu_1(\overline{\lambda};\vartheta_r)(\overline{\lambda}-1)\frac{F_z}{mg}} \tag{6.7}$$

is displayed, as a function of $\overline{\lambda}$, for different road conditions (it is clipped at zero when $\mu_1(\overline{\lambda})>0$). Figure 6.3 shows that the most demanding conditions as far as the lower bound on α is concerned are given by

- values of $\overline{\lambda}$ beyond the peak of the friction curve; and
- high-grip road conditions.

From Figure 6.3 an estimation of α_{Min} can be derived: $\alpha_{\text{Min}}\cong 0.3$. Note that this value has a simple and intuitive interpretation, similar to that given in Section 3.2 for the minimum controller gain needed to stabilise the closed-loop system with a proportional wheel slip controller.

To see this with reference to the (λ,η) plane, consider that the set-point line $\varepsilon=\overline{\varepsilon}$ in (6.4) can be expressed as a function of η as

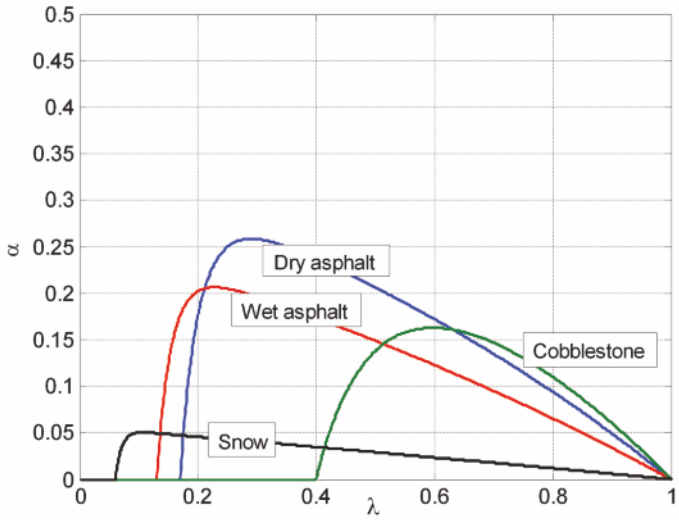

Figure 6.3 Plot of the lower bound on the parameter α in (6.7) as a function of λ, for different road conditions and $F_z = mg$

$$\overline{\eta} = -\frac{\alpha}{1-\alpha}\overline{\lambda} + \frac{1}{1-\alpha}\overline{\varepsilon}. \tag{6.8}$$

Thus, the effect of a proportional controller with gain K can be expressed as a function of η as

$$\overline{\eta} = -K\left[\frac{\alpha}{1-\alpha}\overline{\lambda} + \frac{1}{1-\alpha}\overline{\varepsilon}\right]. \tag{6.9}$$

Hence, the lower bound α_{Min} is the minimum value of α that guarantees that the set-point for the MSD control in (6.8) (see the dashed line in Figure 6.2) has an angular coefficient $-\frac{\alpha}{1-\alpha}$ large enough to ensure that when a proportional controller is used, there exists a minimum value $\overline{K}$ of the gain so that for all $K > \overline{K}$ in the closed-loop system there exists a single equilibrium point. Such an equilibrium is given by the intersection between the equilibrium manifold in the (λ, η) plane and the line in (6.9) and it is locally asymptotically stable for all choices of $\overline{\lambda}$ and for all road conditions.

At the end of this analysis, one can concisely conclude that if $\alpha_{\text{Min}} < \alpha < 1$, MSD control essentially shares the same appealing features as slip control: unique equilibrium, fixed set-point, fixed controller structure. In practice, in order to achieve almost-optimal braking performance with fixed values of α and $\overline{\varepsilon}$, α must be chosen close to 1, as will be clear once the disturbance rejection properties of the MSD controller will be analysed.

A non-negligible advantage of MSD control over slip control is the left half plane zero in the open-loop transfer function (6.5). Note that, more precisely, the advantage of this zero is easy to understand when a linearisation

of the plant dynamics around a locally asymptotically stable equilibrium point is considered. On the other hand, when the considered equilibrium point is unstable, the advantage of this left half plane zero remains, but its explanation is less intuitive.

The major advantage of MSD control, however, is its reduced sensitivity (with respect to slip control) to poor slip measurement. This is a key issue and will be extensively discussed in the following section. It will be shown that while preserving all the appealing features of slip control, MSD control is characterised by superior noise attenuation properties.

6.3 Disturbance Analysis of Slip Control and MSD Control

Consider the general MSD control structure in the block diagram of Figure 6.1. It is easy to see that – in the closed-loop system – the disturbance $d_\varepsilon(\alpha)$ affecting the controlled variable ε is related to the slip and deceleration disturbances d_λ and d_η as follows:

$$D_\varepsilon(s,\alpha) = [\alpha D_\lambda(s) + (1-\alpha)D_\eta(s)]\, S_\varepsilon(s,\alpha),$$

where $D_\varepsilon(s;\alpha)$, $D_\lambda(s)$ and $D_\eta(s)$ are the Laplace-transforms of the signals d_ε, d_λ and d_η, respectively, and $S_\varepsilon(s;\alpha)$ is the closed-loop sensitivity function, given by

$$S_\varepsilon(s;\alpha) = \frac{s + \frac{\mu_1(\overline{\lambda})F_z}{m\overline{v}}\left((1-\overline{\lambda}) + \frac{mr^2}{J}\right)}{s\left[1 + K\frac{r}{Jg}(1-\alpha)\right] + \frac{1}{\overline{v}}\left[\frac{\mu_1(\overline{\lambda})F_z}{m}\left((1-\overline{\lambda})\left(1 + \frac{Kr}{Jg}(1-\alpha)\right) + \frac{mr^2}{J}\right) + K\alpha\frac{r}{J}\right]}. \tag{6.10}$$

We now want to investigate the dependency of the closed-loop disturbance $d_\varepsilon(\alpha)$ on the weighting parameter α. More specifically, we want to analyse the following function:

$$\gamma(\alpha) = \frac{\mathrm{Var}[\mathrm{d}_\varepsilon(\alpha)]}{\mathrm{Var}[\mathrm{d}_\varepsilon(1)]}, \tag{6.11}$$

where $d_\varepsilon(1)$ represents the disturbance in the case of wheel slip control, *i.e.*, for $\alpha = 1$. Thus, $\gamma(\alpha)$ is the ratio between the variance of the disturbance acting on the output variable in MSD control and the that in wheel slip control (note in fact that $\gamma(1) = 1$). In order to develop this analysis, three simple preliminary assumptions are made.

1. It is assumed that the measured output variables λ and η are affected by zero-mean, uncorrelated, band-limited white noises d_λ and d_η in the

frequency range $[0, \Omega_N]$, Ω_N being the Nyquist frequency of the sampled signals: $d_\lambda \approx WN(0, \sigma_\lambda^2)$, $d_\eta \approx WN(0, \sigma_\eta^2)$. Notice that, in practice, all the measured signals are digitally sampled at the frequency of $2\Omega_N$; in order to keep the continuous-time notation used throughout the chapter, a band-limited white noise assumption must be made.

2. It is also assumed that $\sigma_\lambda^2 >> \sigma_\eta^2$. This is motivated by the fact that the noise on the wheel deceleration only comes from the wheel encoder signal processing and the differentiation, while that on the wheel slip is also affected by the vehicle speed estimation error (see Appendix B and Chapter 5).
3. Large values of the feedback gain K are considered, the parameter α is assumed to be close to 1 ($0.8 \leq \alpha \leq 0.95$), and the slip values are assumed to be non-negligible (*i.e.*, $\overline{\lambda} > 0.07$).

First, it is easy to see that $\gamma(\alpha)$ can be re-written as the product of two factors as

$$\gamma(\alpha) = \frac{\mathrm{Var}[\mathrm{d}_\varepsilon(\alpha)]}{\mathrm{Var}[\mathrm{d}_\varepsilon(1)]} = \Psi(\alpha)\Phi(\alpha),$$

where

$$\Psi(\alpha) = \frac{\alpha^2\sigma_\lambda^2 + (1-\alpha)^2\sigma_\eta^2}{\sigma_\lambda^2}$$

and

$$\Phi(\alpha) = \frac{\int_{\omega=0}^{\Omega_N} |S_\varepsilon(j\omega;\alpha)|\mathrm{d}\omega}{\int_{\omega=0}^{\Omega_N} |S_\varepsilon(j\omega;1)|\mathrm{d}\omega}.$$

The analysis of the first factor $\Psi(\alpha)$ is very simple. As we assumed that $0.8 \leq \alpha \leq 0.95$ and that $\sigma_\lambda^2 >> \sigma_\eta^2$, $\Psi(\alpha)$ can be approximated as follows:

$$\Psi(\alpha) \cong \alpha^2.$$

Clearly, this factor has little influence on the noise attenuation properties (a slightly better attenuation in the case of MSD control is provided with respect to wheel slip control).

The analysis of the factor $\Phi(\alpha)$ is far more complicated. This analysis can be carried out by inspecting the main features of the magnitude of the frequency response of the sensitivity function (6.10), which is a first-order transfer function, characterised by a pole and a zero. For the analysis of $\Phi(\alpha)$, the behaviour of $S_\varepsilon(s;\alpha)$ can be condensed into four main features: the high-frequency gain, the low-frequency (DC) gain, the angular frequency position of the zero and the angular frequency position of the pole. A simple qualitative analysis and discussion of these four features is now provided.

High-frequency Gain: $\mathrm{HF}(\alpha)$

From Equation 6.10, $\mathrm{HF}(\alpha)$ can be computed as

$$\mathrm{HF}(\alpha) = \frac{1}{1 + K\frac{r}{Jg}(1-\alpha)}. \tag{6.12}$$

This term shows that MSD control can provide a large attenuation benefit at high frequencies. As a matter of fact the HF gain for slip control $\mathrm{HF}(1) = 1$, whereas, for large values of K, $\mathrm{HF}(\alpha) << 1$.

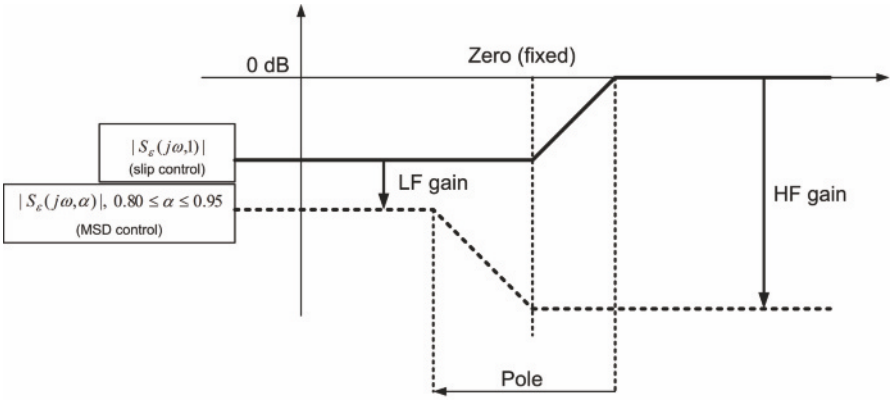

Figure 6.4 Sensitivity function features, when $\alpha = 1$ and $0.8 \le \alpha \le 0.95$

Low-frequency gain: $\mathrm{LF}(\alpha)$

From Equation 6.10, $\mathrm{LF}(\alpha)$ can be computed as

$$\mathrm{LF}(\alpha) = \frac{\frac{\mu_1(\overline{\lambda})F_z}{m}\left((1-\overline{\lambda}) + \frac{mr^2}{J}\right)}{\frac{\mu_1(\overline{\lambda})F_z}{m}\left((1-\overline{\lambda})\left(1 + K\frac{r}{J}(1-\alpha)\right) + \frac{mr^2}{J}\right) + K\alpha\frac{r}{J}}. \tag{6.13}$$

The analysis of Equation 6.13 is less trivial than that of Equation 6.12. For the analysis of the attenuation benefits achievable with MSD control it is useful to analyse the ratio $\mathrm{LF}(\alpha)/\mathrm{LF}(1)$

$$\frac{\mathrm{LF}(\alpha)}{\mathrm{LF}(1)} = \frac{\left[\frac{\mu_1(\overline{\lambda})F_z}{m}\left((1-\overline{\lambda}) + \frac{mr^2}{J}\right)\right] + \left[K\frac{r}{J}\right]}{\left[\frac{\mu_1(\overline{\lambda})F_z}{m}\left((1-\overline{\lambda}) + \frac{mr^2}{J}\right)\right] + \left[K\alpha\frac{r}{J}\right] + \left[\frac{\mu_1(\overline{\lambda})F_z}{m}(1-\overline{\lambda})(1-\alpha)K\frac{r}{J}\right]}. \tag{6.14}$$

Note that the dominant term both in the numerator and in the denominator of (6.14) is

$$\frac{K\frac{r}{J}}{K\alpha\frac{r}{J}} = \frac{1}{\alpha} \cong 1.$$

The LF gain ratio (6.14) henceforth is approximately equal to 1. More specifically, when $\mu_1(\overline{\lambda}) > 0$, note that all the terms at the denominator of Equation 6.14 are positive; hence, in this case, $\mathrm{LF}(\alpha)/\mathrm{LF}(1)$ can be significantly lower than 1. When $\mu_1(\overline{\lambda}) < 0$, notice that the third term in the denominator is small, since, despite the presence of K, the factors $(1-\overline{\lambda})$, $(1-\alpha)$ and $|\mu_1(\overline{\lambda})|$ are all very small; henceforth, $\mathrm{LF}(\alpha)/\mathrm{LF}(1) \cong 1$.

We can conclude that at low frequencies the MSD control and the slip control provide almost the same attenuation (or MSD control can provide a small attenuation benefit).

Frequency-domain Position of the Zero: $Z(\alpha)$

The angular frequency of the zero does not depend on the parameter α; it is given by

$$Z(\alpha) = Z(1) = \left| \frac{\mu_1(\overline{\lambda})F_z}{m} \left((1-\overline{\lambda}) + \frac{mr^2}{J} \right) \right|.$$

Frequency-domain Position of the Pole: $P(\alpha)$

The angular frequency of the pole is given by

$$P(\alpha) = \left| \frac{\frac{1}{\overline{v}} \left[\frac{\mu_1(\overline{\lambda})F_z}{m} \left((1-\overline{\lambda}) \left(1 + K\frac{r}{J}(1-\alpha) \right) + \frac{mr^2}{J} \right) + K\alpha\frac{r}{J} \right]}{\left[1 + K\frac{r}{Jg}(1-\alpha) \right]} \right|. \quad (6.15)$$

It is interesting to analyse the relative position of the pole, for $0.8 \leq \alpha \leq 0.95$, and for $\alpha = 1$, namely

$$\frac{P(\alpha)}{P(1)} = \left| \frac{\left[\frac{\mu_1(\overline{\lambda})F_z}{m} \left((1-\overline{\lambda}) \left(1 + K\frac{r}{J}(1-\alpha) \right) + \frac{mr^2}{J} \right) + K\alpha\frac{r}{J} \right]}{\left[\frac{\mu_1(\overline{\lambda})F_z}{m} \left((1-\overline{\lambda}) + \frac{mr^2}{J} \right) + K\frac{r}{J} \right] \left[1 + K\frac{r}{Jg}(1-\alpha) \right]} \right|. \quad (6.16)$$

The analysis of Equation 6.16 clearly shows that the pole angular frequency decreases when α decreases, since the ratio $P(\alpha)/P(1)$ is dominated by the factor

$$1 + K\frac{r}{Jg}(1-\alpha)$$

at the denominator.

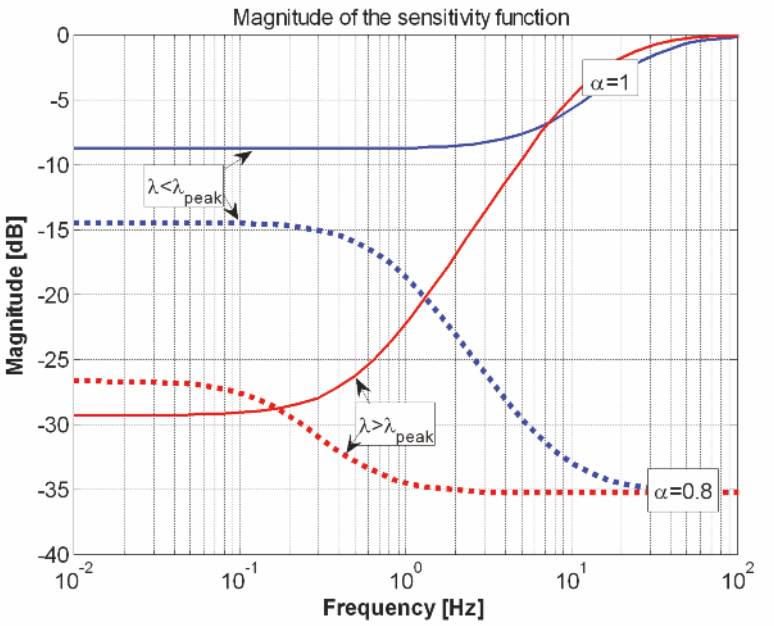

(a)

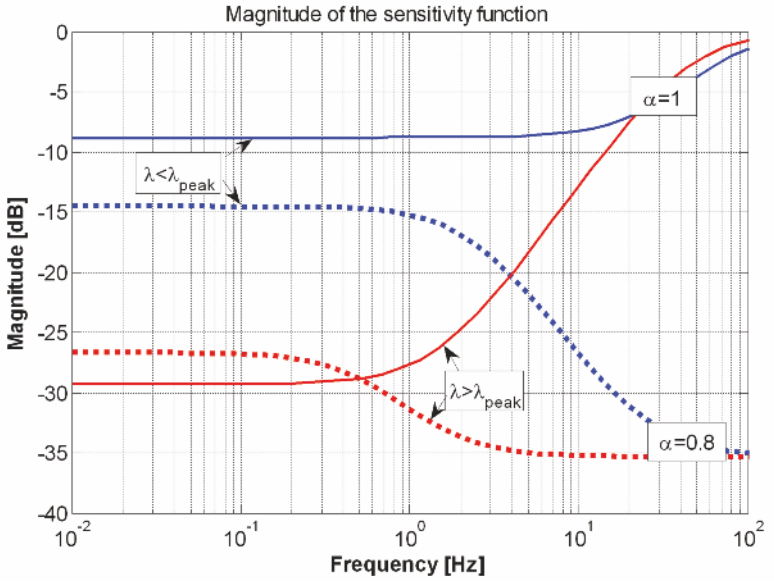

(b)

Figure 6.5 Bode plot of the frequency response associated with the sensitivity function: behaviour for $v = 30$ m/s (a) and for $v = 10$ m/s (b)

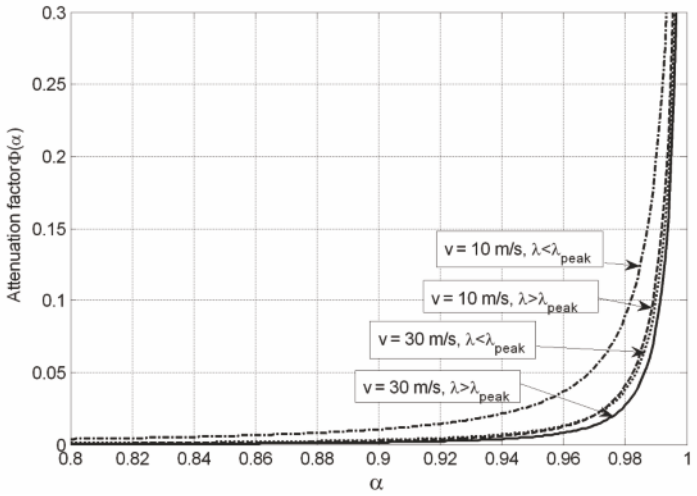

Figure 6.6 Plot of $\Phi(\alpha)$ in different working conditions

The results of the above analysis of $|S_\varepsilon(s;\alpha)|$ and $|S_\varepsilon(s;1)|$ can be summarised as in Figure 6.4:

- The LF gain is slightly sensitive to α; moving from $\alpha = 1$ to $0.8 \leq \alpha \leq 0.95$, it remains almost unchanged, or it can slightly decrease.
- The HF gain strongly decreases when $0.8 \leq \alpha \leq 0.95$.
- The angular frequency of the zero is unchanged, whereas that of the pole decreases when $0.8 \leq \alpha \leq 0.95$.

These approximate results are confirmed by Figures 6.5(a) and 6.5(b), where the magnitude Bode plots of the frequency response associated with the sensitivity function for $\alpha = 1$ and $\alpha = 0.8$ are displayed for different conditions (two different forward speed values and two different values of $\overline{\lambda}$). The analysis of the magnitude Bode plots of the frequency response associated with $S_\varepsilon(s;\alpha)$ clearly shows that the factor $\Phi(\alpha)$ rapidly becomes much lower than 1 when $\alpha < 1$.

In order to have a more immediate feeling on the attenuation level, in Figure 6.6 the behaviour of $\Phi(\alpha)$ is displayed in the range $\alpha \in [0.8, 1]$, for different conditions (two different forward speed values, and two different values of $\overline{\lambda}$). Interestingly enough, it can be observed that:

- As α moves from $\alpha = 1$ to $\alpha < 1$, $\Phi(\alpha)$ decreases very rapidly (*e.g.*, in every condition, if $\alpha = 0.95$, the value of $\Phi(\alpha)$ is lower than 0.05). This means that a slight use of the wheel deceleration in the feedback controlled variable is enough to obtain large noise attenuation benefits.
- The spread of $\Phi(\alpha)$ is comparatively small. Thus, the attenuation effect is large in every working condition.

This analysis has shown that MSD control can provide large benefits in terms of noise attenuation with respect to slip control. This advantage has been assessed by means of a quantitative analysis.

6.4 Steady-state Slip Values in MSD Control

Before moving on to assess the MSD performance *via* simulation results, it is worth analysing the steady-state behaviour of the wheel slip when the vehicle is controlled *via* MSD control.

To perform the analysis, recall first that the the equilibrium manifold in the (λ, η) domain is given by

$$\eta(\lambda) = N(1-\lambda)\mu(\lambda), \tag{6.17}$$

where $N = F_z/mg$, see also (2.53), is the ratio between the actual and the static vertical load. Thus, when MSD control is applied to the single-corner model, the dependence of the equilibrium point on the load transfer N makes the steady-state value of the wheel slip $\overline{\lambda}$ change according to the value of N itself. In fact, by imposing a set-point value $\overline{\varepsilon}$ one has to satisfy the relationship (6.4), *i.e.*,

$$\overline{\varepsilon} = \alpha\overline{\lambda} + (1-\alpha)\overline{\eta}.$$

Thus, if N increases, the set-point value $\overline{\eta}$ increases in view of (6.17) and thus the steady-state wheel slip $\overline{\lambda}$ decreases to satisfy the set-point expression (6.4).

To see this, consider Figure 6.7, which shows the time histories of the closed-loop front and rear wheel slip in a hard braking manoeuvre on dry asphalt in four different cases: the front wheel slip obtained when only the front wheels are controlled (dashed line), the rear wheel slip obtained when only the rear wheels are controlled (dash-dotted line) and the front (dotted line) and rear (solid line) wheel slip obtained when all four wheels are controlled via MSD control with equal values for $\overline{\varepsilon}$ and α.

As can be seen, when only the front or the rear wheels are controlled with the same $\overline{\varepsilon}$ and α, the steady-state wheel slip is different and, consistently with what has been previously noticed, lower at the front wheels (where N is larger) and higher at the rear wheels (where N is smaller).

However, in a full vehicle setting, that is when the same MSD controller (*i.e.*, with a common set-point value $\overline{\varepsilon}$ and an equal value for α) is used to regulate each of the four wheels, the steady-state value of the wheel slip goes back to being the same at all wheels.

To see this, consider for simplicity the double-corner model, where the longitudinal chassis dynamics is given by (see also Section 2.4)

$$\dot{v} = -\frac{1}{m}(F_{zf}\mu(\lambda_f) + F_{zr}\mu(\lambda_r)), \tag{6.18}$$

where F_{zf} and F_{zr} are the vertical forces at the front and rear wheel and λ_f and λ_r are the front and rear wheel slip, respectively.

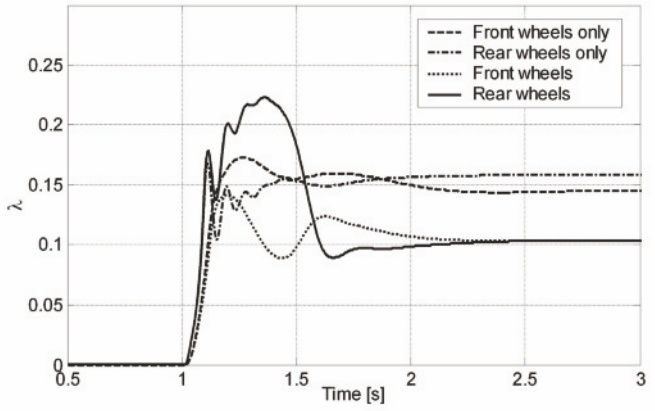

Figure 6.7 Time histories of the wheel slip during a hard braking manoeuvre on dry asphalt: front wheel slip when only the front wheels are controlled (*dashed line*), rear wheel slip when only the rear wheels are controlled (*dash-dotted line*) and front (*dotted line*) and rear (*solid line*) wheel slip when all four wheels are controlled

Recalling now the analysis in Section 2.5.1 one has that, letting $\dot{\lambda}_i = 0$, $i = \{f, r\}$, the expression linking the wheel acceleration $\dot{\omega}_i$ and the chassis acceleration $\dot{v}$ has the form

$$\dot{\omega}_i = \frac{1 - \lambda_i}{r_i}\dot{v}. \tag{6.19}$$

Accordingly, recalling that $\eta_i = -\dot{\omega}_i\, r_i/g$, and substituting into this relationship the expression for $\dot{v}$ in (6.18) one has

$$\overline{\eta}_i = \frac{(F_{zf}\mu(\overline{\lambda}_f) + F_{zr}\mu(\overline{\lambda}_r))}{mg}(1 - \overline{\lambda}_i) = \zeta(\overline{\lambda}_f, \overline{\lambda}_r)(1 - \overline{\lambda}_i), \tag{6.20}$$

where the term $\zeta(\overline{\lambda}_f, \overline{\lambda}_r)$ is the same for the front and for the rear wheel.

Further, imposing the same MSD control set-point for the controlled variable, *i.e.*, $\overline{\varepsilon}_i = \overline{\varepsilon}$, $i = \{f, r\}$, the expression for the equilibrium values of $\overline{\eta}_i$ becomes

$$\overline{\eta}_i = \frac{1}{1 - \alpha}\overline{\varepsilon} - \frac{\alpha}{1 - \alpha}\overline{\lambda}_i. \tag{6.21}$$

Combining Equation 6.21 with Equation 6.20 and solving for $\overline{\lambda}_i$, one obtains

$$\overline{\lambda}_i = \frac{\zeta(\overline{\lambda}_f, \overline{\lambda}_r) - \frac{1}{1-\alpha}\overline{\varepsilon}}{\zeta(\overline{\lambda}_f, \overline{\lambda}_r) - \frac{\alpha}{1-\alpha}}, \tag{6.22}$$

which shows that, at steady-state, the wheel slip value will be the same at the front and rear wheels, *i.e.*, $\overline{\lambda}_i = \overline{\lambda}$.

This allows us to re-write the term $\zeta(\overline{\lambda}_f, \overline{\lambda}_r)$ as

$$\zeta(\overline{\lambda}_f, \overline{\lambda}_r) = \mu(\overline{\lambda}) \left[\frac{(F_{zf} + F_{zr})}{mg} \right] = \mu(\overline{\lambda}), \tag{6.23}$$

where the last equality comes from the fact that $(F_{zf} + F_{zr})$ equals the overall vertical load, independently of its distribution between front and rear wheels.

Inspecting Figure 6.7 again, note that when both the front and rear controllers are employed, the steady-state wheel slip values are the same at all wheels, coherently with the performed analysis.

6.5 Numerical Analysis

The MSD control approach has been presented in the previous sections in a simplified setting: only the single-corner dynamics have been modelled and a simple proportional controller has been used. This simplified setting is particularly useful to focus on the heart of the control problem and to gain a deep insight in the algorithm behaviour.

However, the theoretical analysis developed in this simple setting must be corroborated by simulation results obtained on a full-vehicle simulator.

To implement the control algorithms in a fully-realistic setting, the simulation environment must also include the description of the EMB actuator dynamics given in (1.4). Finally, the simulations are performed replacing the proportional controllers with dynamic controller structures. More specifically:

- The wheel slip controller $R_\lambda(s)$ is implemented with the PID control architecture presented in Section 3.4, which has been tuned to work satisfactorily in every working condition (for different slip set-points, different road surfaces and different speed values).
- The MSD controller $R_\varepsilon(s)$ is implemented with a simpler PI control architecture (notice that this is another additional advantage of MSD control)

$$R_\varepsilon(s) = K_\varepsilon \frac{(1 + \tau_\varepsilon s)}{s},$$

and with $\alpha = 0.9$. Also the MSD controller has been tuned to work satisfactorily in every working condition.

The results presented in the following refer to a front wheel.

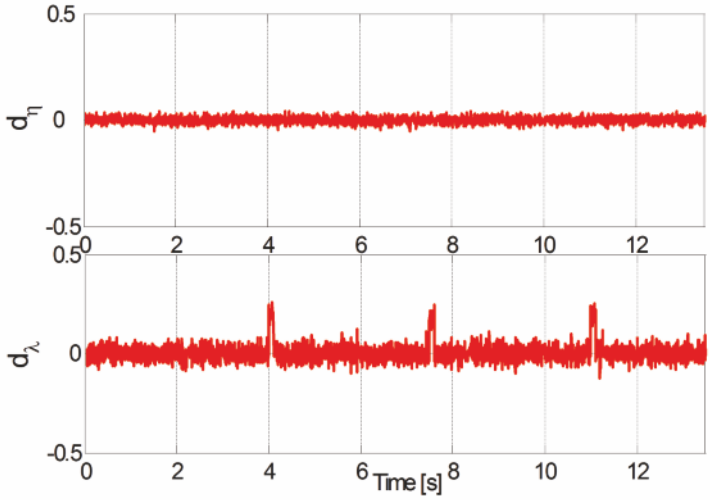

Figure 6.8 An example of measurement noises on λ and η used in the simulator

The first simulations have the goal of comparing the noise attenuation properties of the two control algorithms. In Figure 6.8 the measurement noises affecting the wheel deceleration and the wheel slip measurement are displayed. Notice that the variance of d_η is smaller than the variance of d_λ. Moreover, notice the different behaviour of the two measurement noises: d_η is essentially a broad-band stationary signal, while d_λ is characterised by huge spikes, due to poor speed estimation. Unfortunately, these spikes can hardly be reduced and they occur during hard braking, which is the typical working condition of active braking controllers.

In Figure 6.9 the time histories of the wheel slip during a hard braking manoeuvre on dry asphalt are displayed and MSD and slip control are compared. Notice that, as expected, the noise sensitivity of MSD control is remarkably lower than that of slip control; this results in a much smaller variation range of the actual wheel slip. Moreover, notice that MSD control has slightly better phase margin properties at low speed; as a matter of fact, the typical unstable behaviour that occurs at the end of the braking manoeuvre, *i.e.*, when the vehicle speed is very low (see the time interval $t \in [12, 14]$ s in Figure 6.9), arises later in MSD control. This result fully confirms the theoretical analysis performed in the simplified setting.

Finally, in Figures 6.10 and 6.11 the time histories of the wheel slip obtained with the MSD controller during a hard braking manoeuvre (in a noise-free setting) is shown, when a sudden change in the road surface occurs (from dry asphalt to snow in Figure 6.10, and from snow to dry asphalt in Figure 6.11). Very similar results can be obtained with the slip controller. Notice the remarkable robustness of the fixed-structure MSD controller; also notice that according to the MSD control rationale, the steady-state value of

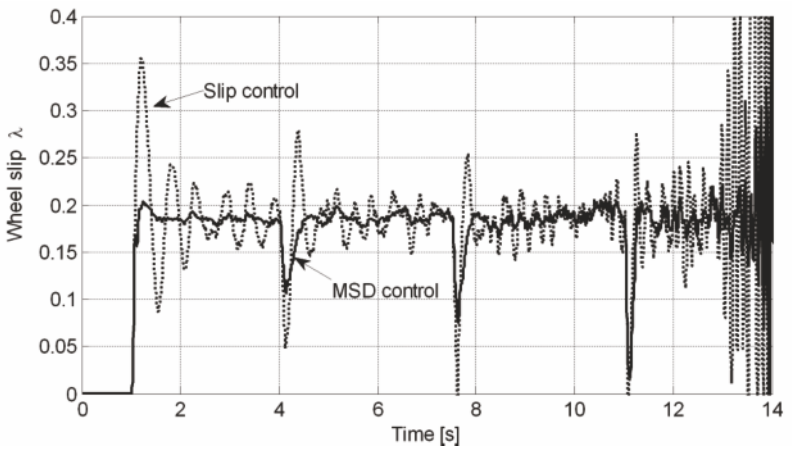

Figure 6.9 Time history of the wheel slip during a hard-braking manoeuvre on dry asphalt

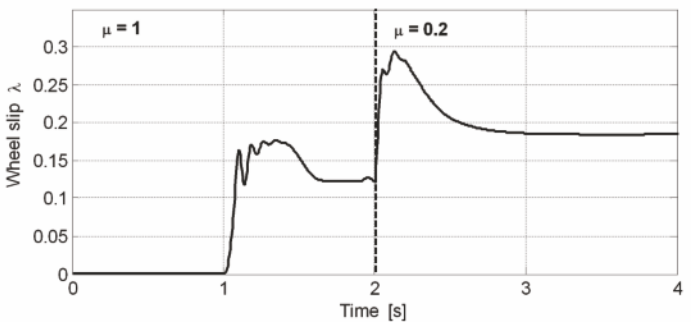

Figure 6.10 MSD control performance in a hard braking manoeuvre, with a sudden road-surface change from high to low grip road

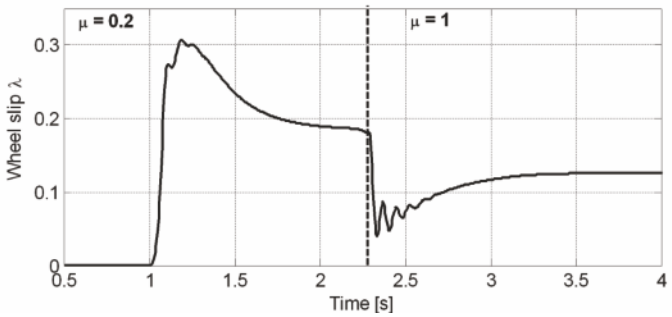

Figure 6.11 MSD control performance in a hard braking manoeuvre, with a sudden road-surface change from low to high grip road

the wheel slip changes when the friction curve changes according to different road surfaces (see Figure 6.2, which clearly shows this fact).

6.6 Summary

This chapter presented a wheel slip control strategy based on the idea of designing a standard SISO regulation loop on an output variable constituted by the convex combination of wheel slip and wheel deceleration. This control approach was referred to as MSD control.

The starting point of the MSD approach is to be found in [41, 69], where braking controllers based on modern electro-mechanical brakes are described, and which can be regarded as the state-of-the art in slip-controlled braking systems. The MSD approach was conceived to move one step further, so as to improve the performance of slip control by mixing slip and deceleration measurements.

Using a simple proportional-control regulation scheme this control structure was deeply analysed. Interestingly enough, MSD control inherently embodies, as extremal cases, also the more classical slip control and deceleration control schemes. Hence MSD control can move seamlessly between deceleration control and slip control. This is very appealing in sophisticated BBW systems, which may require a time-varying setting: emphasis on deceleration control during soft braking and emphasis on slip control in anti-lock conditions.

It has been shown that MSD control inherits all the appealing characteristics of slip control (unique equilibrium, fixed set-point, guaranteed closed-loop stability with a fixed structure linear time-invariant controller), but it overcomes the major flaw of slip control: its sensitivity to slip measurement errors.

Chapter 7
Nonlinear Wheel Slip Control Design

7.1 Introduction

Up to now, for the case of actuators with continuous dynamics, we have discussed how to design braking controllers based on linearised models of the braking dynamics of interest.

In this chapter, we discuss a nonlinear approach to wheel slip control design, namely a Lyapunov-based dynamic feedback control law. For an introduction to the control approach employed in this chapter, the reader is referred to Appendix A.

As a matter of fact, the braking dynamics are nonlinear due to the tyre–road interaction model; as such, the proposed approach allows us to take these nonlinearities directly into account and to consider their effects on the control algorithm. Further, the proposed control strategy is grounded on theoretical tools which allow us analyse its characteristics and to highlight its advantages with respect to the linear approaches.

Specifically, the nonlinear slip controller discussed in this chapter relies on a nonlinear dynamic feedback control law, based on wheel slip and wheel speed measurements, which guarantees bounded control action and thus copes with input constraints. The main advantage of the proposed controller with respect to a wheel slip controller based on a linearised model of the braking dynamics is that the closed-loop system properties allows one to detect if the current operating condition is such that the chosen wheel slip set-point determines a closed-loop equilibrium point which is beyond the peak of the tyre–road friction curve, thereby enabling us to adapt the set-point and yielding a significant enhancement of both performance and safety. This is a special feature of the proposed control law, which in general is not offered by other active braking control systems unless they are complemented with tyre–road friction estimators.

7.2 Lyapunov-based Wheel Slip Control

One of the main challenges in designing ABS systems is to devise a control logic that is robust and can offer good performance irrespectively of the (unknown) tyre–road friction conditions. Due to this fact, significant efforts have been devoted to explicitly estimating the road characteristics online (see *e.g.*, [12, 24, 29, 65, 69, 92, 93, 114, 118, 127, 129], in an attempt to devise viable solutions to complement braking controllers with tyre–road friction estimation capabilities, so as to enhance both performance and safety.

However, due to the limited computing resources commonly available on commercial vehicles' ECUs, a robust control logic that does not require online estimation algorithms or adaptive control laws is usually preferred.

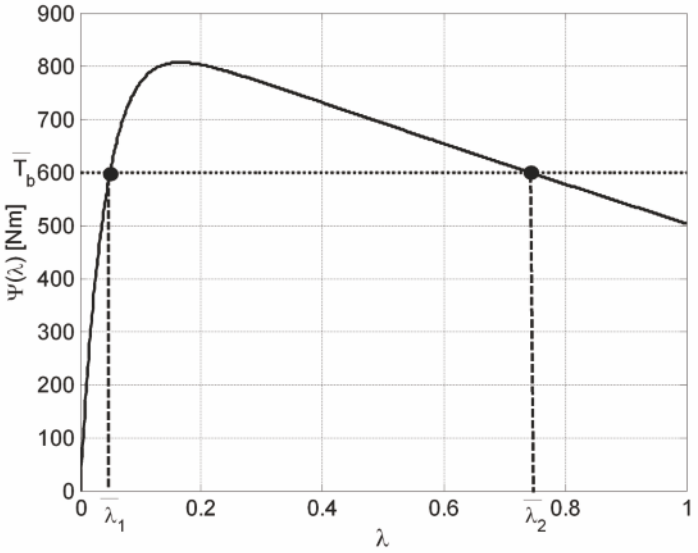

Figure 7.1 Equilibrium points for the single-corner model (7.1) in the (λ, T_b) plane (example with $F_z = mg$ and dry asphalt)

As for the braking dynamics, we consider the single-corner model and work again under the assumption (see also Chapter 2) of regarding the vehicle speed v as a slowly-varying parameter (see also Section 2.3). Thus, we consider the wheel slip dynamics

$$\dot{\lambda} = -\frac{1-\lambda}{J\omega}\left(\Psi(\lambda) - T_b\right), \tag{7.1}$$

with $\omega > 0$ and

$$\Psi(\lambda) = \left(r + \frac{J}{rm}(1-\lambda)\right) F_z \mu(\lambda). \tag{7.2}$$

7.2.1 Assumptions

In developing the nonlinear approach discussed in this chapter, the following assumptions are considered:

1. The control input T_b takes values in a non-empty subset of the real axis, *i.e.*, $T_b \in [T_{b\mathrm{Min}}, T_{b\mathrm{Max}}]$, for some known values $T_{b\mathrm{Min}}$ and $T_{b\mathrm{Max}}$ such that $0 \leq T_{b\mathrm{Min}} < T_{b\mathrm{Max}}$.
   Note that this assumption is always verified in practice, as the values $T_{b\mathrm{Min}}$ and $T_{b\mathrm{Max}}$ represent the lower and upper limits of the braking torque and are imposed by the actuator characteristics.
   We consider that the actuator limits $T_{b\mathrm{Min}}$ and $T_{b\mathrm{Max}}$ are such that
   $$T_{b\mathrm{Min}} = 0,$$
   and
   $$T_{b\mathrm{Max}} > \max_{\lambda} \Psi(\lambda),$$
   where $\Psi(\lambda)$ is as in (7.2). Note that this last inequality simply requires that the actuator saturation occurs for values of the braking torque larger than the maximum equilibrium torque admissible for any road surface, which is a prerequisite for any actuator to guarantee that the friction capability of any tyre–road friction condition can be fully exploited.
2. The steady-state value of the control input $\overline{T}_b$ associated with the wheel slip set-point $\overline{\lambda}$ is such that $\overline{T}_b \in [T_{b\mathrm{Min}}, T_{b\mathrm{Max}}]$.
   Further, the longitudinal wheel slip set-point $\overline{\lambda}$ is selected such that
   $$\overline{T}_b < \max_{\lambda} \Psi(\lambda).$$
   This inequality (see Figure 7.1) is verified for all choices of the set-point $\overline{\lambda}$, but for the abscissa of the exact peak point of the $\Psi(\lambda)$ curve, where $\overline{T}_b = \max_{\lambda} \Psi(\lambda)$.

7.2.2 Controller Design

The main idea here is to design a control law in the form of a dynamic update law, such that system (7.1) is robustly stabilised around a desired equilibrium point in the sense of Lyapunov with respect to the uncertainties lying in the function $F_z\mu(\lambda)$.

To this aim, we can state the following result.

Proposition 7.1. *Consider the single-corner model described by Equation 7.1 and assume that assumptions 1 and 2 illustrated in Section 7.2.1 hold.*

With reference to Figure 7.1, let the wheel slip set-point $\overline{\lambda} \in (0,1)$ *be the smallest solution of* $\overline{T}_b = \Psi(\lambda)$.

Further, suppose that either[1]

$$\overline{\lambda}_2 \left(1 + \frac{1}{\ln(1-\overline{\lambda}_2)}\right) \leq \overline{\lambda} < \overline{\lambda}_2 \quad \text{or} \quad \overline{\lambda}_2 \geq 1. \tag{7.3}$$

Then, for any[2] $\theta(0) \in (0, T_{b\mathrm{Max}})$, *the dynamic output feedback control law*

$$\begin{cases} T_b = \theta, \\ \dot{\theta} = k_\lambda \frac{1}{J\omega}(\lambda - \overline{\lambda})(\theta - T_{b\mathrm{Max}})(\theta - T_{b\mathrm{Min}}), \end{cases} \tag{7.4}$$

with $k_\lambda > 0$ *and* $\omega > 0$ *is such that the closed-loop system*

$$\begin{cases} \dot{\lambda} = -\frac{1-\lambda}{J\omega}\left(\Psi(\lambda) - \theta\right), \\ \dot{\theta} = k_\lambda \frac{1}{J\omega}(\lambda - \overline{\lambda})(\theta - T_{b\mathrm{Max}})(\theta - T_{b\mathrm{Min}}). \end{cases} \tag{7.5}$$

has a locally stable *equilibrium point* $(\overline{\lambda}, \overline{\theta})$ *and for any initial condition* $\lambda(0)$ *in the region*

$$\Lambda = \{\lambda \in \mathbb{R} \mid 0 \leq \lambda \leq 1\}, \tag{7.6}$$

$\lambda(t)$ *remains in this region. Moreover, if* $\lambda(0) \neq 1$, $\lambda(t)$ *converges asymptotically to* $\overline{\lambda}$.

Now let $\overline{\lambda}$ *be the largest solution of* $\overline{T}_b = \Psi(\lambda)$. *Then the control law* (7.4) *is such that for any initial condition* $\lambda(0) \in \Lambda$, $\lambda(t)$ *remains in this region. Moreover, if* $\lambda(0) \neq 1$, *the closed-loop system trajectory* $(\lambda(t), \theta(t))$ *converges to an attractive periodic orbit encircling the equilibrium* $(\overline{\lambda}, \overline{\theta})$.

Finally, in both cases, the control variable T_b *remains in the set* $[T_{b\mathrm{Min}}, T_{b\mathrm{Max}}]$ *for all* $t \geq 0$.

Proof. To begin with note that, for a constant value of the braking torque $\overline{T}_b$, the vector field $\dot{\lambda}$ exhibits the behaviour shown in Figure 7.2. This, coupled with the wheel slip definition given in (2.5) which implies that $\lambda \in [0,1]$, ensures that the region Λ in (7.6) is invariant. Note that Figure 7.2 was plotted considering a dry asphalt road surface, a static value of the vertical load $F_z = mg$ and a value of $\overline{T}_b$ satisfying assumption 2 (namely, see also Section 2.5.1, the value $\overline{T}_b = 600$ Nm was used). However, note that in view of assumption 2, as the road surface or the vertical load vary, a constant value of the braking torque $\overline{T}_b$ can always be selected such that the qualitative vector field behaviour does not change, the only modification being in the different numerical values of the wheel slip equilibrium points $\overline{\lambda}_1$ and $\overline{\lambda}_2$.

[1] Note that if $\overline{\lambda}_2 < 1$, that is if two intersections exist between $T_b = \overline{T}_b$ and $\Psi(\lambda)$, condition (7.3) holds trivially if $\overline{\lambda} \leq \overline{\lambda}_2$ and $\overline{\lambda}_2 \leq 1 - \mathrm{e}^{-1} \cong 0.6321$. Note, moreover (see Figure 7.1), that the case $\overline{\lambda}_2 \geq 1$ corresponds, for the considered friction model, to the case when only one point of intersection exists between $\overline{T}_b$ and $\Psi(\lambda)$, hence to low values of $\overline{\lambda}$.

[2] Recall that by assumption 1, $\underline{T}_b = 0$.

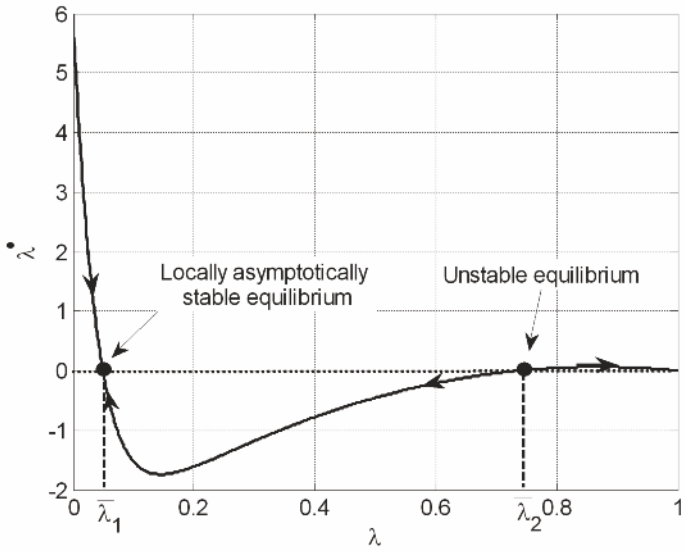

Figure 7.2 Graph of $\dot{\lambda}$ as a function of λ

Consider now the candidate Lyapunov function

$$W(\lambda, \theta) = V(\lambda) + \xi(\theta) + c, \tag{7.7}$$

where $V(\lambda)$ has the form

$$V(\lambda) = -\lambda + (\overline{\lambda} - 1)\ln(1 - \lambda), \tag{7.8}$$

the function $\xi(\theta)$ is defined as

$$\xi(\theta) := \ln(T_{b\mathrm{Max}} - \theta)^{\tau/k_\lambda} - \ln(\theta - T_{b\mathrm{Min}})^{(\tau+1)/k_\lambda}, \tag{7.9}$$

with $\tau = \dfrac{\overline{\theta} - T_{b\mathrm{Max}}}{T_{b\mathrm{Max}} - T_{b\mathrm{Min}}} < 0$ and $\tau + 1 > 0$, and the constant c is chosen such that

$$W(\overline{\lambda}, \overline{\theta}) = 0.$$

Notice that the function $W(\lambda, \theta)$ is positive definite in

$$(\lambda, \theta) \in (0, 1) \times (T_{b\mathrm{Min}}, T_{b\mathrm{Max}}).$$

Moreover, note that

$$\begin{aligned}\dot{W} &= \frac{\partial V}{\partial \lambda}\dot{\lambda} + \frac{\partial \xi}{\partial \theta}\dot{\theta} - \left[\frac{(\overline{\lambda}-1)}{(1-\lambda)}+1\right]\dot{\lambda} + \frac{\partial \xi}{\partial \theta}\dot{\theta} \\ &= -\frac{(\overline{\lambda}-\lambda)}{(1-\lambda)}\left\{-\frac{1-\lambda}{\omega r}\left(\frac{(1-\lambda)}{m}+\frac{r^2}{J}\right)F_z\mu(\lambda)+\frac{r}{J}\frac{1-\lambda}{\omega r}\overline{\theta}\right\} \\ &+ (\lambda-\overline{\lambda})\frac{1}{J\omega}(\theta-\overline{\theta}) + \frac{\partial \xi}{\partial \theta}\dot{\theta} \\ &= -\frac{(\overline{\lambda}-\lambda)}{(1-\lambda)}\left\{-\frac{1-\lambda}{\omega r}\left(\frac{(1-\lambda)}{m}+\frac{r^2}{J}\right)F_z\mu(\lambda)+\frac{r}{J}\frac{1-\lambda}{\omega r}\overline{\theta}\right\} \\ &+ (\lambda-\overline{\lambda})\frac{1}{J\omega}\left[(\theta-\overline{\theta}) + \frac{\partial \xi}{\partial \theta}\sigma(\theta)\right].\end{aligned}$$

Recalling the definition of $\Psi(\lambda)$ in Equation 7.2, we can re-write $\dot{W}$ as

$$\dot{W} = -\frac{(\lambda-\overline{\lambda})}{J\omega}\left(\Psi(\lambda)-\overline{\theta}\right) + (\lambda-\overline{\lambda})\frac{1}{J\omega}\left[(\theta-\overline{\theta}) + \frac{\partial \xi}{\partial \theta}\sigma(\theta)\right].$$

In view of assumptions 1 and 2 in Section 7.2.1, if $\overline{\lambda}$ is the smallest solution of $\overline{T}_b = \Psi(\lambda)$, $(\lambda-\overline{\lambda})$ and $\left(\Psi(\lambda)-\overline{\theta}\right)$ have the same sign for all $\lambda \in (0, \overline{\lambda}_2)$. Hence, their product can be written as

$$(\lambda-\overline{\lambda})^2\Xi(\lambda),$$

where $\Xi(\lambda) > 0, \forall \lambda \in (0, \overline{\lambda}_2)$.

Moreover, for $T_b = \theta$ and given the expression of $\xi(\theta)$ in Equation 7.9, if one chooses

$$\sigma(\theta) = k_\lambda(\theta - T_{b\mathrm{Max}})(\theta - T_{b\mathrm{Min}}), \tag{7.10}$$

then

$$(\theta-\overline{\theta}) + \frac{\partial \xi}{\partial \theta}\sigma(\theta) = 0.$$

Hence,

$$\dot{W} = -(\lambda-\overline{\lambda})^2\Xi(\lambda) \leq 0, \tag{7.11}$$

for all $\lambda \in (0, \overline{\lambda}_2]$ and $\theta \in (T_{b\mathrm{Min}}, T_{b\mathrm{Max}})$.

Note in passing that the control law is inspired by the result presented in Appendix A.3 (see Proposition A.1). Specifically, with respect to the setting of Proposition A.1 note that the control law proposed herein is constructed as $\dot{\theta} = \dfrac{\partial V}{\partial x}g(x)\sigma(\theta)$, where $g(x) = \frac{1}{J\omega}(1-\lambda)$, $V(\lambda)$ is the Lyapunov function in (7.8) and $\sigma(\theta)$ is as in (7.10).

As a result, recalling that $\overline{\lambda} < \overline{\lambda}_2$, we have shown that the equilibrium point $(\overline{\lambda}, \overline{\theta})$ is locally stable. To complete the proof we must show that any trajectory of the closed loop system such that $\theta(0) \in (0, T_{b\mathrm{Max}})$ and $\lambda(0) \in [0, 1)$ converges to this equilibrium.

To this end, first of all one has to consider that since the system under study is two-dimensional, the only possible attractors are either zero-

dimensional, *i.e.,* equilibrium points, or one-dimensional, *i.e.,* limit cycles (see Appendix A.2.2).

We now analyse the stability properties of the closed-loop equilibrium points different from $(\overline{\lambda}, \overline{\theta})$ *via* linearisation and show directly that no limit cycles can occur in the closed-loop system.

Specifically, The closed-loop system dynamics are given by (7.5). In view of assumption 1, the equilibrium points $(\lambda^{ss}, \theta^{ss})$ different from $(\overline{\lambda}, \overline{\theta})$ to be studied are the following:

(i) $\lambda = 1$ and $\theta = T_{b\mathrm{Max}}$;
(ii) $\lambda = 1$ and $\theta = T_{b\mathrm{Min}} = 0$; and
(iii) $\lambda = 0$ and $\theta = T_{b\mathrm{Min}} = 0$.

If we define

$$\delta\lambda := \lambda - \lambda^{ss},$$
$$\delta\theta := \theta - \theta^{ss},$$

and

$$\mu_1(\lambda) := \frac{\mathrm{d}}{\mathrm{d}\lambda}\mu(\lambda)\bigg|_{\lambda=\lambda^{ss}},$$

where $\mu(\lambda)$ is as in Equation 2.13, the linearisation of system (7.5) has the form

$$\begin{cases} \dot{\delta\lambda} = \{-rF_z\left[-\mu(\lambda^{ss}) + (1-\lambda^{ss})\mu_1(\lambda^{ss})\right] \\ \quad -\frac{JF_z}{m}\left[-2(1-\lambda^{ss})\mu(\lambda^{ss}) + (1-\lambda^{ss})^2\mu_1(\lambda^{ss})\right] \\ \quad -\theta^{ss} + (1-\lambda^{ss})\theta^{ss}\}\,\delta\lambda + (1-\lambda^{ss})\delta\theta, \\ \dot{\delta\theta} = -k_\lambda\overline{\lambda}(\theta^{ss} - T_{b\mathrm{Max}})(\theta^{ss} - T_{b\mathrm{Min}})\delta\lambda \\ \quad +k_\lambda(\lambda^{ss} - \overline{\lambda})\left[2\theta^{ss} - (T_{b\mathrm{Min}} + T_{b\mathrm{Max}})\right]\delta\theta. \end{cases} \tag{7.12}$$

Accordingly, the dynamic matrix of the linearised system in the equilibrium $\lambda^{ss} = 1$ and $\theta^{ss} = T_{b\mathrm{Max}}$ is given by

$$A_{(1,T_{b\mathrm{Max}})} = \begin{bmatrix} rF_z\mu(1) - T_{b\mathrm{Max}} & 0 \\ 0 & k_\lambda(1-\overline{\lambda})[T_{b\mathrm{Max}} - T_{b\mathrm{Min}}] \end{bmatrix},$$

which shows that $(1, T_{b\mathrm{Max}})$ is a saddle point (see also Section A.2.2). Now note that as can easily be seen from Figure 7.3(a), the only initial conditions yielding trajectories that converge to this equilibrium are such that $\lambda(0) = 1$ and $\theta(0) \in (0, T_{b\mathrm{Max}}]$.

The dynamic matrix of the linearised system in the equilibrium $\lambda = 1$ and $\theta = T_{b\mathrm{Min}}$ is given by

$$A_{(1,T_{b\mathrm{Min}}} = \begin{bmatrix} rF_z\mu(1) - T_{b\mathrm{Min}} & 0 \\ 0 & k_\lambda(1-\overline{\lambda})[T_{b\mathrm{Min}} - T_{b\mathrm{Max}}] \end{bmatrix},$$

which shows that also $(1, T_{b\mathrm{Min}})$ is a saddle point. Moreover, the only initial conditions yielding trajectories that converge to this equilibrium are such that $\lambda(0) \in (0, 1]$ and $\theta(0) = 0$.

Finally, the dynamic matrix of the linearised system in the equilibrium $\lambda = 0$ and $\theta = T_{b\mathrm{Min}}$ is given by

$$A_{(0,T_{b\mathrm{Min}})} = \begin{bmatrix} rF_z\mu(0) - T_{b\mathrm{Min}} & 0 \\ 0 & -k_\lambda \overline{\lambda}[T_{b\mathrm{Min}} - T_{b\mathrm{Max}}] \end{bmatrix},$$

which shows that $(0, T_{b\mathrm{Min}})$ is an unstable saddle-node point.

According to this analysis, if we study the closed-loop trajectories, which are qualitatively depicted in Figure 7.3(a), we can see that the region

$$\mathcal{D} = \left\{(\lambda, \theta) \in \mathbb{R}^2 \;\mid\; 0 \leq \lambda < 1, \theta \in (T_{b\mathrm{Min}}, T_{b\mathrm{Max}})\right\} \tag{7.13}$$

is a *trapping* region for the closed-loop system (7.5) (see Appendix A.2.2).

To complete the proof we need to show that all trajectories with initial condition in $\mathcal{D}$ do converge to $(\overline{\lambda}, \overline{\theta})$. To do this, we only need to show that there are no limit cycles in this region. However, by index theory (see again Appendix A.2.2), the only limit cycles that may exist within $\mathcal{D}$ should encircle the equilibrium $(\overline{\lambda}, \overline{\theta})$. To rule out the existence of such limit cycles, consider the level set[3] of the Lyapunov function $W(\lambda, \theta)$ defined as

$$\Omega = \left\{(\lambda, \theta) \in \bar{\mathcal{D}} \;\mid\; W(\lambda, \theta) \leq W(0, \overline{\theta})\right\}.$$

By condition (7.3), this set is contained in the set

$$\widetilde{\mathcal{D}} = \left\{(\lambda, \theta) \in \bar{\mathcal{D}} \;\mid\; \lambda \leq \overline{\lambda}_2\right\}.$$

Hence, in view of (7.11), any trajectory starting in the set Ω will remain inside Ω and converge to the equilibrium $(\overline{\lambda}, \overline{\theta})$. This implies that any limit cycle encircling the equilibrium $(\overline{\lambda}, \overline{\theta})$ should be contained in

$$\mathcal{D}_r = \mathcal{D} \setminus \Omega.$$

However, it is impossible to construct a closed curve contained in $\mathcal{D}_r$ and encircling the point $(\overline{\lambda}, \overline{\theta})$. As a consequence, all trajectories starting in $\mathcal{D}$ will converge to the equilibrium $(\overline{\lambda}, \overline{\theta})$.

To complete the proof, we now study the case when $\overline{\lambda}$ is the largest solution of $\overline{T}_b = \Psi(\lambda)$. In this case, $(\lambda - \overline{\lambda})$ and $\left(\Psi(\lambda) - \overline{\theta}\right)$ have opposite sign for all $\lambda \in (\overline{\lambda}_1, 1)$ (see also Figure 7.1). Hence, in a neighbourhood of $(\overline{\lambda}, \overline{\theta})$ one has $\dot{W} \geq 0$ (see Equation 7.11) and this allows us to conclude that $(\overline{\lambda}, \overline{\theta})$ is an *unstable* equilibrium.

To study the closed-loop system trajectories in this case we can employ the analysis of the linearised system performed before and refer to Figure 7.3(b).

[3] The closure of a set D is denoted by $\bar{D}$.

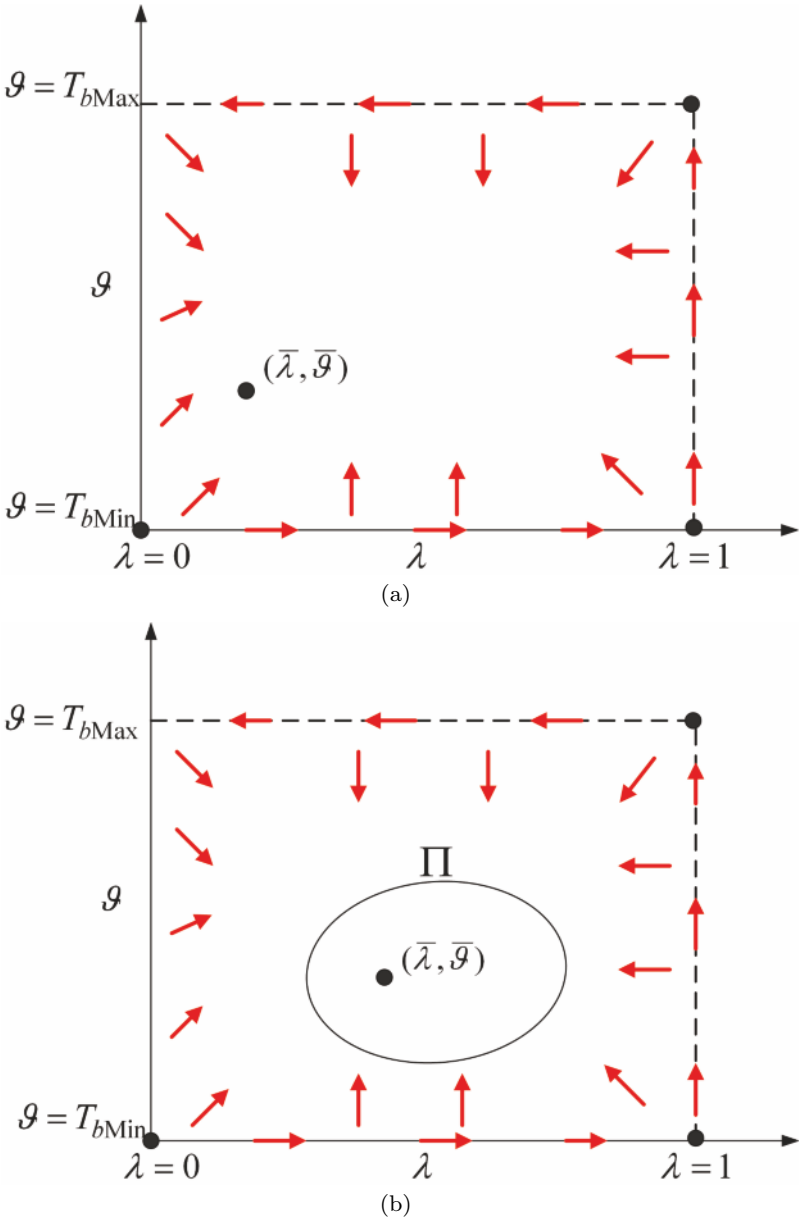

Figure 7.3 Qualitative behaviour of the closed-loop vector field in the region $\bar{\mathcal{D}}$ when $\overline{\lambda}$ is the smallest solution of $\overline{T}_b = \Psi(\lambda)$ (a) and when $\overline{\lambda}$ is the largest solution of $\overline{T}_b = \Psi(\lambda)$ (b)

Let $\mathcal{B} \subset \mathcal{D}$ be a sufficiently small neighbourhood of the unstable equilibrium $(\overline{\lambda}, \overline{\theta})$. Consider now the region

$$\widetilde{\mathcal{C}} = \{(\lambda, \theta) \in \mathcal{D} \setminus \mathcal{B} \mid \lambda \in (0, 1)\}.$$

Due to the instability of the equilibrium $(\overline{\lambda}, \overline{\theta})$ all the trajectories starting in $\mathcal{B}$ (except that with initial condition $(\overline{\lambda}, \overline{\theta})$) converge to the set $\widetilde{\mathcal{C}}$ and remain in this set.

As the set $\mathcal{D}$ (see (7.13)) has been shown to be a *trapping* region for the closed-loop system (7.5) and recalling the Poincaré–Bendixon theorem (see Appendix A.2.2), all the trajectories starting in the set $\widetilde{\mathcal{C}}$ remain inside $\widetilde{\mathcal{C}}$. Moreover, the Poincaré-Bendixon theorem ensures that as $\widetilde{\mathcal{C}}$ does not contain any equilibrium point, these trajectories either are periodic orbits or tend to a periodic orbit. Further, as $(\overline{\lambda}, \overline{\theta})$ is an *unstable* equilibrium, index theory guarantees that the periodic orbit is unique.

Hence, according to the stability properties of the closed-loop system equilibrium points shown in Figure 7.3(b), we can conclude that any trajectory in $\widetilde{\mathcal{C}}$ converges to an attractive periodic orbit and this completes the proof. □

The results given in Proposition 7.1 prove that if the selected set-point $\overline{\lambda}$ is the smallest solution of $\overline{T}_b = \Psi(\lambda)$, *i.e.,* if, in practice, $\overline{\lambda}$ lies to the left of the friction curve peak (see also Section 2.5.1), then the closed-loop equilibrium $(\overline{\lambda}, \overline{\theta})$ is locally asymptotically stable. On the other hand, if $\overline{\lambda}$ is the largest solution of $\overline{T}_b = \Psi(\lambda)$, *i.e.,* if $\overline{\lambda}$ lies beyond the friction curve peak, then the control law stabilises the system around a stable periodic orbit. Note that this periodic closed-loop behaviour of the wheel slip is that commonly achieved with ABS systems based on actuators with on/off dynamics (see Chapter 4).

Hence, on the one hand the system stability and the related safety of the braking manoeuvre are always guaranteed by the nonlinear controller considered while, on the other hand, the periodic behaviour of the closed-loop trajectory can be monitored to detect if the closed-loop working condition lies in the unstable region of the friction curve. This very peculiar feature of the proposed control law provides a crucial information for optimising the braking performance (see, *e.g.,* [29,118,129]). This feature, cannot usually be found in other active braking control systems unless they are complemented with tyre–road friction estimators.

Clearly this peculiarity can be profitably employed to adjust online the wheel slip set-point, once the periodic behaviour is detected. This is shown in Figure 7.4, where the time histories of the wheel slip in a hard braking manoeuvre on dry asphalt for two different values of the wheel slip set-point $\overline{\lambda}$ are depicted both when a linear wheel slip controller of the type discussed in Chapter 3 is adopted and with the nonlinear control law (7.4). Specifically, the two set-point values are $\overline{\lambda} = 0.08$, which is to the left of the peak of the friction curve and $\overline{\lambda} = 0.3$, which is beyond the peak (see also Figure 2.3).

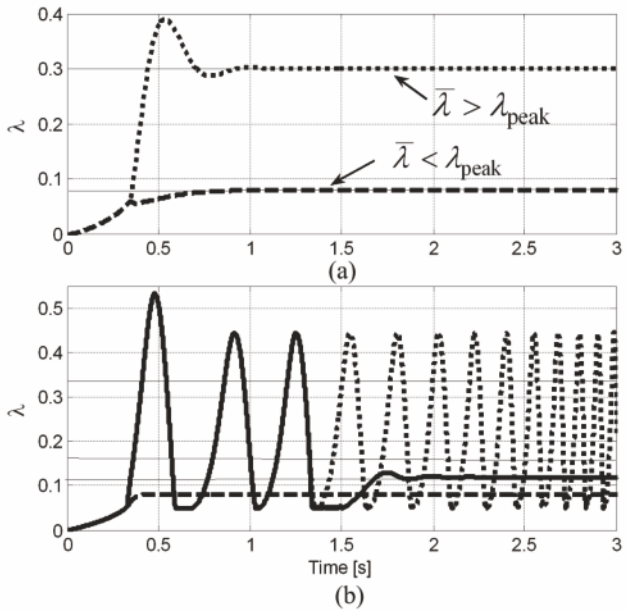

Figure 7.4 Time histories of the wheel slip in a hard braking manoeuvre for two different values of the wheel slip set-point $\bar{\lambda}$: to the left of the peak of the friction curve (*dashed line*) and beyond the peak of the friction curve (*dotted line*) obtained with a linear wheel slip controller (a) and with the nonlinear control law (7.4) (b). The *solid line* in (b) plot was obtained by adapting the set-point value after the limit cycle was detected

Note that, even though the linear controller stabilises the system also for operating points in the unstable region of the friction curve, it has no means of detecting whether the current operating condition is such that the chosen wheel slip set-point determines a closed-loop equilibrium point which is before or beyond the peak of the tyre–road friction curve. The nonlinear control law (7.4), instead, allows one to detect such a condition by simply monitoring the wheel slip. Moreover, as shown in Figure 7.4 (see the solid line in the bottom plot), it is possible to adapt the set-point value online after the limit cycle behaviour has been detected.

We now exploit this property to search in real time for the wheel slip value that maximises the friction force so to always operate with the best possible braking performance. To this end, we observed that the amplitude of the limit cycle on the wheel slip is a monotonously increasing function of the distance between the set-point and the wheel slip value that corresponds to the peak of the function $\Psi(\lambda)$; hence, a map between these two quantities has been estimated *via* simulations and used to adapt the set-point value online.

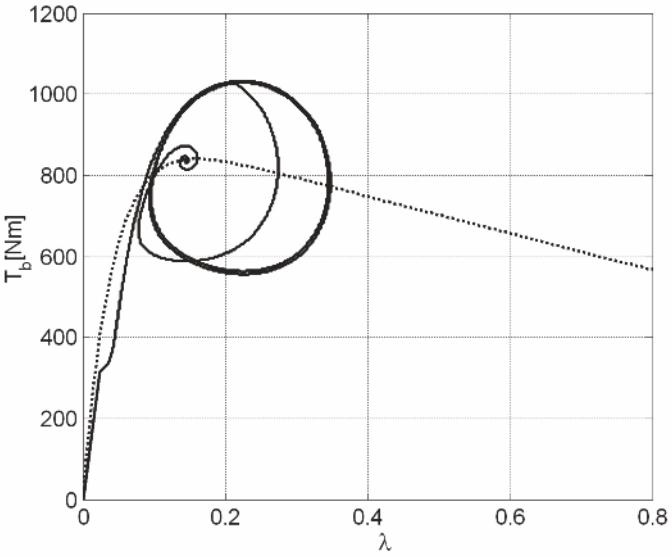

Figure 7.5 Plot of the trajectory of the closed-loop system (7.5) (*solid line*) and of the function $\Psi(\lambda)$ in (7.2) (*dotted line*) with the adaptation logic that searches online for the wheel slip set-point value that allows optimising the braking performance

Figure 7.5 shows the results obtained with this adaptation strategy, which assess the possibility – with little extra computation effort – of significantly enhancing the braking performance.

As final remarks on the nonlinear control law (7.4), it is interesting to point out that the role of the term $(\theta - T_{b\mathrm{Max}})(\theta - T_{b\mathrm{Min}})$ is to keep the control input $\theta(t)$ in the admissible set $[T_{b\mathrm{Min}}, T_{b\mathrm{Max}}]$ at any time t, so that it intrinsically takes into account saturation constraints. Note also that the control law has – in principle – three design parameters, namely $T_{b\mathrm{Max}}$, $T_{b\mathrm{Min}}$ and k_λ. In our case, though, $T_{b\mathrm{Max}}$ and $T_{b\mathrm{Min}}$ are determined by the physical limits of the braking system, hence the only free parameter is k_λ, which can be tuned in principle as the integral gain of the linear controller.

Finally, with respect to other braking control algorithms, the control law (7.4) has the additional advantage that it is reliable also at low speed values. In this respect, rewriting the update law as

$$\omega\dot{\theta} = k_\lambda \frac{1}{J}(\lambda - \overline{\lambda})(\theta - T_{b\mathrm{Max}})(\theta - T_{b\mathrm{Min}}),$$

we can see that as $\omega \to 0$, either $\theta \to T_{b\mathrm{Min}}$, or $\theta \to T_{b\mathrm{Max}}$, or $\lambda \to \overline{\lambda}$.

Nevertheless, the structure of the Lyapunov function (7.7) ensures that no closed-loop trajectory can be such that $\sup_{t\in[0,+\infty)} = T_{b\mathrm{Max}}$ or $\inf_{t\in[0,+\infty)} = T_{b\mathrm{Min}}$. As a result, $\lambda \to \overline{\lambda}$ as ω approaches 0.

Accordingly, even though it remains of course true that the open-loop wheel dynamics become faster and faster as speed decreases, the proposed control law speeds up the convergence to the desired wheel slip set-point as $\omega \to 0$. This means that although also the proposed output feedback controller needs to be deactivated at low speed, its performance improves as the speed decreases (up to a certain lower bound) while that of linear controllers generally worsens.

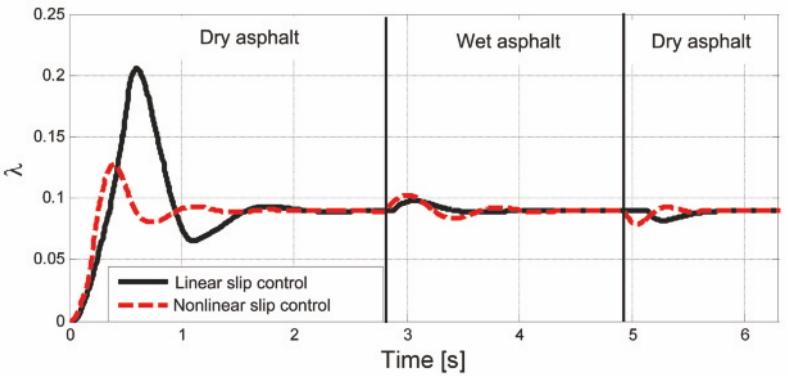

Figure 7.6 Time histories of the wheel slip λ with the linear slip controller (*solid line*) and with the nonlinear output feedback control (*dashed line*) in a double μ-jump braking manoeuvre from dry asphalt, $\mu = 1$, to wet asphalt, $\mu = 0.5$ and back to dry asphalt, for initial speed $v_{\text{in}} = 150$ km/h

7.3 Numerical Analysis

The simulation results presented refer to a front wheel. The wheel slip set-point value was set to $\overline{\lambda} = 0.09$. The MSC CarSim® simulator was complemented with the EMB dynamics given in (1.4). For comparison purposes, a fixed structure wheel slip controller based on a linearised model of the single-corner dynamics is also considered. The linear slip controller $R_\lambda(s)$ has been implemented with a PID control architecture of the type presented in Chapter 3. To propose a fair comparison between the two control approaches the fixed structure linear controller has been tuned to exhibit a similar transient behaviour to that given by the nonlinear output feedback controller in a nominal working condition, *i.e.,* a hard braking manoeuvre on dry asphalt. The linearisation was carried out around a value of the wheel slip beyond the peak of the $\mu(\lambda)$ curve.

Further, as discussed in Chapter 3, the linear wheel slip controller has been implemented together with the activation logic discussed in Section 3.7.

As for the nonlinear controller, it is always kept switched on also when the system is is manual mode, so as to provide a reliable output when it needs to be activated. The controller state is initialised with a value $\theta(0)$ lower than the steady-state value of the braking torque under any road condition. This is a conservative choice, which might be improved if an estimation of the road condition is available before the braking begins. Nonetheless, as the controller is active also before being activated, the simulation results confirm that the time interval before activation is usually long enough to achieve a good transient behaviour upon switching to automatic mode.

In Figure 7.6 the behaviour of the nonlinear controller is compared to that of the fixed structure linear slip controller during a hard braking manoeuvre when two successive changes in the road surface occur. As can be seen, the settling times of the wheel slip obtained with the two controllers are indeed quite similar. The larger overshoot of the linear controller is due on the one hand to the worst-case choice adopted for the design and on the other hand to the activation logic tuning and could be easily reduced by choosing another linearisation condition for the controller design or by tuning the activation logic thresholds differently (see Section 3.7).

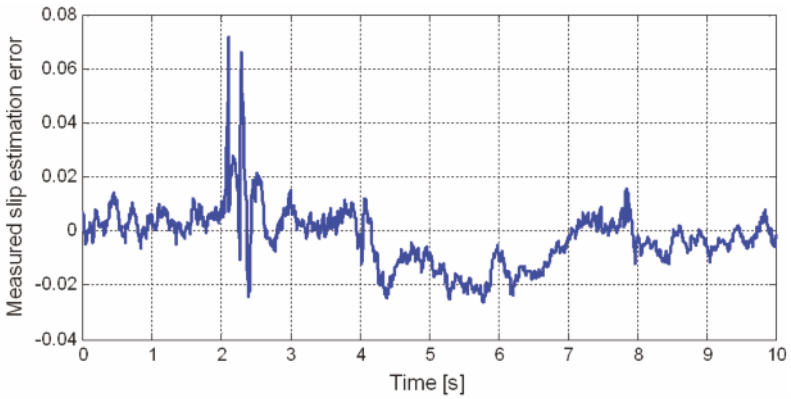

Figure 7.7 Time history of the measured wheel slip estimation error

Another important issue to analyse is the noise sensitivity of the nonlinear controller and, again, to compare it to that of the linear wheel slip controller. Figure 7.7 shows a time history of the wheel slip estimation error (obtained with the estimation algorithm described in Chapter 5) measured in experimental tests, which will be used in the simulations to model realistic noise on the wheel slip. In Figure 7.8 the time histories of the wheel slip λ and of the braking torque T_b during a hard braking manoeuvre with noisy slip measurements are displayed, and the nonlinear controller performance is again compared to that of the linear slip controller. Note that the noise sensitivity

of the nonlinear controller is remarkably lower than that of the linear one and this results in a much smoother transient of the wheel slip.

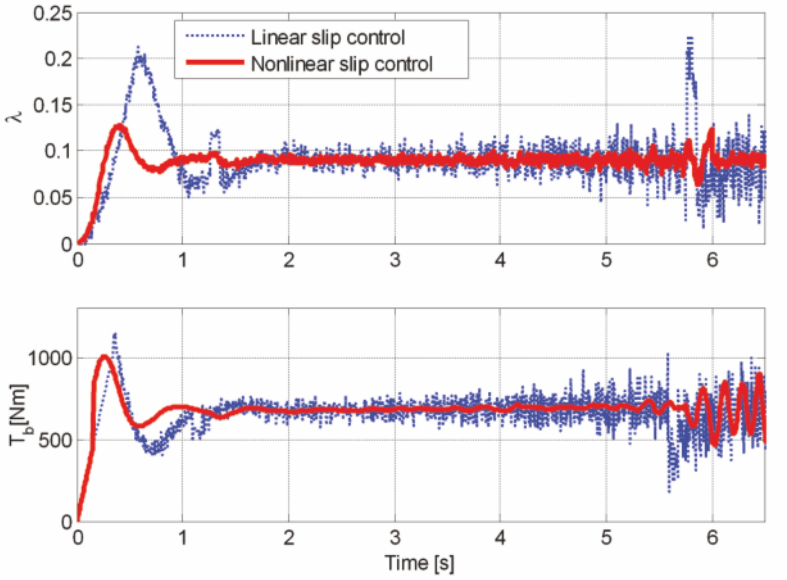

Figure 7.8 Time histories of the longitudinal wheel slip λ (a) and of the braking torque T_b (b) in a hard braking manoeuvre on dry asphalt obtained with the linear (*dotted line*) and with the nonlinear (*solid line*) wheel slip controller in the case of noisy wheel slip measurements, for initial speed $v_{\text{in}} = 150$ km/h

7.4 Summary

In this chapter, a nonlinear control law for wheel slip control was presented. The controller yields bounded control action and can cope with actuator constraints. Moreover, the control algorithm allows us to detect if the closed-loop system is operating in the unstable region of the friction curve, thereby allowing us to adapt the set-point and ensuring a great enhancement of both performance and safety.

Note that the proof of the closed-loop system stability was carried out without explicitly considering the actuator dynamics. To take these into account formally and prove that they do not alter the results obtained without considering them, one needs to resort to perturbation analysis (see, *e.g.,* [44]). This method, under the assumption that the actuator bandwidth is sufficiently large, allows one to separate the system dynamics from the actuator

ones, in view of their dynamic frequency decoupling (the system dynamics are seen as *slow*, whereas the actuator ones as *fast*). Based on the fact that the system and the actuator evolve on two separated time scales, it can be proved that the stability and tracking properties of the closed-loop system given in Proposition 7.1 are maintained by explicitly taking into account the actuator dynamics for sufficiently large values of the actuator bandwidth. Further, the analysis of the closed-loop system behaviour can be analysed *via* bifurcation theory to show that the the closed-loop system exhibits a Hopf bifurcation and to study its characteristics to optimise the braking performance. The interested reader is referred to [109].

Chapter 8
Identification of Tyre–road Friction Conditions

8.1 Introduction

Tyre–road friction characteristics are deeply interlaced with all vehicle safety oriented control systems as road conditions strongly affect the controlled system behaviour. Thus, the capability of estimating in real-time the friction conditions may provide a valuable source of information for any active vehicle control system. In particular, friction information can be used to enhance the performance of wheel slip control systems.

In this chapter we address three different problems related with friction estimation. Specifically, Section 8.2 illustrates an approach that is capable of estimating the sign of the slope of the friction curve, thereby allowing one to detect if the system is operating in the stable or in the unstable region of the friction curve. In fact, as largely discussed in this book, the equilibrium points associated with the wheel braking dynamics are stable for values of the wheel slip before the peak and unstable for those beyond the peak.

Hence, an online detection of the slope of the friction curve can be exploited to adapt and to optimise the closed-loop performance of wheel slip control systems. The advantage of this identification method is that it can be implemented also with a very limited set of sensors.

Secondly, in Section 8.3 an approach to the problem of estimating both the slip value corresponding to the peak of the friction curve and the parameters of the Burckhardt friction model (see Section 2.1) is presented. This is done by setting up a curve fitting problem which is then solved by two different identification approaches, namely a least squares and a maximum likelihood approach, arising from different parametrisations of the friction curve. A detailed analysis of the merits and drawbacks of the two approaches is also provided, which considers both the obtained accuracy in the estimated parameters and the convergence issues which have to do with the length of the available data set.

Finally, Section 8.4 presents an approach for estimating the instantaneous vertical and longitudinal forces from in-tyre acceleration measurements. Specifically, an appropriate set of sensors and regressors is illustrated, based on the measurements provided both by standard vehicle sensors (wheel encoders) and an accelerometer mounted directly in the tyre. Such estimates are based on the idea of extracting information from the phase shift between the wheel hub and the tyre, which is due to the transmission of traction and braking forces exerted on the tyre itself.

8.2 Detection of the Friction-curve Peak by Wheel-deceleration Measurements

In this section we focus on estimating the sign change of the slope of the curve $\mu(\lambda)$, which is responsible for the stability properties of the open-loop equilibrium points of the wheel dynamics. In particular, recall that for constant values of the braking torque, *i.e.*, for $T_b = \overline{T}_b$, the open-loop equilibrium points associated with slip values beyond the peak of the tyre–road friction curve are unstable (see Section 2.5.1).

The identification algorithm is formulated based on two different sensors configurations, *i.e.*, with and without wheel slip measurement (or estimation) available. This allows us to cover all the possible equipments available on commercial vehicles. Moreover, it is illustrated how such an identification algorithm can be employed within a supervisory control logic to enhance safety properties and performance of active braking systems.

To develop the identification approach, the considered dynamical model is the single-corner model discussed in Section 2.3. Once again, we treat the vehicle speed as a slowly-varying parameter and concentrate on the wheel dynamics only.

As discussed in Section 2.5.1, if we linearise the wheel dynamics (see the first equation of system (2.18)), the transfer functions $G_\lambda(s)$ from δT_b to $\delta\lambda$ and $G_\eta(s)$ from δT_b to $\delta\eta$ can be obtained. Specifically, they have the form

$$G_\lambda(s) = \frac{\frac{r}{J\overline{v}}}{s + \frac{\mu_1(\overline{\lambda})F_z}{m\overline{v}}\left((1-\overline{\lambda}) + \frac{mr^2}{J}\right)}, \tag{8.1}$$

and

$$G_\eta(s) = \frac{\frac{r}{Jg}\left(s + \frac{\mu_1(\overline{\lambda})F_z}{m\overline{v}}(1-\overline{\lambda})\right)}{s + \frac{\mu_1(\overline{\lambda})F_z}{m\overline{v}}\left((1-\overline{\lambda}) + \frac{mr^2}{J}\right)}. \tag{8.2}$$

For what follows, it is worth recalling that $G_\lambda(s)$ and $G_\eta(s)$ are both first-order transfer functions, characterised by the same pole. Moreover, recall also that the vehicle speed value $\overline{v}$ considered for the linearisation acts only as a scaling parameter on such pole, but it does not affect its sign.

In fact, as was shown in Section 2.5.1, the (real) pole of the transfer functions (8.1) and (8.2) is negative if and only if the following inequality holds

$$\frac{\mu_1(\overline{\lambda})F_z}{m\overline{v}}\left((1-\overline{\lambda})+\frac{mr^2}{J}\right)>0,$$

which can be reduced to

$$\mu_1(\bar{\lambda})>0,$$

where $\mu_1(\bar{\lambda})$ is as in (2.37) and it represents the slope of the tyre–road friction curve. Thus, the linear systems with transfer functions $G_\lambda(s)$ and $G_\eta(s)$ are unstable if the equilibrium point $\overline{\lambda}$ is *beyond* the peak of the friction curve. Accordingly, to detect the stability properties of wheel dynamics equilibrium points it is necessary to monitor the sign-change of $\mu_1(\bar{\lambda})$, *i.e.*, the slope of the tyre–road friction curve. It is worth pointing out that detecting a change of stability also gives a means for detecting the pair $(\mu_{\text{Max}}, \lambda_{\text{Max}})$ *i.e.*, the maximum tyre–road friction coefficient available on the current road condition and the corresponding value of the wheel slip.

8.2.1 Online Detection of the Sign of the Friction Curve Slope

We will now propose a strategy to monitor online the sign-change of $\mu_1(\bar{\lambda})$, *i.e.*, the slope of the tyre–road friction curve. To this end, we deal directly with the wheel dynamics, trying to find approximate static algebraic relationships linking measurable variables to the slope sign itself.

Differentiating the wheel dynamics given in the first equation of the single-corner model (2.15), we obtain

$$\begin{aligned}\ddot{\omega}&=\frac{\mathrm{d}}{\mathrm{dt}}\left(\frac{rF_x}{J}-\frac{T_b}{J}\right)=\frac{\mathrm{d}}{\mathrm{dt}}\left(\frac{rF_z\mu(\lambda)}{J}-\frac{T_b}{J}\right)\\&=\frac{r\,F_z}{J}\left.\frac{\mathrm{d}\mu(\lambda)}{\mathrm{d}\lambda}\right|_{\lambda=\bar{\lambda}}\dot{\lambda}-\frac{\dot{T}_b}{J}=\frac{r\,F_z}{J}\mu_1(\bar{\lambda})\dot{\lambda}-\frac{\dot{T}_b}{J}.\end{aligned}$$

We then define

$$H:=\ddot{\omega}+\frac{1}{J}\dot{T}_b=\frac{r}{J}F_z\mu_1(\bar{\lambda})\dot{\lambda}=\gamma\mu_1(\bar{\lambda})\dot{\lambda},\quad \gamma\in\mathbb{R}^+. \tag{8.3}$$

Equation (8.3) shows that we can relate the sign of $\mu_1(\bar{\lambda})$ to the wheel deceleration derivative (*i.e.*, the wheel *Jerk*) and to the braking torque derivative.

The above relation, though, has to be further analysed before being directly employed. In fact, the sign of H depends both on the sign of $\mu_1(\bar{\lambda})$ and on the sign of the wheel slip derivative $\dot{\lambda}$. In fact, it holds that

$$H > 0 \Leftrightarrow \left(\mu_1(\bar{\lambda}) > 0 \text{ AND } \dot{\lambda} > 0\right) \text{ OR } \left(\mu_1(\bar{\lambda}) < 0 \text{ AND } \dot{\lambda} < 0\right),$$

while

$$H < 0 \Leftrightarrow \left(\mu_1(\bar{\lambda}) < 0 \text{ AND } \dot{\lambda} > 0\right) \text{ OR } \left(\mu_1(\bar{\lambda}) > 0 \text{ AND } \dot{\lambda} < 0\right).$$

Based on this, two alternative strategies for solving such ambiguity and for deriving an expression for H suitable for online detection of the sign of the friction curve slope can be derived. The two strategies differ one from in other in that they are devised assuming that wheel slip measurement (or estimation) is either available or not available.

Let us start by assuming that the wheel slip can be either measured or estimated (for wheel slip estimation see Chapter 5). This assumption implies that the proposed strategy can be implemented on all passenger cars equipped with ABS and ESC sensors.

In this case, the slope sign can be derived as

$$\text{sign}(H) = \text{sign}\left(\ddot{\omega} + \frac{1}{J}\dot{T}_b\right)\text{sign}(\dot{\lambda}) = \text{sign}(\mu_1(\bar{\lambda})). \tag{8.4}$$

Hence, slope sign detection becomes a pure signal processing problem.

To cope with the disturbances affecting the measured signals, in the implementation of the friction curve slope sign detection strategy based on Equation 8.4, one should not use a pure zero-crossing detection algorithm, but it is necessary to define a small negative threshold on H. Such a threshold must been experimentally tuned according to the measurement noise in the available data and should fit all road conditions.

We now discuss how to estimate the slope sign when no slip measurement (or estimation) is available. The motivation for this analysis is to devise an identification strategy that can be implemented in any passenger car equipped only with standard ABS sensors (*i.e.*, wheel encoders and pressure sensors, but no longitudinal accelerometer).

Consider the expression of the wheel slip derivative

$$\dot{\lambda} = \frac{r}{v}\left(\frac{\omega}{v}\dot{v} - \dot{\omega}\right) = \frac{r}{v}\left(\frac{\omega}{v}\dot{v} + \frac{g}{r}\eta\right).$$

Assuming that the rate of change of the vehicle acceleration $\dot{v}$ is negligible with respect to that of the wheel deceleration $\dot{\omega}$, one has

$$\dot{\lambda} = -\dot{\omega}\frac{r}{v} = \eta\frac{g}{v}.$$

Accordingly, the slope sign estimator becomes

$$\text{sign}(H) = \text{sign}\left(\ddot{\omega} + \frac{1}{J}\dot{T}_b\right)\text{sign}(\dot{\lambda}) \cong \text{sign}\left(\ddot{\omega} + \frac{1}{J}\dot{T}_b\right)\text{sign}(\eta). \tag{8.5}$$

Thus, the estimation of the sign of $\mu_1(\bar{\lambda})$ can be recast as the detection of the sign of two components, both of which are measurable on every passenger car.

It is worth analysing the effects of the approximation used in deriving (8.5). As we are concerned with braking manoeuvres, by approximating the slip velocity $\dot{\lambda}$ with the normalised wheel acceleration η, we neglect a negative term dependent on $\dot{v}$. Hence the following inequality holds:

$$\frac{\omega}{v}\dot{v} + \frac{g}{r}\eta < \frac{g}{r}\eta. \tag{8.6}$$

Inequality (8.6) shows that η changes sign before $\dot{\lambda}$ when the wheel slip is increasing, while the opposite is true when the wheel slip is decreasing (*i.e.*, during the pedal release phase). In both cases, there is a time interval during which η and $\dot{\lambda}$ lose their concordance and the algorithm based on Equation 8.5 fails in detecting the slope sign. This means that expression (8.5) can be error prone at the beginning of very hard braking manoeuvres.

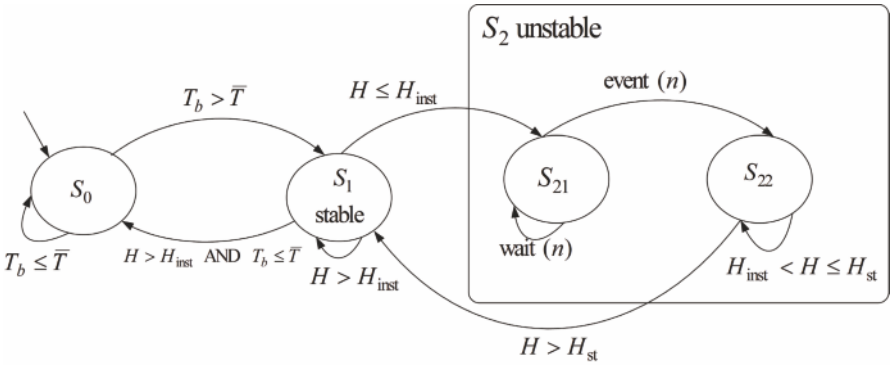

Figure 8.1 FSM representation of the proposed ABS supervisory control logic

8.2.2 ABS Supervisory Control Logic

To enhance passenger safety, it is possible to employ the slope sign detection strategy as a supervisory control logic, that commands, for example, the ABS system control actions. To this end, we are interested in detecting the slope sign change in both directions, *i.e.*, from positive to negative and *vice versa*.

In order for the proposed logic to be integrated with standard ABS systems, we assume that no slip measurement (or estimation) is available. Hence, the proposed results are based on Equation 8.5. An FSM representation of a supervisory control logic is depicted in Figure 8.1.

As can be seen, it is composed of three states, each with an associated control action. Specifically, one has:

- S_0: the initial and final state. No control action is sent to the core ABS system.
- S_1: the system is in the stable region of the tyre–road friction curve, hence the ABS system is allowed to increase the braking torque T_b.
- S_2: the system is in the unstable region of the tyre–road friction curve, hence the ABS system is commanded to decrease the braking torque T_b. S_2 is further decomposed into S_{21} and S_{22}, whose meaning will be clarified below.

The overall supervisory logic works as follows: the system remains in S_0 while no braking occurs, *i.e.*, while $T_b < \bar{T}$, where $\bar{T}$ is a properly tuned threshold. When $T_b \geq \bar{T}$, a transition to the stable region S_1 occurs. The system remains in this state until $H > H_{\text{inst}}$ where H_{inst} is the (negative) threshold identifying a negative slope sign.

Once $H \leq H_{\text{inst}}$, the system signals the crossing of the stability boundary and enables the transition to the state S_2. Actually, the system enters the substate S_{21}, where it waits for n ms before entering S_{22}. The rationale under the *wait* action is that even if the release action is triggered by the transition from S_1 to S_2, current ECU network topologies do not allow for an immediate system response.

Accordingly, the substate S_{21} ensures that the detection of a positive slope sign is not missed by evaluating H at the same time instant at which the release action takes place. While the instability condition persists (*i.e.*, as long as the estimated slope sign is negative), the system remains in S_{22} and the release phase is continued by the ABS system. When $H \geq H_{\text{st}}$ (H_{st} being the positive threshold identifying positive slope sign), stability is re-gained and a transition to S_1 takes place. Finally, when the braking manoeuvre is over, the system goes back to the final state S_0.

8.2.3 Experimental Results

To analyse the performance of the identification algorithm, test drives have been carried out by performing strong braking manoeuvres on two different road conditions, *i.e.,* a high-grip asphalt road and a low-grip off-road.

All the measured signals (wheel encoders, longitudinal accelerometer and pressure sensors) are assumed to come from properly calibrated sensors. For a discussion on the processing issues related to wheel encoders the reader is referred to Appendix B.

Figures 8.2(a) and 8.2(b) show the time histories of the wheel slip and of the detection of the stability boundary crossings obtained *via* Equation 8.4, *i.e.*, assuming that wheel slip measurements are available, on high-grip and

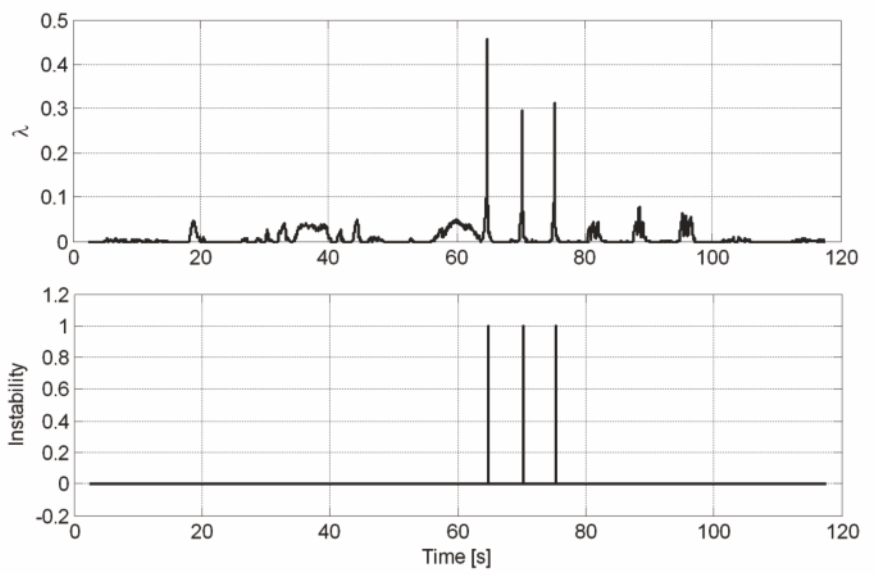

(a)

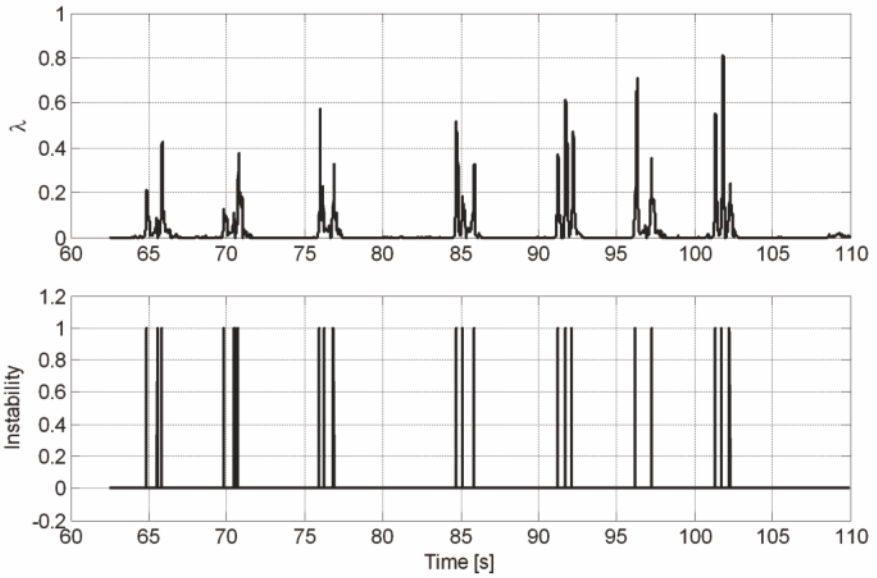

(b)

Figure 8.2 Time histories of the wheel slip (top) and of the detection of the stability boundary crossings (bottom) obtained with (8.4). (a) high-grip road, (b) low-grip off-road

low-grip roads, respectively. Notice that the slope sign detection is very accurate on both road conditions. In fact, analysing the results obtained with the friction curve slope sign change detection algorithm based on Equation 8.4 (averaging the results obtained in all tests on both road conditions), we have $E[\lambda_{\text{Max}}] = 0.0854$ on the high-grip road and $E[\lambda_{\text{Max}}] = 0.1357$ on the low-grip off-road, which is compatible with the tyre–road friction conditions of the test grounds.

To visually inspect the performance of the estimation algorithms when no wheel slip measurement (or estimation) is available, refer to Figures 8.3(a) and 8.3(b), which depict the time histories of the wheel slip and of the detection of the stability boundary crossings obtained via Equation 8.5 on high-grip and low-grip roads, respectively. Analysing the results obtained with the slope sign detection algorithm based on (8.5), (averaging the results obtained in all tests on both road conditions) one finds $E[\lambda_{Max}] = 0.0648$ on the high-grip road and $E[\lambda_{Max}] = 0.1283$ on the low-grip off-road. Thus, the slope sign detection can also be reliably performed with no direct information on the wheel slip.

Finally, it is worth investigating the adaptation of the identification algorithm to the supervisory control logic presented in Section 8.2.2. We recall that it asks us to detect the slope sign change in both directions.

Figures 8.4(a) and 8.4(b) show the results obtained on dry and off-roads, respectively. Apparently, the proposed supervisory logic can be profitably employed both to enhance the safety properties of ABS systems and to optimise their performance. In fact, the parameters of the ABS controller might be adaptively tuned according to the current system stability properties.

8.3 Real-time Identification of Tyre–road Friction Conditions

In this section, we consider the problem of estimating the wheel slip value corresponding to the abscissa of the peak of the tyre–road friction curve combined with the capability of identifying also the full parametrisation of the tyre–road friction curve itself.

The characteristics of the friction estimation strategies are analysed and tested both in simulation and on experimental data. In the latter case, the performance of the identification techniques is tested also in combination with the wheel speed estimation algorithm discussed in Section 5.3, in order to discuss its effects on the accuracy of the final results.

Specifically, the identification approach is based on the solution of a curve fitting problem formulated using a properly parameterised friction model. The slip value corresponding to the curve peak is subsequently estimated from the fitted curve. To this aim, the Burckhardt friction model (see Section 2.1) is considered.

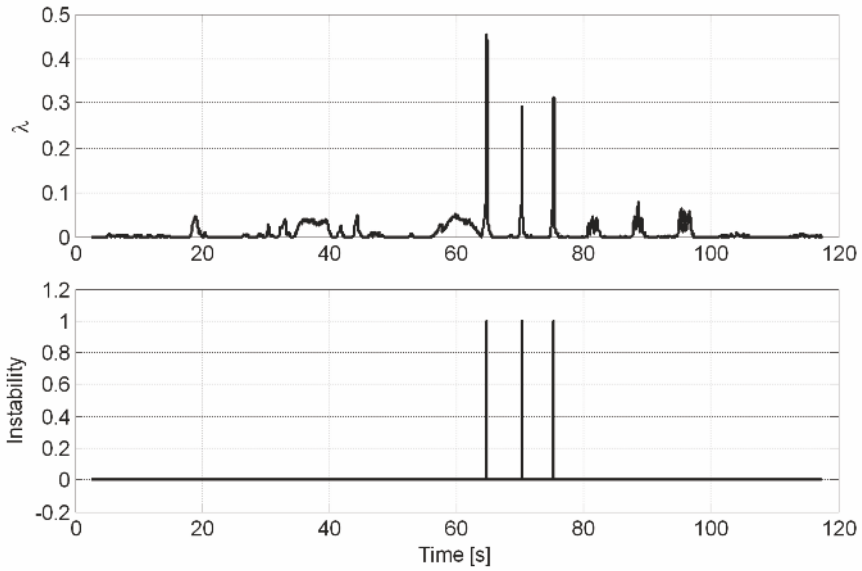

(a)

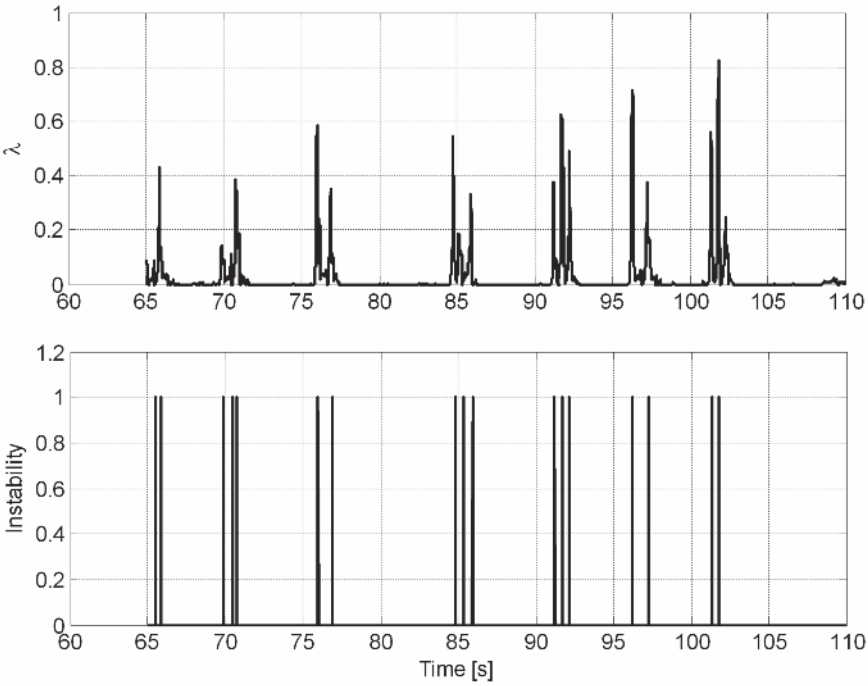

(b)

Figure 8.3 Time histories of the wheel slip (top) and of the detection of the stability boundary crossings (bottom) obtained with (8.5). (a) high-grip road, (b) low-grip off-road

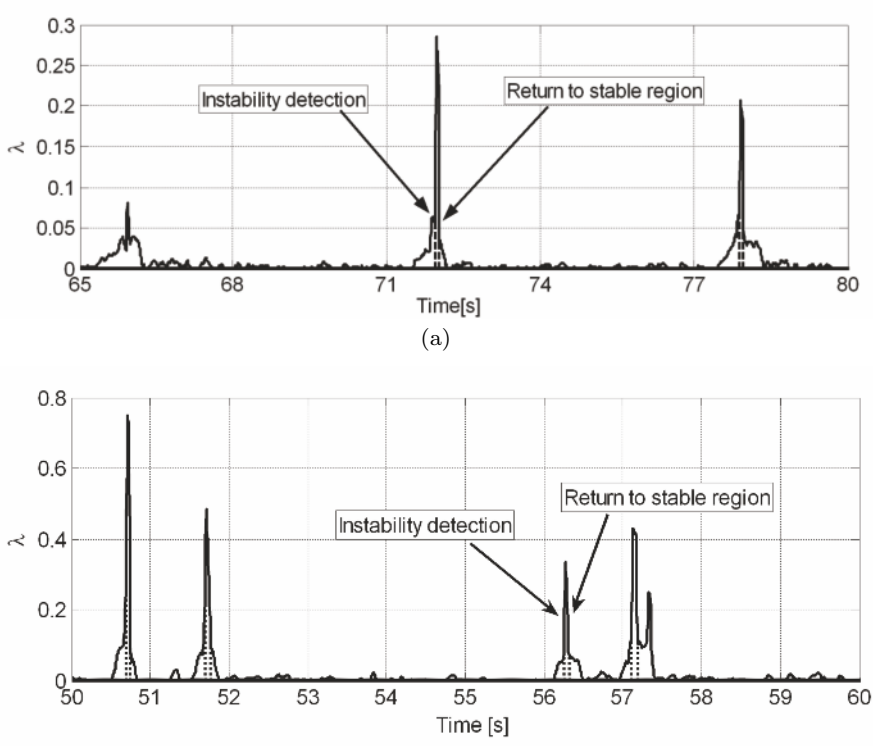

Figure 8.4 Time histories of the wheel slip (*solid line*) and detection of the stability boundary crossings (*dashed line*). (a) high-grip road, (b) low-grip off-road

In presenting this topic, we assume that the reader has a basic familiarity with linear system identification methods, specifically with the least squares (LS) approach and with the maximum likelihood (ML) approach. For more details on the identification algorithms, the interested reader is referred to, *e.g.*, [61, 62, 99].

Since the Burckhardt model is nonlinear in the parameters, an iterative ML estimation technique is applied first. Further, to evaluate the practical applicability of the method for online use, a recursive version of the algorithm is also investigated. Secondly, a (recursive) LS method is introduced, based on an *ad hoc* parametrisation of the friction model which is linear in the parameters.

To set up the identification problem, let us assume that the signals ω, v, λ and T_b are available. As such, one can work on the single-corner dynamics (see also Equation 2.18)

$$\dot{\lambda} = -\frac{1}{v}\left(\frac{(1-\lambda)}{m} + \frac{r^2}{J}\right) F_z \mu(\lambda) + \frac{r}{vJ} T_b, \tag{8.7}$$

and invert it to obtain data points of the type $\mu(\omega, v, T_b, \lambda)$, which constitute the basis for collecting data suitable for the estimation of the tyre–road friction curve $\mu(\lambda)$. Actually, note that the angular wheel velocity ω and the braking torque T_b can be assumed to be measurable (in particular, T_b is assumed to be proportional to the pressure in the hydraulic braking circuit by a known coefficient, see Equation 1.1), while v is generally not available and needs to be estimated. Finally, λ can be determined from ω and v.

Namely, expressing v as $\omega r/(1-\lambda)$, $\mu(\lambda)$ can be easily obtained from (8.7) as

$$\mu(\lambda; t) = \frac{\frac{1-\lambda(t)}{J\omega(t)} T_b(t) - \dot{\lambda}(t)}{\frac{1-\lambda(t)}{\omega(t) r} F_z(t) \left(\frac{1-\lambda(t)}{m} + \frac{r^2}{J}\right)}, \tag{8.8}$$

where the dependence on time is made explicit in order to point out that (8.8) holds at each time instant. Note that the right-hand side of (8.8) depends on $\omega(t)$, $\lambda(t)$, $\dot{\lambda}(t)$, r, $T_b(t)$ and $F_z(t)$. Thus, in principle, if noise-free measurements of such variables were available, one could estimate the corresponding sample of $\mu(\lambda; t)$ exactly.

However, $\omega(t)$ and $T_b(t)$ are measured from noisy sensors, $\lambda(t)$ is derived *via* speed estimation and hence it is affected by the estimation error and the vertical load $F_z(t)$, together with the wheel radius r, differs from its static value depending on the braking (or traction) induced pitch angle and tyre characteristics (see also Appendix B). Note, however, that according to the longitudinal tyre force model given in (2.12), the vertical load $F_z(t)$ acts only as a scaling factor on the friction curve, thus not altering the abscissa of the maximum.

In summary, (8.8) is in fact a highly nonlinear function of data and noise, which can only provide approximate and noisy samples of $\mu(\lambda; t)$. Accordingly, to set up a curve fitting problem with the aim of identifying tyre–road friction conditions, (8.8) is used to compute the observations from data, while suitable parametrisations based on Burckhardt model in (2.13) are employed to formulate the tyre–road friction relation (see the next section).

8.3.1 Identification Strategies

Based on the problem setting given in the previous section, a curve fitting problem can be set up to estimate $\mu(\lambda)$, and thus to obtain λ_{Max} from the estimated friction curve. The first of these two tasks is addressed by minimisation of a standard quadratic error function of the form

$$J(\vartheta) = \frac{1}{N}\sum_{i=1}^{N}\epsilon(\lambda_i,\vartheta)^2, \tag{8.9}$$

where N is the number of samples and $\epsilon(\lambda_i,\vartheta) = \mu(\lambda_i) - \widehat{\mu}(\lambda_i,\vartheta)$ is the estimation error. The next subsections focus on the derivation of suitable methods for fitting the tyre–road friction curve.

8.3.1.1 The Maximum Likelihood Approach

The most direct approach for the estimation of the tyre–road friction curve involves the use of the Burckhardt model (2.13), where ϑ_r is the vector of unknown parameters to be determined. Unfortunately, the structure of that model is nonlinear in the parameters and simple algorithms like the LS method cannot be applied to this case. The computationally more intensive ML approach must be used instead, [99].

The method performs an iterative minimisation of the fitting error criterion (8.9) by means of a quasi-Newton method [99], which ultimately amounts to adjusting the parameter vector at each iteration on the basis of the following expression:

$$\vartheta^{(r+1)} = \vartheta^{(r)} + \Big(\sum_{i=1}^{N}\xi(\lambda_i)\xi(\lambda_i)^T\Big)^{-1}\Big(\sum_{i=1}^{N}\xi(\lambda_i)\epsilon(\lambda_i)\Big), \tag{8.10}$$

where

$$\xi(\lambda_i) = -\frac{\mathrm{d}\epsilon(\lambda_\mathrm{i})^\mathrm{T}}{\mathrm{d}\vartheta} = [\,1 - e^{-\lambda_i\vartheta_{r2}} \quad \vartheta_{r1}\lambda_i e^{-\lambda_i\vartheta_{r2}} \quad -\lambda_i\,]^T.$$

A crucial step in the ML approach is the initialisation of the parameter vector. An *ad hoc* empirical approach has been adopted for this purpose. Actually, for low values of the wheel slip, the Burckhardt model can be approximated as

$$\mu(\lambda,\vartheta_r) \cong (\vartheta_{r1}\vartheta_{r2} - \vartheta_{r3})\lambda - \vartheta_{r1}\vartheta_{r2}^2\lambda^2. \tag{8.11}$$

Now, since the parameter ϑ_{r3} varies in an extremely small range, from 0.06 for snow to 0.67 for cobblestone (see Table 8.1), an average value of 0.4 can be reasonably assumed as initial value $\widehat{\vartheta}_{r3}(0)$. Then, using the first available data, which appropriately correspond to low slip values, one can interpolate the quadratic approximation above to derive the initial values $\widehat{\vartheta}_{r1}(0)$ and $\widehat{\vartheta}_{r2}(0)$.

Several recursive versions of the general iterative batch algorithm described above have been developed in the literature, see *e.g.,* [62]. These exploit the structural similarity between the iteration equation of the ML method and the well-known LS equation and recover the same computational schemes of the

recursive LS (RLS) methods. Notice, however that in this case the recursive scheme mixes the data recursion with the iterative mechanism inherent in the ML approach, so that convergence may be harder to obtain with recursive ML (RML), as opposed to RLS.

8.3.1.2 The Least Squares Approach

In view of the potential convergence problems of the RML approach discussed in the previous section (which will be thoroughly analysed on the data of interest in Section 8.3.2), an alternative estimation scheme is presented based on a linear regression reformulation of the friction model and LS estimation.

The Burckhardt model (2.13) is nonlinear by way of the exponential term in ϑ_{r2}, which varies in a relatively small range of values depending on the road conditions. As an alternative, such a term can be approximated using a linear combination of fixed exponentials, suitably dispersed to cover the whole range of interest [33]. This results in the model

$$\widehat{\mu}(\lambda) = a_1 e^{-b_1\lambda} + a_2 e^{-b_2\lambda} + \cdots + a_{n-2} e^{-b_{n-2}\lambda} + a_{n-1}\lambda + a_n, \qquad (8.12)$$

where a_{n-1} and a_n equal $-\vartheta_{r3}$ and ϑ_{r1} in model (2.13). If the $b_i, i = 1, \cdots, n-2$ exponents are fixed *a priori*, model (8.12) can be recognised as a linear regression

$$\widehat{\mu}(\lambda) = \varphi(\lambda)^T \theta,$$

where

$$\varphi(\lambda) = \left[e^{-b_1\lambda}, \cdots, e^{-b_{n-2}\lambda}, \lambda, 1\right]^T$$
$$\theta = \left[a_1, \cdots, a_n\right]^T,$$

to which LS estimation methods can be directly applied. The number of exponentials in the approximate model has been set to four *via* a trial and error process, aimed at establishing a satisfactory compromise between model flexibility and size (to avoid overfitting).

Parameters $b_i, i = 1, \cdots, 4$ have been chosen as uniformly distributed in the range $[4,\ 100]$, which includes all the values of ϑ_{r2} in the considered road conditions. More precisely, $b_1 = 4$, $b_2 = 36$, $b_3 = 68$ and $b_4 = 100$.

8.3.2 Numerical Analysis

In order to evaluate the behaviour of the estimation strategies described in the previous section, it is important to preliminarily discuss which are the performance levels to be sought in the considered application.

Specifically, accuracy requirements are set by the characteristics of typical vehicle electronic and control devices. More precisely, as far as the expected performances are concerned, a reasonable objective is to obtain an overall accuracy in the estimation of the abscissa of the peak of the friction curve of $\pm 5\%$, which is considered appropriate for ABS control [90]. Furthermore, the estimator should provide reliable information within the time instant at which the braking controller would be activated. Since this time interval can be approximately quantified to be at most of 500 ms, and data in these applications are typically sampled at 200 Hz, the estimation algorithms have been tested with 100 samples.

To investigate the performance of the two estimation strategies introduced in the previous section, simulation tests, which were carried out based on the single-corner model dynamics, are now presented. In order to consider a more realistic setting, though, all identification methods have been tested on noisy simulation data.

Specifically, zero mean white noises have been added to the wheel speed ω, to the vehicle speed v and to the braking torque T_b, with $\sigma_\omega^2 = 0.005$ rad^2/s^2, $\sigma_v^2 = 0.25$ m^2/s^2 and $\sigma_{T_b}^2 = 10$ N^{2}m^2, respectively. In the case of v and ω, which represent the quantities based on which the wheel slip is computed, the noise variance values should correctly model the fact that the noise acting on the wheel speed ω is only due to measurement noise (ω is directly measured by means of a wheel encoder), while the noise acting on the vehicle speed is also due to estimation errors, see also the discussion in Chapter 6.

Let us first analyse the results obtained with the ML approach. To do this, consider Table 8.1, which reports the results on the parameter estimation obtained with ML and RML algorithms. Actually, while an almost perfect curve fitting (and a quite accurate parameter estimation) is obtained with the batch ML approach in all tested road conditions, the same does not apply to the computationally more affordable RML method.

Table 8.1 Summary of the $\mu(\lambda)$ estimation obtained with ML and RML on noisy simulation data

		Dry asphalt	Wet asphalt	Cobblestone	Snow
True values	ϑ_1	1.28	0.86	1.37	0.19
	ϑ_2	23.99	33.82	6.46	94.13
	ϑ_3	0.52	0.35	0.67	0.06
ML	$\widehat{\vartheta}_1$	1.29	0.86	1.48	0.18
	$\widehat{\vartheta}_2$	22.69	31.94	5.79	90.95
	$\widehat{\vartheta}_3$	0.57	0.36	0.85	0.04
	# iter.	4	4	5	4
RML	$\widehat{\vartheta}_1$	1.24	0.86	1.12	0.22
	$\widehat{\vartheta}_2$	27.34	35.36	9.73	60.07
	$\widehat{\vartheta}_3$	0.38	0.37	0.29	0.37

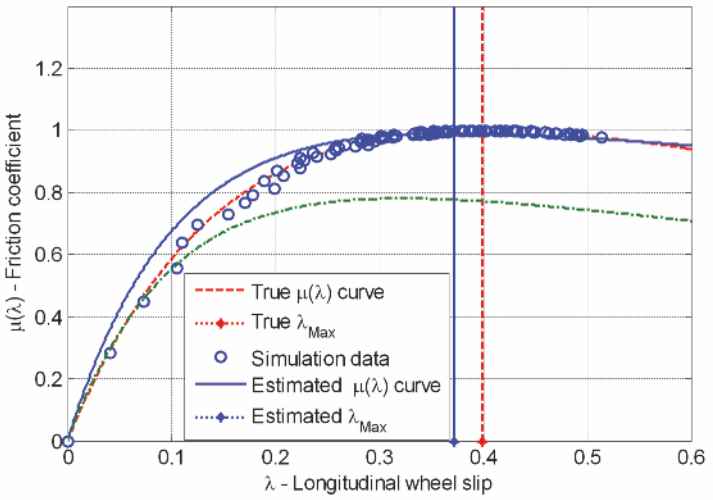

Figure 8.5 Curve fitting results with RML on cobblestone: simulated data (*dots*), theoretical $\mu(\lambda)$ curve (*dashed line*), initial estimation (*dash-dotted line*), estimated $\mu(\lambda)$ curve (*solid line*), true λ_{Max} (*dashed vertical line*) and estimated λ_{Max} (*solid vertical line*)

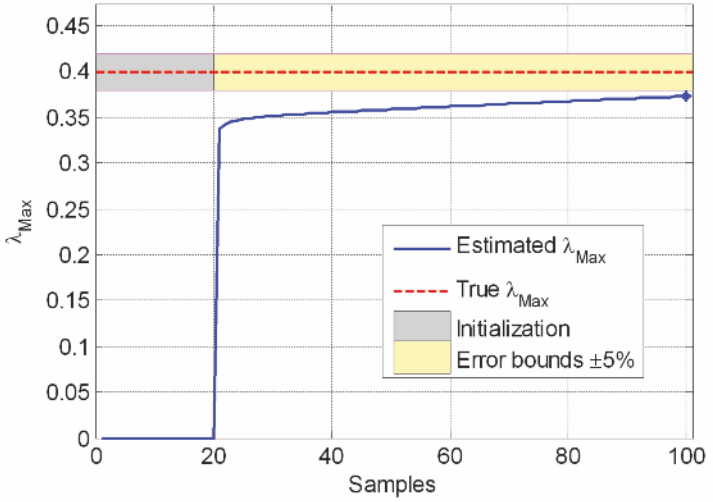

Figure 8.6 Results of $\widehat{\lambda}_{\mathrm{Max}}$ estimation with RML on cobblestone: true value (*dashed line*), estimated value (*solid line*), initialisation period (*dark grey*) and 5% error band (*light grey*)

Let us consider in more detail the cobblestone case, for which simulation results are depicted in Figures 8.5 and 8.6. Note that, among all those avail-

able, this particular type of road condition has been selected for discussion as it represents a particularly hard case for identification purposes, being almost flat in the neighbourhood of the maximum. Notice that data are not available for high slip values, so it should not be surprising that unsatisfactory accuracy is experienced in that range. Recall, however, that the ultimate objective of the estimation problem is the peak abscissa evaluation, which can be satisfactorily addressed, as long as the available data encompass the maximum point of the curve. In the case reported in Figure 8.5, the curve fit is only approximately correct in the operating range, resulting in an under-estimation of λ_{Max}. What is more, while the estimation of λ_{Max} quickly approaches the correct value, after an initialisation period of 20 samples, it converges extremely slowly, revealing that the RML method inefficiently exploits the information in the data. Also, accurate curve fitting is obtained only where the samples are more numerous, that is close to the peak point. In any case, a remarkably low 10% error in the estimation of λ_{Max} is achieved after only 30 samples, *i.e.*, with sufficient advance with respect to the critical point in the braking process. This information, as will be further discussed in Section 8.3.3, can be valuably exploited by ABS and wheel slip control systems.

Table 8.2 reports the results of the estimation of λ_{Max} with both the batch and the recursive ML method, based on the respective estimated friction curves. Apparently, RML provides generally worse peak estimation, an exception being the snow case.

The difference in performance between the ML and RML methods on the snow case is due to the fact (see also Figure 2.3) that the friction curve in this case has an almost flat right portion and this fools the ML method – as the great majority of the available data are not descriptive of the peak dynamics – while better results are achieved with the RML approach. This is because the *ad hoc* initialisation procedure is particularly effective on this surface. As a matter of fact, the λ_{Max} value being very low, the interesting part of the curve is well captured by the initialisation samples (see also Equation 8.11). In the RML case, then, the recursive nature of the method can better exploit a good initialisation than the batch version, which tries to fit, in the ML sense, the whole dataset in one shot.

Some general remarks concerning RML are in order. Apparently, due to numerical ill-conditioning of the gradient term of the parameter tuning equation, parameters ϑ_{r2} and ϑ_{r3} are only slightly moved from the initial values. Given the better performance of the batch version of the algorithm, this can only be ascribed to the fact that RML combines the iterative nature of the ML approach with data recursion. To deal with this problem, it is convenient to modify the update equations for ϑ_{r2} and ϑ_{r3} inserting an additional gain factor to speed up convergence. If computationally viable, a few batch iterations could also be performed as soon as RML convergence does not significantly improve. This last variation, denoted in the following as RML+ML, has yielded significantly better results in simulation and its performance on experimental data will be analysed in Section 8.3.3.

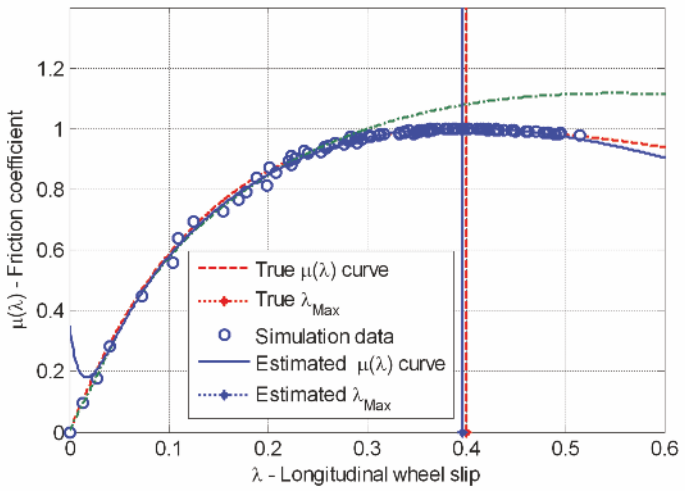

Figure 8.7 Curve fitting results with RLS on cobblestone: simulated data (dots), theoretical $\mu(\lambda)$ curve (*dashed line*), initial estimation (*dash-dotted line*), estimated $\mu(\lambda)$ curve (*solid line*), true λ_{Max} (*dashed vertical line*) and estimated λ_{Max} (*solid vertical line*)

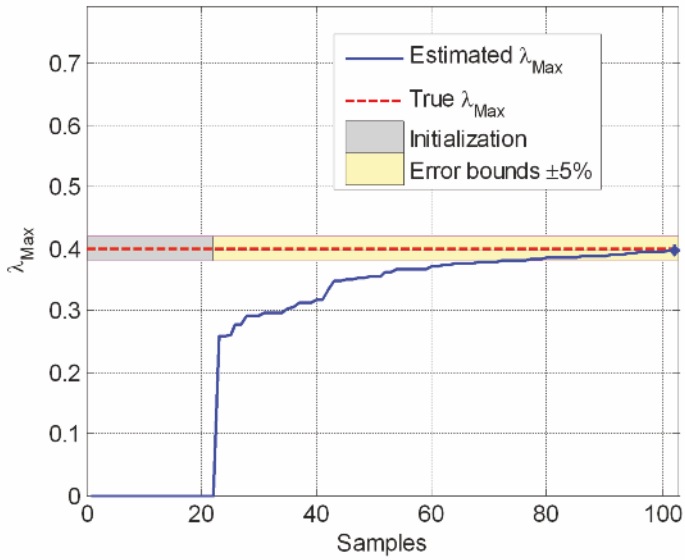

Figure 8.8 $\widehat{\lambda}_{\mathrm{Max}}$ estimation results with RLS on cobblestone: true value (*dashed line*), estimated value (*solid line*), initialisation period (*dark grey*) and 5% error band (*light grey*)

Table 8.2 Summary of the λ_{Max} estimation performances obtained with ML and RML on noisy simulation data

		Dry asphalt	Wet asphalt	Cobblestone	Snow
True values	λ_{Max}	0.1700	0.1307	0.3995	0.0605
	μ_{Max}	1.1699	0.8039	1.0014	0.1857
ML	$\widehat{\lambda}_{\text{Max}}$	0.1737	0.1350	0.3989	0.0656
	$\widehat{\mu}_{\text{Max}}$	1.1700	0.8035	0.9998	0.1848
	$\epsilon_\lambda\%$	2.17%	3.28%	0.15%	8.42%
RML	$\widehat{\lambda}_{\text{Max}}$	0.1641	0.1242	0.3723	0.0594
	$\widehat{\mu}_{\text{Max}}$	1.1679	0.8048	0.9906	0.1929
	$\epsilon_\lambda\%$	3.47%	4.97%	6.8%	1.81%

Table 8.3 Summary of the λ_{Max} estimation performances obtained with LS and RLS on noisy simulation data

		Dry asphalt	Wet asphalt	Cobblestone	Snow
True values	λ_{Max}	0.1700	0.1307	0.3995	0.0605
	μ_{Max}	1.1699	0.8039	1.0014	0.1857
LS and RLS	$\widehat{\lambda}_{\text{Max}}$	0.1786	0.1370	0.3966	0.0658
	$\widehat{\mu}_{\text{Max}}$	1.1696	0.8024	1.0019	0.1849
	$\epsilon_\lambda\%$	5.05%	4.84%	0.73%	8.76%

Let us now move to investigate the performance of the LS and the RLS algorithms. In the simulations, the RLS algorithm was initialised using the batch LS method on the first 20 available data. The estimation performances for λ_{Max} are reported in Table 8.3. Notice that 100 data are sufficient for the RLS to converge exactly to the estimates obtained with the LS method. Overall, the LS approach is slightly less accurate than ML, but no significant deterioration resulting from the recursive version of the algorithm is experienced.

Also for the RLS method, the snow case experiences the worst estimation performance in terms of relative error (note that the absolute one is still comparable to the other surfaces). This is mainly because, as observed analysing the ML approach, λ_{Max} takes on a very low value which makes relative error an unfair metric for this specific case. Moreover, because of the large difference between the numerical values of all the snow parameters ϑ_r (all of them differ of more than an order of magnitude from each other), one would need specific scalings in the RLS gains to significantly improve performance. However, as the results are acceptable also on this kind of surface, scaling has been avoided, as it would be surface dependent and therefore not applicable in practice.

For comparison purposes, consider again the cobblestone case, for which simulation results are represented in Figures 8.7 and 8.8. In Figure 8.7 notice the significant estimation error in the initial part of the curve, which is a result

of using an empirical model as opposed to the Burckhardt one. Nevertheless, a remarkable accuracy is achieved near the peak, so that λ_{Max} can be estimated almost exactly.

Concerning the convergence properties of λ_{Max} estimation (see Figure 8.8), one can observe that with RLS the initialisation process is not so efficient in approaching the correct value quickly as in the RML case, but convergence is faster, so that 10% λ_{Max} estimation error is achieved only slightly later (after 40 samples) and 5% error after 70 samples.

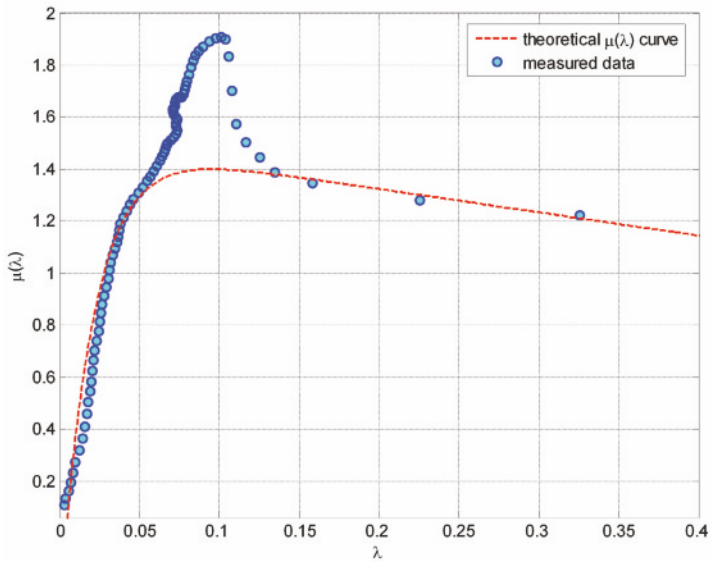

Figure 8.9 Example of data (*dots*) measured on the front wheel on high-grip asphalt road and the theoretical $\mu(\lambda)$ curve (*red dashed line*)

8.3.3 Experimental Results

Before analysing the estimation results obtained with the identification approaches on measured data, some remarks are due. Specifically, refer to Figure 8.9, where an example of the samples of $\mu(\lambda; t)$ measured on the front left wheel on high-grip asphalt road is shown together with the theoretical tyre–road friction curve related to the road condition used in the tests. Note that the theoretical curve in Figure 8.9 has been derived considering also the increased vertical load experienced by the front wheel during braking. As is apparent by inspection of Figure 8.9, experimental data are significantly dif-

ferent from those obtained in simulation, and this is due to several concurring phenomena:

1. First of all, the $\mu(\lambda)$ curve is intrinsically a static description of the tyre–road friction condition, in that it represents the collection of the steady-state friction coefficient values associated with the corresponding value of the wheel slip. Note that this fact does not depend on the analytical model chosen (the Burckhardt one in this case); the same would have held true if, for example, the Pacejka model had been used (see Section 2.2). When looking at real data, instead, several dynamic phenomena, mainly suspension elasticity and tyre relaxation, cause the real $\mu(\lambda)$ values to exhibit the overshoot clearly visible in Figure 8.9, which also accounts for dynamic load transfer effects.
2. Secondly, as the test was carried out with a real, albeit professional, driver, it is very unlikely that the measured data go significantly beyond the peak value of the $\mu(\lambda)$ curve. When this happens, in fact, the car experiences a significant loss of driveability, and the driver is forced to release the brake pedal to avoid losing control of the vehicle.
3. Finally, the initialisation phase for both algorithms on experimental data has been linked to the wheel slip behaviour. Specifically, both RLS and RML+ML are initialised when the wheel slip is be such that $\lambda > \lambda_{\text{init}}$. The value of $\lambda_{\text{init}} = 0.07$ was chosen based on the analysis of the measured data.

Notice that even though these dynamic phenomena apparently change the shape of the $\mu(\lambda)$ curve, they cause a very small change (if any) of the value of λ_{Max}, that is the abscissa of its peak. Therefore, as the main aim of the identification procedure is that of estimating such a value so that it can be used as input for braking control systems, the identification algorithms do not lose their capability of pursuing this objective.

8.3.3.1 Wheel Slip Measurements Available

We first discuss the estimation results obtained when the vehicle speed is exactly measurable, *i.e.*, by employing the speed signal obtained with an optical sensor, and thus the wheel slip can be directly measured.

Note that here the main aim is to verify that upon controller activation, the proposed estimation algorithm is able to provide a consistent estimate $\widehat{\lambda}_{\text{Max}}$ of the value of the abscissa of the peak point of the friction curve. To this end, we assume that the ABS is switched on when the current wheel slip value exceeds a predefined threshold, which has been set to $\lambda = 0.15$. Note that on real ABS systems, see Section 3.7, it is possible to have a dynamic activation threshold selection, which tunes the activation slip value also based on the braking intensity. Nonetheless, as the aim of the experiments is that of testing the identification performance obtainable with a limited number

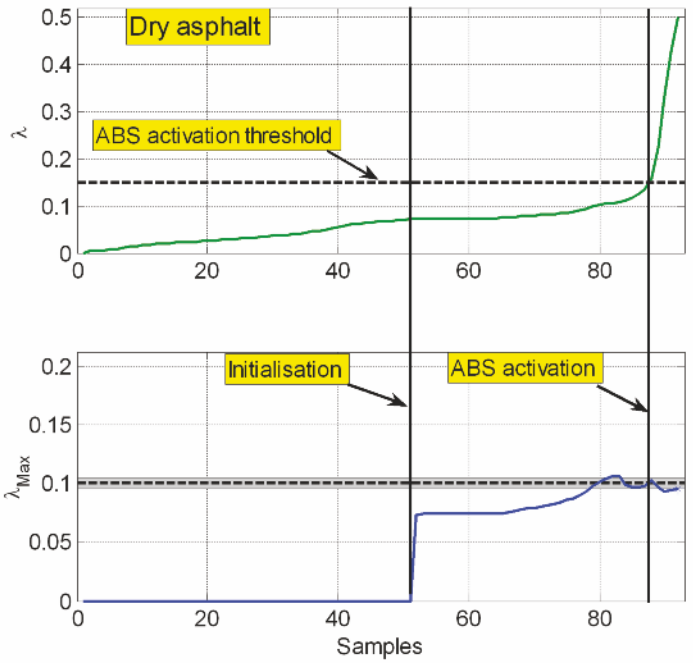

Figure 8.10 Plot of the slip λ as function of samples (*top, solid line*) and the ABS activation threshold (*top, dashed line*) and $\widehat{\lambda}_{\mathrm{Max}}$ estimation results with RLS on high-grip asphalt road (*bottom*): theoretical value (*dashed line*), estimated value (*solid line*), initialisation period (*grey*) and 5% error band (*grey*)

of data a constant threshold is appropriate. Accordingly, besides evaluating the final results of the estimation when all the available 100 samples are processed, we also monitor at which sample the ABS would virtually be activated and how accurate our estimation is at that time instant.

The estimation results obtained on dry asphalt road with the RLS method are shown in Figure 8.10, while those obtained on low-grip off-road with the RML+ML method are shown in Figure 8.11. Both these figures also show the time history of the wheel slip and highlight the ABS activation threshold. As can be seen, the estimation of λ_{Max} is quite satisfactory and, most importantly, it is reliable also at the time instant at which the ABS would be activated, even if this happens when less than 100 samples have been processed.

A quantitative summary of the overall results obtained with RLS and RML+ML with measured vehicle speed for both friction conditions is provided in Table 8.4. As can be seen, while on dry asphalt the performances of the two algorithms are comparable, RLS shows its better features with respect to RML+ML on low-grip off-roads, where the availability of fewer

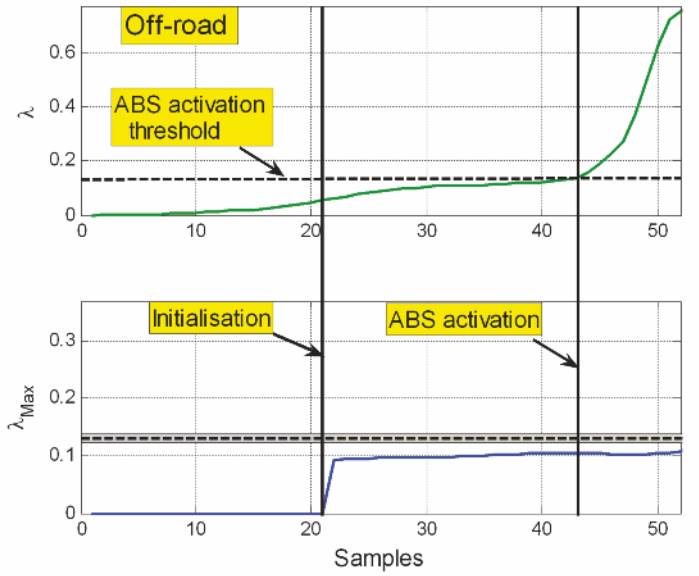

Figure 8.11 Plot of the slip λ as function of samples (*top, solid line*) and the ABS activation threshold (*top, dashed line*) and $\widehat{\lambda}_{\mathrm{Max}}$ estimation results with RML+ML on low-grip off-road (*bottom*): theoretical value (*dashed line*), estimated value (*solid line*), initialisation period (*grey*) and 5% error band (*grey*)

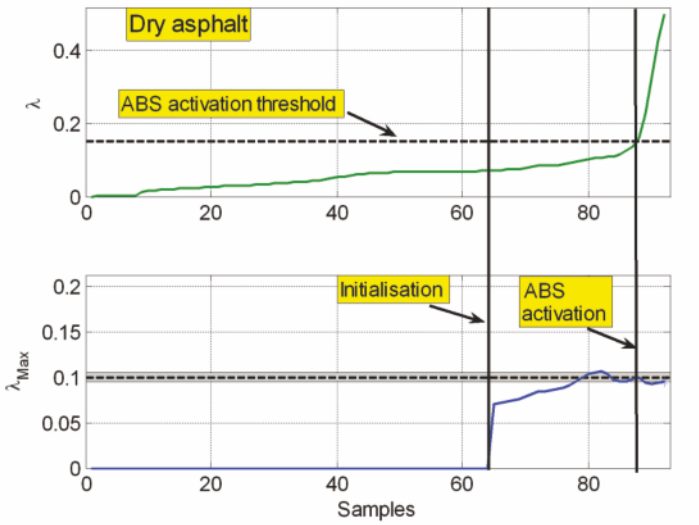

Figure 8.12 Plot of the slip λ as function of samples (*top, solid line*) and the ABS activation threshold (*top, dashed line*) and $\widehat{\lambda}_{\mathrm{Max}}$ estimation results with RLS and speed estimation on high-grip asphalt road (*bottom*): theoretical value (*dashed line*), estimated value (*solid line*), initialisation period (*grey*) and 5% error band (*grey*)

Table 8.4 Summary of the λ_{Max} estimation performance obtained with RLS and RML+ML on experimental data with measured vehicle speed

v measured	Dry – RLS	Dry – RML+ML	Off-road – RLS	Off-road – RML+ML
True λ_{Max}	0.1	0.1	0.13	0.13
# samples	92 [0.46 s]	92 [0.46 s]	52 [0.26 s]	52 [0.26 s]
$\widehat{\lambda}_{\text{Max}}$	0.0955	0.0942	0.1226	0.1063
$\epsilon_{\lambda}\%$	-4.5%	-5.8%	-5.69%	-18.23%
# samples at ABS activation	88 [0.44 s]	88 [0.44 s]	44 [0.22 s]	44 [0.22 s]
$\epsilon_{\lambda_{\text{ACT}}}\%$	1.9%	4.7%	-1.69%	-19.46%

samples makes the initialisation phase crucial, thereby confirming the theoretical analysis of the two algorithms.

8.3.3.2 Wheel Slip Measurements not Available

The estimation results obtained when non-exact wheel slip measurements are available are now discussed. This analysis reflects the practical case in which the tyre–road friction estimation is in fact implemented on a passenger vehicle equipped with standard ABS/ESC sensors (*i.e.*, wheel encoders and a longitudinal accelerometer), in which the wheel slip is estimated. Specifically, the estimation algorithm described in Chapter 5 has been used.

Due to the superior properties of the RLS algorithm observed in the case of measured vehicle speed, we only present results obtained with this algorithm in combination with estimated vehicle speed. The results obtained with the RLS method on a dry asphalt road and on a low-grip off-road are shown in Figures 8.12 and 8.13, respectively. Again, these figures also show the time history of the wheel slip and highlight the ABS activation threshold. As can be seen, the reliability of the estimation remains unchanged (both looking at the ABS activation time instant and at the overall estimation results) if the estimated value of the vehicle speed is provided as input to the algorithm, thereby confirming its practical applicability. Similar results with respect to the consistency between the case of measured and estimated vehicle speed have been obtained also for the RML+ML algorithm. A quantitative summary of the overall results on experimental data obtained with RLS and estimated vehicle speed is provided in Table 8.5.

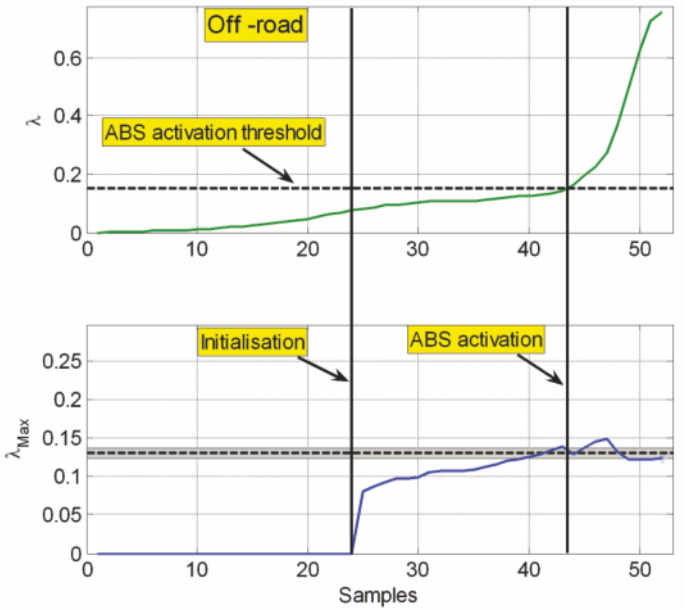

Figure 8.13 Plot of the slip λ as function of samples (*top, solid line*) and the ABS activation threshold (*top, dashed line*) and $\widehat{\lambda}_{\mathrm{Max}}$ estimation results with RLS and speed estimation on low-grip off-road (*bottom*): theoretical value (*dashed line*), estimated value (*solid line*), initialisation period (*grey*) and 5% error band (*grey*)

Table 8.5 Summary of the λ_{Max} estimation performance obtained with RLS on experimental data with estimated vehicle speed

v estimated	Dry – RLS	Off road – RLS
True λ_{Max}	0.1	0.13
# samples	92 [0.46 s]	52 [0.26 s]
$\widehat{\lambda}_{\mathrm{Max}}$	0.0953	0.123
ϵ_{λ}%	-4.7%	-5.3%
# samples at ABS activation	88 [0.44 s]	44 [0.22 s]
$\epsilon_{\lambda_{\mathrm{ACT}}}$%	0.2%	-1.38%

8.4 Direct Estimation of Contact Forces *via* In-tyre Sensors

Traditionally, tyre–road contact forces are indirectly estimated from vehicle-dynamics measurements (*e.g.*, chassis accelerations, yaw and roll rates, suspension deflections). The emerging of the *smart-tyre* concept (tyre with embedded sensors and digital-computing capability) has made possible, in principle, a more direct estimation of contact forces. In this field, which is still in

its infancy, a basic and fundamental problem is the choice of the sensor(s) and of the regressor(s) that are most appropriate to be used for force estimation.

The objective of this section is to illustrate a sensor-regressor choice tailored to accomplish this task, and to provide some experimental results to discuss the validity of this choice. The idea is to use a wheel encoder and an accelerometer mounted directly in the tyre (see Figure 8.14). The measurement of the in-tyre acceleration is transmitted through a wireless channel. The key concept is to use the *phase shift* between the wheel encoder and the pulse-like signals provided by the accelerometer as the main regressor for force estimation.

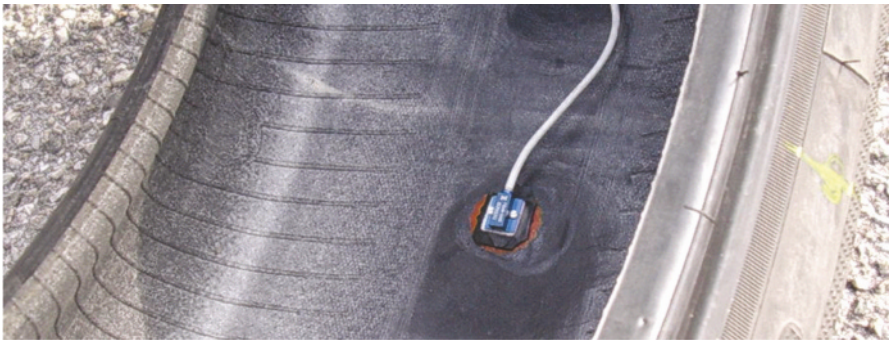

Figure 8.14 Detail of the in-tyre accelerometer

8.4.1 Introduction

In the field of smart-tyres, *i.e.*, tyres equipped with electronic devices that make them active components of the vehicle, one of the main challenges is the direct real-time estimation of the tyre–road contact forces *via* in-tyre sensors. This research is still actively ongoing and a number of non-trivial issues are still open. Among others: the choice of in-tyre sensors, the in-tyre preprocessing of the signal, the wireless transmission, the post-processing, the regressor choice and the estimation algorithm. The problem is made even more complicated by technological and industrial issues like durability, cost and energy consumption of the in-tyre electronic devices.

The great interest in a smart-tyre capable of providing a real-time estimation of the tyre–road contact forces is easily explained by its huge potential benefits: the direct measurement of tyre–road contact forces can stimulate the development of a new generation of traction, braking and stability control systems which may outperform the existing ones in terms of safety, driving satisfaction and also energy consumption.

Figure 8.15 Detail of the battery and wireless transmitter installed on the wheel rim

At this stage, no commercial products that can estimate the friction forces directly from on-vehicle measurements are available on the market, but many research groups are exploring and testing different solutions. The two key issues (strictly interwoven), which are still open, can be summarised as follows:

1. What is the best tyre-embedded sensor choice?
2. Given the sensor configuration, what is the best set of regressors to be used for force estimation?

This section presents a possible solution to these two open issues and provides some experimental results as a preliminary validation. Specifically, this method is tailored to estimate the tyre–road vertical and longitudinal forces and it makes use of two sensors in each wheel; namely

- a standard wheel encoder typically used by ABS systems for the wheel speed measurement (see Appendix B); and
- a one-axis accelerometer mounted directly *in the tyre*, which measures the acceleration experienced by the tyre in the radial direction.

Based on these signals, we aim at evaluating the phase shift between the wheel hub and the tyre, based on the wheel encoder and the accelerometer signals, respectively, by detecting when the tyre encounters and leaves the tyre–road contact patch. In fact, such a phase shift appears to be strongly correlated with the longitudinal and vertical tyre deformation; henceforth it can be suitably employed for the direct identification of the contact forces.

8.4.2 Experimental Set Up

The test-car used in the experiments is a rear-wheel-driven BMW, equipped with the following sensors:

- four inductive 48-teeth Hall-effect encoders (see also Appendix B) that measure the wheel rotational speed, whose output is a sinusoidal-like signal, with amplitude and frequency proportional to the rotational wheel speed $\omega(t)$; and
- a one-axis, $\pm 500\,\mathrm{g}$ piezoresistive low-mass linear accelerometer, mounted (glued) inside the tyre (see Figure 8.14), which measures the in-tyre radial acceleration $a_{\mathrm{tyre}}(t)$; the accelerometer has been installed alternatively on the front-left tyre and on the rear-left tyre. Its bandwidth is of approximately 3 kHz.

The wireless data transmission of the in-tyre acceleration signal is made via a transmitter, which is mounted on the wheel rim together with its battery (see Figure 8.15); the receiver antenna is placed on the car roof. All signals are sampled at 10 kHz, with a resolution of 16 bit.

The driving tests were all made on the same road surface, a high-grip flat dry-asphalt road. Two main types of tests were carried out, namely

- quasi-static tests: very slow decelerations and accelerations (with no gear shifts) in the range 10-25 m/s; and
- dynamic tests: strong braking and acceleration manoeuvres, interleaved with constant-speed intervals.

All the tests were performed on a straight road. Two tyre-pressure conditions were tested: 2.0 bar (nominal condition) and 1.6 bar (low-pressure condition).

8.4.3 Main Concept

Consider the signal detected by the in-tyre accelerometer. It measures the instantaneous acceleration experienced by the tyre at the installation point in the radial direction. An example of this signal (the raw signal, without any kind of pre-processing) over a 0.7 s time window is displayed in Figure 8.16. The analysis of this signal reveals that:

- The radial acceleration is approximately constant over a short time-window (it is the centripetal acceleration, proportional to the wheel speed), but when the accelerometer passes through the contact patch the acceleration is characterised by two impulse-like signals. This twin-spike is obviously repeated every wheel revolution.
- The two main *fronts* of the acceleration signal around the contact patch (the first is descending, the second is ascending) can be used to detect

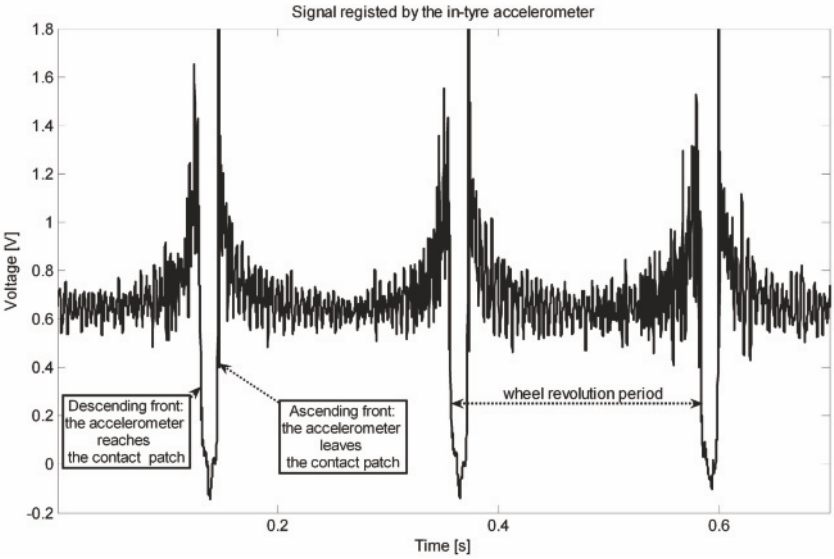

Figure 8.16 Raw signal detected by the radial in-tyre accelerometer

the time instants when the accelerometer reaches and leaves the contact patch, respectively.

Based on this signal and on the wheel encoders measurements, the aim is to estimate the vertical and the longitudinal force acting on the tyre by exploiting the information contained in the phase shift between the wheel hub and the tyre.

In order to obtain a more visual description of this idea, consider Figure 8.17(a), where a schematic picture of a wheel and its contact patch is displayed. If we consider the two acceleration spikes, and their absolute position in the angular reference frame α given by wheel encoder (which is not subject to elastic deformation), three quantities can be computed at each wheel revolution:

1. the angular position α_1 of the initial position of the contact patch;
2. the angular position α_2 of the final position of the contact patch; and
3. the length $\Delta\phi = \alpha_2 - \alpha_1$ of the contact patch.

In Figures 8.17(b) and 8.17(c) the phase shift phenomenon is pictorially described. More specifically:

- Due to the elastic properties of the tyre in the radial direction (see *e.g.*, [7, 8, 71]), the vertical tyre–road contact force F_z is assumed to be strictly correlated with the length

$$\Delta\phi = \alpha_2 - \alpha_1 \tag{8.13}$$

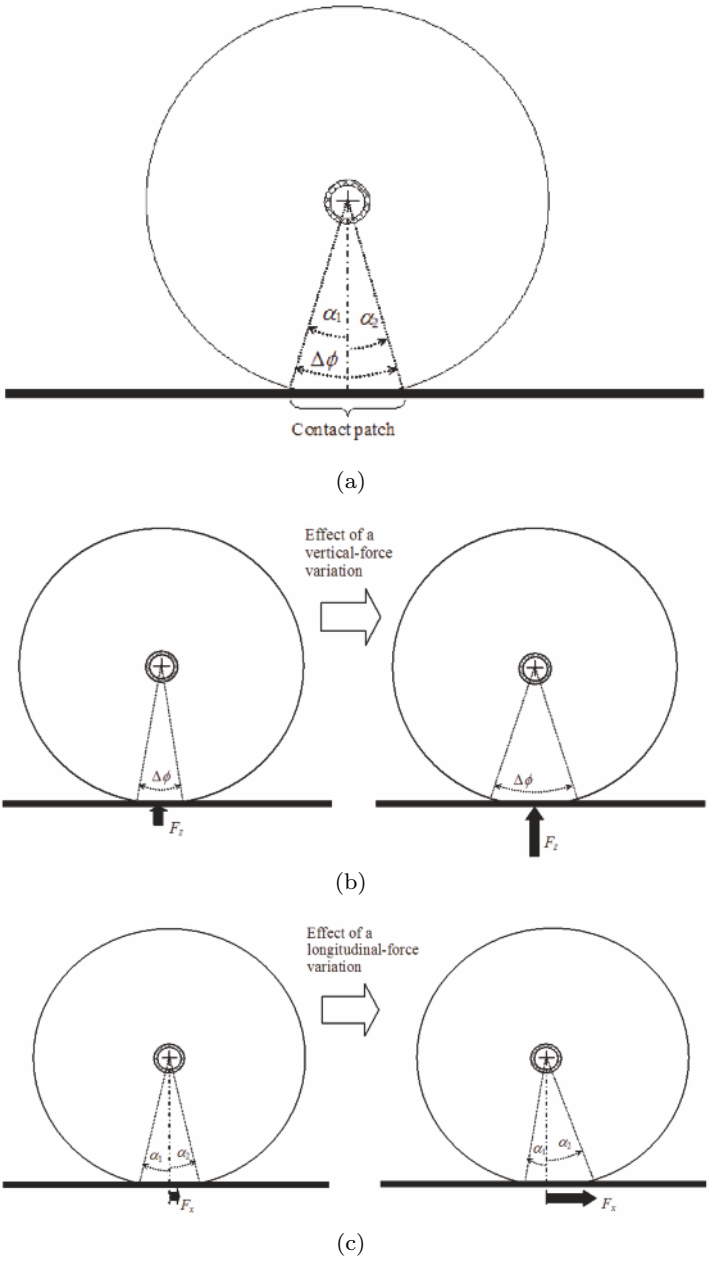

Figure 8.17 A schematic representation of a wheel and its contact patch (a), the effect of a vertical force variation (b) and the effect of a longitudinal force variation (c)

of the contact patch (see Figure 8.17(b)); the idea hence is to use the measured angle $\Delta\phi$ to estimate F_z, *i.e.,*

$$F_z = f_z(\Delta\phi). \tag{8.14}$$

- Due to the elastic properties of the tyre in the longitudinal (tangential) direction (see again [7, 8, 71]), the longitudinal tyre–road contact force F_x is assumed to be strictly correlated to the phase shift of the centre of the contact patch (see Figure 8.17(c)), given by

$$\delta\phi = (\alpha_1 + \alpha_2)/2. \tag{8.15}$$

The idea is to use the measured angle $\delta\phi$ to estimate F_x, *i.e.*,

$$F_x = f_x(\delta\phi). \tag{8.16}$$

In particular, note that $\delta\phi$ is expected to be negative during braking and positive during acceleration; in other words, this means that the centre of the contact patch is assumed to rotate backwards or forwards (with respect to a conventional zero position), respectively. Also notice that, in general, the real centre of the contact patch is not perpendicular to the wheel hub. Hence, (8.15) provides a *conventional* centre of the contact patch. This, however, does not affect the estimation procedure, since it is insensitive to the conventional choice of the contact patch centre.

8.4.4 Signal Processing

The whole method is based on the measurement of two signals for each wheel: the wheel rotational speed ω and the radial acceleration a_{tyre} experienced by a point in the tyre.

The wheel encoder is the standard 48-teeth encoder used by the ABS and ESC control systems (see also Appendix B). The original signal coming from the encoder is a sinusoidal-like voltage signal. An example of this signal is displayed in Figure 8.18(a), over a time-window of 100 ms. The wheel rotational speed is computed from the sinusoidal wheel encoder *via* a frequency tracking algorithm, see [83], and the wheel radius is calibrated as detailed in Section B.2.2.

In Figure 8.18(b), an example of the calibrated linear wheel speed signal (for the front-left wheel) is displayed. Notice that the estimation of the wheel radius is not particularly critical for this application, since the considered regressors are based on phase shifts, which are not strongly correlated with the actual wheel radius.

The last step of the pre-processing of the wheel encoder signal, specific to the considered estimation problem, is to estimate the instantaneous angular

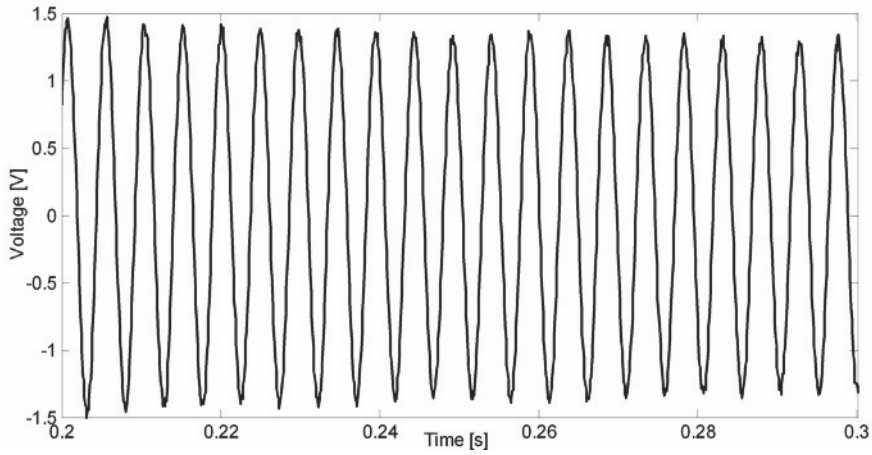

(a)

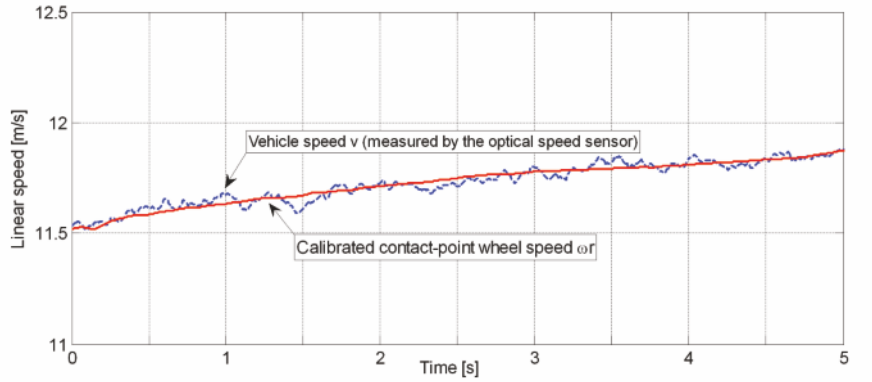

(b)

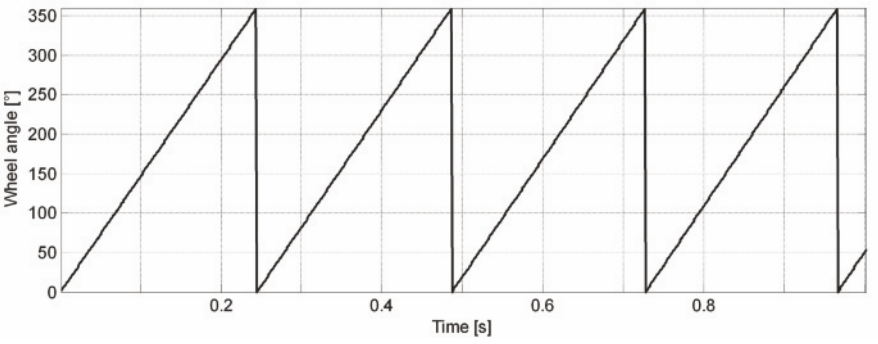

(c)

Figure 8.18 Examples of the measured wheel encoder signal (a), the calibrated wheel speed at the contact point (b) and the estimated angular position α of the wheel from the wheel encoder (c)

position α of the wheel. This estimation is fundamental since it represents the baseline for the identification of the phase shift. The basic idea for the estimation of the angular position is simply to make an incremental step counter, which resets every wheel revolution (or 360°). Since in a 48-teeth encoder the peak-to-peak distance of one period corresponds to 7.5° of wheel rotation, the whole sinusoidal profile of the signal (Figure 8.18(a)) must be used to improve the accuracy of the angular position. The angular resolution obtained can be estimated to be about 0.1°, which is suitable for this application. An example of the estimated wheel angular position is displayed in Figure 8.18(c).

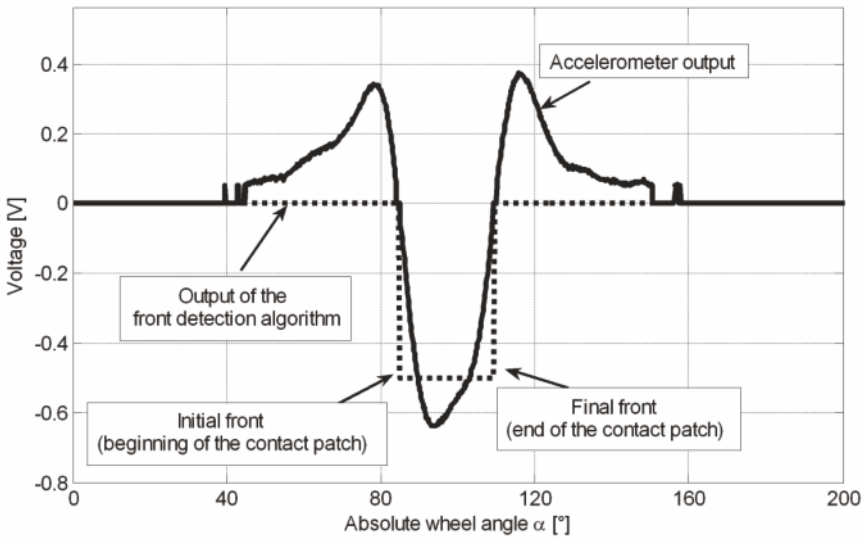

Figure 8.19 Example of output of the front-detection algorithm

As has already been mentioned, in-tyre accelerometer is a one-axis sensor (oriented in the radial direction) linear accelerometer glued inside the tyre (see Figure 8.14). The output signal is a voltage signal, characterised by a bump (or a twin-impulse) around the tyre–road contact patch. The main signal processing issue is to detect the time instant when each impulse takes place, namely to detect the angular position α_1 and α_2 of the two fronts (one descending and one ascending) of the bump.

In Figure 8.19 an example of the output of the front-detection algorithm is displayed (dotted line). The implemented front-detection algorithm essentially performs a simple zero-crossing search in the neighbourhood of the two main fronts; the zero-crossing algorithm is applied to the normalised and detrended signal. Note that in Figure 8.19 the signals are plotted as a function of the wheel's absolute angular position α, not as a function of time. This is

a key step that allows us to eliminate most of the dependency of the phase shift from the wheel rotational frequency.

Starting from α_1 and α_2, the estimation of the length of the contact patch $\Delta\phi$ is straightforward, as $\Delta\phi = \alpha_2 - \alpha_1$. For the computation of the phase shift of the centre of the contact patch Ω_0 the following procedure was used. The first part of every test drive is always characterised by a low, constant-speed (lasting approximately 10 ms) condition. It is conventionally assumed that the phase shift in that condition is zero, namely

$$\delta\phi = \frac{\alpha_1 + \alpha_2}{2} + \Omega_0 = 0.$$

The calibration offset Ω_0 is then added to the absolute angular position of the wheel for the entire experiment. In other words, it is assumed that at the beginning of each experiment the phase shift is zero, and all the phase shifts of the rest of the experiment are referred to that conventional zero-condition. As has already been remarked, the choice of this conventional *zero* does not affect the quality of the estimation.

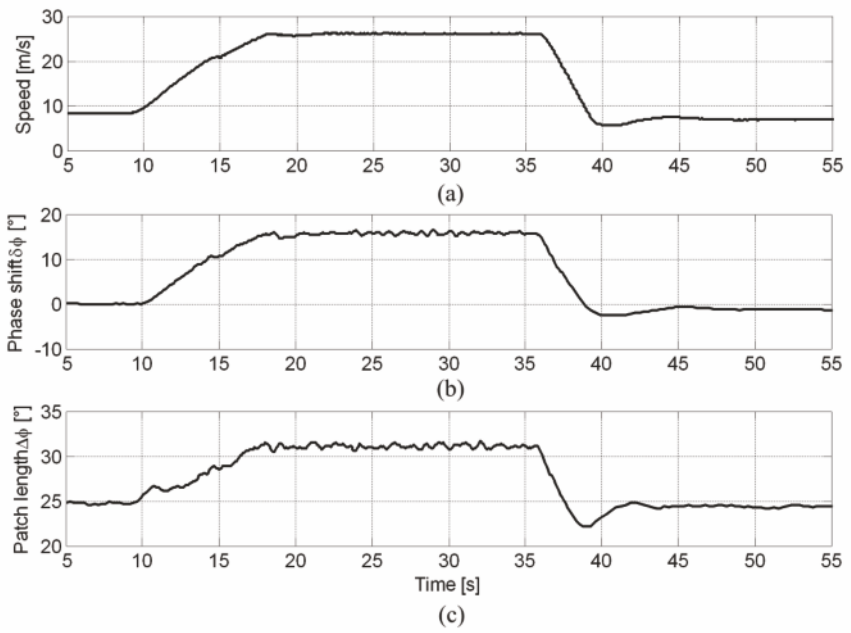

Figure 8.20 Example of a complete dynamic test: vehicle speed (a), estimated phase shift (b) and estimated length of the contact patch (c). The phase shift and length of the contact patch refer to the rear-left wheel

The results of the above described pre-processing of the two main signals can be appreciated in Figure 8.20, where the vehicle speed, the phase shift of

the mid-point of the contact patch $\delta\phi$ and the contact patch length $\Delta\phi$ are displayed, for a 1 min long dynamic experiment. From the behaviour of the vehicle speed, note that experiment is constituted by five main parts: a first part of constant low-speed, an acceleration, a new long constant-speed window, a strong braking manoeuvre and a final constant low-speed condition.

By inspecting the estimated $\delta\phi$ and $\Delta\phi$ in Figure 8.20 it is immediately apparent that their behaviour is highly correlated with the vehicle speed. Unfortunately, this speed-dependency phenomenon almost completely hides the important part of the relationships between the pair ($\delta\phi$, $\Delta\phi$) and the contact forces (F_x, F_z).

The removal of the speed-dependent trends in $\delta\phi$ and $\Delta\phi$ hence is mandatory. Note that this effect was somehow expected and it is mainly due to the effects of the aerodynamic forces and (at mid/low speed values) of the rolling resistance.

In order to remove this speed dependence, a simple quasi-static experiment was performed: the car was slowly accelerated (without gear-shift) from 10 m/s to 25 m/s; the same experiment was repeated in deceleration (coasting down).

Since the acceleration/deceleration ramp is extremely slow, in this experiment the dynamic effects can be neglected. At each wheel revolution, the pairs $(\omega r, \delta\phi)$ and $(\omega r, \Delta\phi)$ have been computed. The results are plotted in Figures 8.21(a) and 8.21(b).

As the experiment has been made in a quasi-static setting, the relationships depicted in Figures 8.21(a) and 8.21(b) are static and can be easily fitted with one-dimensional nonlinear functions. In particular, both maps were fitted with simple second-order polynomials. A unique map was used both for the front and the rear tyres. The estimated maps are displayed in Figures 8.21(a) and 8.21(b).

Using the estimated maps, the speed-dependent trends have been removed from the dynamic experiments. The results are displayed in Figures 8.22 and 8.23, for both the rear and the front wheels. Note that after the trend-removal, the phase shift and the length of the contact patch have the same value (0° and 25°, respectively) in every constant-speed condition.

By carefully inspecting Figure 8.23 (front tyre), another residual spurious effect can be observed. As a matter of fact, notice that – during the acceleration phase – no significant longitudinal force F_x should be developed by the front wheels; as a consequence, we know *a priori* that the phase shift of the contact patch on a front wheel in that condition should be zero. This condition is not perfectly met by the data displayed in Figure 8.23 (see the time interval $t \in [15, 20]$ s in the middle plot). This phenomenon has a simple and intuitive explanation: there is a slight dependency (or *cross-talk*) between the phase shift and the vertical force. Hence, the phase shift must be subject to an additional correction as follows:

$$\delta\phi = \delta\widetilde{\phi} + f_F(F_z), \tag{8.17}$$

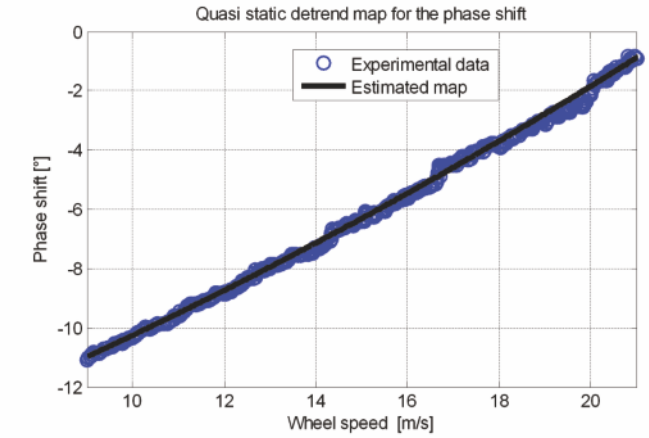

(a)

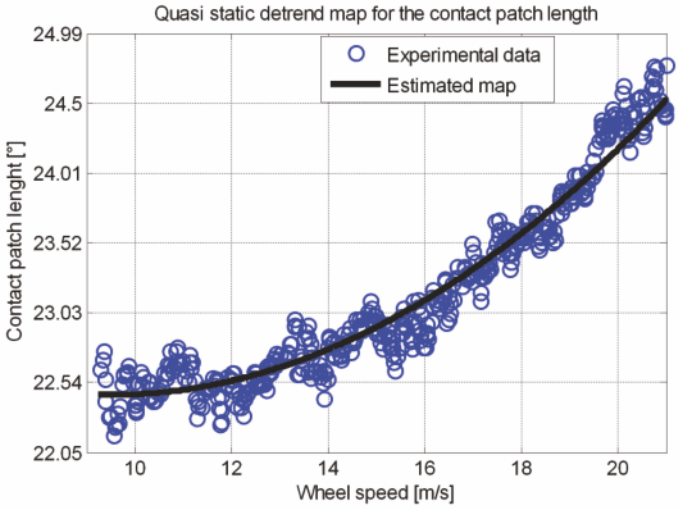

(b)

Figure 8.21 Quasi-static maps of the phase shift (a) and contact patch length (b) as functions of wheel speed

where $\delta\widetilde{\phi}$ is the phase shift without correction and $f_F(F_z)$ is the correction term (to be estimated). Unfortunately, F_z is not directly known. However, since we have assumed a direct static relationship between F_z and $\Delta\phi$, we can approximate Equation 8.17 with the following equation:

$$\delta\phi = \delta\widetilde{\phi} + f_F(\Delta\phi). \tag{8.18}$$

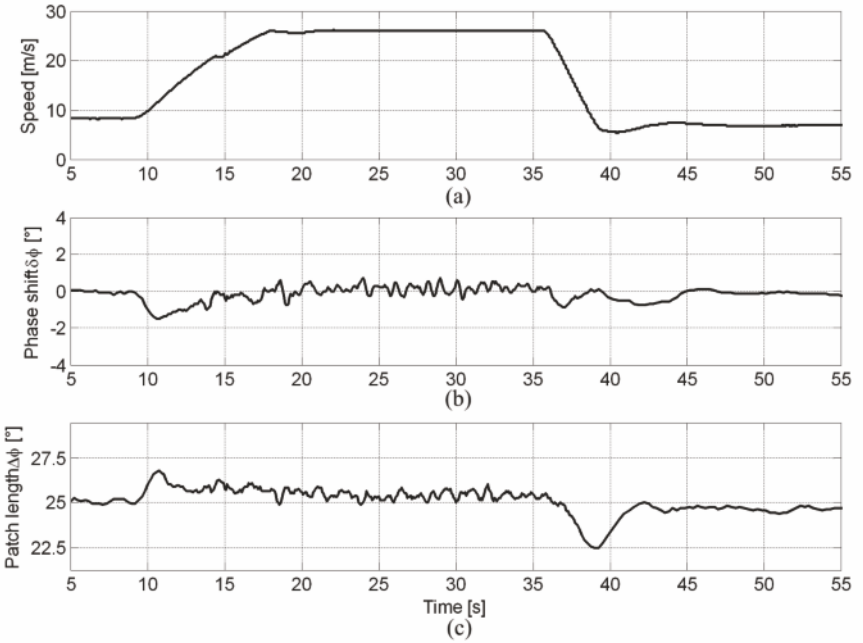

Figure 8.22 Example of a complete dynamic experiment: vehicle speed (a), estimated phase shift (b) and estimated length of the contact patch (c). Rear-left wheel; nominal pressure

For simplicity, we have assumed a linear dependency in the correction term, namely

$$\delta\phi = \delta\tilde{\phi} + \beta(\Delta\phi - \Delta\phi_0). \tag{8.19}$$

The term $(\Delta\phi - \Delta\phi_0)$ in Equation 8.19 is the dynamic variation of the contact patch length ($\Delta\phi_0$ is the average value of the contact patch, at constant speed). The only unknown term in Equation 8.19 is the coefficient β. The optimal value of β has been identified by numerical optimisation from data, in order to guarantee no phase shift on the front tyre during acceleration in every working condition.

In Figure 8.24 the detail of the acceleration phase for the front tyre before and after the correction with (8.19) is shown. Using the estimated value of β, the phase shift signals of both the front and the rear wheels have been modified according to Equation 8.19. After the single (for the contact patch length) and the double (for the phase shift) trend removal, all the main spurious effects are eliminated, and data can be employed to extract the phase shift and contact patch length information.

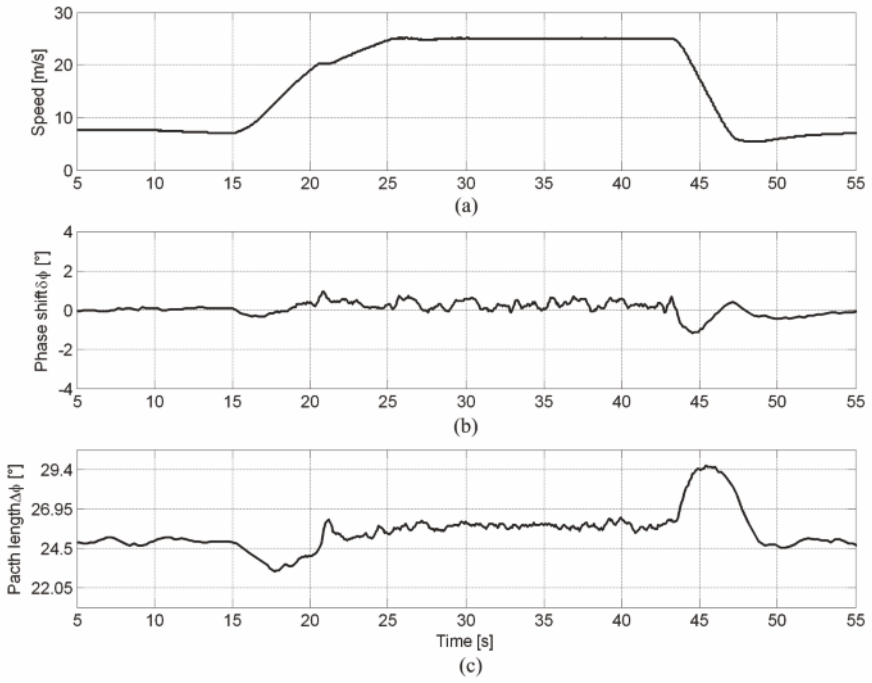

Figure 8.23 Example of a complete dynamic experiment: vehicle speed (a), estimated phase shift (b) and estimated length of the contact patch (c). Front-left wheel; nominal pressure

8.4.5 Experimental Results

The experimental results are based on a set of test drives performed on a flat dry-asphalt surface, when driving in a straight line at low/mid-range speed (0-80) km/h. Two tyre pressure settings have been tested, in order to analyse the sensitivity of the method with respect to this critical parameter. Specifically, a nominal pressure of 2.0 bar and a reduced pressure of 1.6 bar were considered.

Figures 8.25 and 8.26 show the results for the nominal pressure at the rear and front wheels, respectively. By carefully inspecting these figures, the following observations can be made.

- *Acceleration phase – Longitudinal force*
  During this phase no longitudinal force is applied at the front wheel: $F_{x_{\text{Front}}} = 0$, whereas a positive force is applied at the rear (drive) wheel: $F_{x_{\text{Rear}}} > 0$.
  Accordingly, since we have assumed a direct monotone static relationship $F_x = f_x(\delta\phi)$ between the longitudinal force F_x and the phase shift of

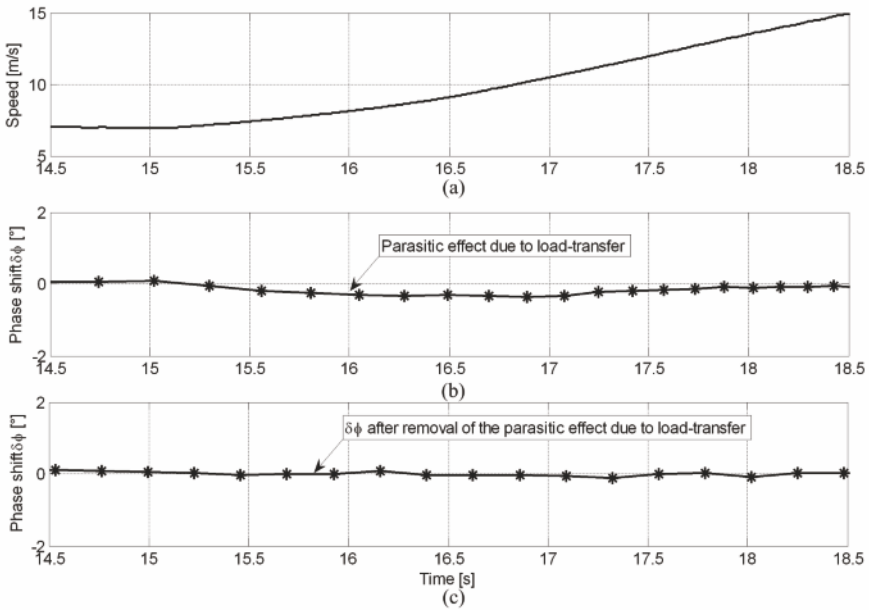

Figure 8.24 Detail of the acceleration phase (front wheel): vehicle speed (a) and estimated phase shift before (b) and after (c) the removal of the load-transfer parasitic effect

the contact patch $\delta\phi$, the phase shift of the front wheel should be zero ($\delta\phi_{\text{Front}} = 0$).
Conversely, the phase shift at the rear wheel should be positive ($\delta\phi_{\text{Rear}} > 0$). From Figures 8.25 and 8.26 it is easy to see that both these conditions are met.

- *Acceleration phase – Vertical force*
  During this phase the front wheel should experience a decrease of the vertical force, *i.e.,* $F_{z_{\text{Front}}} < \overline{F}_{z_{\text{Front}}}$, where $\overline{F}_{z_{\text{Front}}}$ is the static load at the front wheel, whereas the vertical force at the rear wheel should increase, *i.e.,* $F_{z_{\text{Rear}}} > \overline{F}_{z_{\text{Rear}}}$, where $\overline{F}_{z_{\text{Rear}}}$ is the static load at the rear wheel.
  Accordingly, since we have assumed a direct monotone static relationship $F_z = f_z(\Delta\phi)$ between the vertical force F_z and the length of the contact patch $\Delta\phi$, the length at the front wheel should decrease, *i.e.,* $\Delta\phi_{\text{Front}} < \Delta\phi_0$, whereas that at the rear wheel should increase *i.e.,* $\Delta\phi_{\text{Rear}} > \Delta\phi_0$.
  From Figures 8.25 and 8.26 it is easy to see that also both these conditions are met.
- *Braking phase – Longitudinal force*
  During this phase, a negative longitudinal force is applied at both wheels *i.e.,* $F_{x_{\text{Front}}} < 0$, $F_{x_{\text{Rear}}} < 0$. Accordingly, we expect that $\delta\phi_{\text{Rear}} < 0$ and $\delta\phi_{\text{Front}} < 0$.
  From Figures 8.25 and 8.26 it is easy to see that these conditions are met.

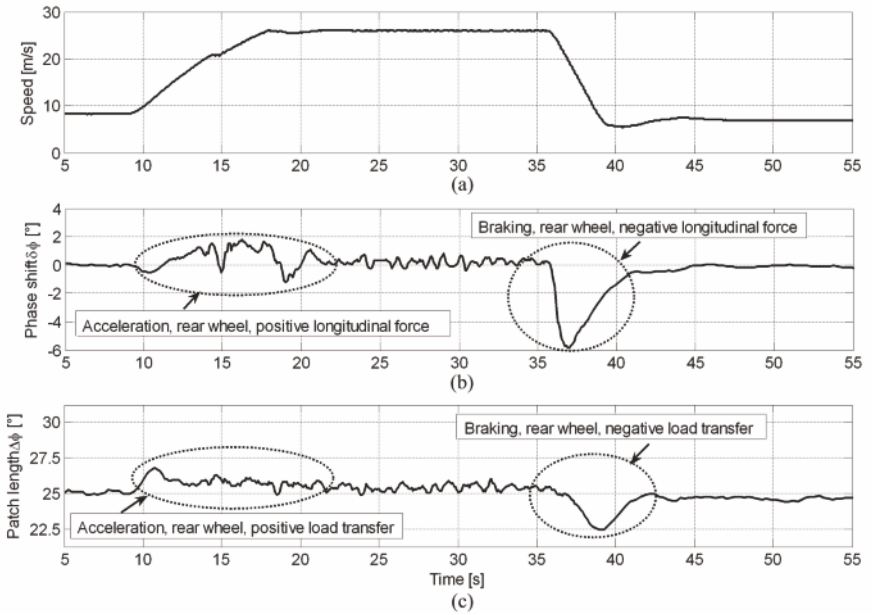

Figure 8.25 Final results on a complete dynamic experiment: vehicle speed (a), estimated phase shift (b) and estimated length of the contact patch (c). Rear-left wheel; nominal pressure

- *Braking phase – Vertical force*
  During this phase, the front wheel should experience an increase of the vertical force, *i.e.,* $F_{z_{\text{Front}}} > \overline{F}_{z_{\text{Front}}}$, whereas the vertical force at the rear wheel should decrease, *i.e.,* $F_{z_{\text{Rear}}} < \overline{F}_{z_{\text{Rear}}}$.
  Accordingly, we expect that $\Delta\phi_{\text{Front}} > \Delta\phi_0$ and $\Delta\phi_{\text{Rear}} < \Delta\phi_0$.
  From Figures 8.25 and 8.26 it is easy to see that both these conditions are met.

In Figures 8.27 and 8.28 the results of the experiments performed with low-pressure tyres on rear and front wheels, respectively, are displayed. Notice that the results displayed in Figures 8.27 and 8.28 were obtained without recalibration; they were computed using the same pre-processing and calibrations as for the 2.0 bar case in order to test the robustness of the method. All the considerations made in the nominal-pressure case still hold; this fact is encouraging as the method shows a good robustness with respect to pressure variations.

By carefully comparing the results at nominal and low pressure, one can notice that, as expected, the contact patch length is slightly larger in the case of low-pressure tyres; the variations in the phase shift instead are very similar to the nominal-pressure setting.

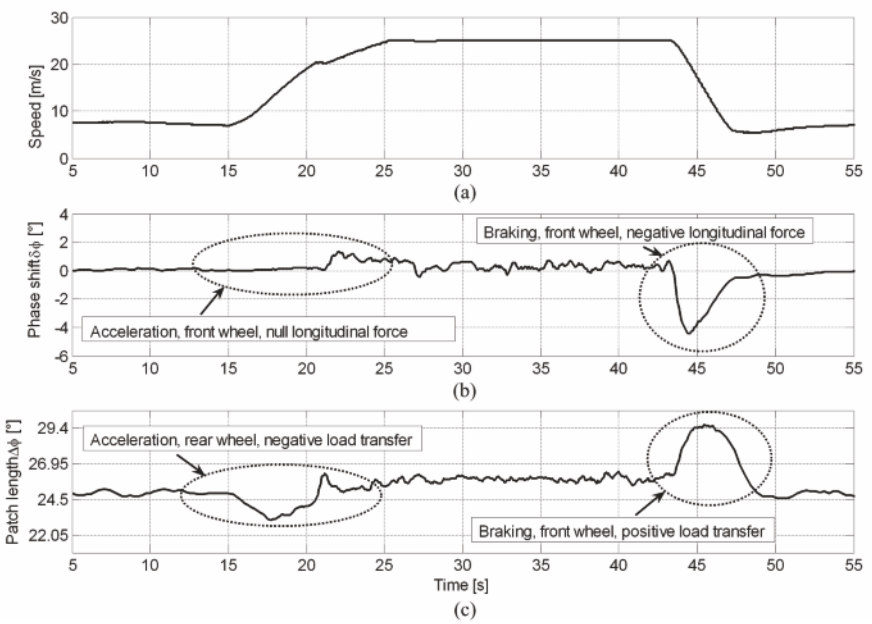

Figure 8.26 Final results on a complete dynamic experiment: vehicle speed (a), estimated phase shift (b) and estimated length of the contact patch (c). Front-left wheel, nominal pressure

8.5 Summary

This chapter provided some approaches to estimate online the tyre–road friction characteristics. As friction information can be extremely valuable for all active vehicle control systems, much research activity has focused on the estimation and monitoring of tyre–road friction characteristics (see, *e.g.*, the detailed review in [65]), resulting in the proposal of many different approaches, which differ both regarding the estimation technique and the required sensor equipment.

Some interesting approaches are tyre-oriented. For example, in [12] an acoustic sensor is used to gain information on road-condition by registering the acoustic waves emitted by the tyres. The drawback of such an approach is the high noise level in the acoustic signal, which makes it very hard to extract the real effect of friction changes on the measured signal. Another tyre-oriented approach is documented in [12] and [24], where tyre-tread deformation sensors are employed. Such an approach, besides suffering from the same drawbacks as the former, is also quite expensive and of difficult implementation, as the tyre-tread sensors have to be embedded in the tyre with specific vulcanisation processes.

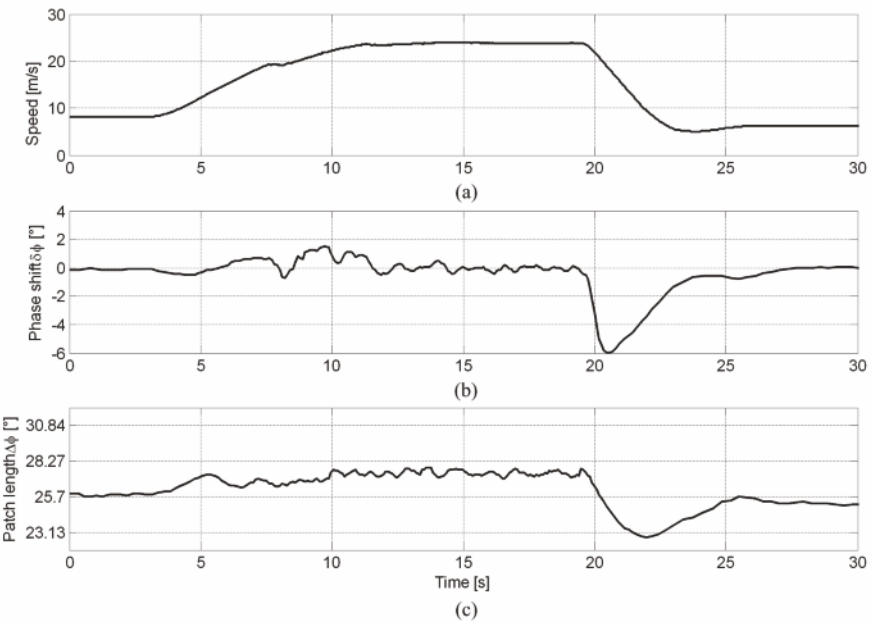

Figure 8.27 Final results on a complete dynamic experiment: vehicle speed (a), estimated phase shift (b) and estimated length of the contact patch (c). Rear-left wheel, reduced pressure

Another approach for the estimation of tyre–road friction is the so-called *slip-based* approach, which appears particularly appealing as it needs only standard ABS-ESC sensor equipment. Slip-based estimation is mostly addressed during braking manoeuvres, where sufficiently large slip levels are encountered, although estimation techniques based on low slip measurements, as available during traction, are also documented in the literature (see, *e.g.*, [65]). In [29], an adaptive estimation method is proposed based on a linear approximation of the tyre–road friction description. In the last few years, the interest has also shifted towards the estimation of the dynamic behaviour of tyre friction forces (see, *e.g.*, [12,24,29,85,86,93,129]). Another example of this field of research is given in [69], where the authors estimate the tyre extended braking stiffness – *i.e,* the derivative of the longitudinal friction force with respect to the wheel slip, which indicates the residual longitudinal friction force available to the driver. Such an estimate serves as additional information for the design of an ABS system.

Further, developments in tyre materials, structure and manufacturing techniques have been enormous in the last decades. However, as has already been remarked, the tyre has up to now essentially remained a *passive* object.

In the last few years a new trend has emerged, whose aim is to equip the tyre with embedded sensors and digital-computing capability; the measure-

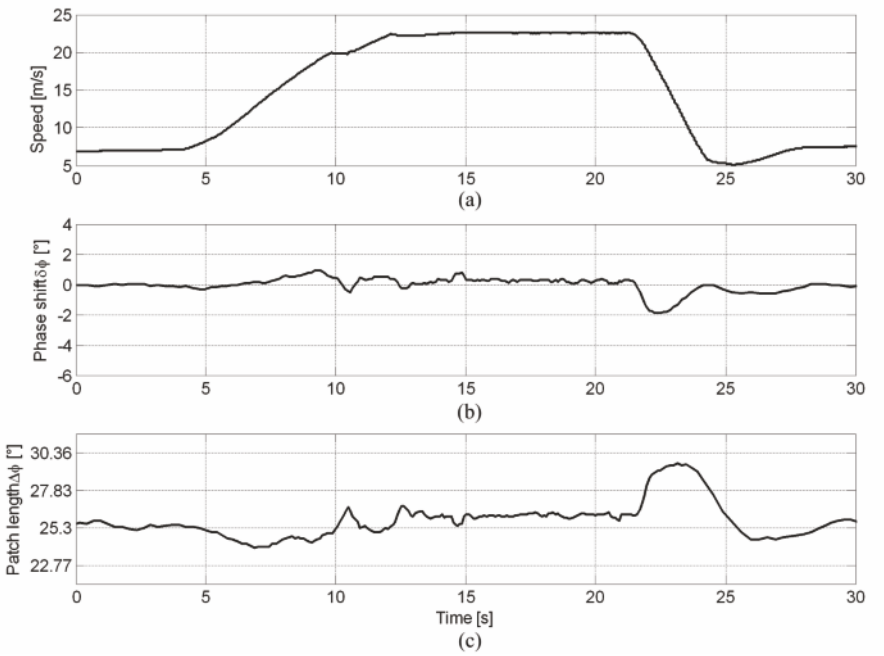

Figure 8.28 Final results on a complete dynamic experiment: vehicle speed (a), estimated phase shift (b) and estimated length of the contact patch (c). Front-left wheel, reduced pressure

ment and low-bandwidth transmission of the tyre pressure is an industrial reality (tyre pressure monitoring systems, see, *e.g.*, [31]) and new in-tyre sensors and electronics are currently under research [63, 75]. This trend is mainly driven by information and communication technology methods and devices and it represents a sort of revolution in tyre manufacturing. The term *smart-tyre* is frequently used to label this new generation of tyres.

In the open scientific literature, little has been published so far on the topic of direct estimation of tyre–road contact forces by in-tyre sensors.

Most of the current research activity on this topic has up to now been described in industrial patents (see, *e.g.*, [13, 79]) or in oral presentations (see, *e.g.*, [63]).

Appendix A
Analysis and Synthesis Tools for Dynamical Systems

A.1 Introduction

The objective of this appendix is to briefly survey the main concepts of dynamical systems analysis and synthesis used in this book. Specifically, we will review notions of stability theory for dynamical systems, which allows one to draw conclusions about the behaviour of a dynamical system without actually computing its solution.

The first researcher to study stability in the modern sense was Lagrange, who analysed the qualitative behaviour of mechanical systems (his famous book *Mécanique Analytique* was published in 1788). One of his conclusions was that in the absence of external forces, an equilibrium of a conservative mechanical system is *stable* if it corresponds to a minimum of the potential energy.

Since then, the most important progress in stability theory was due to the theory introduced by the Russian mathematician Lyapunov who was able to extend the results obtained by Lagrange to a large class of dynamical systems. These achievements were mainly presented in his Ph.D. thesis *The general problem of the stability of motion*, which was developed at the University of Moscow and dates back to 1892. Lyapunov's theory includes two important methods for stability analysis: the *direct method* and the *linearisation method* (also called the *linear approximation method*).

The direct method determines the stability properties of the equilibrium points of a nonlinear dynamical system by constructing an energy-like function for the system and studying how this function varies with time. The linearisation method gives results about the local stability of a nonlinear dynamical system around an equilibrium point by analysing the stability properties of its linear approximation.

Besides stability analysis tools, we will provide the reader with the basic notions that allow us to qualitatively investigate the behaviour of second-order dynamical systems *via* the state trajectories and to classify the system

equilibrium points. We also present the notions of periodic orbit and limit cycle and introduce some results mainly due to Poincaré, which enable one to assess the existence and stability of periodic orbits. These results were developed at the beginning of the 20th century.

As for the synthesis methods, we introduce the general problem of feedback stabilisation and present and discuss a specific result that falls within the class of Lyapunov-based design methods and is used in this book.

In general, the various results are reported without proofs, but complemented with explanations about their meaning and their use in practical applications. In fact, this appendix is intended to provide the reader who is not familiar with these results with a description of the methodological tools needed to understand the more advanced control analysis and design approaches employed in this book.

Note that all the main definitions and theorems mentioned in this chapter are taken from the books *Nonlinear Systems* by Khalil [44], *Nonlinear Dynamics and Chaos* by Strogatz [102] and *Introduction to Applied Nonlinear Dynamical Systems and Chaos* by Wiggins [126] which can be consulted for an in-depth exposition of the different topics.

A.2 Dynamical Systems Analysis

This section begins with some background definitions concerning nonlinear systems and stability of equilibrium points. Specifically, Section A.2.1 first recalls the fundamental theorems of Lyapunov, which enable us to characterise the behaviour of nonlinear systems. This is followed by a simple explanation of Lyapunov's linearisation method. Finally, an extension of the basic theory due to LaSalle is presented.

Further, the special case of second-order dynamical system is analysed in Section A.2.2, providing notions about both equilibrium points classification and limit cycles.

A finite dimensional continuous time[1] nonlinear dynamical system can be represented by a set of nonlinear differential equations in the form

$$\dot{x} = f\big(x, t\big), \tag{A.1}$$

where $x \in \mathbb{R}^n$ and $f : G \times [0, +\infty) \longrightarrow \mathbb{R}^n$ with $G \subset \mathbb{R}^n$. We assume that for all initial conditions $x(t_0) = x_0 \in G$ there exists a unique $x(\cdot) : [0, +\infty) \longrightarrow G$ such that (A.1) holds (possibly in a sense to be suitably specified) for all $t \in [0, +\infty)$. Such $x(t)$ is a *solution* of Equation A.1 and it is generally referred to as *state motion*. Thus, the state motion is a curve in the space

[1] In the case when time evolves over the integers rather than over the reals, we talk of discrete time systems, whose dynamics can be expressed as $x_{k+1} = f(x_k, k)$, $k \in \mathbb{N}$.

$G \times [0, +\infty)$, while the projection of the state motion onto the space G is called *state trajectory* or *system trajectory*.

It is worth noting that although Equation A.1 is *unforced*, that is it does not explicitly contain the control input as a variable, yet it can represent the *closed-loop* dynamics of a feedback control system, where the control input is a function of the state x and of the time t and which therefore "disappears" in the closed-loop dynamics. Thus, if the system dynamics are of the form

$$\dot{x} = h(x, u, t), \tag{A.2}$$

and the control law is given by

$$u = g(x, t), \tag{A.3}$$

then the closed-loop dynamics can be expressed as

$$\dot{x} = h\big(x, g(x, t), t\big) = f(x, t), \tag{A.4}$$

thereby yielding an unforced system of the form (A.1).

Definition A.1. The nonlinear system (A.1) is said to be *time-invariant* if the function $f(\cdot, \cdot)$ does not depend explicitly on time, *i.e.*, if the system (A.1) can be written as

$$\dot{x} = f(x). \tag{A.5}$$

Otherwise, the system is called *time-varying*.

If a system is both time-invariant and unforced, then it is called *autonomous*. If one of the two properties does not hold, conversely, it is called *non-autonomous*.

A special class of dynamical systems are *linear systems*. The dynamics of linear systems are described in general by equations of the form

$$\dot{x} = A(t)x, \tag{A.6}$$

where $A(t)$ is an $n \times n$ matrix. Also linear systems are classified as either time-varying or time-invariant, depending on whether the system matrix A varies with time or not.

The main difference between time-invariant and time-varying systems is that the state trajectory of a time-invariant system is independent of the initial time, while that of a time-varying system generally is not. This difference requires us to consider the initial time explicitly in defining stability concepts for time-varying systems and makes the analysis more difficult than that of time-invariant ones. As a matter of fact, when analysing time-invariant systems the initial time is set, without loss of generality, to $t_0 = 0$.

Note that the concept of an autonomous system is an idealised notion, as it is the concept of a linear system. In practice, all these classes of systems

are intended to provide analytical representations used to model physical systems, and have to be chosen according to the desired degree of accuracy in describing the reality of interest.

Further, note also that in the case where Definition A.1 is applied to the *closed-loop dynamics*, the control system is composed of a controller and a plant, and the time-varying nature of the control system may be due to a time variation either in the plant or in the control law (or both).

However, some system properties often change slowly with respect to the time scales of the dynamics of interest; hence it makes sense to neglect their time variation when developing their analytical models without incurring any significant error.

This is also the approach taken in this book to develop and analyse the proposed control laws, both in the linear and the nonlinear setting.

Hence, in the following only autonomous systems will be considered. For such a class of systems, we are interested in analysing under which conditions the nonlinear differential equation (A.5) actually admits a solution and when such a solution is unique.

Theorem A.1 (Existence and Uniqueness of Solutions). *Consider the nonlinear differential equation*

$$\dot{x} = f(x), \tag{A.7}$$

with initial condition $x(0) = x_0$. *Assume that* $f : G \subset \mathbb{R}^n \to \mathbb{R}^n$, *where* G *is an open and connected*[2] *subset of* $\mathbb{R}^n$, *is continuously differentiable. Then, for all* $x_0 \in G$ *there exist a time instant* $\tau > 0$ *and a unique solution* $x(t)$ *of* (A.7) *defined over the time interval* $t \in [0, \tau)$.

Note that there exist stronger versions of this theorem, which allow us to extend the existence and uniqueness of the solution over all times $t \geq 0$ (the interested reader may refer to Chapter 3 of [44] for details), but the one given above suffices for our purposes. Also, it is worth mentioning that the concept of solution can be appropriately extended to the case where the function $f(\cdot)$ is not continuous. Most importantly, under the assumptions of the existence and uniqueness theorem, the following crucial implication holds.

Corollary A.1. *Different system trajectories never intersect.*

As a matter of fact, if two trajectories were to intersect, it would imply that there are two solutions starting from the same point (the point of intersection), and hence the uniqueness theorem would be violated. This fact will be discussed further in Section A.2.2.

[2] An open set S is said to be connected if any two points in S can be can be joined with an arc lying entirely in S.

We now investigate the notion of equilibrium point of a nonlinear system. To this end, let

$$\dot{x} = f(x), \tag{A.8}$$

where $x \in \mathbb{R}^n$ and $f : G \longrightarrow \mathbb{R}^n$ with $G \subset \mathbb{R}^n$.

Definition A.2. A state $\overline{x} \in G$ is an *equilibrium state* or *equilibrium point* for the system (A.8) if

$$x(t) = \overline{x}$$

is a solution of the differential equation (A.8). Thus, $x(t) = \overline{x}$ is a constant state motion. In the case where $f(\cdot)$ is continuous, the equilibrium state $\overline{x}$ can be computed as the solution of

$$f(\overline{x}) = 0.$$

Note that a linear time-invariant system

$$\dot{x} = Ax$$

has a single equilibrium point represented by the origin $x = 0$ if and only if A is non-singular. If A is singular and $G = \mathbb{R}^n$, the set of equilibrium points consists of all x such that $Ax = 0$, namely the null-space of the matrix A. This set is a continuum: in the neighbourhood of any equilibrium point there is an infinity of equilibrium points (*i.e.*, no equilibrium point is isolated). A nonlinear system can instead have one or several isolated equilibrium points, or even a continuum of them.

For notational and analytical simplicity, nonlinear system equations are often transformed by means of a change of coordinates such that the considered equilibrium point is the origin of the new coordinate system. By introducing the new variable

$$\tilde{x} = x - \overline{x}, \tag{A.9}$$

and substituting

$$x = \tilde{x} + \overline{x}$$

into Equation A.1, a new set of equations on the variable $\tilde{x}$ is obtained, *i.e.*,

$$\dot{\tilde{x}} = f(\tilde{x} + \overline{x}) := \tilde{f}(\tilde{x}). \tag{A.10}$$

It is worth noticing that there is a one to one correspondence between the solutions of (A.7) and those of (A.10). Moreover, $\tilde{x} = 0$, corresponding to $x = \overline{x}$, is an *equilibrium point* of system (A.10). Therefore, instead of studying the stability properties of $x = \overline{x}$ for (A.1), the behaviour of (A.10) in the neighbourhood of the origin can be equivalently examined.

A.2.1 Stability of Equilibrium Points: Lyapunov's Theory

In this section some fundamental stability concepts are formally defined and their practical significance is shortly discussed.

First, we recall the properties of the norm of a vector $x \in \mathbb{R}^n$ denoted by $\|x\|$, which will be used in the following.

Definition A.3. The norm $\|x\|$ of a vector $x \in \mathbb{R}^n$ is any real-valued function such that

1. $\|x\| \geq 0$;
2. $\|x\| = 0 \iff x = 0$;
3. $\|\alpha x\| = |\alpha| \|x\|, \quad \forall \alpha \in I\!R, \ \forall x \in I\!R^n$; and
4. $\|x + y\| \leq \|x\| + \|y\|, \quad \forall x, y \in I\!R^n$.

Note that in the case of finite dimensional systems, all norms are equivalent as far as stability analysis is concerned. Thus, without loss of generality, in the following we employ the Euclidean norm, which is defined as

$$\|x\| = \sqrt{\sum_{i=1}^{n} |x_i|^2}.$$

We are now ready to define stability in the sense of Lyapunov. In this respect, it is worth pointing out that in the general case this analysis is focused on studying the stability properties of the state motion $x(t)$. However, for our purposes it is sufficient to focus on the stability of the constant state motions, that is of the equilibrium points.

Definition A.4. An equilibrium point $\overline{x}$ is *stable in the sense of Lyapunov* if, for each $\varepsilon > 0$, there exists a $\delta = \delta(\varepsilon) > 0$ such that

$$\|x(0) - \overline{x}\| < \delta \implies \|x(t) - \overline{x}\| < \varepsilon, \quad \forall t \geq 0.$$

This means that an equilibrium point is *stable in the sense of Lyapunov* (or *Lyapunov stable*) when the state motion $x(t)$ originating from all initial points $x(0)$ sufficiently close to $\overline{x}$ remains within a specified distance ε of $\overline{x}$. An equilibrium that is not stable, is said to be *unstable*.

Definition A.5. An equilibrium state $\overline{x}$ is *asymptotically stable* if it is stable and if δ can be chosen such that

$$\big\|x(0) - \overline{x}\big\| < \delta \implies \lim_{t \to +\infty} x(t) = \overline{x}.$$

This means that an equilibrium point is asymptotically stable if all solutions starting at nearby points not only stay nearby, but also converge to the equilibrium point as time approaches infinity.

The intuitive meaning of these notions is illustrated in Figure A.1, where the curves (a), (b) and (c) represent, respectively, prototype state motions of systems having $\overline{x}$ as an asymptotically stable, stable or unstable equilibrium point.

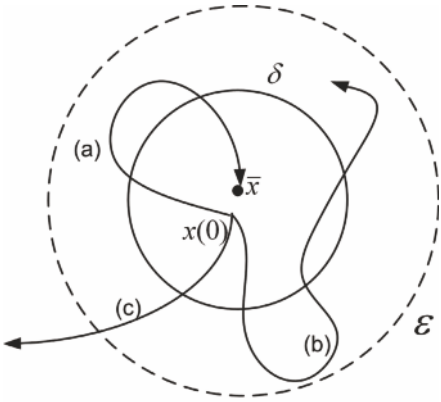

Figure A.1 Geometric interpretation of the stability notions

With the notions of stability and asymptotic stability defined above, one can address the problem of how to determine if and when such properties hold. In 1892, Lyapunov proved that certain types of functions could be used to determine stability of an equilibrium point. These results will be discussed in the following section.

A.2.1.1 Lyapunov's Direct Method

The *direct method*, also called the *second method of Lyapunov*, provides a general approach to the study of the stability of dynamical systems described by linear or nonlinear ordinary differential equations. Since this method requires no knowledge of the solutions of the equations, it provides a useful practical approach to the study of stability.

It is a generalisation of the energy concept of classical mechanics. Indeed, it is based on the concept of *total energy*, which is a non-negative function having the property of being zero at the equilibrium point and positive everywhere else.

Lyapunov used this fact to create a generalised energy function, satisfying some pre-specified properties with which he was able to establish the stability properties for a system of differential equations.

Theorem A.2 (Lyapunov's Stability Theorem). *Let $x = \overline{x}$ be an equilibrium point for system* (A.8), i.e.,

$$\dot{x} = f(x),$$

and $G \subset \mathbb{R}^n$ be a domain containing $\overline{x}$. Let $V : G \to \mathbb{R}$ be a continuously differentiable function such that

$$V(\overline{x}) = 0 \quad \text{and} \quad V(x) > 0 \quad \text{in} \quad G - \{\overline{x}\}, \tag{A.11}$$

$$\dot{V}(x) = \frac{\mathrm{d}V}{\mathrm{d}x} f(x) \leq 0 \quad \text{in} \quad G. \tag{A.12}$$

Then, the equilibrium point $\overline{x}$ of system (A.8) is *stable*.

Moreover, if

$$\dot{V}(x) < 0 \quad \text{in} \quad G - \{\overline{x}\} \tag{A.13}$$

then the equilibrium point $\overline{x}$ is *asymptotically stable*.

A continuously differentiable function $V(x)$ satisfying the two conditions (A.11) and (A.12) is called a *Lyapunov function*, while the surface $V(x) = c > 0$ is known as a *Lyapunov surface* or a *level surface*. The condition (A.12) implies that when a trajectory enters a Lyapunov surface $V(x) = c$, it continues to move inside the set $\Omega_l = \{x \in \mathbb{R}^n \mid V(x) \leq c\}$ and never leaves it. The set Ω_l is usually referred to as a *level set*.

If $\dot{V}(x) < 0$, the state trajectory moves from one level surface to an inner one, which corresponds to a smaller value of the constant c. In general, as c decreases, the level surface $V(x)$ shrinks to the equilibrium point showing that the trajectories come closer and closer to it.

If $\dot{V}(x) \leq 0$, it is not possible to guarantee that the state trajectory converges to the equilibrium state, but only to conclude that the equilibrium point is stable.

To state the stability notions introduced above in a more compact way, we introduce the following classification for the function $V(x)$.

Definition A.6. The function $V(x)$ is said to be *positive definite* on $G \subset \mathbb{R}^n$ if it satisfies condition (A.11), *i.e.*,

$$V(\overline{x}) = 0 \quad \text{and} \quad V(x) > 0 \quad \text{in} \quad G - \{\overline{x}\}. \tag{A.14}$$

Definition A.7. The function $V(x)$ is said to be *positive semidefinite* on $G \subset \mathbb{R}^n$ if it satisfies the weaker condition

$$V(\overline{x}) = 0 \quad \text{and} \quad V(x) \geq 0 \quad \text{in} \quad G - \{\overline{x}\}.$$

Similarly, a function $V(x)$ is *negative definite* or *negative semidefinite* if -$V(x)$ is positive definite or positive semidefinite, respectively.

By using these new definitions, it is straightforward to rephrase Lyapunov's stability theorem A.2 with the following statement.

Theorem A.3. *Consider the system* (A.8) *with equilibrium point* $\overline{x}$*. This equilibrium point is* stable *if there exists a continuously differentiable function* $V : G \to \mathbb{R}$*, with* $G \subset \mathbb{R}^n$*, such that*

- $V(x)$ *is positive definite on* G*; and*
- $\dot{V}(x)$ *is negative semidefinite on* G*.*

The equilibrium $\overline{x}$ *is* asymptotically stable *if*

- $V(x)$ *is positive definite on* G*; and*
- $\dot{V}(x)$ *is negative definite on* G*.*

An interesting class of scalar functions $V(x)$ for which positive or negative definiteness can easily be checked is the class of quadratic functions

$$V(x) = (x - \overline{x})^T P (x - \overline{x}),$$

where P is a real symmetric[3] matrix. In this case, $V(x)$ is *positive definite* or *positive semidefinite* if and only if all the eigenvalues of the matrix P are positive or non-negative, respectively. If $V(x)$ is positive definite, then it is possible to define P as a *positive definite matrix* and write $P > 0$.

When an equilibrium point is asymptotically stable, it is interesting to determine how large the constant δ can be taken in Definition A.5. This leads to the definition of *domain of attraction*.

Definition A.8. The set

$$G(\overline{x}) = \left\{ x(0) \in \mathbb{R}^n \mid \lim_{t \to +\infty} x(t) = \overline{x} \right\}$$

is called the *domain of attraction* of the equilibrium point $\overline{x}$.

Determining analytically the exact domain of attraction might be difficult or even impossible. However an interesting question that may arise is under what conditions the domain of attraction corresponds to the whole space $\mathbb{R}^n$, *i.e.*, the equilibrium $\overline{x}$ is *globally asymptotically stable*.

Theorem A.4 (Barbashin–Krasovskii's theorem). *Consider the system* (A.8) *and let* $x = \overline{x}$ *be an equilibrium state. Suppose that there exists a continuously differentiable function* $V : \mathbb{R}^n \to \mathbb{R}$ *such that*

$$V(\overline{x}) = 0 \quad \text{and} \quad V(x) > 0, \quad \forall x \neq \overline{x},$$

$$\|x - \overline{x}\| \to +\infty \quad \Longrightarrow \quad V(x) \to +\infty,$$

$$\dot{V}(x) < 0 \quad \forall x \neq \overline{x}.$$

Then the equilibrium state $\overline{x}$ *is a* stable *equilibrium point and any trajectory converges asymptotically to* $\overline{x}$*,* i.e.*,* $\overline{x}$ *is* globally asymptotically stable *(GAS).*

[3] Recall that a symmetric matrix has real eigenvalues.

The above theorem establishes the conditions that make a state trajectory approach the equilibrium point for any initial state as time progresses, no matter how far from the equilibrium point the initial state is. It must be noted that if an equilibrium point is globally asymptotically stable, this must be the *unique equilibrium* state of the system. In fact, if there were another equilibrium point, the solution trajectory starting in this equilibrium would stay in it forever. Therefore, it would not move toward the original equilibrium point and this contradicts the claim of the theorem.

In some cases, it is also necessary to estimate how fast the state will approach the equilibrium point. For this reason, the concept of *exponential stability* is introduced.

Definition A.9. An equilibrium state $\overline{x}$ is *globally exponentially stable* if there exist two constants $k > 0$ and $\gamma > 0$ such that

$$\|x(t) - \overline{x}\| \leq k\|x(0) - \overline{x}\|e^{-\gamma t}, \quad \forall t \geq 0 \quad \forall x(0).$$

Therefore, exponential stability means that trajectories of the closed-loop system converge to the equilibrium point at least as fast as an exponential function. Note, finally, that exponential stability implies asymptotic stability but not *vice versa*.

The previous results deal with the problem of establishing the stability properties of an equilibrium point. However, sometimes it might also be of interest to prove that an equilibrium is unstable. To this end, several results are available, the most powerful of which is Chetaev's theorem.

Theorem A.5 (Chetaev's theorem). *Let $x = \overline{x}$ be an equilibrium point for the system* (A.8)*,* i.e.*,*

$$\dot{x} = f(x),$$

and $G \subset \mathbb{R}^n$ be a domain containing $\overline{x}$. Let $V : G \to \mathbb{R}$ be a continuously differentiable function such that $V(\overline{x}) = 0$ and $V(\tilde{x}) > 0$ for some $\tilde{x}$ arbitrarily close to $\overline{x}$, i.e., with arbitrarily small norm $\|\tilde{x} - \overline{x}\|$. Consider now a ball of radius $r > 0$ defined as

$$\mathcal{B}_r = \{x \in \mathbb{R}^n | \, \|x - \overline{x}\| < r\} \tag{A.15}$$

contained in G and define the set

$$U = \{x \in \mathcal{B}_r \, | \, V(x) > 0\}. \tag{A.16}$$

Then, if

$$\dot{V}(x) > 0 \quad \text{in } U \tag{A.17}$$

the equilibrium point $\overline{x}$ is unstable*.*

The instability of the equilibrium comes from the fact that it is possible to choose an initial condition $x_0 = \tilde{x}$ arbitrarily close to $\overline{x}$ so that the trajectory

$x(t)$ which starts from it will eventually leave the ball $\mathcal{B}_r$ and this contradicts the $\varepsilon - \delta$ requirement used in the definition of a stable equilibrium point in the sense of Lyapunov (see Definition A.4).

A.2.1.2 Lyapunov's Linearisation Method

Lyapunov's linearisation method involves the concept of *local stability* of a nonlinear dynamical system. It derives from the idea that a nonlinear system should exhibit, in the neighbourhood of the linearisation point, a behaviour similar to that of its linear approximation.

Consider again the autonomous system

$$\dot{x} = f(x), \tag{A.18}$$

where $f : G \subset \mathbb{R}^n \to \mathbb{R}^n$ is a continuously differentiable function. Suppose that the state $x = \overline{x} \in G$ is an equilibrium point for the system (A.18), which implies $f(\overline{x}) = 0$. Then, the system dynamics (A.18) can be written, using a Taylor series expansion about $x = \overline{x}$, as

$$\dot{x} = \frac{\mathrm{d}f}{\mathrm{d}x}(x)\bigg|_{x=\overline{x}} (x - \overline{x}) + f_{\mathrm{h.o.t}}(x)(x - \overline{x}), \tag{A.19}$$

where $f_{\mathrm{h.o.t}}(x)$ indicates higher-order terms in $x - \overline{x}$. Let A be the Jacobian matrix of $f(x)$ at $x = \overline{x}$, *i.e.*,

$$A = \left[\frac{\partial f_i}{\partial x_j}(\overline{x})\right]_{\{i,j\}=1,\ldots,n}.$$

The system

$$\dot{x} = Ax \tag{A.20}$$

is called the *linear approximation* of the nonlinear system (A.18) about the equilibrium point $x = \overline{x}$.

The following theorem outlines the main condition under which it is possible to draw conclusions about the local stability of an equilibrium point for a nonlinear system by analysing the stability of the linearised system.

Theorem A.6. *Let $x = \overline{x}$ be an equilibrium point of the nonlinear system*

$$\dot{x} = f(x),$$

where $f : G \to \mathbb{R}^n$ is a continuously differentiable function and G is a subset of $\mathbb{R}^n$ containing $\overline{x}$. Let

$$A = \left[\frac{\partial f_i}{\partial x_j}(\overline{x})\right]_{\{i,j\}=1,\ldots,n}.$$

Then, the equilibrium point $\overline{x}$ *is* locally asymptotically stable *if all eigenvalues of A have negative real parts,* i.e., $\mathrm{Re}(\lambda_i) < 0, \forall i = 1 \ldots, n$. *Moreover, the equilibrium point* $\overline{x}$ *is* unstable *if at least one eigenvalue of A has a positive real part,* i.e., $\exists\, i \ : \mathrm{Re}(\lambda_i) > 0$.

The proof of the above theorem (see [44]) shows that when $\mathrm{Re}(\lambda_i) < 0$ for all eigenvalues of A, a suitable Lyapunov function, which works in some neighbourhood of the equilibrium point $\overline{x}$, is given by the quadratic form

$$V(x) = (x - \overline{x})^T P (x - \overline{x}),$$

where P is the solution of the Lyapunov equation

$$A^T P + PA = -Q,$$

with Q being any positive definite symmetric matrix.

Note that if the linearised system is such that all eigenvalues of A are in the left half complex plane, but at least one of them is located on the complex axis, then one cannot conclude anything from the linear approximation about the stability of the equilibrium point of the original nonlinear system.

A.2.1.3 LaSalle's Theory

As has already been discussed, Lyapunov stability theory provides an important tool for analysing the stability of an equilibrium state *without solving the system equations*. To prove asymptotic stability using Lyapunov theory the condition

$$\dot{V}(x) < 0, \qquad \forall x \in G - \{\overline{x}\}, \qquad G \subset \mathbb{R}^n$$

must be checked. This means that $\dot{V}(x)$ should be strictly negative for all $x \in G - \{\overline{x}\}$. In some cases, finding a candidate Lyapunov function $V(x)$ satisfying the weaker condition

$$\dot{V}(x) \leq 0, \qquad \forall x \in G \tag{A.21}$$

may be much easier. In this case, $\dot{V}(x)$ is not necessarily strictly negative for $x \neq \overline{x}$, hence Lyapunov's stability theorem A.2 cannot be applied.

LaSalle was able to show that if in a domain containing the equilibrium state $\overline{x}$ it is possible to find a Lyapunov function whose derivative along the trajectories of the system is negative semidefinite and if it is possible to establish that the only solution of the system satisfying the condition $\dot{V}(x) = 0$ is the trivial solution $x(t) = \overline{x}$, then $\overline{x}$ is asymptotically stable [51]. To formally state LaSalle's invariance theorem, it is necessary to introduce a few definitions.

Definition A.10. A set $G \subseteq \mathbb{R}^n$ is called an *invariant set* with respect to system (A.8) if

$$x(0) \in G \implies x(t) \in G, \quad \forall t \in \mathbb{R}. \tag{A.22}$$

Moreover, the set G is said to be a *positively invariant set* if

$$x(0) \in G \implies x(t) \in G, \quad \forall t \geq 0. \tag{A.23}$$

That is, a set is invariant if, for any initial state in the set, it is possible to find a suitable initial time such that the resulting trajectory stays in the set for all future times.

Definition A.11. A function $V(x)$ such that

$$\|x - \overline{x}\| \to +\infty \quad \implies \quad V(x) \to +\infty$$

is said to be *proper* or *radially unbounded*.

Definition A.12. A function $V(x) : \Omega \subset \mathbb{R}^n \to [0, +\infty)$ is said to be *proper in* Ω if

$$\lim_{x \to \partial\Omega} V(x) = +\infty$$

where $\partial\Omega$ is the boundary of the set Ω.

Theorem A.7 (LaSalle's theorem). *Let $\Omega \subset G$ be a compact set that is positively invariant with respect to* (A.8)*. Let $V : G \to \mathbb{R}$ be a continuously differentiable function such that $\dot{V}(x) \leq 0$ in Ω. Let E be the set of all points in Ω where $\dot{V}(x) = 0$. Let M be the largest invariant set in E. Then every solution starting in Ω approaches M as $t \to +\infty$.*

As a consequence, Theorems A.2 and A.4 may be modified as follows.

Corollary A.2. *Consider the autonomous system*

$$\dot{x} = f(x) \tag{A.24}$$

and let $x = \overline{x}$ be an equilibrium point of the system. Let the function $V : G \to \mathbb{R}$ be a continuously differentiable positive definite function on the domain $G \subset \mathbb{R}^n$ containing the equilibrium state $\overline{x}$, such that $\dot{V}(x) \leq 0$ in G.

Let $E = \{x \in G \mid \dot{V}(x) = 0\}$ and suppose that no solution can stay identically in E, other than the trivial solution. Then, the equilibrium state $\overline{x}$ is asymptotically stable.

Corollary A.3. *Consider the autonomous system* (A.24) *and let $x = \overline{x}$ be an equilibrium point of the system. Let the function $V : \mathbb{R}^n \to \mathbb{R}$ be a continuously differentiable, radially unbounded, positive definite function such that $\dot{V}(x) \leq 0$ for all $x \in \mathbb{R}^n$. Let $E = \{x \in \mathbb{R}^n \mid \dot{V}(x) = 0\}$ and suppose that no solution can stay identically in E, other than the trivial solution. Then, the equilibrium state $\overline{x}$ is* globally asymptotically stable.

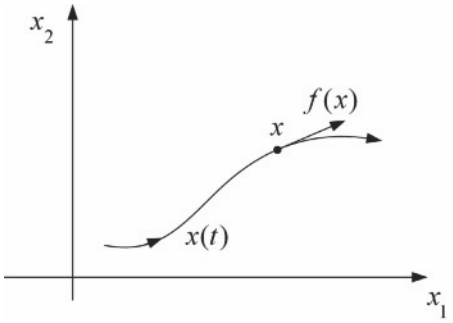

Figure A.2 Representation of the vector field in a second-order system

A.2.2 A Special Case: Second-order Dynamical Systems

Second-order systems are of particular interest in the study of dynamical systems, mainly because the system solutions can be pictorially represented by curves in the plane. Further, they also play an important role in some parts of this book and therefore deserve a dedicated treatment.

An autonomous, time-invariant second-order nonlinear dynamical system is a system of the form (A.8) that can be represented by two scalar equations of the form

$$\begin{aligned} \dot{x}_1 &= f_1(x_1, x_2), \\ \dot{x}_2 &= f_2(x_1, x_2). \end{aligned} \tag{A.25}$$

Assume that $f(x) = [f_1(x)\ f_2(x)]^T$, with $x = [x_1\ x_2]^T$, satisfies the assumptions of Theorem A.1 and let $x(t) = [x_1(t)\ x_2(t)]^T$ be the unique solution associated with the initial condition $x_0 = [x_{10}\ x_{20}]^T$. The locus in the plane (x_1, x_2) described by the solution $x(t)$ is a curve passing through x_0, usually called the *trajectory* of system (A.25). The (x_1, x_2) plane is called the *state plane*. Thus, $x(t)$ represents a point in the state plane and the right-hand side of (A.25) represents the velocity vector at that point. Hence, $f(x)$ can be considered as a *vector field*, in that with each point x of the state plane we associate a vector $f(x)$, which is tangent to the trajectory in x, see Figure A.2.

The collection of all trajectories in the state plane is often called the *state portrait* of system (A.25). Often, it is interesting to investigate the qualitative behaviour of such portrait, as it can reveal many interesting features of the system solution. This can be done by solving the nonlinear equation (A.25) for a large number of initial conditions *via* commonly available software routines and plotting the corresponding trajectories in the state plane.

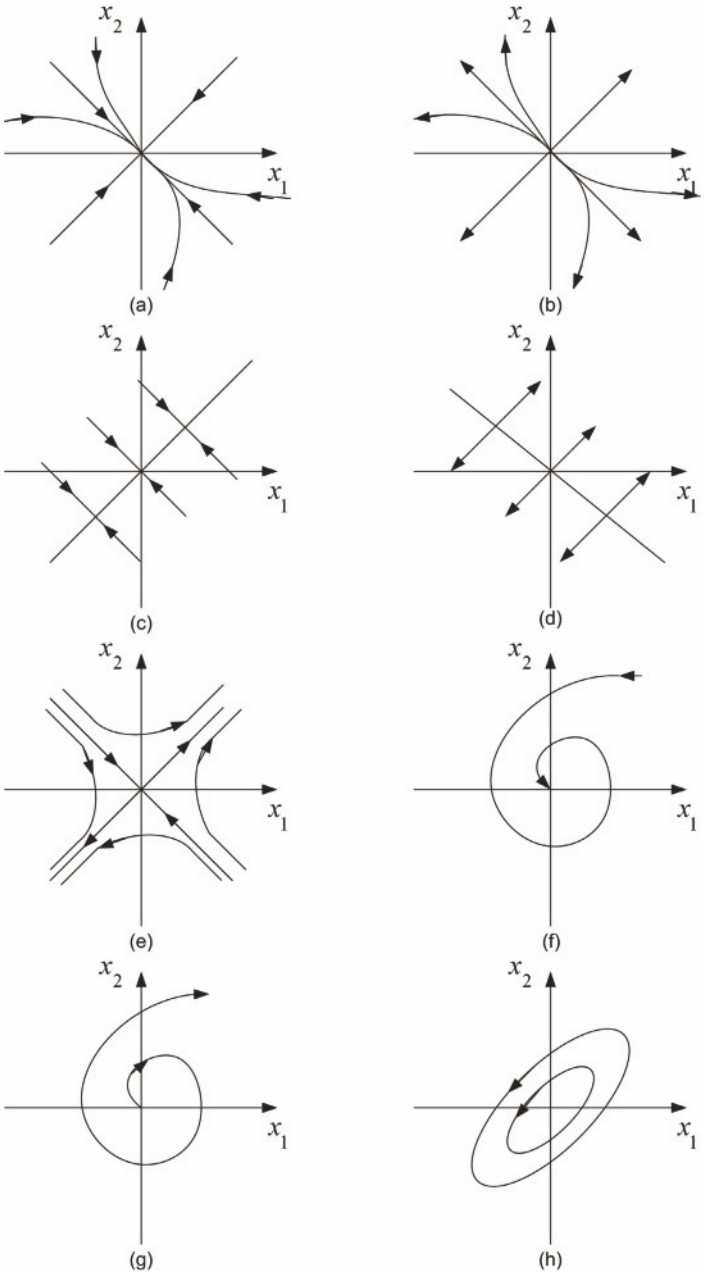

Figure A.3 Qualitative portrait of the trajectories of system (A.26)

A.2.2.1 Qualitative Analysis of Linear Systems

We now study the qualitative behaviour of the trajectories in the case of linear systems. To this end, consider the second-order linear time-invariant system

$$\dot{x} = Ax, \tag{A.26}$$

where A is a 2×2 real matrix. For simplicity, we limit the analysis to the case of A having two distinct eigenvalues λ_1 and λ_2 (see, *e.g.*, [44,126] for the more general case). Then, there exists a square and non-singular matrix T such that, with a coordinate change $\tilde{x} = Tx$, the system in the new coordinates has the form

$$\dot{\tilde{x}} = TAT^{-1}\tilde{x} = A_d\tilde{x}, \tag{A.27}$$

with A_d diagonal, *i.e.*,

$$A_d = \begin{bmatrix} \lambda_1 & 0 \\ 0 & \lambda_2 \end{bmatrix}. \tag{A.28}$$

Hence, the system solution $x(t)$ associated with the initial condition x_0 is given by

$$x(t) = T^{-1}e^{A_d\,t}T\,x_0 = T^{-1}\begin{bmatrix} e^{\lambda_1 t} & 0 \\ 0 & e^{\lambda_2 t} \end{bmatrix} T\,x_0, \tag{A.29}$$

which finally yields

$$x(t) = k_1 e^{\lambda_1 t} + k_2 e^{\lambda_2 t}, \tag{A.30}$$

where the constant vectors k_1 and k_2 depend on the initial condition x_0. In this setting, the following cases can be distinguished:

(a) Both eigenvalues are real and $\lambda_2 < \lambda_1 < 0$: the origin, which is an isolated equilibrium, is called a *stable node* (see Figure A.3 (a)). Note that if the initial state x_0 is on one of the two eigenvectors v_1 and v_2 associated with the eigenvalues λ_1 and λ_2, respectively, then the system trajectory will entirely evolve on the eigenvector itself. In the general case, instead, the trajectory will asymptotically converge to the origin, where it is tangent to the eigenvector v_1 associated with the *slow*[4] eigenvalue.

(b) Both eigenvalues are real and $\lambda_2 > \lambda_1 > 0$: the origin, which is an isolated equilibrium, is called a *unstable node* (see Figure A.3 (b)). The state portrait is similar to the previous case, except for the fact that the trajectories now move away from the origin.

(c) Both eigenvalues are real and $\lambda_2 < \lambda_1 = 0$: in this case the matrix A is singular, hence the system has an infinity of equilibrium points (forming an equilibrium subspace), which are all the points of the state plane spanned by the eigenvector v_1 associated with the zero eigenvalue λ_1. Thus, all trajectories are parallel to the eigenvector v_2 associated with the non-zero eigenvalue λ_2 and move toward the equilibrium subspace

[4] We call λ_1 the slow eigenvalue, with respect to λ_2, as the condition $\lambda_2 < \lambda_1 < 0$ implies that (see also Equation A.30) $e^{\lambda_1 t}$ goes to zero *more slowly* than $e^{\lambda_2 t}$.

(see Figure A.3 (c)). Such equilibrium point is sometimes called a *stable saddle-node*.

(d) Both eigenvalues are real and $\lambda_2 > \lambda_1 = 0$: this case is analogous to the previous one except for the fact that the trajectories now move away from the equilibrium subspace (see Figure A.3 (d)). Such equilibrium point is sometimes called an *unstable saddle-node*.

(e) Both eigenvalues are real and $\lambda_2 > 0, \lambda_1 < 0$: the origin, which is an isolated equilibrium, is called a *saddle* (see Figure A.3 (e)).

(f) The eigenvalues are complex conjugates, *i.e.*, $\lambda_{1,2} = \alpha \pm j\beta$

- If $\alpha < 0$ the origin, which is an isolated equilibrium, is called a *stable focus* (see Figure A.3 (f)). In this case the trajectories spiral toward the origin.
- If $\alpha > 0$ the origin, which is an isolated equilibrium, is called a *unstable focus* (see Figure A.3 (g)). In this case the trajectories spiral away from the origin.
- If $\alpha = 0$ the origin, which is an isolated equilibrium, is called a *centre* (see Figure A.3 (h)) and the trajectories are closed curves encircling the origin.

Note that, in the general case of an $n \times n$ A matrix, it is always possible to group its eigenvalues into three different classes, according to the sign of their real part: n^- eigenvalues with negative real part, n^+ eigenvalues with positive real part and n^0 eigenvalues with zero real part. Obviously, $n = n^- + n^+ + n^0$. The associated eigenvectors form three disjoint invariant subspaces: S^-, S^+ and S^0, respectively, of dimension n^+, n^- and n^0. Accordingly, initial states belonging to S^- generate trajectories that converge to zero, whereas initial states belonging to S^+ generate trajectories that grow to infinity. Due to this fact, S^- is referred to as a *stable manifold* and S^+ as an *unstable manifold*. The subspace S^0 is called the *centre manifold*: the trajectories generated from an initial state $x_0 \in S^0$ can either be bounded (but not convergent to the origin), if the system is marginally stable, or can tend to infinity but with a slower than exponential rate, in the case of a so-called *weakly unstable* system.

Systems that do not possess a centre manifold, hence that do not have any eigenvalue with zero real part, are called *hyperbolic* (the same term is used for indicating the equilibrium points of an hyperbolic system, which are called hyperbolic equilibrium points). The system (and corresponding equilibrium points) are called *attractors* if $n = n^-$, hence $S^- \equiv R^n$ and *repulsors* if $n = n^+$, hence $S^+ \equiv R^n$. Finally, systems with a non-empty centre manifold, *i.e.*, which possess eigenvalues with zero real part, are called *non-hyperbolic* (the same term is used for indicating the equilibrium points of a non-hyperbolic system, which are called non-hyperbolic equilibrium points).

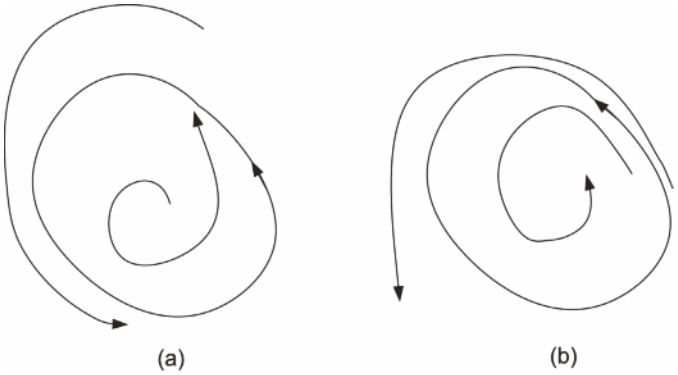

Figure A.4 Stable (a) and unstable (b) limit cycles

A.2.2.2 Limit Cycles

In dynamical systems, oscillations are a very important phenomenon. A system is said to oscillate if it admits a *non-trivial periodic solution*, *i.e.*, if there exists a $T > 0$ such that

$$x(t+T) = x(t), \quad \forall\, t \geq 0. \tag{A.31}$$

The term non-trivial refers to the fact that we want to exclude constant solutions that correspond to equilibrium points. These solutions indeed satisfy condition (A.31), but do not represent oscillations in the usual sense. The closed curve formed by a periodic solution in the state plane is called an *orbit* or a *periodic orbit*.

A *limit cycle* is an isolated periodic orbit (or, equivalently, an isolated periodic solution). The term isolated means that nearby trajectories are not closed. In fact, they either spiral toward (Figure A.4 (a)) or away (Figure A.4 (b)) from the limit cycle itself. If all neighbouring trajectories approach the limit cycle, this is called *stable* or *attracting*. If, on the contrary, all nearby trajectories move away from the limit cycle, it is called *unstable*.

Note that limit cycles are inherently nonlinear phenomena. As we have seen before in the case when the origin is a *centre*, linear systems admit trajectories that are orbits, but they are not isolated. In fact, if $x(t)$ is a periodic solution, so is $\alpha x(t)$, for any non-negative α. Thus, in the case of linear systems, there is a continuum of closed orbits.

In general, it is difficult to say if a system admits a limit cycle, or any periodic orbit. For second-order systems, periodic orbits have a particular importance as, due to Corollary A.1, they divide the state space into two parts: the interior and the exterior of the periodic (closed) orbit. This makes it possible to define specific criteria for analysing the presence or the absence of periodic orbits that do not generalise to higher-order systems.

For the purpose of this book, we focus on discussing a result that gives a condition for the existence of periodic orbits, which is known as the Poincaré–Bendixon theorem. The idea behind this theorem is linked to Corollary A.1. Suppose in fact that a second-order system possesses a periodic orbit $\mathcal{O}$ in the state plane. Due to the fact that different trajectories cannot intersect, a trajectory starting in the region of the state plane inside the orbit is forced to remain there forever. So, what can happen to such a bounded trajectory as time grows to infinity? If the region within the periodic orbit $\mathcal{O}$ contains asymptotically stable equilibrium points, then intuition says that the trajectory might approach one of them. However, if there are no equilibrium points, or only repulsor ones, then the (bounded) trajectory will eventually approach the periodic orbit, as it cannot wander forever within the region $\mathcal{O}$.

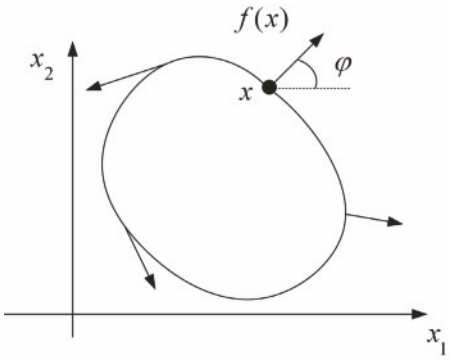

Figure A.5 Computation of the index of a closed curve

Before stating the theorem, we introduce an additional, crucial tool to relate the existence of periodic orbits and equilibrium points. These results are known as index theory, and are mainly due to the work of Poincaré.

To this end, consider the second-order autonomous and time-invariant nonlinear system

$$\dot{x} = f(x), \tag{A.32}$$

and assume that $f(x)$ is continuously differentiable. Let C be a simple[5] closed curve not passing through any equilibrium of system (A.32). Note that C does not need to be a trajectory. Then, at each point $x \in C$, there is a well defined angle φ between the vector field $f(x)$ and the positive x_1 axis (see Figure A.5), which is given by

$$\varphi = \arctan\left(\frac{f_2}{f_1}\right). \tag{A.33}$$

[5] A closed curve is said to be *simple* if it does not intersect itself.

As the point x moves counterclockwise along C, the angle φ varies continuously and it returns to its original position when x gets back to its starting place. Thus, along one full cycle of x along C, φ varies of a multiple of 2π. Let φ_C be the total angle variation over one cycle. Then the index of the curve C can be computed as

$$I_C = i, \quad i \in \mathbb{N} \quad \text{such that} \quad \varphi_C = 2\pi\, i. \tag{A.34}$$

If the simple closed curve C encircles an isolated equilibrium point $\overline{x}$, then I_C is called the index of $\overline{x}$. Since in this case the index is a property of the equilibrium alone, C being *any* simple closed curve encircling it, we drop the subscript C and indicate the index of a point as I. According to this definition, and recalling the state portraits of the second-order system discussed in Section A.2.2.1, it is easy to verify the next lemma.

Lemma A.1. *For a second-order system, the following hold:*

- *the index of a node, a focus or a centre is* $I = +1$*;*
- *the index of a (hyperbolic) saddle is* $I = -1$*;*
- *the index of a periodic orbit is* $I = +1$*;*
- *the index of a closed curve not encircling any equilibrium point is* $I = 0$*; and*
- *the index of a closed curve is equal to the sum of the indices of the equilibrium points in the region within it.*

Notably, from the above lemma we can derive the following.

Corollary A.4. *Inside any periodic orbit* $\mathcal{O}$ *there must be at least one equilibrium point. If there is only one equilibrium point inside a periodic orbit, then it cannot be a saddle point. If there is more than one equilibrium point inside a periodic orbit and they are all hyperbolic, then if* N *is the number of nodes and foci and* S *is the number of saddles, it must be that* $N - S = 1$*.*

We are now ready to state the following theorem.

Theorem A.8 (Poincaré–Bendixon theorem). *Consider the second-order autonomous and time-invariant nonlinear system* (A.32)*. Let* $M \in \mathbb{R}^2$ *be a closed bounded subset of the state plane, which contains no equilibrium points and assume that* $f(x)$ *is continuously differentiable on an open set containing* M*. If there exists a trajectory* $\mathcal{T}$ *that is trapped in the region* M*,* i.e.*, it starts in* M *and stays within it for all future time, then either* $\mathcal{T}$ *is a periodic orbit or asymptotically tends to a periodic orbit as time grows to infinity. In both cases, the region* M *contains a periodic orbit.*

When applying the Poincaré–Bendixon theorem, the tricky part is to show that there is indeed a trajectory $\mathcal{T}$ trapped in the region M. To do this, the usual procedure is to construct a *trapping region* M in the state plane, which is a closed connected set such that the vector field points inward everywhere

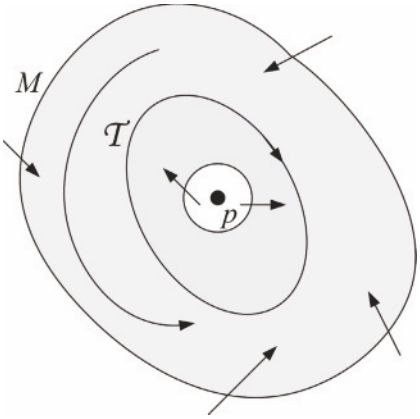

Figure A.6 Pictorial representation of the Poincaré–Bendixon theorem

on the boundary of M (see Figure A.6). If this is the case, then all trajectories that start in M are confined within it (thus, M is a positively invariant set). Then, if we can also show that there are no equilibrium points in M, the Poincaré–Bendixon theorem applies and ensures that M contains a periodic orbit. Note, further, that in Figure A.6 the region M is represented as an annular region because we have seen that the closed orbit must enclose (at least) an equilibrium point, represented by p in Figure A.6.

The fact that the periodic orbit must contain at least one equilibrium point combined with the necessity that M be a trapping region leads to a useful corollary of the Poincaré–Bendixon theorem, known as the Poincaré–Bendixon criterion.

Corollary A.5 (Poincaré-Bendixon criterion). *Consider the second-order autonomous and time-invariant nonlinear system* (A.32). *Let $M \in \mathbb{R}^2$ be a closed bounded subset of the plane and assume that $f(x)$ is continuously differentiable on an open set containing M. Assume further that M contains either no equilibrium points or only one equilibrium point such that the linearised system at this point has eigenvalues with positive real part (thus the equilibrium is an unstable node or an unstable focus). If every trajectory $\mathcal{T}$ that starts in M stays within it for all future time, then M contains a periodic orbit.*

Now that we have discussed how the existence of periodic orbits can be checked, we are interested in introducing a tool which allows us to assess their stability (or attractiveness): the *Poincaré map*.

Consider an n-dimensional nonlinear dynamical system (this tool also applies to systems or order greater than 2, so we discuss it in the general case). Let S be a surface of dimension $n-1$, which is *transversal* to the system flow, that is such that there is no point $x \in S$ to which the vector $f(x)$ is tangent (see Figure A.7). The Poincaré map is a mapping from S onto itself,

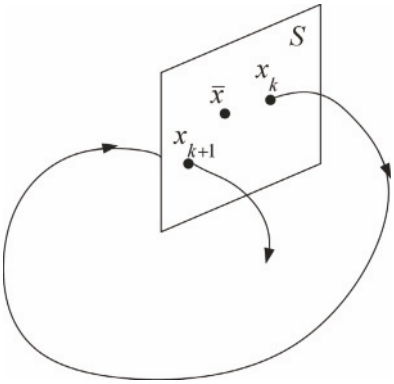

Figure A.7 Pictorial representation of the Poincaré map

obtained by monitoring the successive intersections of the system trajectory with S. Specifically, if x_k is the kth intersection, then the Poincaré map is defined as

$$x_{k+1} = P(x_k). \tag{A.35}$$

Suppose now that the map P has an equilibrium point $\overline{x}$, *i.e.*, $P(\overline{x}) = \overline{x}$. Then this implies that a trajectory that starts at $x = \overline{x}$ returns to $\overline{x}$ after some time T. Thus, such a trajectory is a closed orbit for the underlying nonlinear dynamical system. This means that Poincaré maps allow us to convert problems about closed orbits in $\mathbb{R}^n$ into problems of equilibrium points of a discrete time dynamical system of order $n-1$, which in principle are easier to analyse.

The problem we want to solve is the following: given an n-dimensional nonlinear dynamical system $\dot{x} = f(x)$ which admits a periodic orbit, how can we say if such a periodic orbit is stable? As we have seen, we can reformulate such a problem into that of assessing whether the corresponding equilibrium point $\overline{x}$ of the Poincaré map is stable. To do this, consider an infinitesimal perturbation δx_0 such that $\overline{x} + \delta x_0$ is still on the surface S. If we choose $\overline{x} + \delta x_0$ as initial condition for the system trajectory, after its first return onto S, we have

$$\overline{x} + \delta x_1 = P(\overline{x} + \delta x_0) = P(\overline{x}) + \frac{\partial P}{\partial x}(x)\bigg|_{x=\overline{x}} \delta x_0 + P_{\text{h.o.t}}(x)(\delta x_0), \tag{A.36}$$

where

$$\frac{\partial P}{\partial x}(x)\bigg|_{x=\overline{x}} = \left[\frac{\partial P_i}{\partial x_j}(\overline{x})\right]_{\{i,j\}=1,\ldots,n}$$

is the Jacobian of the Poincaré map at $x = \overline{x}$ and $P_{\text{h.o.t}}(x)(\delta x_0)$ indicates higher-order terms in δx_0. As $P(\overline{x}) = \overline{x}$, and assuming that we can neglect the higher-order terms, Equation A.36 becomes

$$\delta x_1 = \frac{\partial P}{\partial x}(x)\bigg|_{x=\overline{x}} \delta x_0. \tag{A.37}$$

Thus, we can express the stability criterion for the closed orbit in terms of the eigenvalues λ_i, $i = 1, \ldots, n$ of the Jacobian of the Poincaré map as follows.

Theorem A.9 (Stability of closed orbits). *The closed orbit is locally asymptotically stable if* $|\lambda_i| < 1$ *for all eigenvalues of the Jacobian of the Poincaré map*[6].

A.3 Nonlinear Design Tools

As can be easily understood, the design of a nonlinear feedback controller is a very challenging task, as one cannot expect that a single design procedure may apply to all sort of nonlinear systems. Moreover, different control problems provide specifications and requirements that the designer needs to meet, and each application domain leads to a different degree of reliability of the mathematical representation of the underlying physical system. Hence, many different design tools have been developed for nonlinear systems, each of which is particularly suitable to come up with a control law that allows the closed-loop system to possess the desired properties and fulfil the necessary requirements.

In this section we introduce the *feedback stabilisation* problem, and then state a specific result that shows how a dynamical control law can be designed so that the closed-loop system is stabilised around a desired equilibrium point without the need to know in advance which is the associated (constant) control input and which also ensures a bounded control action.

Before stating the main result employed in this book, we introduce the problem of equilibrium stabilisation. Guaranteeing that the equilibrium of interest can be stabilised *via* feedback, in fact, is the basic requirement that the controller has to fulfil. In typical control problems there are also additional requirements like achieving desired convergence rates, meeting constraints on the control input, achieving the attenuation or rejection of measurable or unmeasurable disturbances acting on the system and ensuring robustness against modeling uncertainties.

[6] Note that the condition $|\lambda_i| < 1$, $\forall i = 1 \ldots, n$ is the discrete time counterpart of the condition $\text{Re}(\lambda_i) < 0$, $\forall i = 1 \ldots, n$ for the continuous time case.

The basic feedback stabilisation problem for a nonlinear system time-invariant of the form

$$\dot{x} = f(x, u) \tag{A.38}$$

is that of finding a feedback control law

$$u = g(x) \tag{A.39}$$

such that the origin (recall that, in view of (A.10), without loss of generality any equilibrium point can be translated to the origin) is an asymptotically stable equilibrium of the closed-loop system

$$\dot{x} = f(x, g(x)). \tag{A.40}$$

The control law (A.40) is usually called a *static state feedback*, because it is an algebraic function of the state x. Conversely, a *dynamic state feedback* is a control law of the form

$$u = g(x, z), \tag{A.41}$$

where z is the solution of the dynamical system

$$\dot{z} = f(z, x). \tag{A.42}$$

If the state x is not available for feedback but we can design a control law based only on the measurable output y, the resulting stabilisation problem is called *output feedback* stabilisation. This entails the design of a control law for the system

$$\begin{aligned} \dot{x} &= f(x, u), \\ y &= h(x, u), \end{aligned} \tag{A.43}$$

of the form

$$u = g(y) \tag{A.44}$$

in the case of *static output feedback* or of the form

$$\begin{aligned} u &= g(y, z), \\ \dot{z} &= f(y, z) \end{aligned} \tag{A.45}$$

in the case of *dynamic output feedback*.

Further, we point out again that even if the aforementioned stabilisation problem is defined with reference to an equilibrium point at the origin, the same formulation can be used to stabilise the system around an arbitrary equilibrium (or steady-state) point x_{ss}. To do this, we of course require the existence of an associated steady-state value of the input, u_{ss}, which can maintain the state of the closed-loop system at $x = x_{ss}$, *i.e.*, so that it ensures

$$f(x_{ss}, u_{ss}) = 0. \tag{A.46}$$

To recast the problem as one of stabilising the origin, it is sufficient to perform a change of coordinates in exactly the same way as discussed in Section A.2, *i.e.*, defining

$$\begin{aligned} \tilde{x} &= x - x_{ss}, \\ \tilde{u} &= u - u_{ss}, \end{aligned} \tag{A.47}$$

which allows the closed-loop system to be expressed as

$$\dot{\tilde{x}} = f(\tilde{x} + x_{ss}, \tilde{u} + u_{ss}) := \tilde{f}(\tilde{x}, \tilde{u}), \tag{A.48}$$

where $\tilde{f}(0, 0) = 0$.

Within the context of feedback stabilisation, we now introduce a result given in [4], which provides a method for the design of a stabilising dynamic feedback control law. The proof is constructive, as it shows how to design the stabilising feedback and prove the stability of the closed-loop system equilibrium *via* Lyapunov's methods. It is therefore reported and briefly commented on here.

Proposition A.1. *Consider the system*

$$\dot{x} = f(x) + g(x)u, \tag{A.49}$$

with state $x \in \mathbb{R}^n$ and control $u \in \mathbb{R}$. Suppose that there exists an unknown constant control $u = u_{\rm ss}$ and a positive definite and proper function $V(x)$ such that

$$\dot{V}(x) = \frac{\mathrm{d}V}{\mathrm{d}x} f(x) + \frac{\mathrm{d}V}{\mathrm{d}x} g(x) u_{\rm ss} < 0 \tag{A.50}$$

for all non-zero x. Then, for any $u_{\min}$ and $u_{\max}$ such that $u_{\min} \leq u_{\rm ss} \leq u_{\max}$, there exists a dynamic control law, which does not require prior knowledge of $u_{\rm ss}$, namely

$$\begin{aligned} u &= \theta, \\ \dot{\theta} &= \Theta(x, \theta), \end{aligned} \tag{A.51}$$

with $\theta(0) \in (u_{\min}, u_{\max})$, such that the equilibrium $(x, \theta) = (0, u_{\rm ss})$ of the closed-loop system (A.49),(A.51) *is stable in the sense of Lyapunov, the variable x converges to zero and, along the trajectories of the closed-loop system, $\theta(t) = u(t) \in [u_{\min}, u_{\max}]$.*

Proof. Consider the function

$$V(x) + \omega(\theta), \tag{A.52}$$

where (see Figure A.8)

$$\omega(\theta) = \ln(u_{\max} - \theta)^{\tau/k} - \ln(\theta - u_{\min})^{(\tau+1)/k}, \tag{A.53}$$

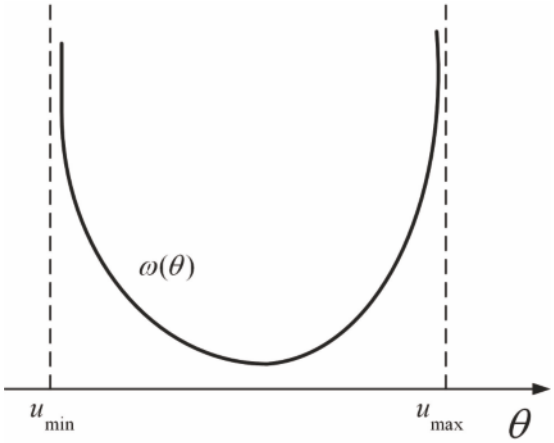

Figure A.8 The function $\omega(\theta)$

with $k > 0$, $\tau = \dfrac{u_{\rm ss} - u_{\max}}{u_{\max} - u_{\min}} < 0$ and $\tau + 1 > 0$. Note that $V(x) + \omega(\theta)$ is positive definite and proper in $\Omega_{x\theta} = \{(x, \theta) \in \mathbb{R}^{(n+1)} \mid u_{\min} < \theta < u_{\max}\}$. Then, differentiation with respect to time gives

$$\begin{aligned} \dot{V}(x) + \dot{\omega}(\theta) &= \frac{\partial V}{\partial x}\Big[f(x) + g(x)\theta\Big] + \frac{\partial \omega}{\partial \theta}\dot{\theta} \\ &= \frac{\partial V}{\partial x}\Big[f(x) + g(x)u_{\rm ss}\Big] + \frac{\partial V}{\partial x}g(x)(\theta - u_{\rm ss}) + \frac{\partial \omega}{\partial \theta}\dot{\theta}. \end{aligned} \tag{A.54}$$

Setting

$$\dot{\theta} = \frac{\partial V}{\partial x}g(x)\sigma(\theta), \tag{A.55}$$

with

$$\sigma(\theta) = k(\theta - u_{\max})(\theta - u_{\min}) \tag{A.56}$$

and noting that

$$\theta - u_{\rm ss} + \frac{\partial \omega}{\partial \theta}\sigma(\theta) = 0$$

yields

$$\begin{aligned} \dot{V}(x) + \dot{\omega}(\theta) &= \frac{\partial V}{\partial x}\Big[f(x) + g(x)u_{\rm ss}\Big] + \frac{\partial V}{\partial x}g(x)\Big[\theta - u_{\rm ss} + \frac{\partial \omega}{\partial \theta}\sigma(\theta)\Big] \\ &= \frac{\partial V}{\partial x}\Big[f(x) + g(x)u_{\rm ss}\Big] < 0 \end{aligned} \tag{A.57}$$

for all non-zero x. As a result the closed-loop system

$$\begin{aligned} \dot{x} &= f(x) + g(x)\theta, \\ \dot{\theta} &= \Theta(x, \theta) \end{aligned} \tag{A.58}$$

has a locally stable equilibrium $(x, \theta) = (0, u_{\text{ss}})$ and any trajectory starting in the set $\Omega_{x\theta}$ converges asymptotically to the equilibrium $(0, u_{\text{ss}})$ and $\theta(t) = u(t) \in [u_{\min}, u_{\max}], \forall t$.

□

Note that Lemma A.1 shows that if the system (A.49) admits a globally asymptotically stable equilibrium associated with the constant control $u = u_{\text{ss}}$, then it is possible to design a dynamic control law that *does not* require precise knowledge of the value u_{ss}, yielding a closed-loop system with a locally stable equilibrium such that $\lim_{t \to +\infty} x(t) = 0$. Note that, in general, this dynamic control law requires that the state of the system can be measured.

Further, the dynamic control law proposed in the proof of Lemma A.1 requires only the knowledge of an upper and lower bound on the constant input u_{ss} and ensures a *bounded* control action. This is a particularly important feature in engineering applications, where actuator saturation must always be taken into account.

A.4 Summary

This chapter has reviewed some concepts from stability theory and dynamical systems analysis that are useful for analysing nonlinear systems.

Specifically, background definitions concerning the stability of equilibrium points were provided, as well as the main notions of Lyapunov's stability theory. In particular, the various concepts of stability, *i.e.*, asymptotic stability, global asymptotic stability and exponential stability, which characterise different aspects of the behaviour of dynamical systems, have been briefly described.

The most useful theorems of the Lyapunov's direct method were recalled, together with the main results of Lyapunov's linearisation method. Further, the special class of second-order dynamical systems was given special attention, with the purpose of showing how to classify the systems equilibrium points and qualitatively describe their trajectories. The important concept of closed orbits and limit cycles was presented, together with mathematical tools to investigate their existence and stability properties.

As for the synthesis part, we introduced the general framework of feedback stabilisation. Based on that, we discussed a specific instance of Lyapunov-based controller design employed in this book for the design of nonlinear braking controllers.

Appendix B
Signal Processing of Wheel Encoders

B.1 Introduction

In this book different braking control approaches and estimation problems are presented. In practice, all of them rely on the ability to correctly process the measured signals in order to extract the relevant information to be employed for either control or estimation purposes.

This appendix presents the signal processing issues that need to be dealt with in order to manage the measurements coming from the wheel encoder signals, which are the basic sensors on board of any vehicle equipped with active control systems.

Specifically, we illustrate the management of the wheel encoder signals with specific reference to the most common algorithms used to estimate velocity from the measurements of these sensors. For these algorithms, we discuss advantages and disadvantages in terms of estimation error and estimation delay as these features may affect the control algorithms properties and impact on the closed-loop system performance.

Further, we discuss the wheel radius calibration, which constitutes another fundamental step for correct wheel speed computation.

Finally, a spectral analysis of the wheel speed signals allows us to highlight which dynamic components appear in these signals and to discuss how such signals must be filtered in order to be properly employed within active braking control systems.

B.2 Wheel Encoders' Signals

There are mainly two types of instruments to measure rotational speed: electromagnetic speedometers and digital speedometers. The electromagnetic

speedometer was invented in 1902 and it is based on the measurement of the current generated by a rotating magnet.

In the past few years, the electro-magnetic speedometer has been replaced by the digital speedometer (or discrete position encoder). Different types of discrete position encoders exist but they all fall under the same functional definition. They may employ different technologies (Hall's effect or optical sensors, for example), but are mainly made of two elements: a rotating part with teeth (or lines) and a fixed sensor that detects the passage of a line outputting a pulse for each line.

Note that some of the available encoders provide as first output a sinusoidal signal, whose amplitude and frequency depend on the current wheel speed. However, the last generation of such type of encoders is complemented with a digital chip that extracts a square wave from the sinusoidal signal. The latter is then seen as a sequence of pulses, which is processed for vehicle speed estimation.

Figure B.1 Example of a wheel encoder installed on a motorbike

Figure B.1 depicts the rear wheel encoder of a motorbike. Digital encoders do not directly measure the rotational velocity, which must be reconstructed from the pulses received. The velocity estimation problem is usually addressed with two approaches: either *model-based* or *signal-based* techniques can be applied.

All techniques that assume the availability of a model of the system whose velocity is under estimation fall in the model-based approach category. In the literature, the problem has been addressed with techniques such as model reference adaptive systems [57, 76], sliding mode observers [82], neural networks [11, 46], Kalman filters [10] and extended Kalman filters [6, 97]. These techniques have had many successful applications in electrical motors for

which simple and fairly accurate models exist. Conversely, in the automotive field accurate wheel models are rare, since the dynamics is affected by the highly nonlinear and uncertain tyre–road friction description; this reason makes the non-model-based approach more suited for automotive applications.

Signal-based approaches are based on signal processing techniques; the signal processing community has produced plenty of algorithms; there are solutions based on first-order approximations of the velocity [42,43,66], higher-order approximations [14], exact polynomial interpolation [36], least squares interpolation of the position trajectory [56] and on linear or nonlinear numerical integration methods [103,104]. Each of the above-mentioned algorithms has its advantages and disadvantages, which depend on velocity and acceleration; in fact, it was shown through simulations that for a system with a wide range of speed values a globally optimal velocity estimator does not exist, see [56,78].

The same result is achieved in [9] with the help of analytical tools. It should be noted that, despite the numerous available signal-based methods, they can all be seen as refinements, specialisations or improvements of two basic algorithms for speed estimation: the *lines per period* algorithm and the *fixed position* algorithm.

Although the limitations and features of these two methods are known to the signal processing community, it is worth providing the derivation of their properties in an analytical way.

To this end, the next section is devoted to deriving analytical closed-form models of the error and delay properties of the two basic algorithms. This analysis is then used to draw guidelines for the choice of the estimation algorithm for a given application. Note that it may happen that the braking control system engineer is provided with angular speed signals that have already been processed, as there are digital chips available on the market that are directly attached to the encoder sensor. Even if this is the case, it is advisable that the control engineer be well aware of the vehicle estimation method used and of how it works, as it may pose some limitations on the control system design phase.

B.2.1 Velocity Estimation Algorithms

As has already been mentioned the velocity estimation algorithm available in the literature can be classified into two families: the lines-*per*-period (LPP) algorithms and the fixed-position algorithms, also called $1/\Delta$T. Both algorithms will now be studied, and the two main features that characterise their behaviour, *i.e.*, the estimation error and the estimation delay, will be discussed.

B.2.1.1 The Lines-*per*-period Algorithm

In the LPP algorithm (also known as fixed-time algorithm) the speed $\hat{\omega}_{\text{LPP}}$ is estimated every sampling period of duration T_s, as the ratio between the angular rotation and the sampling interval, *i.e.*,

$$\hat{\omega}_{\text{LPP}} = \frac{n_c \frac{2\pi}{N}}{T_s}, \tag{B.1}$$

where n_c is the number of teeth counted in the last sampling period and N is the number of teeth of the encoder (note that even if the encoder tooth has a finite width, the processing hardware detects only the ascending fronts). The main source of estimation error is the position measurement truncation [19], caused by the impossibility of counting a fractional number of lines. The truncation induces a succession of underestimation and overestimation errors, whose pattern can either repeat itself after a finite number of sampling intervals or not. A periodic pattern is generated if and only if there exists a *least common multiple* between the sampling interval T_s and the time interval T_T between two successive teeth.

Formally, as the sampling interval T_s is always a non-negative rational number[1] ($T_s \in \mathbb{Q}^+$), the existence of a least common multiple is guaranteed only if also $T_T \in \mathbb{Q}^+$. Nonetheless (see [64]), T_T is a function of the speed ω; then, with probability 1 (the rational numbers are a zero Lebesgue measure set) T_T is irrational, that is $T_T \in \mathbb{R}^+ \backslash \mathbb{Q}^+$ *almost surely*. Hence, the analytical expression of the estimation error is derived here in the general case $T_T \in \mathbb{R}^+ \backslash \mathbb{Q}^+$.

First, notice that for any value of the angular speed ω, there always exists an integer k (which implicitly depends on ω, namely $k = k(\omega)$) such that

$$kT_T < T_s < (k+1)T_T. \tag{B.2}$$

Using (B.1), such an expression can be rewritten as

$$\frac{2\pi k}{NT_s} < \omega < \frac{2\pi(k+1)}{NT_s}. \tag{B.3}$$

If $T_T \in \mathbb{Q}^+ \backslash \mathbb{Q}^+$, the under/overestimation pattern never repeats itself. Instead, letting $t \to +\infty$, T_s assumes all the possible relative positions with respect to T_T. More specifically, the sampling instant can occur in any position $[0, T_T]$ between two pulses, and the probability of this occurrence is uniformly distributed [64]. Accordingly, the probabilities of counting k and $k+1$ lines, respectively, are given by

$$p_{n_c=k} = \frac{(k+1)T_T - T_s}{T_T}, \quad p_{n_c=k+1} = \frac{T_s - kT_T}{T_T}. \tag{B.4}$$

[1] The set of non-negative rational numbers is indicated with $\mathbb{Q}^+$.

Based on these relations and recalling (B.1), the expected value of the overall estimation error e_{LPP} can be computed as

$$\begin{aligned} E[e_{\mathrm{LPP}}] &= p_{n_c=k} E[e_{\mathrm{LPP}\{\mathrm{n_c=k}\}}] + p_{n_c=k+1} E[e_{\mathrm{LPP}\{\mathrm{n_c=k+1}\}}] \\ &= \frac{(k+1)T_T - T_s}{T_T} \underbrace{\left[\frac{\frac{2\pi}{N}}{T_T} - \frac{k\frac{2\pi}{N}}{T_s}\right]}_{e_{\mathrm{LPP}\{\mathrm{n_c=k}\}}} + \frac{T_s - kT_T}{T_T} \underbrace{\left[\frac{\frac{2\pi}{N}}{T_T} - \frac{(k+1)\frac{2\pi}{N}}{T_s}\right]}_{e_{\mathrm{LPP}\{\mathrm{n_c=k+1}\}}} \\ &= \frac{\frac{2\pi}{N}}{T_T}\left\{((k+1)T_T - T_s)\left[\frac{\omega N}{2\pi} - \frac{k}{T_s}\right] + (T_s - kT_T)\left[\frac{\omega N}{2\pi} - \frac{k+1}{T_s}\right]\right\} \\ &= \frac{\frac{2\pi}{N}}{2\pi T_s T_T}[\omega N T_s T_T - 2\pi T_s] = \frac{\frac{2\pi}{N}}{2\pi T_T}\left[\omega N \frac{2\pi}{\omega N} - 2\pi\right] = 0. \end{aligned} \tag{B.5}$$

Hence, (B.5) shows that the overall estimation error is zero-mean, as the under and overestimation errors compensate each other. Based on (B.5), the variance of the overall estimation error has the form

$$\begin{aligned} \mathrm{Var}[e_{\mathrm{LPP}}] &= p_{n_c=k} E[e_{\mathrm{LPP}\{\mathrm{n_c=k}\}}]^2 + p_{n_c=k+1} E[e_{\mathrm{LPP}\{\mathrm{n_c=k+1}\}}]^2 \\ &= \frac{(k+1)T_T - T_s}{T_T}\left[\frac{\frac{2\pi}{N}}{T_T} - \frac{k\frac{2\pi}{N}}{T_s}\right]^2 + \frac{T_s - kT_T}{T_T}\left[\frac{\frac{2\pi}{N}}{T_T} - \frac{(k+1)\frac{2\pi}{N}}{T_s}\right]^2, \end{aligned}$$

which, after some manipulations, can be finally expressed as

$$\mathrm{Var}[e_{\mathrm{LPP}}] = -\omega^2 + \frac{(2k(\omega)+1)}{T_s}\frac{2\pi}{N}\omega - \frac{k(\omega)(k(\omega)+1)}{T_s^2}\left(\frac{2\pi}{N}\right)^2. \tag{B.6}$$

Notice from (B.6) that the error variance has a non-trivial dependency on the problem data (the actual speed ω, the encoder resolution $2\pi/N$ and the sampling time T_s).

As for the estimation delay, in the LPP algorithm it is only due to sampling; hence, it is constant and equal to $\frac{1}{2}T_s$. Figures B.2(a) and B.2(b) depict the standard deviation of the relative error and the estimation delay as functions of the angular velocity. The relative error is defined as the ratio (in percent) of the estimation error and the (true) angular velocity.

For convenience, the angular velocity has been also converted into longitudinal speed assuming a tyre radius $r = 0.3$ m. Figure B.2(a) shows the dependence of the standard deviation of the estimation error and of the estimation delay on the sampling period (with $T_s = \{5, 10, 20\}$ ms), for a 48-teeth encoder; in Figures B.3(a) and B.3(b) the characteristic parameters are plotted for three different encoder resolutions ($N = \{32, 48, 64\}$) and for $T_s = 5$ ms.

The figures clearly show the main features and trade-offs of the LPP algorithm, which can be summarised as follows:

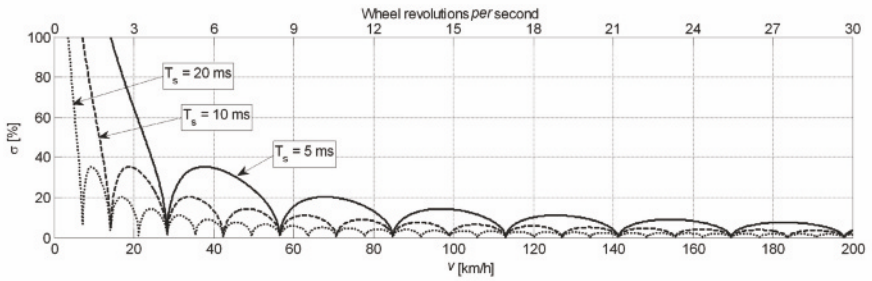

(a)

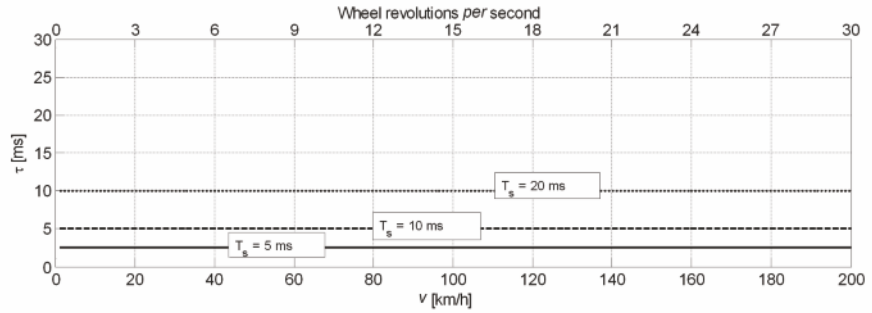

(b)

Figure B.2 Standard deviation of the estimation error (a) and delay (b) for different sampling periods and N = 48

- The choice of the sampling period is affected by a trade-off: longer sampling periods guarantee smaller errors but yield larger delays.
- From the signal processing standpoint, the choice of the number of teeth is easier: the higher the number of teeth the better the precision, without estimation delay degradation. Only mechanical and manufacturing considerations, besides cost restrictions, limit the number of teeth.
- The relative error variance is zero when the sampling time T_s is exactly a multiple of T_T. As has already been pointed out, this event occurs with probability 0.

B.2.1.2 The Fixed-position Algorithm

The second type of algorithm used for speed estimation is usually referred to as the fixed position algorithm or $1/\Delta$T (see, *e.g.*, [19, 130]).

In this case, the angular speed is estimated as

$$\hat{\omega}_{\Delta} = \frac{\frac{2\pi}{N}}{\left\lfloor \frac{T_T}{\Delta t} \right\rfloor \Delta t}, \tag{B.7}$$

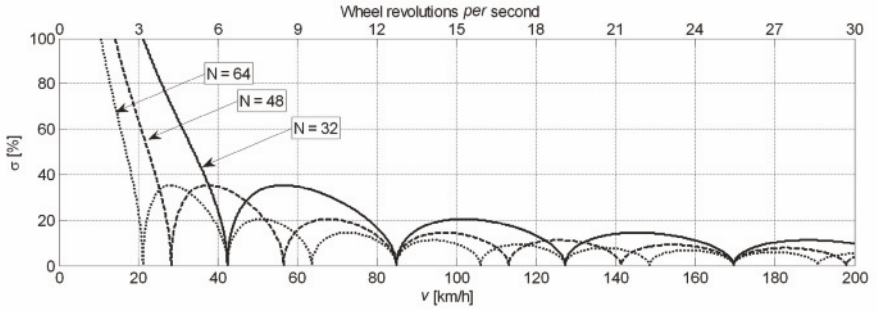

(a)

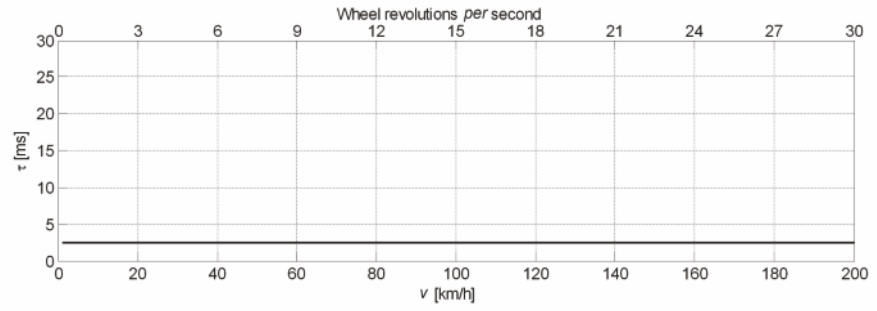

(b)

Figure B.3 Standard deviation of the estimation error (a) and delay (b) for different wheel encoder resolutions and $T_s = 5$ ms

where the symbol $\lfloor \cdot \rfloor$ indicates the floor truncation of a real number. For this algorithm, the condition $\Delta t < T_T$ must be fulfilled, where Δt is the microprocessor clock time resolution; note that this corresponds to an upper bound on the maximum measurable speed, *i.e.*, $\omega < 2\pi/N\Delta t$.

The corresponding estimation error e_Δ has the form

$$e_\Delta = \frac{\frac{2\pi}{N}}{T_T} - \frac{\frac{2\pi}{N}}{\left\lfloor \frac{T_T}{\Delta t} \right\rfloor \Delta t}. \tag{B.8}$$

Note that (B.8) shows that the estimation error for the $1/\Delta$T speed estimation algorithm is zero when the time interval between two lines is a multiple of the clock time resolution.

As a function of ω, the estimation error has a sawtooth behaviour, which is bounded; the envelope of the worst-case estimation error, say $\bar{e}_\Delta$, is given by

$$\bar{e}_\Delta = \frac{\frac{2\pi}{N}}{T_T} - \frac{\frac{2\pi}{N}}{T_T \Delta t},$$

which can be further simplified and finally written as

$$\bar{e}_{\Delta} = \frac{2\pi}{N}\left[\frac{\Delta t}{T_T(\omega)(T_T(\omega) - \Delta t)}\right]. \tag{B.9}$$

As can be seen from (B.9), the envelope of the sawtooth is a quadratic function of the speed. Instead, if the relative estimation error is computed, such an envelope becomes a linear function of the speed.

Finally, under the assumption that $\Delta t < T_T$, the estimation delay is given by

$$d_{\Delta} = T_T(\omega) + \frac{T_s}{2}. \tag{B.10}$$

As $T_T(\omega)$ is inversely proportional to the speed, notice that at low speed the delay d_{Δ} is the critical feature of this estimation approach. Figures B.4(a) and B.4(b) depict the relative error upper bound (in percent) and the estimation delay as functions of longitudinal and angular velocity; they are plotted for three different encoder resolutions $N = \{32, 48, 64\}$, with $\Delta t = 1$ μs and $T_s = 1$ ms.

Notice from Equation B.10 that the sampling period is not a critical parameter for this type of algorithm; as a matter of fact, provided that the maximum measurable speed requirement is satisfied it only affects the delay, with a $T_s/2$ contribution).

It is clear that this estimation algorithm guarantees a very high measurement precision. However, the estimation delay becomes critical at low speed; this time delay is critically dependent on the encoder resolution. Figure B.4(b) shows that – assuming that the maximum acceptable delay is 10 ms – using a 48-teeth encoder this limit is reached below approximately 18 km/h. Note that this is another consideration that must be taken into account for braking controller design, as it affects the overall data transmission delay, which must be accounted for. This issue makes impact also on the design of the activation and deactivation logic (see Section 3.7) by determining the maximum speed value below which the closed-loop control must be disengaged.

The comparison of the two estimation algorithms clearly shows that no globally optimal velocity estimation method exists. Each of the two methods performs well under different conditions and for different types of hardware. The LPP algorithm is critical for estimation accuracy, but guarantees small estimation delay also at low speed. On the other hand the $1/\Delta$T algorithm provides high estimation accuracy, but its time delay may be critical at low speed.

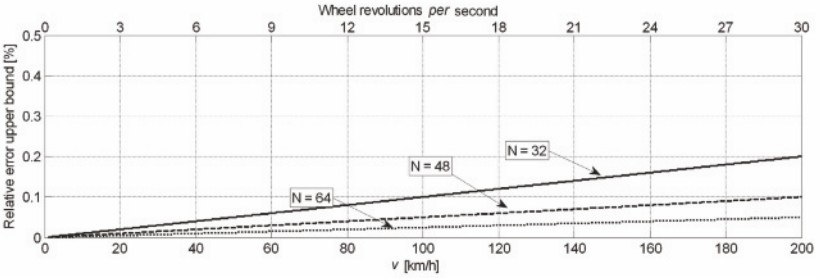

(a)

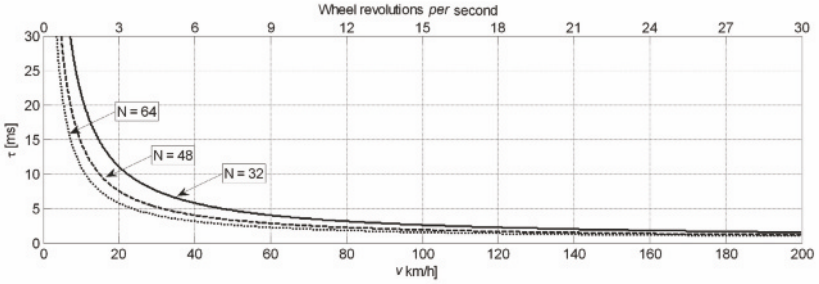

(b)

Figure B.4 Relative estimation error (a) and delay (b) for different wheel encoder resolutions, with $\Delta t = 1$ μs and $T_s = 1$ ms

B.2.2 Wheel Radius Calibration

Starting from the rotational speed of each wheel $\omega_i(t)$, $i = 1, \ldots, 4$ obtained from the wheel encoders, the signals must be low pass filtered. The filter cut-off frequency must be tuned considering both the noise level present in the measured data and the frequency content of the vehicle dynamics of interest. A good compromise is usually given by a cut-off frequency between 20 and 30 Hz.

Then, each $\omega_i(t)$, $i = 1, \ldots, 4$ must be converted into a linear velocity, that is the wheel speed at the tyre–road contact point. In order to do that, each rotational speed $\omega_i(t)$ needs to be multiplied by the corresponding wheel radius r_i. To do this, a reliable measure of the static radius, *i.e.*, the wheel radius measured when a negligible braking/traction force is applied to the four wheels, is required.

The *nominal* wheel radius can be either measured or estimated using an optical velocity sensor that can accurately measure the vehicle speed, with a coasting down test. The test consists of a slow deceleration from high speed to low speed with the transmission disengaged (see Figure B.5).

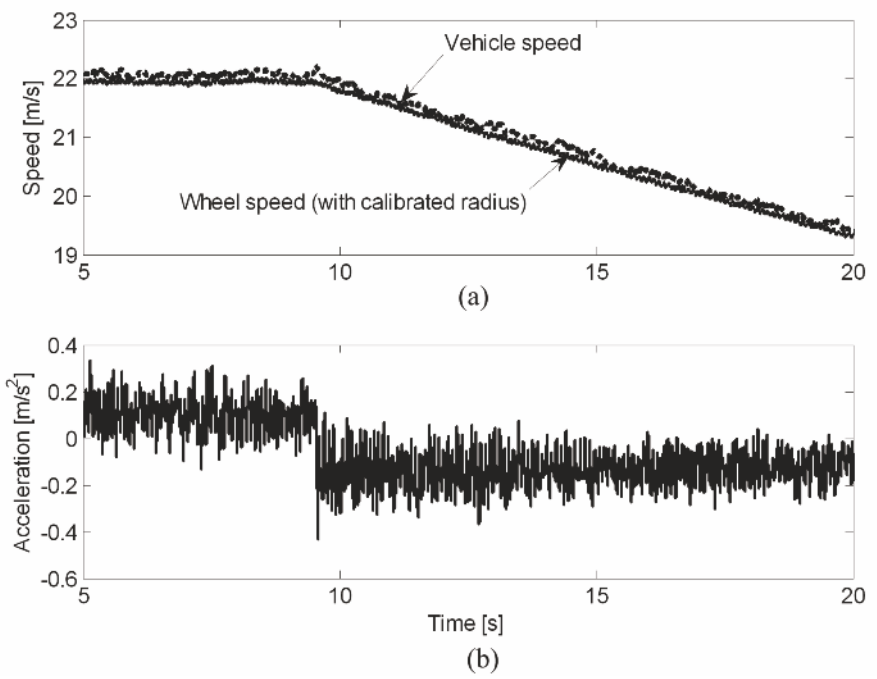

Figure B.5 Example of a coasting down test. (a) vehicle (*dotted line*) and wheel speed (*solid line*) after radius calibration, (b) longitudinal acceleration

In this test, the wheel slip can be assumed to be zero and the entire braking force (see the slightly negative longitudinal acceleration in Figure B.5 after the idle gear is engaged at time $t \cong 9.5$ s) attributed either to aerodynamic drag or rolling friction. The true vehicle speed v measured *via* the optical sensor can be used to calibrate the wheel radius by solving the following minimisation problem:

$$r_i = \underset{r_i}{\operatorname{argmin}} \int_{t_0}^{t_1} |\omega_i r_i - v| \, \mathrm{dt}, \quad i = 1, \cdots, 4, \tag{B.11}$$

where r_i, and $i = 1, \cdots, 4$ are the radii of the four wheels and ω_i are the corresponding wheel rotational speeds. The optimisation is done over the whole coasting-down manoeuvre. Notice that the estimation method described in (B.11) is debatable in principle, since the vertical load on the tyre depends on the load transfer and on the vertical component (lift) of the aerodynamic forces. A more accurate estimation procedure should provide a function $r(v)$ and not a constant number. However, in practice, this simplification is usually accepted. An example of radius calibration is shown in Figure B.6.

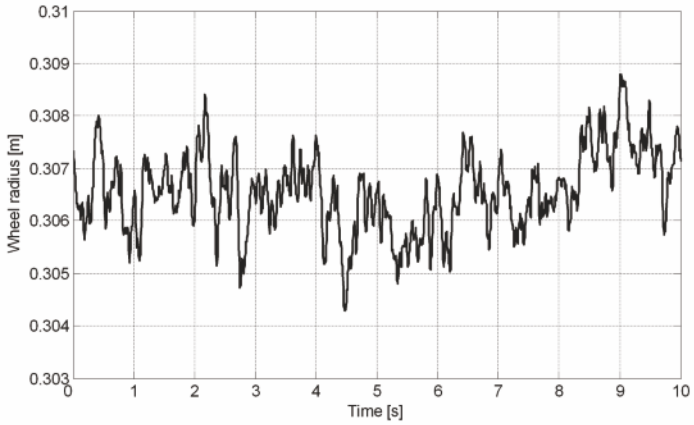

Figure B.6 Wheel static radius calibration results (front-right wheel), measured on a constant-speed test drive on high-grip asphalt road

After this calibration phase, the linear velocity of the four wheels at the tyre-road contact points can be computed as

$$v_i(t) = r_i \omega_i(t), \quad i = 1, \ldots, 4 \quad [\text{m/s}]. \tag{B.12}$$

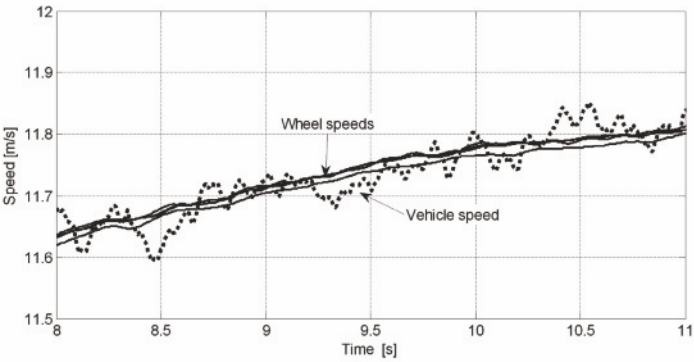

Figure B.7 Comparison between the four wheel linear speeds and the reference vehicle speed after static wheel radius calibration

To evaluate the results of the calibration phase, Figure B.7 shows the four wheel speeds computed according to Equation B.12 compared with the reference vehicle speed in a test with negligible acceleration. In such conditions, *i.e.*, when the wheel slip $\lambda = (v - \omega r)/v$ is close to zero, each wheel speed correctly equals the vehicle speed.

B.3 Analysis and Filtering of the Wheel Encoders' Signal

In the previous section the properties of the two basic velocity estimation algorithms were discussed. In the present section, we analyse some measurements of the velocity signal estimated with the fixed position algorithm. Note that although the experimental data were measured during tests performed on a motorcycle, the same considerations apply to four-wheeled vehicles.

Some interesting features can be highlighted by studying the spectra of the estimated wheel angular velocities in the case of a straight run at constant speed. Figures B.8 and B.9 show the spectra of the two wheels (front and rear); for comparison purposes, the angular velocities are plotted together with the front and rear suspension stroke signals and with the engine speed. The indicated frequencies (1X, 2X, 3X, *etc.*) represent the rotational speed harmonics, starting from the fundamental frequency 1X, *i.e.*, the frequency at which the wheel rolls. Specifically, by inspecting Figures B.8 and B.9, the following issues are of particular interest:

- Both front and rear speeds are clearly affected by a component at the fundamental frequency and at its higher harmonics. This can be explained either by the encoder not being perfectly aligned with the axis of the wheel or by the teeth of the encoder which are not uniformly distributed around the encoder itself. Each of these two situations typically occurs in practical applications.
- The suspension strokes show the intrinsic body resonance of the vehicle; however, it is very interesting to notice that, at the front wheel, the suspension stroke contains a large component at the fundamental rolling frequency of the front wheel. This points to a problem with the front wheel: it is not perfectly balanced (this may be caused by uneven tread consumption or other asymmetries in the tyre). Notice that this problem does not exist at the rear wheel, where the wheel noise at 1X is only due to a measurement problem.
- The speed signal of the front wheel is less noisy than that of the rear wheel, in particular in the frequency range between 1X and 2X. A comparison with the spectrum of the engine speed suggests that noise is mainly due to the transmission (chain pull effect, the anti-hop clutch and the compliance of the chain all transmit vibrations to the rear wheel).

The above analysis has shown the main disturbances contained in the rotational speed of the wheel. From a control system design perspective, any control algorithm that employs the wheel velocity or any other signal estimated using it may suffer from the component at 1X. The magnitude of this disturbance is remarkably large and may become critical if it acts within the closed-loop bandwidth. This limits the bandwidth of any control system that uses the wheel speed as a feedback signal, and this effect should be carefully evaluated and considered. To counteract this problem all wheel

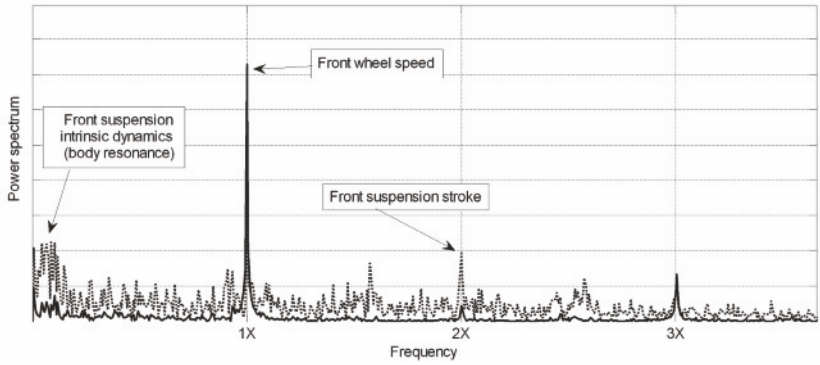

Figure B.8 Power spectra of the front wheel speed (*solid line*) and front suspension stroke (*dotted line*)

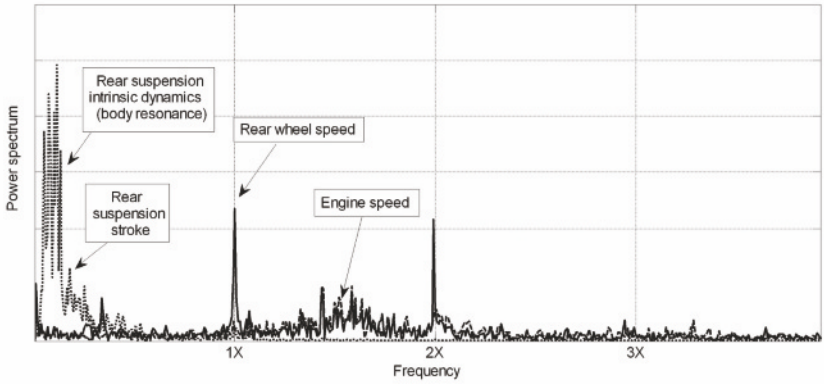

Figure B.9 Power spectra of the rear wheel speed (*solid line*) rear suspension stroke (*dotted line*) and engine speed (*dashed line*)

speed signals experiencing such a disturbance should be filtered, for example using the adaptive notch-filtering scheme illustrated in Figure B.10.

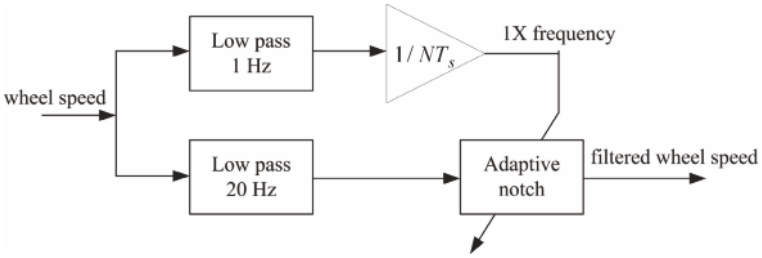

Figure B.10 Adaptive notch filtering scheme

Such a filtering approach works as follows. After a first low pass filtering stage (a first-order low pass filter with a cut-off frequency of approximately 20 Hz can be usually employed to process the considered signal), the 1X component is removed *via* a second-order adaptive notch filter (see, *e.g.*, [58, 89, 125]). To tune such a notch filter online, the rolling frequency of the wheel is estimated using a low pass filter with a cut-off frequency of 1 Hz. Once the rolling frequency is identified its principal harmonic is removed from the signal by means of the adaptive filter

$$H(z) = \frac{1 + W(n)z^{-1} + z^{-2}}{1 + bW(n)z^{-1} + b^2 z^{-2}}, \tag{B.13}$$

where $W(n)$ is given by

$$W(n) = -2\cos\left(\frac{f_{1X}(n)}{f_s} 2\pi\right),$$

and f_{1X} is the wheel rolling frequency, f_s the sampling frequency and b is a positive constant smaller than one representing the bandwidth of the notch filter.

Figures B.11 and B.12 show the effect of the filtering scheme. In Figure B.11 the power spectra of the measured signal and the adaptively filtered one are shown. For comparison purposes, the spectrum of the wheel speed filtered *via* a second-order low pass filter is also shown. In order to reach the same 1X attenuation level of the adaptive structure with a low pass filter, a cut-off frequency of 4 Hz was required. Note, however, that such a low pass filter would cancel many of the relevant dynamic features contained in the signal.

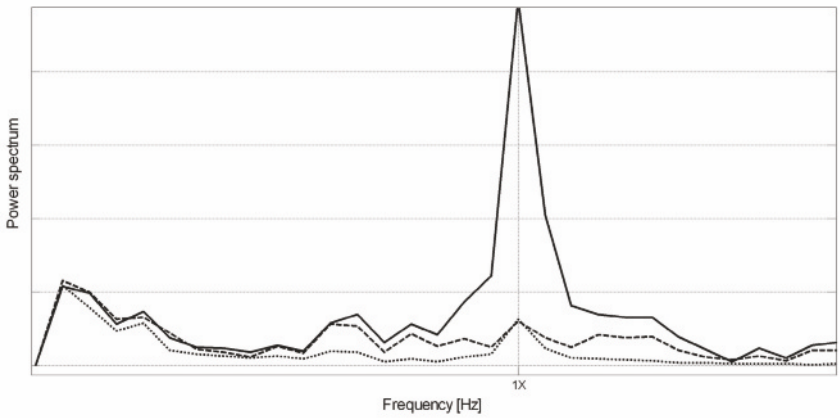

Figure B.11 Power spectra of the speed signal: measured (*solid line*), low pass filtered (*dotted line*) and notch filtered (*dashed line*)

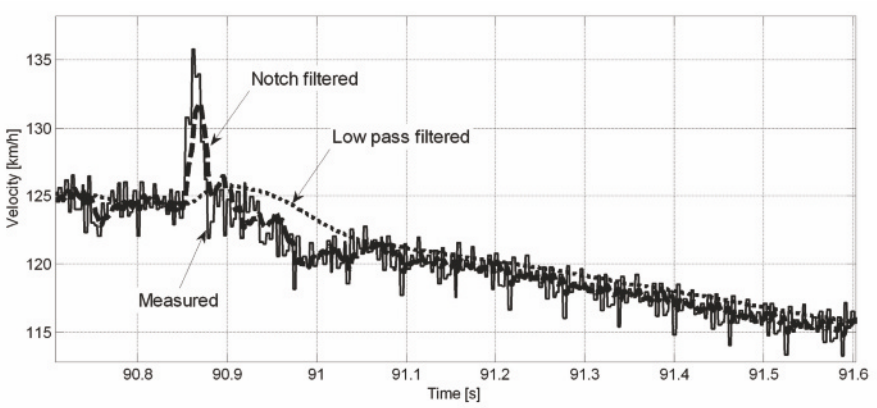

Figure B.12 Time histories of the speed signal: measured (*solid line*), low pass filtered (*dotted line*) and notch filtered (*dashed line*)

The issue is better highlighted with the help of Figure B.12 where the rear wheel velocity during a soft acceleration is shown. The 4 Hz low pass filter completely cancels the peak in the velocity, whereas the adaptive filter allows that feature to be retained.

B.4 Summary

In this appendix the problem of estimating the wheel speed from digital encoders has been discussed. Closed-form expressions for the estimation delay and error of the two most common algorithms used for this task have been derived. These expressions allowed us to draw guidelines and conclusions on the best choice of the estimation algorithm given the available hardware and working conditions. Further, we discussed how to perform the calibration of the wheel radius, which is another crucial step in computing velocity from encoder signals.

In the second part of the Appendix some filtering issues were discussed. They are mainly due to encoder mounting errors or uneven consumption of the tyre tread, which result in a noise component acting at the rolling frequency of the wheel. Finally, an adaptive filtering strategy which allows one to filter the noise without removing the wheel relevant dynamics was discussed.

References

1. Ackermann, J., Sienel, W.: Robust yaw damping of cars with front and rear wheel steering. IEEE Transactions on Control Systems Technology **1**(1), 15–20 (1993)
2. Alvarez, L., Horowitz, R., Olmos, L.: Adaptive emergency braking control with observer-based dynamic tire–road friction model and underestimation of friction coefficient. In: Proceedings of the 15th IFAC World Congress. Barcelona, Spain (2002)
3. Andreasson, J.: Global chassis control based on inverse vehicle dynamics models. Vehicle System Dynamics **44**, 321–328 (2006)
4. Antonelli, R., Astolfi, A.: Continuous Stirred Tank Reactors: Easy to stabilise? Automatica **10**(39), 1817–1827 (2003)
5. Åström, K., Murray, R.: Feedback Systems: An Introduction for Scientists and Engineers. Princeton University Press (2008)
6. Atkinson, D., Acarnley, P., Finch, J.: Observer for induction motor state and parameter estimation. IEEE Transactions on Industry Applications **27**, 1119–1127 (1991)
7. Bakker, E., Nyborg, L., Pacejka, H.B.: Tire modelling for use in vehicle dynamics studies. SAE Paper 870421 (1987)
8. Bakker, E., Pacejka, H.B., Lidner, L.: A new tire model with an application in vehicle dynamics studies. SAE Paper 890087 (1989)
9. Bascetta, L., Magnani, G., Rocco, P.: Velocity estimation: assessing the performance of non model-based techniques. IEEE Transactions on Control Systems Technology **17**(2), 424–433 (2009)
10. Belanger, P., Dobovolny, P., Helmy, A., Zhang, X.: Estimation of angular velocity and acceleration from shaft-encoder measurements. The International Journal of Robotics Research **17**(11), 1225–1230 (1998)
11. Ben-Brahim, L., Tadakum, S., Akdag, A.: Speed control of induction motor without rotational transducers. IEEE Transactions on Industry Applications **35**(4), 844–850 (1999)
12. Breuer, B., Eichorn, U., Roth, J.: Measurement of tyre–road friction ahead of the car and inside the tyre. In: Proceedings of the International Symposium on Advanced Vehicle Control, AVEC'92, pp. 347–353 (1992)
13. Bridgestone/Firestone Inc.: Method of monitoring conditions of vehicle tires and tires containing a monitoring device therein. U.S. Patent 5.573.611 (1996)
14. Brown, R., Schneider, S.: Velocity Observations from Discrete Position Encoders. In: IEEE Conference on Decision and Control, vol. 6, pp. 1111–1118 (1987)

15. Buckholtz, K.: Reference input wheel slip tracking using sliding mode control. In: SAE Technical Paper 2002-01-0301 (2002)
16. Burckhardt, M.: Fahrwerktechnik: Radschlupf-Regelsysteme. Vogel Verlag, Würzburg (1993)
17. Canale, M., Fagiano, L.: Vehicle yaw control using a fast NMPC approach. In: Proceedings of the 47th IEEE Conference on Decision and Control, pp. 5360–5365. Cancun, Mexico (2008)
18. Canale, M., Fagiano, L., Ferrara, A., Vecchio, C.: Comparing internal model control and sliding-mode approaches for vehicle yaw control. IEEE Transactions on Intelligent Transportation Systems **10**(1), 31–41 (2009)
19. Carpenter, P., Brown, R., Heinen, J., Schneider, S.: On algorithms for velocity estimation using discrete position encoders. In: IEEE IECON 21st International Conference on Industrial Electronics, Control and Instrumentation, vol. 2, pp. 844–849 (1995)
20. Chou, H., d'Andréa-Novel, B.: Global vehicle control using differential braking torques and active suspension forces. Vehicle System Dynamics **43**(4), 261–284 (2005)
21. Corno, M., Savaresi, S.M., Tanelli, M., Fabbri, L.: On optimal motorcycle braking. Control Engineering Practice **16**(6), 644–657 (2008)
22. di Bernardo, M., Budd, C., Champneys, A., Kowalczyk, P.: Piecewise smooth dynamical systems: theory and applications (2007). Applied Mathematical Sciences, vol. 163
23. Drakunov, S., Özgüner, U., Dix, P., Ashrafi, B.: ABS control using optimum search *via* sliding modes. IEEE Transactions on Control Systems Technology **3**(1), 79–85 (1995)
24. Eichorn, U., Roth, J.: Prediction and monitoring of tire–road friction. In: Proceedings of 20th FISITA World Congress, Montreal (1992)
25. Falcone, P., Tufo, M., Borrelli, F., Asgari, J., Tseng, H.: A linear time varying model predictive control approach to the integrated vehicle dynamics control problem in autonomous systems. In: 46th IEEE Conference on Decision and Control, CDC 2007, pp. 2980–2985 (2007)
26. Fu, W., Fang, Z., Zhao, Z.: Periodic solutions and harmonic analysis of an antilock brake system with piecewise-nonlinearity. Journal of Sound and Vibration **246**(3), 543–550 (2001)
27. Gissinger, G., Menare, C., Constans, A.: A mechatronic conception of a new intelligent braking system. Control Engineering Practice **11**, 163–170 (2003)
28. Gunsaulus, A.: Rolling wheels gather no skids. SAE Transactions **61**, 191–193 (1953)
29. Gustafsson, F.: Slip-based tire-road friction estimation. Automatica **33**(6), 1087–1099 (1997)
30. Hac, A., Doman, D., Oppenheimer, M.: Unified control of brake-and steer-by-wire systems using optimal control allocation methods. In: Proceedings of the SAE 2006 World Congress and Exhibition. Detroit (2006). SAE paper 2006-01-0924
31. Hakanen, J.: Second-generation TPMS. Tire Technology International **1**, 60–62 (2004)
32. Hedenetz, B., Belschner, R.: Brake-by-wire without mechanical backup by using a TTP-communication network. SAE transactions **107**(6), 1678–1686 (1999)
33. Holmström, K., Petersson, J.: A review of the parameter estimation problem of fitting positive exponential sums to empirical data. Applied Mathematics and Computation **126**(1), 31–61 (2002)
34. Imsland, L., Johansen, T., Fossen, T., Fjær Grip, H., Kalkkuhl, J., Suissa, A.: Vehicle velocity estimation using nonlinear observers. Automatica **42**(12), 2091–2103 (2006)

35. Isidori, A.: Nonlinear control systems, vol. II. Springer, New York (1999)
36. Janabi-Sharifi, F., Hayward, V., Chen, C.: Discrete-time adaptive windowing for velocity estimation. IEEE Transactions of Control Systems Technology **8**(6), 1003–1009 (2000)
37. Jiang, F., Gao, Z.: An adaptive nonlinear filter approach to the vehicle velocity estimation for ABS. In: Proceedings of the 2000 IEEE International Conference on Control Application, Anchorage (2000)
38. Jiang, F., Gao, Z.: An application of nonlinear PID control to a class of truck ABS problems. In: Proceedings of the IEEE Conference on Decision and Control, Orlando, FL, USA (2001)
39. Johansen, T., Petersen, I., Kalkkuhl, J., Lüdemann, J.: Hybrid control strategies in ABS. In: Proceedings of the American Control Conference, Washington DC, USA (2001)
40. Johansen, T., Petersen, I., Kalkkuhl, J., Lüdemann, J.: Wheel slip control in ABS brakes using gain scheduled constrained LQR. In: Proceedings of the American Control Conference, Porto, Portugal (2001)
41. Johansen, T., Petersen, I., Kalkkuhl, J., Lüdemann, J.: Gain-scheduled wheel slip control in automotive brake systems. IEEE Transactions on Control Systems Technology **11**(6), 799–811 (2003)
42. Kavanagh, R.: Shaft encoder characterization *via* theoretical model of differentiator with both differential and integral nonlinearities. IEEE Transactions on Instrumentation and Measurements **49**(4), 795–801 (2000)
43. Kavanagh, R.: Performance analysis and compensation of M/T-type digital tachometers. IEEE Transactions on Instrumentation and Measurements **50**(4), 965–970 (2001)
44. Khalil, H.: Nonlinear Systems. 2nd Edition, Prentice Hall, Upper Saddle River, NJ (1996)
45. Kiencke, U., Nielsen, L.: Automotive Control Systems. Springer, Berlin (2000)
46. Kim, S., Park, T., Yoo, J., Park, G.: Speed-sensorless vector control of an induction motor using neural network speed estimation. IEEE Transactions on Industrial Electronics **48**(3), 609–614 (2001)
47. Klein, R., Daiss, A., Eichfeld, H.: Antilock braking system and vehicle speed estimation using fuzzy logic. In: Proceedings of the 1st Embedded Computing Conference, Paris (1996)
48. Kobayashi, K., Cheok, K., Watanabe, K.: Estimation of absolute vehicle speed using fuzzy logic rule-based Kalman filter. In: Proceedings of the 1995 American Control Conference, Seattle, WA (1996)
49. Kuo, C., Yeh, E.: A four-phase control scheme of an anti-skid brake system for all road conditions. Proceedings of the Institution of Mechanical Engineers. Part D, Journal of Automobile Engineering **206**(4), 275–283 (1992)
50. Kuznetsov, Y.A.: Elements of Applied Bifurcation Theory, second edn. Springer, New York (1998). Applied Mathematical Sciences, vol. 112
51. La Salle, J., Lefschetz, S.: Stability by Lyapunov's Direct Method. Academic Press, New York (1961)
52. Lakehal-Ayat, M., Fenaux, E., Lamnabhi-Lagarrigue, F., Zarka, F.: On global chassis control: combined braking and cornering and yaw rate control. In: Proceedings of the 5th International Symposium on Advanced Vehicle Control, Ann Arbor, MI, pp. 22–24 (2000)
53. Layne, J., Passino, K., Yurkovich, S.: Fuzzy learning control for antiskid braking systems. IEEE Transactions on Control Systems Technology **1**(2), 122–129 (1993)
54. Lee, T., Hsu, C., S, L.: Robust hybrid control for antilock braking systems. In: Proceedings of the IEEE International Conference on Systems, Man and Cybernetics, Washington D.C. (2003)

55. Leen, G., Heffernan, D.: Expanding automotive electronic systems. Computer **35**(1), 88–93 (2002)
56. Lemkin, M., Yang, P., Wuang, A., Jones, J., Auslander, D.: Velocity estimation from widely spaced encoder pulses. In: Proceedings of the American Control Conference, pp. 998–1002. Seattle,Washington D.C. (1995)
57. Levi, E., Wang, M.: A speed estimator for high performance sensorless control of induction motor in the field weakening region. IEEE Transactions on Power Electronics **17**, 365–378 (2002)
58. Lim, Y.C., Zou, Y.X., Zheng, N.: A piloted adaptive notch filter. IEEE Transactions on Signal Processing **53**(4), 1310–1323 (2005)
59. Lin, C., Hsu, C.: Self-learning fuzzy sliding-mode control for antilock braking systems. IEEE Transactions on Control Systems Technology **11**(2), 273–278 (2002)
60. Lin, C., Hsu, C.: Neural-network hybrid control for antilock braking systems. IEEE Transactions on Neural Networks **14**(2), 351–359 (2003)
61. Ljung, L.: System Identification: Theory for the User. Prentice-Hall, Upper Saddle River, NJ (1999)
62. Ljung, L., Söderström, T.: Theory and Practice of Recursive Identification. MIT Press, Cambridge, MA (1983)
63. Mancosu, F.: Data from tire as a full system to be used in the vehicle. In: Tire Technology 2005, Cologne, Germany (2005). Oral presentation
64. Mané: Ergodic Theory and Differentiable Dynamics. Springer, Berlin (1987)
65. Muller, M., Uchanski, M., Hedrick, K.: Estimation of the maximum tire-road coefficient. Journal of Dynamic Systems, Measurement and Control **125**, 607–617 (2003)
66. Ohmae, T., Matsuda, T., Makiyama, K., Tachikawa, M.: A microprocessor controlled high accuracy wide range speed regulator for motor drives. IEEE Transactions on Industrial Electronics **IE-29**, 207–211 (1982)
67. Olson, B., Shaw, S., Stepan, G.: Nonlinear dynamics of vehicle traction. Vehicle Systems Dynamics **40**(6), 377–399 (2003)
68. Olson, B., Shaw, S., Stepan, G.: Stability and bifurcation of longitudinal vehicle braking. Nonlinear Dynamics **40**(4), 339–365 (2005)
69. Ono, E., Asano, K., Sugai, M., Ito, S., Yamamoto, M., Sawada, M., Yasui, Y.: Estimation of automotive tire force characteristics using wheel velocity. Control Engineering Practice **11**, 1361–1370 (2003)
70. Ouwerkerk, H., Guntur, R.: Skid prediction. Vehicle System Dynamics **1**(2), 6788 (1972)
71. Pacejka, H.B.: Tyre and Vehicle Dynamics. Buttherworth–Heinemann, Oxford (2002)
72. Pacejka, H.B., Sharp, R.S.: Shear force developments by pneumatic tyres in steady-state conditions: a review of modeling aspects. Vehicle System Dynamics **29**, 409–422 (1991)
73. Panzani, G., Corno, M., Tanelli, M., Zappavigna, A., Savaresi, S.M., Fortina, A., Campo, S.: Combined performance and stability optimisation via central transfer case active control in four-wheeled vehicles. In: Proceedings of the combined 48th IEEE Conference on Decision and Control and 28th Chinese Control Conference, pp. 3551–3556. Shanghai, China (2009)
74. Pasillas-Lépine, W.: Hybrid modeling and limit cycle analysis for a class of five-phase anti-lock brake algorithms. Vehicle System Dynamics **44**(2), 173–188 (2006)
75. Pasterkamp, W., Pacejka, H.B.: The tire as a sensor to estimate friction. Vehicle System Dynamics **27**, 409–422 (1997)
76. Peng, F., Fukao, T.: Robust speed identification for speed sensorless vector control of induction motors. IEEE Transactions on Industry Applications **30**(5), 1234–1240 (1994)

77. Petersen, I.: Wheel slip control in ABS brakes using gain scheduled optimal control with constraints. Master's thesis, Norwegian University of Science and Technology, Trondheim, Norway (2003)
78. Phillips, S., Branicky, M.: Velocity estimation using quantized measurements. In: Proceedings of the IEEE Conference on Decision and Control, pp. 4847–4852 (2003)
79. Pirelli Pneumatici S.p.A.: Method and system for controlling the behaviour of a vehicle by controlling its tyres. European Patent 1202867B1 (2004)
80. Piyabongkarn, D., Rajamani, R., Lew, J., Yu, H.: On the use of torque-biasing systems for electronic stability control: limitations and possibilities. IEEE Transactions on Control Systems Technology **15**(3), 581–589 (2007)
81. Poussot-Vassal: Robust multivariable linear parameter varying automotive global chassis control. Ph.D. thesis, Grenoble INP, GIPSA-lab, Grenoble, France (2008)
82. Proca, A., Keyhani, A., Akdag, A.: Sensorless sliding-mode control of induction motors using operating condition dependent models. IEEE Transactions on Energy Conversion **18**(2), 205–212 (2003)
83. Quinn, B., Fernandes, M.: A fast technique for the estimation of frequency. Biometrika **78**(3), 489–497 (1991)
84. Rajamani, R.: Vehicle Dynamics and Control. Mechanical Engineering Series, Springer, New York (2006)
85. Ray, L.: Nonlinear state and tire force estimation for advanced vehicle control. IEEE Transactions on Control Systems Technology **3**(1), 117–124 (1995)
86. Ray, L.: Nonlinear tire force estimation and road friction identification: simulation and experiments. Automatica **33**(10), 1819–1833 (1997)
87. Robert Bosch GmbH: Automotive Handbook, 7th Edition. Wiley, New York (2008)
88. SAE Society of Automotive Engineers, Warrendale, PA: Antilock Brake Review (1992). SAE Standard: J2246
89. Savaresi, S.M., Bittanti, S., So, H.: Closed-form unbiased frequency estimation of a noisy sinusoid using notch filters. IEEE Transactions on Automatic Control **48**(7), 1285–1292 (2003)
90. Savaresi, S.M., Tanelli, M., Cantoni, C.: Mixed slip-deceleration control in automotive braking systems. ASME Journal of Dynamic Systems, Measurement and Control **129**(1), 20–31 (2006)
91. Savaresi, S.M., Tanelli, M., Cantoni, C., Charalambakis, D., Previdi, F., Bittanti, S.: Slip-deceleration control in anti-lock braking systems. In: Proceedings of the 16th IFAC World Congress, Prague, Czech Republic (2005)
92. Savaresi, S.M., Tanelli, M., Langthaler, P., Del Re, L.: Identification of tire–road contact forces by in-tire accelerometers. In: Proceedings of the 14th IFAC Symposium on System Identification, SYSID 2006 (2006)
93. Savaresi, S.M., Tanelli, M., Langthaler, P., Del Re, L.: New regressors for the identification of tire deformation in road vehicles *via* in-tire accelerometers. Transactions on Control Systems Technology **16**, 769–780 (2008)
94. Sawase, K., Sano, Y.: Application of active yaw control to vehicle dynamics by utilizing driving/braking force. JSAE Review **20**(2), 289–295 (1999)
95. Schinkel, M., Hunt, K.: Anti-lock braking control using a sliding mode like approach. In: Proceedings of the American Control Conference, Anchorage, Alaska (2002)
96. Semmler, S., Fischer, D., Isermann, R., Schwarz, R., Rieth, P.: Estimation of vehicle velocity using brake-by-wire actuators. In: Proceedings of the 15th IFAC World Congress, Barcelona, Spain (2002)
97. Shi, K., Chan, T., Wong, Y., Ho, S.: Speed estimation on an induction motor drive using an optimized extended kalman filter. IEEE Transactions on Industrial Electronics **49**, 124–133 (2002)

98. Skogestad, S., Postlethwaite, I.: Multivariable feedback control: analysis and design. Wiley, New York (2005)
99. Söderström, T., Stoica, P.: System Identification. Prentice Hall, London (1989)
100. Solyom, S., Rantzer, A., Lüdemann, J.: Synthesis of a model-based tire slip controller. Vehicle System Dynamics **41**(6), 477–511 (2004)
101. Somakumar, R., Chandrasekhar, J.: Intelligent anti-skid brake controller using a neural network. Control Engineering Practice **7**, 611–621 (1999)
102. Strogatz, S.: Nonlinear Dynamics and Chaos: With Applications to Physics, Biology, Chemistry, and Engineering. Addison Wesley, Reading, MA (1994)
103. Su, Y., Zheng, C., Mueller, P., Duan, B.: A simple improved velocity estimation for low-speed regions based on position measurements only. IEEE Transactions on Control Systems Technologies **14**(5), 937–942 (2006)
104. Su, Y., Zheng, C., Sun, D., Duan, B.: A simple nonlinear velocity estimator for high performance motion control. IEEE Transactions on Industrial Electronics **52**(4), 1161–1169 (2005)
105. Tanelli, M., Astolfi, A., Savaresi, S.M.: Non-local extremum seeking control for active braking control systems. In: Proceedings of the Conference on Control and Applications CCA 2006, Munich, Germany, pp. 891–896 (2006)
106. Tanelli, M., Astolfi, A., Savaresi, S.M.: Robust nonlinear proportional-integral control for active braking control systems. In: Proceedings of the 45th Conference on Decision and Control, CDC 2006, San Diego, CA, pp. 1745–1750 (2006)
107. Tanelli, M., Astolfi, A., Savaresi, S.M.: Robust nonlinear output feedback control for brake-by-wire control systems. Automatica **44**(4), 1078–1087 (2008)
108. Tanelli, M., Corno, M., Boniolo, I., Savaresi, S.: Active braking control of two-wheeled vehicles on curves. International Journal of Vehicle Autonomous Sytems **7**(3/4), 243–269 (2009)
109. Tanelli, M., Gragnani, A., Astolfi, A., Savaresi, S.M.: Optimising the braking performance via nonlinear analysis and bifurcation theory. In: Proceedings of the 47th IEEE Conference on Decision and Control. Cancun, Mexico, December 9-11, 2008, pp. 4396–4401 (2008)
110. Tanelli, M., Osorio, G., di Bernardo, M., Savaresi, S.M., Astolfi, A.: Limit cycles analysis in hybrid anti-lock braking systems. In: Proceedings of the 46th Conference on Decision and Control, CDC 2007, New Orleans, LA, pp. 3865–3870 (2007)
111. Tanelli, M., Osorio, G., di Bernardo, M., Savaresi, S.M., Astolfi, A.: Existence, stability and robustness analysis of limit cycles in hybrid anti-lock braking systems. International Journal of Control **82**, 659–678 (2008)
112. Tanelli, M., Osorio, G., di Bernardo, M., Savaresi, S.M., Astolfi, A.: Existence, stability and robustness analysis of limit cycles in hybrid anti-lock braking systems. International Journal of Control **82**, 659–678 (2009)
113. Tanelli, M., Piroddi, L., Savaresi, S.M.: Real-time identification of tire–road friction conditions. IET Control Theory and Applications **3**(7), 891–906 (2009)
114. Tanelli, M., Piroddi, L., Savaresi, S.M.: Real-time identification of tire-road friction conditions. IET Control Theory & Applications **3**, 891–906 (2009)
115. Tanelli, M., Prandini, M., Codecà, F., Moia, A., Savaresi, S.M.: Analysing the interaction between braking control and speed estimation: the case of two-wheeled vehicles. In: Proceedings of the 47th IEEE Conference on Decision and Control. Cancun, Mexico, December 9-11, 2008, pp. 5372–5377 (2008)
116. Tanelli, M., Sartori, R., Savaresi, S.M.: Sliding mode slip-deceleration control for brake-by-wire control systems. European Journal of Control **6**, 593–611 (2007)
117. Tanelli, M., Sartori, R., Savaresi, S.M.: Sliding mode slip-deceleration control for brake-by-wire control systems. In: Proceedings of the fifth IFAC Symposium on Advances in Automotive Control. August 20-22, Aptos, CA, pp. 135–142 (2007)

118. Tanelli, M., Savaresi, S.M.: Friction-curve peak detection by wheel-deceleration measurements. In: Proceedings of the IEEE Conference on Intelligent Transportation Systems, ITSC 2006, Toronto (2006)
119. Tanelli, M., Savaresi, S.M., Cantoni, C.: Longitudinal vehicle speed estimation for traction and braking control systems. In: Proceedings of the 2006 Conference on Control and Applications, CCA 2006, Munich, Germany (2006)
120. Tanelli, M., Savaresi, S.M., Mergenthaler, A.: Dynamic coupling analysis between front and rear axle for ABS systems design. In: Proceedings of the Fifth IFAC Symposium on Advances in Automotive Control, August 20-22, Aptos, CA, pp. 391–398 (2007)
121. Tjønnås, J., Johansen, T.: Adaptive optimizing dynamic control allocation algorithm for yaw stabilization of an automotive vehicle using brakes. In: Proceedings of the 14th Mediterranean Conference on Control and Automation, 2006. MED '06., pp. 1–6 (2006)
122. Ünsal, C., Kachroo, P.: Sliding mode measurement feedback control for antilock braking systems. IEEE Transactions on Control Systems Technology **7**(2), 271–281 (1999)
123. Watanabe, K., Kinase, K., Kobayashi, K.: Absolute speed measurement of vehicles from noisy acceleration and erroneous wheel speed. In: Proceedings of the Symposium on Intelligent Vehicles (1993)
124. Wellstead, P., Pettit, N.: Analysis and redesign of an antilock brake system controller. IEE Proceedings on Control Theory and Applications **144**, 413–426 (1997)
125. Widrowet, B.: Adaptive noise canceling: Principle and applications. Proceedings of IEEE **63**, 1962–1716 (1975)
126. Wiggins, S.: Introduction to Applied Nonlinear Dynamical Systems and Chaos. Springer, New York (2003)
127. Canudas de Wit, C., Petersen, M., Shiriaev, A.: A new nonlinear observer for tire/road distributed contact friction. In: Proceedings of the 42nd IEEE Conference on Decision and Control, Maui, HI (2003)
128. Yi, J., Alvarez, L., Claeys, X., Horowitz, R.: Emergency braking control with an observer-based dynamic tire/road friction model and wheel angular velocity measurement. Vehicle System Dynamics **39**(2), 81–97 (2003)
129. Yi, J., Alvarez, L., Horowitz, R.: Adaptive emergency braking control with underestimation of friction coefficient. Transactions on Control System Technology **10**(3), 381–392 (2002)
130. Yien, C.: Incremental encoder errors: Causes and ways to reduce them. In: Proceedings of the International Intelligent Motion Conference, pp. 110–121. N'urberg,Germany (1992)
131. Yu, J.: A robust adaptive wheel-slip controller for antilock brake system. In: Proceedings of the 36th IEEE Conference on Decision and Control, San Diego, CA (1997)
132. Zin, A., Sename, O., Gaspar, P., Dugard, L., Bokor, J.: An lpv/h-∞ active suspension control for global chassis technology: Design and performance analysis. In: Proceedings of the American Control Conference, Minneapolis, MN, pp. 2945–2950 (2006)

Index

abbreviations, list of, xix

Barbashin–Krasovskii's theorem, 209
braking system
  brake-by-wire, 8
  continuous dynamics, 10
  discrete dynamics, 5, 85
  electro-hydraulic, 8
  electro-mechanical, 8, 65, 138
  hydraulic, 5, 85, 86

Chetaev's theorem, 210

domain of attraction, 209
double-corner model, 27
  equilibrium points, 42
  linearisation, 43
  slip control, 74, 110
  stability, 46

equilibrium point, 31, 42, 205
  unstable, 150, 152, 160
  asymptotically stable, 152, 208, 213
  globally asymptotically stable, 77, 210, 213
  globally exponentially stable, 77, 210
  hyperbolic, 217
  locally asymptotically stable, 32, 36, 76, 212
  non-hyperbolic, 217
  stable, 146, 208
  unstable, 32, 33, 36, 210, 212
equilibrium state, *see* equilibrium point

friction force
  estimation, 182
  lateral, 18
  lateral friction coefficient, 19
  longitudinal, 18, 184
  longitudinal friction coefficient, 19, 23
  vertical, 184
friction model
  Burckhardt model, 23, 166
  Pacejka model, 20
Function
  positive definite, 225
  proper, 225
function
  positive definite, 147, 208
  positive semidefinite, 208
  proper, 213
  radially unbounded, *see* proper, *see* proper

index theory, 150, 219

LaSalle
  invariance theorem, 212
  theory, 212
level set, 150, 208
Level surface, *see* Lyapunov, surface
limit cycle, 85, 88, 149, 150, 218
  stability, 99, 152, 218
limit cycles, 90
linear system, 203
Lyapunov
  direct method, 207
  function, 77, 208
  linear approximation method, *see* linearisation method
  linearisation method, 36, 39, 43, 211
  second method, *see* direct method
  stability, 206
  stability theorem, 207

surface, 208

manifold
centre, 217
stable, 217
unstable, 217

nonlinear system
autonomous, 203
non autonomous, 203
second order, 86, 214
solution of, 204
time-invariant, 203
time-varying, 203
unforced, 203

orbit, 218
periodic, 152, 218
stability of, 152, 223

Poincaré map, 99, 221
Poincaré–Bendixon
criterion, 221
Poincaré-Bendixon
theorem, 152, 219

set
connected, 204
invariant, 146, 212
positively invariant, 213, 221
single-corner model, 24
equilibrium points, 31
linearisation, 36
slip control, 55, 144
stability, 39
stability
local, 146
asymptotic, 206
exponential, 210
in the sense of Lyapunov, 206, 225
local, 211
state plane, 86, 214
state portrait, 214

trapping region, 150, 220
tyre
sideslip angle, 18
angular speed, 19
camber angle, 18
radius, 19
relaxation dynamics, 24

vector field, 214
vehicle speed, 19
estimation, 112
vertical force, 18

wheel deceleration control
linear, 58
wheel slip, 18
estimation, 107
wheel slip control
linear, 55
nonlinear, 144

Other titles published in this series (continued):

Soft Sensors for Monitoring and Control of Industrial Processes
Luigi Fortuna, Salvatore Graziani, Alessandro Rizzo and Maria G. Xibilia

Adaptive Voltage Control in Power Systems
Giuseppe Fusco and Mario Russo

Advanced Control of Industrial Processes
Piotr Tatjewski

Process Control Performance Assessment
Andrzej W. Ordys, Damien Uduehi and Michael A. Johnson (Eds.)

Modelling and Analysis of Hybrid Supervisory Systems
Emilia Villani, Paulo E. Miyagi and Robert Valette

Process Control
Jie Bao and Peter L. Lee

Distributed Embedded Control Systems
Matjaž Colnarič, Domen Verber and Wolfgang A. Halang

Precision Motion Control (2nd Ed.)
Tan Kok Kiong, Lee Tong Heng and Huang Sunan

Optimal Control of Wind Energy Systems
Iulian Munteanu, Antoneta Iuliana Bratcu, Nicolaos-Antonio Cutululis and Emil Ceangă

Identification of Continuous-time Models from Sampled Data
Hugues Garnier and Liuping Wang (Eds.)

Model-based Process Supervision
Arun K. Samantaray and Belkacem Bouamama

Diagnosis of Process Nonlinearities and Valve Stiction
M.A.A. Shoukat Choudhury, Sirish L. Shah, and Nina F. Thornhill

Magnetic Control of Tokamak Plasmas
Marco Ariola and Alfredo Pironti

Real-time Iterative Learning Control
Jian-Xin Xu, Sanjib K. Panda and Tong H. Lee

Deadlock Resolution in Automated Manufacturing Systems
ZhiWu Li and MengChu Zhou

Model Predictive Control Design and Implementation Using MATLAB®
Liuping Wang

Fault-tolerant Flight Control and Guidance Systems
Guillaume Ducard

Predictive Functional Control
Jacques Richalet and Donal O'Donovan

Fault-tolerant Control Systems
Hassan Noura, Didier Theilliol, Jean-Christophe Ponsart and Abbas Chamseddine

Control of Ships and Underwater Vehicles
Khac Duc Do and Jie Pan

Detection and Diagnosis of Stiction in Control Loops
Mohieddine Jelali and Biao Huang

Stochastic Distribution Control System Design
Lei Guo and Hong Wang

Dry Clutch Control for Automotive Applications
Pietro J. Dolcini, Carlos Canudas-de-Wit, and Hubert Béchart

Active Control of Flexible Structures
Alberto Cavallo, Giuseppe De Maria, Ciro Natale and Salvatore Pirozzi

Nonlinear and Adaptive Control Design for Induction Motors
Riccardo Marino, Patrizio Tomei and Cristiano M. Verrelli

Advanced Control and Supervision of Mineral Processing Plants
Daniel Sbárbaro and René del Villar (Eds.)